Helsinki University of Technology Laboratory of Space Technology Publications
Teknillisen korkeakoulun Avaruustekniikan laboratorion julkaisuja
Espoo 2007 REPORT 69

Investigation of the Microwave Signatures of the Baltic Sea Ice

Marko Mäkynen

Dissertation for the degree of Doctor of Science in Technology to be presented with due permission of the Department of Electrical and Communications Engineering, for public examination and debate in Auditorium S4 at Helsinki University of Technology (Espoo, Finland) on the 4th of May, 2007, at 12 noon.

Helsinki University of Technology
Department of Electrical and Communications Engineering
Laboratory of Space Technology

Teknillinen korkeakoulu
Sähkö- ja tietoliikennetekniikan osasto
Avaruustekniikan laboratorio

Distribution:
Helsinki University of Technology
Laboratory of Space Technology
P.O.Box 3000
FIN-02015 HUT
Finland

Tel. +358 9 451 2378
Fax +358 9 451 2898

Email: marko.makynen@tkk.fi
http://www.space.tkk.fi

ISBN-978-951-22-8740-6 (printed)
ISBN-978-951-22-8741-3 (electronic)
ISSN 0786-8154

Picaset Oy
Helsinki 2007

ABSTRACT OF DOCTORAL DISSERTATION	HELSINKI UNIVERSITY OF TECHNOLOGY P.O. BOX 1000, FI-02015 TKK http://www.tkk.fi

Author Marko Mäkynen

Name of the dissertation
Investigation of the Microwave Signatures of the Baltic Sea Ice

Manuscript submitted 16.10.2006	Manuscript revised 2.3.2007

Date of the defence 4.5.2007

☐ Monograph ☒ Article dissertation (summary + original articles)

Department Electrical and Communications Engineering
Laboratory Laboratory of Space Technology
Field of research Microwave remote sensing
Opponent Dr. Wolfgang Dierking, Alfred Wegener Institute, Germany
Supervisor Prof. Martti Hallikainen
Instructor Prof. Martti Hallikainen

Abstract

It is essential for winter shipping in the Baltic Sea to get reliable and up-to-date information of its rapidly changing ice conditions. Spaceborne synthetic aperture radar (SAR) images are the only way to produce this information operationally in fine scale independent of daylight and nearly independent of weather conditions. Currently, classification algorithms for the RADARSAT-1 and ENVISAT SAR images utilize mainly the image structure and only limited information on sea ice geophysics and empirical statistics of backscattering signatures of various ice types are utilized. Therefore, interpretation of the classification results is often difficult. Both classification results and their interpretation should very likely improve with the addition of this information. Spaceborne microwave radiometer data are not suitable for the operational Baltic Sea ice monitoring aiding ship navigation due to their coarse spatial resolution, but they can provide an independent data source on the sea ice conditions for validation of the SAR classification algorithms.

In order to support development of operational classification algorithms for the Baltic Sea ice SAR and radiometer data, following studies have been conducted: (1) statistics of C- and X-band backscattering coefficient (σ°) signatures of various ice types, (2) statistics of L- and C-band polarimetric discriminants of various ice types, (3) radar incidence angle dependence of σ° in RADARSAT-1 SAR images, (4) dependence between standard deviation and measurement length for σ° signatures and its usability in sea ice classification, (5) comparison between SAR σ° time series and results from a thermodynamic snow/ice model, and (6) statistics of passive microwave signatures of various ice types.

The main results of this work include the following. It is not possible to discriminate open water and various ice types using the level of σ°, co- or cross-polarization ratio, or standard deviation of σ°. C-band VH-polarized σ° at high incidence angle provides slightly better ice type discrimination accuracy than any other combination of radar parameters. VH-polarization is more suitable for estimating the degree of ice deformation than co-polarizations. Snow wetness has a large effect on the σ° statistics, e.g. when snow cover is wet then the σ° contrasts between various ice types are smaller than in the dry snow case. Incidence angle dependence of the C-band HH-polarized σ° was derived for level ice and deformed ice. The method for deriving this is applicable for any SAR sensor. There is a large variation of level ice σ° with changing weather conditions. A 1-D high-resolution thermodynamic snow/ice model generally helps to interpret changes in the σ° time series. The modeled snow and ice parameters are related to the changes in σ°. It was found out that the standard deviation of σ° for various ice types depends on the length of measurement. This may be utilized in the SAR image classification. It is not possible to resolve concentrations of thin new ice and all other ice types combined in the Baltic Sea using radiometer data as has been done for the Arctic seasonal ice zones.

Keywords Baltic Sea, microwave radiometry, radar polarimetry, radar scattering, remote sensing, sea ice, synthetic aperture radar.

ISBN (printed) 978-951-22-8740-6	ISSN (printed) 0786-8154
ISBN (pdf) 978-951-22-8741-3	ISSN (pdf)
Language English	Number of pages 146 p. + app. 111 p.

Publisher TKK / Laboratory of Space Technology

Print distribution TKK / Laboratory of Space Technology

☒ The dissertation can be read at http://lib.tkk.fi/Diss/

VÄITÖSKIRJAN TIIVISTELMÄ	TEKNILLINEN KORKEAKOULU PL 1000, 02015 TKK http://www.tkk.fi
Tekijä Marko Mäkynen	
Väitöskirjan nimi Investigation of the Microwave Signatures of the Baltic Sea Ice	
Käsikirjoituksen päivämäärä 16.10.2006	Korjatun käsikirjoituksen päivämäärä 2.3.2007
Väitöstilaisuuden ajankohta 4.5.2007	
☐ Monografia	☒ Yhdistelmäväitöskirja (yhteenveto + erillisartikkelit)

Osasto	Sähkö ja tietoliikennetekniikan osasto
Laboratorio	Avaruustekniikan laboratorio
Tutkimusala	Mikroaaltokaukokartoitus
Vastaväittäjä	Dr. Wolfgang Dierking, Alfred Wegener Institute, Saksa
Työn valvoja	prof. Martti Hallikainen
Työn ohjaaja	prof. Martti Hallikainen

Tiivistelmä

Talvimerenkulku Itämerellä tarvitsee luotettavaa ja ajantasaista informaatiota Itämeren nopeasti muuttuvista jääoloista. Synteettisen apertuurin tutkan (SAR) kuvat ovat ainoa tapa tuottaa operatiivisesti tarvittavaa jääinformaatiota riippumatta päivänvalon määrästä ja lähes riippumatta sääolosuhteista. RADARSAT-1 ja ENVISAT SAR-tutkakuvien luokittelualgoritmit perustuvat tällä hetkellä lähinnä kuvien rakenteeseen, eikä merijään geofysiikkaa ja empiiristä tilastotietoa eri jäätyyppien sirontavasteista hyödynnetä kuin rajallisesti. SAR-kuvien luokittelutulosten tulkitseminen on siten usein vaikeaa. Sekä itse luokittelutulokset, että niiden tulkinta parantuisivat, jos luokittelualgorimit hyödyntäisivät edellä mainittua tietoa. Satelliittiradiometrien kuvat eivät sovellu Itämeren jään operatiiviseen monitorointiin niiden karkean spatiaalisen resoluution vuoksi. Niillä kuitenkin voitaisiin validoida SAR-kuvien luokittelualgoritmeja, koska ne ovat SAR-kuvista riippumaton datalähde Itämeren jääoloista.

Tässä työssä on suoritettu seuraavaa perustutkimusta Itämeren jään mikroaaltokaukokartoituksessa, minkä tarkoituksena on tukea SAR- ja radiometrikuvien operatiivisten luokittelualgoritmien kehitystyötä: (1) eri jäätyyppien C- ja X-kanavien sirontakertoimien (σ°) statistiikka, (2) eri jäätyyppien L- ja C-kanavien polarimetristen diskriminanttien statistiikka, (3) σ° :n mittauskulmariippuvuus RADARSAT-1 SAR-kuvissa, (4) σ° :n keskihajonnan ja mittausmatkan välinen riippuvuus ja hyödyntäminen jäätyyppiluokittelussa, (5) SAR-kuvien sirontakerroinaikasarjojen vertailu merijään termodynamiikkamalliin, ja (6) eri jäätyyppien kirkkauslämpötilojen statistiikka.

Työssä saavutettiin seuraavia merkittäviä tuloksia. Eri jäätyyppien ja avoveden luokittelu ei ole mahdollista käyttäen sirontakerrointa, yhdensuuntais- ja ristipolarisaatiosuhdetta tai σ° keskihajontaa. C-kanavan VH-polarisaation σ° suurella mittauskulmalla luokittelee eri jäätyypit hieman paremmin kuin mikään muu C- ja X-kanavan tutkaparametri-kombinaatio. Merijään deformoitumisasteen estimointiin sopii paremmin VH-polarisaation σ° kuin yhdensuuntaispolarisaation. Lumipeitteen kosteudella on suuri vaikutus sirontakerroinstatistiikkaan; erityisesti, kun lumipeite on märkä on sirontakerroinkontrasti eri jäätyyppien välillä pienempi kun lumipeite on kuiva. C-kanavan HH-polarisaation σ° :n mittauskulmariippuvuus määritettiin tasaiselle ja deformoituneelle jäälle. Mittauskulmariippuvuuden laskentamenetelmää voidaan käyttää mille tahansa SAR-tutkakuvalle. Muuttuvat sääolosuhteet aiheuttavat suuria muutoksia tasaisen jään σ° :ssa. Merijään termodynamiikkamalli yleensä auttaa selittämään muutoksia σ° :n aikasarjassa. σ° :n muutokset ovat yhteydessä termodynamiikkamallilla laskettuihin lumen ja jään parametreihin. σ° :n keskihajonnan havaittiin riippuvan etäisyydestä. Tätä riippuvuutta voitaneen hyödyntään SAR-kuvien luokittelussa. Itämerellä satelliittiradiometridatalla pystytään määrittämään vain merijään kokonaiskonsetraatio, toisin kuin arktisten merien kausiluontoisilla merijäänalueilla, missä myös eri jäätyyppien konsentraatioiden määrittäminen on mahdollista.

Asiasanat	Itämeri, kaukokartoitus, merijää, mikroaaltoradiometri, synteettisen apertuurin tutka, tutkapolarimetria, tutkasironta.		
ISBN (painettu)	978-951-22-8740-6	ISSN (painettu)	0786-8154
ISBN (pdf)	978-951-22-8741-3	ISSN (pdf)	
Kieli	englanti	Sivumäärä	146 s. + liit.. 111 s.
Julkaisija	TKK / Avaruustekniikan laboratorio		
Painetun väitöskirjan jakelu	TKK / Avaruustekniikan laboratorio		
☒ Luettavissa verkossa osoitteessa http://lib.tkk.fi/Diss/			

Table of Contents

Preface

This thesis has been conducted in the Laboratory of Space Technology in Helsinki University of Technology under supervision of Professor Martti Hallikainen. My work for the thesis started back in 1994 and continued with varying intensity up to 2006. The work was carried out within five TEKES and one EU funded projects on operational monitoring of the Baltic Sea ice with SAR data.

I want to express my gratitude to Professor Martti Hallikainen for acting my supervisor and tutor in all thesis papers and in my thesis, and for being patient in waiting my thesis to be completed. I am greatly grateful to following colleagues, who co-authored my thesis papers: Markku Similä, Dr. Juha Karvonen, Dr. Bin Cheng at FIMR, Dr. Terhikki Manninen and Dr. Timo Vihma at FMI. Markku and Terhikki also helped me in many theoretical aspects of data analysis. I also thank Ari Seinä (FIS/FIMR) and Robin Berglund (VTT) for co-operation in the sea ice projects.

I want to thank Jenny and Antti Wihuri Foundation for supporting my studies.

Finally, I thank my parents for encouragement.

Espoo, AVA - March 29, 2007.

Marko Mäkynen

Abstract

It is essential for winter shipping in the Baltic Sea to get reliable and up-to-date information of its rapidly changing ice conditions. Spaceborne synthetic aperture radar (SAR) images are the only way to produce this information operationally in fine scale independent of daylight and nearly independent of weather conditions. Currently, classification algorithms for the RADARSAT-1 and ENVISAT SAR images utilize mainly the image structure and only limited information on sea ice geophysics and empirical statistics of backscattering signatures of various ice types are utilized. Therefore, interpretation of the classification results is often difficult. Both classification results and their interpretation should very likely improve with the addition of this information. Spaceborne microwave radiometer data are not suitable for the operational Baltic Sea ice monitoring aiding ship navigation due to their coarse spatial resolution, but they can provide an independent data source on the sea ice conditions for validation of the SAR classification algorithms. Both SAR and radiometer data based sea ice products can also be utilized in the geophysical studies of the Baltic Sea ice.

In order to support development of operational classification algorithms for SAR and radiometer data, basic research on the microwave remote sensing of the Baltic Sea ice has been conducted in this work. The research work included the following topics: (1) statistics of C- and X-band backscattering signatures of various ice types, (2) statistics of L- and C-band polarimetric discriminants of various ice types, (3) radar incidence angle dependence of backscattering coefficient (σ°) in RADARSAT-1 SAR images, (4) dependence between standard deviation and measurement length for σ° signatures and its usability in sea ice classification, (5) comparison between SAR σ° time series and results from a thermodynamic snow/ice model, and (6) statistics of passive microwave signatures of various ice types. Additionally, a comprehensive literature review of the previous work on the microwave remote sensing of the Baltic Sea ice is presented.

The main results of this work include the following. It is not possible to discriminate open water and various ice types using the level of σ°, co- or cross-polarization ratio, or standard deviation of σ°. C-band VH-polarized σ° at high incidence angle provides slightly better ice type discrimination accuracy than any other combination of C- and X-band radar parameters. VH-polarization is more suitable for estimating the degree of ice deformation than co-polarizations. Snow wetness has a large effect on the σ° statistics. Notably, when snow cover is wet then the σ° contrasts between various ice types are smaller than in the dry snow case. Incidence angle dependence of the C-band HH-polarized σ° was derived for level ice and deformed ice. It is utilized in the operational SAR classification algorithms developed by Finnish Institute of Marine Research. The method for deriving the σ° incidence angle dependence is applicable for any SAR sensor. There is a large variation of level ice σ° with changing weather conditions. A 1-D high-resolution thermodynamic snow/ice model generally helps to interpret changes in the σ° time series. The modeled snow and ice surface temperature, cases of snow melting, and evolution of snow and ice thickness are related to the changes in σ°. It was found out that the standard deviation of σ° for various ice types depends on the length of measurement. This may be utilized in the SAR image classification. It is not possible to resolve concentrations of thin new ice and all other ice types combined in the Baltic Sea using radiometer data as has been done for the Arctic seasonal ice zones.

Keywords: Baltic Sea, microwave radiometry, radar polarimetry, radar scattering, remote sensing, sea ice, synthetic aperture radar.

Tiivistelmä

Talvimerenkulku Itämerellä tarvitsee luotettavaa ja ajantasaista informaatiota Itämeren nopeasti muuttuvista jääoloista. Synteettisen apertuurin tutkan (SAR) kuvat ovat ainoa tapa tuottaa operatiivisesti tarvittavaa jääinformaatiota riippumatta päivänvalon määrästä ja lähes riippumatta sääolosuhteista. RADARSAT-1 ja ENVISAT SAR-tutkakuvien luokittelualgoritmit perustuvat tällä hetkellä lähinnä kuvien rakenteeseen, eikä merijään geofysiikkaa ja empiiristä tilastotietoa eri jäätyyppien sirontavasteista hyödynnetä kuin rajallisesti. SAR-kuvien luokittelutulosten tulkitseminen on siten usein vaikeaa. Sekä itse luokittelutulokset, että niiden tulkinta parantuisivat, jos luokittelualgorimit hyödyntäisivät edellä mainittua tietoa. Satelliittiradiometrien kuvat eivät sovellu Itämeren jään operatiiviseen monitorointiin niiden karkean spatiaalisen resoluution vuoksi. Niillä kuitenkin voitaisiin validoida SAR-kuvien luokittelualgoritmeja, koska ne ovat SAR-kuvista riippumaton datalähde Itämeren jääoloista. SAR- ja radiometrikuviin perustuvia merijäätuotteita voidaan merenkulun lisäksi hyödyntää myös Itämeren jään geofysikaalisissa tutkimuksissa.

Tässä työssä on suoritettu perustutkimusta Itämeren jään mikroaaltokaukokartoituksessa, minkä tarkoituksena on tukea SAR- ja radiometrikuvien operatiivisten luokittelualgoritmien kehitystyötä. Tämä perustutkimus käsitti seuraavat aiheet: (1) eri jäätyyppien C- ja X-kanavien sirontakertoimien statistiikka, (2) eri jäätyyppien L- ja C-kanavien polarimetristen diskriminanttien statistiikka, (3) sirontakertoimen mittauskulmariippuvuus RADARSAT-1 SAR-kuvissa, (4) sirontakertoimen keskihajonnan ja mittausmatkan välinen riippuvuus ja hyödyntäminen jäätyyppiluokittelussa, (5) SAR-kuvien sirontakerroinaikasarjojen vertailu merijään termodynamiikkamalliin, ja (6) eri jäätyyppien kirkkauslämpötilojen statistiikka. Lisäksi työssä tehtiin kattava kirjallisuusselvitys aikaisemmasta tutkimuksesta Itämeren jään mikroaaltokaukokartoituksessa.

Työssä saavutettiin seuraavia merkittäviä tuloksia. Eri jäätyyppien ja avoveden luokittelu ei ole mahdollista käyttäen sirontakerrointa, yhdensuuntais- ja ristipolarisaatiosuhdetta tai sirontakertoimen keskihajontaa. C-kanavan VH-polarisaation sirontakerroin suurella mittauskulmalla luokittelee eri jäätyypit hieman paremmin kuin mikään muu C- ja X-kanavan tutkaparametrikombinaatio. Merijään deformoitumisasteen estimointiin sopii paremmin VH-polarisaation sirontakerroin kuin yhdensuuntaispolarisaation. Lumipeitteen kosteudella on suuri vaikutus sirontakerroinstatistiikkaan; erityisesti, kun lumipeite on märkä on sirontakerroinkontrasti eri jäätyyppien välillä pienempi kun lumipeite on kuiva. C-kanavan HH-polarisaation sirontakertoimen mittauskulmariippuvuus määritettiin tasaiselle ja deformoituneelle jäälle. Tätä hyödynnetään Merentutkimuslaitoksen operatiivisissa SAR-kuvien luokittelualgoritmeissä. Mittauskulmariippuvuuden laskentamenetelmää voidaan käyttää mille tahansa SAR-tutkakuvalle. Muuttuvat sääolosuhteet aiheuttavat suuria muutoksia tasaisen jään sirontakertoimessa. Merijään termodynamiikkamalli yleensä auttaa selittämään muutoksia sirontakertoimen aikasarjassa. Sirontakertoimen muutokset ovat yhteydessä termodynamiikkamallilla laskettuihin lumen ja jään pintalämpötiloihin, lumen sulamisajankohtiin ja lumen ja jään paksuuden muutoksiin. Sirontakertoimen keskihajonnan havaittiin riippuvan etäisyydestä. Tätä riippuvuutta voitaneen hyödyntään SAR-kuvien luokittelussa. Itämerellä satelliittiradiometridatalla pystytään määrittämään vain merijään kokonaiskonsetraatio, toisin kuin arktisten merien kausiluontoisilla merijääalueilla, missä myös eri jäätyyppien konsentraatioiden määrittäminen on mahdollista.

Avainsanat: Itämeri, kaukokartoitus, merijää, mikroaaltoradiometri, synteettisen apertuurin tutka, tutkapolarimetria, tutkasironta.

List of Acronyms

ACF	autocorrelation function
ALOS	Advanced Land Observing Satellite
APP	alternating polarization precision ENVISAT ASAR image
AMSR-E	Advanced Microwave Scanning Radiometer
ASAR	Advanced SAR (SAR instrument of ENVISAT)
AVHHR	Advanced Very High Resolution Radiometer
BEPERS	Bothnian Experiment in Preparation of ERS-1
CCRS	Canada Centre for Remote Sensing
DI	deformed ice
DGPS	differential Global Positioning System
DN	day number
ECMWF	European Centre for Medium-Range Weather Forecasts
EM	electromagnetic induction
EMAC	European Multisensor Airborne Campaign
EO	Earth Observation
ESA	European Space Agency
ESSI	ENVISAT and the Baltic Sea Ice Conditions
FBI	frozen brash ice
FIMR	Finnish Institute of Marine Research
FIS	Finnish Ice Service
FMI	Finnish Meteorological Institute
FY	first-year ice
FW-CW	frequency modulated - carrier wave
GPS	Global Positioning System
H	horizontal polarization
HDI	highly deformed ice
HH	horizontal-horizontal polarization
HIGHTSI	1-D high-resolution thermodynamic snow/ice model
HUTRAD	Helsinki University of Technology microwave radiometer system
HUTSCAT	Helsinki University of Technology scatterometer
HV	horizontal-vertical polarization
IID	independent, identically distributed variables
IEM	Integral Equation Method
IMP	image mode precision ENVISAT ASAR image

IMSI	Integrated Use of New Microwave Satellite Data for Improved Sea Ice Observation
InSAR	SAR interferometry
LFD	local fractal dimension
LI	level ice
LBI	loose brash ice
MODIS	Moderate Resolution Imaging Spectroradiometer
MY	multiyear sea ice
NASA	National Aeronautics and Space Administration
NI	nilas
NOAA	National Oceanic & Atmospheric Administration
OSIC	Operational Sea Ice Charting using ERS-1 SAR images
OW	open water lead
PALSAR	Phased Array type L-band Synthetic Aperture Radar
PCNN	Pulse Coupled Neural Networks
PIPOR	Programme for International Polar Oceans Research
RLI	rough level ice
SAR	Synthetic Aperture Radar
SDI	slightly deformed ice
SLI	smooth level ice
SLAR	side-looking airborne radar
SSM/I	Special Sensor Microwave Imager
SMMR	Scanning Multichannel Microwave Radiometer
TEKES	Finnish Funding Agency for Technology and Innovation
TKK	Helsinki University of Technology
UTM	Universal Transverse Mercator – projection
V	vertical polarization
VH	vertical-horizontal polarization
VV	vertical-vertical polarization
WMO	Word Meteorological Organization
WSM	Wide Swath Mode ENVISAT ASAR image
fBm	fractional Brownian motion
fGn	fractional Gaussian noise
pdf	probability density function
rms	root mean square
std	standard deviation

List of Symbols

A	area illuminated by radar; ice disk major facet area
A_h	projection of the ice disk on the horizontal plane
B	logarithmic scale
$B_H(t)$	continuous self-similar Gaussian process
B_n	InSAR baseline normal to the line of sight
C_{FY}	concentration of first-year ice
C_{MY}	concentration of multiyear ice
C_T	total ice concentration
D	fractal dimension
G	logarithmic gain factor
GR	gradient ratio
E_p^s	scattered field
E_q^i	incident field
F	fading random variable; fractional area coverage of the flat dielectric mirrors over the first Fresnel zone in radar altimetry
F_{pp}	complementary field coefficient
H	radar height above surface; Hurst parameter
I	backscattered power from the target
J_1	Bessel function of the first kind
L	correlation length
L_1	one-way power loss factor through snow layer
L_2	one-way power loss factor through sea ice layer
L_∞	population correlation length
L_e	exponential correlation length
L_g	Gaussian correlation length
N	number on independent samples
P	measured backscattered power; 8-bit pixel value
PR	polarization ratio
R	range between target and radar; Fresnel power reflection coefficient
R_{co}	co-polarization ratio
R_{cr}	cross-polarization ratio
R_{depol}	depolarization ratio

$\mathbf{S}$	complex backscattering matrix
S	sea ice salinity
S_m	shadowing function of ice block main facets
S_{pq}	components of $\mathbf{S}$
S_s	shadowing function of ice block side facets
$SL(\theta)$	slope index
SNR	signal-to-noise ratio
$Span$	total power in the backscattered field
T	texture random variable; Fresnel power transmission coefficient; physical temperature
T_B	brightness temperature
$T_{B,atmos}$	reflected down-welling apparent atmospheric T_B
$T_{B,atmos\downarrow}$	down-welling apparent atmospheric T_B
T_a	air temperature
T_i	ice surface temperature
T_s	snow bulk temperature; snow surface temperature; surface temperature
T_1	Fresnel power transmission coefficient across snow top surface
T_2	Fresnel power transmission coefficient across sea ice top surface
$W^{(n)}$	Fourier transform of the nth power of the surface autocorrelation function
$\langle \mathbf{C} \rangle$	average covariance matrix
$\langle \mathbf{M} \rangle$	average Stokes matrix
$\langle \mathbf{T} \rangle$	average coherency matrix
a	intercept of equation (4.6)
a, b, h	dimensions of rectangular polyhedron
b	slope term of equation (4.6)
c	speed of light
d	volume thickness; length of profile segment
$d_{\max}$	maximum length of profile segment
$d_{\min}$	maximum length of profile segment
e	emissivity
f	frequency; area fraction of a surface roughness class
f_0	relaxation frequency
$f_{1s}(\theta)$	pdf of the Euler angle θ

$f_{2s}(\varphi)$	pdf of the Euler angle φ
$f_{3s}(\psi)$	pdf of the Euler angle ψ
f_k	conditional ice thickness density
f_p	fractional polarization
f_{pp}	Kirchhoff field coefficient
h_f	vertical distance between the radar and sea ice
h_i	sea ice thickness
h_r	sail height of the ice ridge
h_s	snow thickness
h_{si}	superimposed ice thickness
k	wave number
k_0	slope term of equation (4.7)
l	measurement length of a profile
m	half-value point of the Cauchy pdf; number of samples
m_v	volumetric liquid water content of snow in percent (wetness)
n	additive radar system noise power; number of samples
p	probability density function; ice ridge porosity
p , q	received and transmitted polarizations
r	distance from the center of the illuminated area to the point of observation
r^2	coefficient of determination for linear regression
s	surface rms height; sample standard deviation
s^2	sample variance
s_∞	population surface rms height
s_T	standard deviation of texture
t	atmospheric transmissivity
vc	variation coefficient
x_0	length of the surface profile
z'_x	surface height derivative in the x-z plane
z'_y	surface height derivative in the y-z plane
Δh	topographic height relative the reference surface
$\Delta\varphi$	InSAR phase difference
$\Delta\theta_0$	incidence angle difference
$\Delta\sigma^\circ$	backscattering coefficient difference

$\Delta\eta$	small temporal movement of large objects in the radar look direction between the SAR image acquisitions
Γ	incomplete gamma function
$\alpha_{\downarrow}$	atmospheric profile factor for determining the effective downwelling temperature
ε_r	relative dielectric constant (permittivity)
ε_{rds}	ε_r for dry snow
ε_{rsi}	ε_r for sea ice
ε_{rws}	ε_r for wet snow
ϕ_{HH-VV}	phase difference between co-polarized channels
ϕ_{noise}	phase noise due to temporal changes of scatterers and radar system noise
ϕ_{pq}	phase of the backscattered wave at pq-polarization
$\phi(\theta)$	anisotrophy index
φ	polar coordinate, azimuthal angle; Euler horizontal rotation angle
φ_0	azimuth angle between the radar look direction and the normal of the ridge direction
γ	coefficient of variation; interferometric coherence
κ_a	volume absorption coefficient
κ_e	volume extinction coefficient
κ_s	volume scattering coefficient
λ	wavelength
v_b	relative brine volume fraction
θ	polar coordinate, vertical angle; Euler vertical rotation angle
θ_0	radar incidence angle from the vertical direction
θ_d	distal slope angle of the ice ridge sail
θ_i	local incidence angle
θ_m	measured vertical inclination of ice block main facet
θ_p	proximal slope angle of the ice ridge sail
θ_{t1}	transmitted angle in snow
θ_{t2}	transmitted angle in ice
ρ	surface autocorrelation function
ρ_T	autocorrelation coefficient of texture
ρ_{co}	correlation coefficient between co-polarized channels

ρ_{ds}	dry snow density
σ	backscattering cross section; standard deviation
σ_{mc}	coherent (specular) radar cross section of the ice block major facet
σ^2	variance
σ°	backscattering coefficient
σ^o_M	measured average σ°
σ^o_N	noise equivalent σ°
σ^o_{ct}	total coherent σ°
σ^o_{is}	sea ice top surface backscattering coefficient
σ^o_{isv}	ice surface-volume interaction scattering coefficient
σ^o_{iv}	ice volume backscattering coefficient
σ^o_{mc}	coherent (specular) σ° of the ice block major facet
σ^o_{mi}	incoherent (diffuse) σ° of the ice block major facet
σ^o_{sc}	coherent (specular) σ° of the ice block side facet
σ^o_{si}	incoherent (diffuse) σ° of the ice block side facet
σ^o_{ss}	snow surface backscattering coefficient
σ^o_{sv}	snow volume backscattering coefficient
σ^o_{ssv}	snow surface-volume interaction scattering coefficient
σ^o_t	total incoherent σ°
σ^o_{ws}	sea ice bottom surface backscattering coefficient
τ	radar pulse length
ψ	Euler rotation angle of the main facet around its normal vector

List of Appended Papers

This thesis is based on the work contained in the following publications, hereafter referred to as publications [P1] to [P6]:

[P1] Mäkynen, M., and M. Hallikainen, "Investigation of C- and X-band backscattering signatures of the Baltic Sea ice," *International Journal of Remote Sensing*, vol. 25, no. 11, pp. 2061-2086, 2004.

[P2] Similä, M., I. Heiler, M. Mäkynen, and M. Hallikainen, "Observations about the discrimination properties of polarimetric SAR data over the Baltic Sea ice," *Proceedings of Earth Surface Remote Sensing II*, Barcelona, Spain, SPIE vol. 3496, pp. 150-165, 1998.

[P3] Mäkynen, M., T. Manninen, M. Similä, J. Karvonen, and M. Hallikainen, "Incidence angle dependence of the statistical properties of the C-band HH-polarization backscattering signatures of the Baltic Sea ice," *IEEE Transactions on Geoscience and Remote Sensing*, vol. 40, no. 12, pp. 2593-2605, 2002.

[P4] Mäkynen, M., M. Similä, T. Manninen, J. Karvonen, and M. Hallikainen, "Dependence between standard deviation and measurement length for C-band backscattering signatures of the Baltic Sea ice," *IEEE Transactions on Geoscience and Remote Sensing*, vol. 44, no. 10, pp. 2890-2898, 2006.

[P5] Mäkynen, M., B. Cheng, M. Similä, T. Vihma, and M. Hallikainen, "Comparisons between SAR backscattering coefficient and results of a thermodynamic snow/ice model for the Baltic Sea land-fast sea ice," accepted to *IEEE Transactions on Geoscience and Remote Sensing*, January 2007.

[P6] Mäkynen, M., and M. Hallikainen, "Passive microwave signature observations of the Baltic Sea ice," *International Journal of Remote Sensing*, vol. 26, no. 10, pp. 2081-2106, 2005.

In publications [P1] and [P6] the research work was carried out by M. Mäkynen, who acted alone and also prepared the manuscripts.

M. Similä and I. Heiler initiated the research work for publication [P2]. They studied classification of airborne polarimetric L- and C-band SAR images. M. Mäkynen studied various polarimetric discriminants for different ice types and compared their values for those of the Arctic Sea first-year ice types. Data sets for his study were prepared by I. Heiler. The Chapter 4 in [P2] was mainly written by M. Mäkynen.

Publication [P3] was initiated by M. Mäkynen. He studied the incidence angle dependence of σ° using HUTSCAT scatterometer and RADARSAT-1 data sets. He also prepared these data sets for analysis. Dr. T. Manninen investigated σ° incidence angle dependence using a theoretical σ° model for deformed ice. M. Similä and Dr. J. Karvonen demonstrated the effect of the incidence angle variation in the automatic classification of the SAR images by classifying a single SAR image with and without incidence angle scaling. M. Similä also contributed on mathematical data analysis. The manuscript was mainly written by M. Mäkynen in close co-operation with Dr. T. Manninen and M. Similä.

M. Mäkynen also initiated publication [P4]. Dr. T. Manninen had previously studied dependence between measurement length and standard deviation for the Baltic Sea ice surface roughness profiles and now this analysis was conducted for the first time for the Baltic Sea ice σ° data. M. Mäkynen conducted all the empirical data analysis using C-band HUTSCAT scatterometer and ENVISAT SAR data and simulated σ° profiles, and summarized the

results. He also prepared all data sets for analysis. M. Similä contributed greatly on the mathematical aspects of the study. The manuscript was mainly written by M. Mäkynen in close co-operation with Dr. T. Manninen and, especially, with M. Similä. Dr. J. Karvonen provided some comments for the manuscript.

The research work for the publication [P5] was initiated by M. Mäkynen. Dr. B. Cheng simulated time series of sea ice thermodynamic parameters. Dr. B. Cheng and Dr. T. Vihma validated the model results using ground truth data prepared by them and M. Mäkynen. M. Mäkynen conducted qualitative analysis between time series of ENVISAT SAR σ° and the simulated sea ice parameters. Statistical quantitative analysis of the data sets was conducted by M. Similä. The manuscript was written in close co-operation by M. Mäkynen, Dr. B. Cheng, M. Similä and Dr. T. Vihma.

In all publications the last author prof. M. Hallikainen provided editorial assistance in writing them. Additionally, he acted as a scientific advisor in [P1], [P3] and [P6].

1 Introduction

The Baltic Sea is a semi-enclosed brackish sea water basin in Northern Europe. The ice cover in the Baltic Sea usually begins to form in November, and has its largest extent between January and March (Seinä and Peltola 1991). The normal ice break-up starts in April and the ice melts completely by the beginning of June. The maximum annual ice cover ranges from 12% to 100% of the whole Baltic Sea area, and the average is 50% (Seinä and Palosuo 1996). The ice in the Baltic Sea occurs as fast ice and drift ice. Fast ice occurs in the coastal and archipelago areas. Drift ice has a dynamic nature due to forcing by winds and currents. The motion of drift ice results in an uneven and broken ice field with distinct floes up to several kilometers in diameter, leads and cracks, brash ice barriers, rafted ice and ice ridges. The thickness of level ice is typically less than 1 m (Seinä and Peltola 1991), and the thickness of ice ridges is typically 5 to 15 m (Leppäranta and Hakala 1992). The salinity of the Baltic Sea ice is typically less than 2‰ depending on the ambient water salinity, growth conditions and thermal history of the ice, e.g. (Palosuo 1963, Kawamura et al. 2001).

It is essential for winter shipping in the Baltic Sea to get reliable and up-to-date information of its rapidly changing ice conditions. Spaceborne synthetic aperture radar (SAR) images are the only way to produce this information operationally in fine scale (currently from 100 m to few hundred meters) independent of daylight and nearly independent of weather conditions. Identification of different ice types and open water in RADARSAT-1 and ENVISAT SAR images over the Baltic Sea ice has been studied e.g. in (Karvonen 2004, 2006), (Karvonen et al. 2005). Interpretation of the classification results is often difficult, because the algorithms utilize mainly the image structure and very little general geophysical information or empirical statistics of backscattering signatures of various ice types are utilized. The classification results should very likely improve with the addition of this information.

Currently, spaceborne microwave radiometer data (e.g. NASA Advanced Microwave Scanning Radiometer (AMSR-E)) is not utilized in the operational monitoring of the Baltic Sea ice. The main reason for this is the very coarse resolution of the data, e.g. in the AMSR-E data the resolution is from 56 to 6.4 km. However, even single channel radiometer data is highly suitable for determination of sea ice concentration due to the large brightness temperature contrast between sea ice and water (Eppler et al. 1992). Radiometers can also map concentrations of new ice (i.e. thin ice) and all other ice types combined in the Arctic seasonal ice areas (Cavalieri 1994). Consequently, in the Baltic Sea, ice concentration maps based on radiometer data could help to validate classification algorithms of the SAR images. They could also show general sea ice conditions and their temporal evolution over the whole Baltic Sea area. To enable this, radiometer concentration algorithms for the Arctic Sea, e.g. NASA Team algorithm (Cavalieri et al. 1984, 1991), must be modified for the Baltic Sea ice conditions.

Besides in ship navigation, sea ice products based on SAR and microwave radiometer data can also be utilized in the geophysical studies of the Baltic Sea ice.

In order to support development of operational classification algorithms for radiometer data and, especially, for SAR data, basic research on microwave remote sensing of the Baltic Sea ice has been conducted in this work. The outcome provides the following contributions and improvements to the state of the art: (1) statistics of C- and X-band backscattering signatures of various ice types [P1], (2) statistics of L- and C-band polarimetric discriminants of various ice types [P2], (3) determination of radar incidence angle dependence of backscattering coefficient (σ°) in RADARSAT-1 SAR images [P3], (4) determination of dependence between standard deviation and measurement length for σ° signatures and its usability in sea ice classification [P4], (5) comparison between SAR σ° time series and results of a

thermodynamic snow/ice model [P5], and (6) statistics of passive microwave signatures of various ice types [P6].

This thesis is organized as follows. Chapter 2 presents an overview of the Baltic Sea ice including its operational monitoring in Finland. Emphasis is on those aspects that are regarded relevant for this thesis. In Chapter 3 basics of the theoretical background of the microwave remote sensing of sea ice are presented. Measurement principles of microwave radiometers and radars are not discussed here. They can be found e.g. in (Ulaby et al. 1981, 1982). Chapter 4 presents a comprehensive review of previous research conducted in the microwave remote sensing of the Baltic Sea ice. Also those topics in which no further research was pursued in this thesis are included. Only recent studies in each topic were reviewed in case they included results from older studies by the same authors. In the end of Chapter 4, previous results relevant for this thesis are summarized. Chapters 5 and 6 present the research work conducted in this thesis. They start with the introduction of microwave sensors and data sets used along with definitions of general sea ice and snow cover classes used, and then proceed to the discussion of the results in [P1]-[P6]. Finally, Chapter 7 includes conclusions and recommendations for further research.

This thesis is solely concentrated on microwave remote sensing of the Baltic Sea ice. Artic Sea and Antarctic Sea ice studies are not discussed here, except briefly in context with [P5], and the Baltic Sea ice results obtained here are not compared with them. This is due to the following unique combination of properties for the Baltic Sea ice: (1) only first-year ice occurs in the Baltic Sea, (2) salinity of the Baltic Sea ice is drastically lower than that of other ice covered seas, (3) periods of snow fall, rain, surface melt, and refreezing can frequently alternate even in mid-winter, and generate rapid variations in the ice and snow properties, and (4) formation of superimposed ice (refreezing of the surface melt water and freezing of rainfall) and snow-ice (freezing of slush from snow and ocean flooding of ice) often have a significant contribution to the total mass of sea ice, e.g. (Leppäranta and Seinä 1982, Granskog et al. 2004).

The results of this thesis combined with an extensive review of previous studies serve as a summary on the studies of the Baltic Sea ice microwave remote sensing conducted up to 2006 and help to plan further studies.

2 Overview of the Baltic Sea Ice

In this chapter, a brief introduction to the properties of the Baltic Sea ice is given with an emphasis on the aspects regarded relevant for this thesis. Additionally, geophysical research work on the Baltic Sea ice, capability of satellite remote sensing to monitor the Baltic Sea ice, and operational sea ice monitoring in Finland are shortly reviewed.

2.1 General Baltic Sea Ice Conditions

The Baltic Sea (locating approximately 53°50´ - 64°50´N and 09°20´- 30°20´E) is a shallow, brackish-water, semi-closed sea connected to the North Sea through the Kattegat and Skagerrak. The Baltic Sea is a basin with a mean depth of 55 m and maximum depth of 459 m. Between October and March the water column is well mixed, being homogenous to some 60-80 m depth. The water in the Baltic Sea is brackish, with surface water salinity ranging from 12‰ in the south-west to 2-7‰ in the northern Baltic Sea and to fresh water at the mouth of large rivers. (Voipio 1981).

The Baltic Sea freezes annually, and the maximum annual ice cover ranges from 12 to 100% of 420,000 km^2 being on average 52%, 218,000 km^2 (Seinä and Palosuo 1996). Ice seasons are typically classified into the following five classes: extremely mild, mild, average, severe and extremely severe winters; three classes are depicted in Figure 2.1. Large-scale atmospheric circulation patterns are significantly correlated with the ice conditions in the Baltic Sea (Jevrejeva 2001). During average and mild winters, warm air masses associated with westerly moving cyclones from the Atlantic dominate the Baltic climate, while in severe winters blocking anticyclonic patterns dominate (Jevrejeva and Moore 2001). Normally ice formation begins in the northern Bay of Bothnia in November, and in the Gulf of Finland in December (Seinä and Peltola 1991). The maximum annual ice extent occurs between January and March. During an average winter ice covers the entire Bay of Bothnia by mid-January, and at the time of the maximum ice extent, at the turn of February and March, the ice covers the Gulfs of Bothnia, Finland, and Riga. Some coastal regions further south also freeze, see Figure 2.1. The normal ice break-up starts at large in April and the ice melts completely by the end of May - beginning of June (Seinä and Peltola 1991).

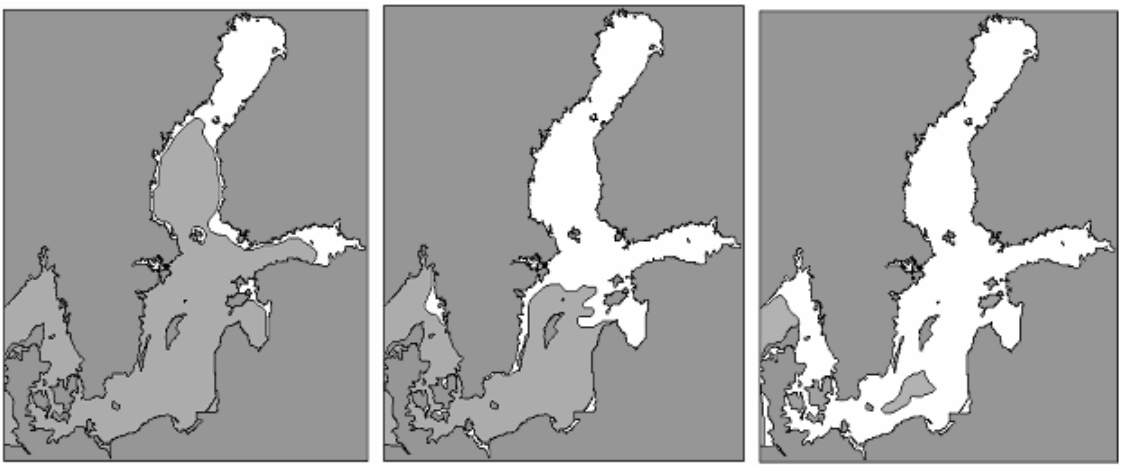

Figure 2.1 Classification of ice seasons in the Baltic Sea. Examples of (left) extremely mild (1994/95 with 68,000 km²), (middle) average (1993/94 with 206,000 km²) and (right) extremely severe (1986/87 with 405,000 km²) ice seasons (Grönvall and Seinä 1999).

Ice in the Baltic Sea occurs as fast ice and drift ice. Fast ice exists in coastal archipelago areas. It grows typically only by thermodynamic and snow-ice formation processes. It is usually less than one meter thick (Seinä and Peltola 1991). Drift ice has a dynamic nature

being forced by winds and currents. Its movements can be large; in stormy wind conditions the ice field can move 20-30 km in a day. The motion results in an uneven and broken ice field with distinct floes up to several kilometers in diameter, leads and cracks, brash ice barriers, rafted ice and ridges. The thickness of ice ridges is typically 5 to 15 m and at maximum about 30 m (Leppäranta and Hakala 1992). The largest amount of ridging occurs in the Bay of Bothnia next to the fast ice boundary. Over large areas ridges account for an average of 10-30% of the total ice mass (Leppäranta and Hakala 1992).

Despite low surface water salinity (from 2 to 7‰) in the northern Baltic Sea, the ice formed resembles that of sea ice with preferred horizontal c-axis in columnar ice, jagged grain boundaries, and a substructure within the grains associated with brine layers (Palosuo 1961, Kawamura et al. 2001). When the parent water salinity is higher than 0.6‰ then ice has these characteristics, and only in proximity of river estuaries the ice is basically freshwater ice (Palosuo 1961). The bulk ice salinities in the northern Baltic Sea are generally less than 2‰, and even lower depending on the ambient water salinity, growth conditions and thermal history of the ice, e.g. (Palosuo 1963, Kawamura et al. 2001).

Periods of snow-fall, rain, surface melt, and refreezing can frequently alternate even in mid-winter, and generate rapid variations in the ice and snow properties. Superimposed ice (refreezing of the surface melt water and freezing of rainfall) and snow-ice (freezing of slush from snow and sea flooding of ice) often have a significant contribution to the total mass of sea ice (Leppäranta and Seinä 1982, Kawamura et al. 2001, Granskog et al. 2004).

2.2 Classification of the Baltic Sea Ice

Baltic Sea ice can be divided into different types in the following ways: (1) surface structure, (2) stage of ice development and ice thickness, (3) ice concentration, (4) stage of melting, (5) texture classification which describes the structural properties of the ice matrix (Eicken and Lange 1989), and (6) genetic classification which describes the meteorological and oceanographic conditions that cause the growth of the ice (Eicken and Lange 1989). The ways (1)-(4) describe large scale structure of ice, whereas (5) and (6) describe fine scale structure of sea ice medium. These different classifications are described below.

1. Surface structure

Based on ice surface structure both fast ice and drift ice are divided into two basic ice type classes: level ice and deformed ice. Level ice is sea ice which has not been affected by any deformation and it is formed by thermal growth and formation of snow-ice and superimposed ice. Thicker level ice is originated from the initial ice freezing. Deformed ice is formed by ice motion which can be diverging, compacting or shearing, where rotational forces are present. Divergent motion produces leads of fractures in ice. Deformed ice produced by convergent motion in the sea ice is divided into following sub-classes (WMO 1989, Seinä et al. 2001):

- rafted ice: Type of deformed ice formed by one piece of ice overriding another.
- finger rafted ice: Type of rafted ice in which floes thrust ‘fingers’ alternately over and under the other.
- ice ridge: A line or wall of broken ice forced up by pressure. May be fresh or weathered. The submerged volume of broken ice under a ridge is termed an ice keel.
- ridged ice: Ice piled haphazardly one piece over another in form of ridges and walls.
- hummocked ice: Hillocks of broken ice which has been forced upwards by pressure. May be fresh or weathered.
- rubble field: An area of extremely deformed sea ice of unusual thickness formed during the winter by the motion of drift ice against or around a protruding rock, islet or other obstruction.

- brash ice: Accumulations of floating ice made up of fragments not more than 2 m across, the wreckage of other forms of ice.

2. Stage of ice development and ice thickness

Level ice is further divided according to its phase of development, which also indicate its thickness range, for example: new ice, dark nilas (less than 5 cm thick), light nilas or ice rind (5-10 cm), grey ice (10-15 cm), grey-white ice (15-30 cm), white ice - first stage (30-50 cm), white ice - second stage (50-70 cm), medium first year ice (70-120 cm) (WMO 1989). New ice a general term for recently formed ice where ice crystals are only weakly frozen together. Grey ice and grey-white ice are also called as young ice.

Some other stages of ice development are (WMO 1989):

- frazil ice: Fine spicules or plates of ice suspended in water.
- grease ice: A later stage of freezing than frazil ice when the crystals have coagulated to form a soupy layer on the surface. Grease ice reflects little light, giving the sea a matt appearance.
- slush: Snow which is saturated and mixed with water on land or ice surfaces, or as a viscous floating mass in water after a heavy snowfall.
- shuga: An accumulation of spongy white ice lumps, a few centimeters across.
- pancake ice: Predominantly circular pieces of ice from 30 cm to 3 m in diameter, and up to 10 cm in thickness, with raised rims due to the pieces striking against one another. It may be formed on slight swell from grease ice, shuga or a result of the breaking of ice rind, nilas or, under severe conditions of swell or waves, of grey ice.

3. Ice concentration

Sea ice concentration is described with the following classes (WMO 1989): compact ice (concentration is 10/10), very close ice (9/10 - < 10/10), close ice (7/10-8/10), open ice (4/10-6/10), very open ice (1/10-3/10), open water (<1/10), ice free.

4. Stage of ice melting

Sea ice melting starts with melting of snow cover on ice. Melt water from snow, and in more advanced stages of melting also ice melt water, accumulates as puddles on ice surface (WMO 1989). Surface puddles can melt through the ice cover creating so called thaw holes. Dried ice is sea ice from the surface of which melt water disappeared after the formation of cracks and thaw holes. During the period of drying, the ice surface whitens. The last stage of ice melting is called rotten ice which is sea ice with honeycombed structure and which is in an advanced state of disintegration.

5. Texture classification

The three main ice texture classes are (Eicken and Lange 1989): (1) columnar ice; elongated ice grains with size of 1-10 cm, brine inclusions are parallel layers within grains, (2) intermediate columnar/granular; grain size 1-10 cm, very irregular horizontal banding with crystals exhibiting a slight elongation in the vertical (growth) direction, brine inclusions are string of isolated oblong pockets, (3) granular ice; grain size < 1 cm, brine inclusions are irregular pockets or droplets between grains.

6. Genetic classification

The three ice genetic classes recognized by Eicken and Lange (1989) are: frazil, tranquil and disturbed congelation. Frazil ice is formed after a surface accumulation of ice crystals that have been formed in the upper part of the water column (dynamic conditions; ice is formed during turbulent conditions in supercooled water). Congelation ice (tranquil and disturbed) is formed by the freezing of seawater at the ice-water interface (static conditions) and has columnar texture. Granskog (2004) proposed to add sea ice with a meteoric ice contribution

(snow-ice and superimposed ice) as the fourth genetic ice class, since its formation mechanisms differ considerably from those of the other three classes (see Section 2.3).

2.3 Effect of Snow Cover

Snow usually accumulates rapidly on sea ice after its formation and has a great effect on sea ice evolution; for example, ice growth at the ice bottom is much reduced by the presence of snow, since the thermal conductivity of snow is much smaller than that of sea ice. Snow undergoes constantly metamorphic processes that change its properties. Snowpack can deform very rapidly especially during the melt season and due to rainfall. The percolating water in the snowpack can refreeze deeper in the snow forming ice lenses and hard crust layers, or contribute to a slush layer on sea ice. Wind redistribution of snow forms greatly variable snow thickness, even in small spatial scales. Ice ridges and other deformations act as obstacles for the wind field and greatly increase the spatial variation of snow thickness.

In the presence of liquid water, the snow layer may contribute to the ice thickness via a snow-to-ice transformation. This takes place by two processes: (1) A heavy snow loading on top of the ice may cause a negative freeboard and subsequently sea water flooding of the ice surface and basal snow. A salty slush layer may be generated that subsequently freezes above the original ice cover. This is called snow-ice formation due to ocean flooding. (2) Melt water from snow or rainfall may percolate downwards and refreeze above the original ice cover. This process is called superimposed ice formation. Besides snow surface melting, there can also be snow internal melting in spring time caused by the large amount of solar radiation penetrating into the snowpack. This internal melting is sensitive to the snow extinction coefficient. e.g. (Cheng et al. 2003). Generally, (1) and (2) are also called as meteoric ice, i.e. part of the sea ice cover which contains atmospherically derived ice.

The physical properties of snow-ice differ from those of congelation ice. Snow-ice includes more air bubbles and is very distinctive from the coarser columnar crystal structure of congelation ice. However, it is difficult to distinguish between frazil ice and snow-ice crystal structure. Brine inclusions in snow-ice are typically spherical droplets at grain junctions. The mechanical properties of snow-ice are also quite different from those of congelation ice, snow-ice being much weaker. (Saloranta 2000).

Superimposed ice has distinctive polygonal granular structure, e.g. (Kawamura et al. 2001). It usually has a very low salinity. However, if superimposed layers are flooded with seawater their salinity can increase, and this may destroy the texture of the ice, making its origin hard to recognize (Granskog et al. 2004).

The contribution of snow-ice and superimposed ice to the total ice thickness is usually significant. First studies indicated that in the northern Baltic Sea from December to February, snowfall accounts on average for 25-45 mm equivalent water per month (Kolkki 1969), and the snow-ice may contribute to some 1/3 of the total ice thickness (Leppäranta and Seinä 1982). Measurements conducted in the Gulf of Finland in winter 1998/99 indicated that as much as 43-55% of the total coastal landfast ice was snow-ice (Kawamura et al. 2001). Granskog et al. (2004) studied properties of landfast ice in the Gulf of Finland during three winters in 1999-2001 and found out that the superimposed ice contributed up to 20% of the total ice mass in a seasonal scale. The contribution of meteoric ice varied from 0 to 35% by mass, depending on season and year. During a four week study period of spring melt-freeze in 2004, a 15 cm snow layer on landfast ice was transformed into 7 cm thick layer of superimposed ice (Granskog et al. 2006). The total formation of the superimposed ice during the whole ice season was 14 cm (22% of the total ice thickness).

2.4 Typical Structure of Level Ice and Deformed Ice

Several studies of the textural characteristics of level ice have shown a large variability in ice structure and the contribution from different genetic ice types to the total ice thickness (Granskog 2004). Structurally, the level landfast ice cover can roughly be divided into a two layer medium, with a granular upper layer and a columnar ice bottom layer (Kawamura et al. 2001). The upper layer is partly composed of snow-ice or superimposed ice and the remaining is frazil ice. Often also a third ice type is present, the transition ice (or intermediate columnar/granular), e.g. (Weeks et al. 1990). Transition ice may be associated with nearby leads, ice deformation and a rough hydrodynamic regime (Weeks et al. 1990).

Properties of deformed ice in a vertical space have not been studied much in the Baltic Sea. In a few studies the structure of ice ridges has been investigated, e.g. (Leppäranta and Hakala 1992). Typically an ice ridge consists of ice, loose ice blocks, air voids and slush. In six ice ridges measured by Leppäranta and Hakala (1992) the porosity (fraction of voids) varied from 23 to 33%.

2.5 Ice Salinity and Density

When seawater freezes, most impurities are rejected from the ice lattice, resulting in plates of pure ice. The plates originate as dendrites with tips protruding into the seawater. The plate width can vary from a few tenths of a millimeter to 1 mm and is dependent on the ice growth rate. The brine is trapped between these tips. The salinity of sea ice at a given time is governed by initial brine entrapment and by desalination processes such as brine pocket migration, brine expulsion, gravity drainage and flushing. Initial brine entrapment increases with increasing ice growth rate and seawater salinity. When sea ice warms, disconnected brine inclusions coalesce into vertical channels that can lead to redistribution, drainage and desalination of the ice. Quantitative information on desalination processes in the Baltic Sea ice is still limited. For ice with a bulk salinity of 1‰ temperatures as high as -1°C are needed for to have brine volumes large enough (over 5‰) for the Baltic Sea ice to become permeable (Leppäranta and Manninen 1988). (Granskog 2004).

Sea ice salinities and densities, both bulk values and profiles, have been measured since the 1950's in many field campaigns. The bulk ice salinities in the northern Baltic Sea are generally less than 2‰, and even lower depending on the ambient water salinity, growth conditions and thermal history of the ice, e.g. (Palosuo 1963, Kawamura et al. 2001). In a three year study of the properties of landfast ice in the Gulf of Finland Granskog et al. (2004) observed that the bulk salinity of landfast ice is on average 10-20% of the parent seawater salinity. In winter, the bulk ice salinity changes are insignificant, while in spring the salinity decreases rapidly from winter values to almost zero. Flooding and snow-ice formation produce large and rapid salinity variations in the uppermost parts of the ice cover. For landfast ice a representative instantaneous winter time salinity profile is close to uniform, with slightly higher values at the surface (Weeks et al. 1990).

In a two-year dielectric study of sea ice, the bulk ice density of samples taken from the Gulf of Finland near Helsinki was 0.84 g/cm^3, and 95% of those samples had a density between 0.78 and 0.90 g/cm^3 (Hallikainen 1983). Carlström and Ulander (1995) reported ice surface densities from 0.81 to 0.90 g/cm^3 for level ice in the Bay of Bothnia.

2.6 Geophysical Research Work on the Baltic Sea Ice

Sea ice cover on the Baltic Sea largely modifies or even eliminates the ocean-atmospheric heat, radiation and momentum fluxes because the surface properties of the ice, especially its albedo, temperature and roughness, are different from those of open water. The ocean-atmosphere heat exchange is especially very sensitive to the thin portion of the sea ice

thickness distribution (Maykut 1978, 1982). Ice cover also limits the exchange of gases and particulates between the ocean and atmosphere. The release and absorption of latent heat due to the freezing and melting of ice may alter the seasonal air temperature cycle and induce local climate. Ice cover contributes to salt and fresh water budgets as freezing at the ice bottom rejects salt, increasing the ocean salinity, whereas melting of sea ice will decrease the ocean surface salinity. In addition, the sea ice cover restricts wintertime navigation in the Baltic Sea.

For studying above mentioned geophysical effects of the Baltic Sea ice cover many sea ice parameters are needed, for example: (1) general history of ice season; e.g. dates of freezing and break-up of permanent ice cover, time history of ice extent, (2) ice concentration and movement of drift ice, (3) ice thickness, (4) snow/ice albedo, (5) snow parameters; thickness, density, wetness, grain size, (6) ice salinity and density, (7) ice surface roughness, i.e. degree of ice deformation. For marine navigation the most important sea ice parameters are ice thickness, ice concentration, locations and sizes of ice deformations like ice ridges and rubble fields, and locations of leads. For geophysical studies typically time series of sea ice data are required, whereas for marine navigation instant values of sea ice parameters and their near-future predictions are needed.

Studies related to the Baltic Sea ice have been conducted over 100 years, first motivated by the development of winter navigation and later including geophysical studies on the Baltic Sea ice properties and climatology. Since 1950's studies have focused on large scale problems, such as sea ice climatology and dynamics, sea ice thermodynamics, sea ice ecology, thickness distributions of level ice and deformed ice, ice ridge statistics (e.g. ridge density), mechanical properties of sea ice (e.g. shear strength of ridges), and on sea ice properties particularly relevant for microwave remote sensing (e.g. surface roughness). In recent years, theoretical geophysical modeling of sea ice has included the following topics:

1. Seasonal sea ice climate, e.g. (Haapala 2000).
2. Sea ice dynamics, e.g. (Zhang 2000).
3. Sea ice thermodynamics and air-ice interaction, e.g. (Cheng 2002).

These studies are mainly focused on the numerical model constructions, validations and to better reproduce sea ice physics with numerical modeling on the basis of seasonal and synoptic time scales. In general, the large scale ice conditions, like ice extent, in the Baltic Sea are well known, but little is still known about the small scale properties of the ice, the processes during initial ice formation, and the temporal development of the ice properties (Granskog 2004). The main reason for this is the need of time consuming and expensive logistical efforts for studying sea ice processes in harsh field conditions.

A review on the operational monitoring of the Baltic Sea ice in Finland is presented in Section 2.8.

2.7 Capability of Satellite Remote Sensing to Monitor Baltic Sea Ice

Satellite remote sensing can produce several sea ice parameters for both geophysical studies and marine navigation. Only microwave instruments, SAR-radars, scatterometers and radiometers, can produce sea ice information operationally independent of daylight and nearly independent of weather conditions. However, only SAR-radars have very fine resolution (10 to 100 m). The resolution of current radiometer data is at best around only 6 by 4 km (AMSR-E 89 GHz channel). The finest resolution of scatterometer data is around 12.5 km. In the following is a list of the Baltic Sea ice parameters which can be estimated with remote sensing data (Baltic Sea ice references mentioned when applicable), for details see Chapter 4:

- Ice extent and ice concentration: SAR (Karvonen et al. 2005), scatterometer (Grandell et al. 1996), microwave radiometer (Grandell and Hallikainen 1994, Grandell et al. 1996); optical and thermal infrared images, but only under cloud-free conditions.
- Ice thickness: SAR (Karvonen et al. 2003, 2004), (Similä et al. 2006) and possibly also radar altimetry (through freeboard estimation).
- Ice types: SAR e.g. (Karvonen 2004); possibly some ice types (e.g. new ice, snow covered ice) with optical images.
- Ice dynamics: time series of SAR images (Sun 1996, Leppäranta et al. 1998).
- Small horizontal deformations in level ice: SAR repeat-pass interferometry with small baseline when ice is stationary (Dammert et al. 1998).
- Ice topography: SAR repeat-pass interferometry with large baseline when ice is stationary and no ice deformation occurs (Dammert et al. 1998).
- Ice surface temperature: thermal infrared images under totally cloud-free conditions.
- Ice surface albedo: broad band optical and infrared reflectance data with multiple viewing and irradiance angles.

Remote sensed sea ice data can be used in the development and validation of geophysical models. Assimilation of remote sensed data with geophysical models should increase the accuracy of various sea ice products, e.g. ice extent, movement and thickness. This has not yet been conducted operationally for the Baltic Sea ice.

2.8 Operational Monitoring of the Baltic Sea Ice in Finland

The marine transportation in the Baltic Sea in year is about 700 million tons, some 40% of which occurs during winter. The winter time traffic in the Baltic Sea is the largest of all ice covered seas. In Finland almost 90% of foreign trade is transported by sea. Annual turnover in 2004 was 95 million tons. During the winter months there are more than 25,000 port-calls in Finnish harbors transporting about 40 million tons of goods. The increase of marine transportation in Finland is around 3-4% per year. In 2001 the number of vessels sailed in the Gulf of Finland was 38,000 and in 2015 this is expected to increase to 53,000 vessels. (Seinä et al. 2006).

Winter navigation in Finland is made possible by the use of eight icebreakers, ice-strengthened vessels, restricting navigation, and by operational monitoring of the Baltic Sea ice cover. Navigation is restricted by closing half of the harbors for the winter and giving assistance only to vessels suitable for ice navigation. Powerful, ice-strengthened vessels can break through ice up to 80 cm thick, but they are not capable of navigating through ridges and heavy brash ice barriers without icebreaker assistance. On an average ice season ice hampers ship navigation 6-7 months in the Bay of Bothnia and 3-4 months in the Gulf of Finland. Under normal ice conditions the sailing time from the ice-edge to e.g. the northern Bay of Bothnia is one day (400 nautical miles), but under severe conditions it can extend to nearly one week. (Seinä et al. 2006).

Finnish Institute of Marine Research (FIMR) has been responsible for the sea-ice information service in Finland since 1918. The Service, called Finnish Ice Service (FIS), operates under Department of Physical Oceanography, and it is intended to meet the needs of national and international shipping and activities where sea-ice information is required. (Seinä et al. 2006).

FIS issues daily during the ice season the following sea ice products: ice chart, ice report and ice movement forecast for the next 54 hours. Ice chart is the most important and widely used ice information product of FIS. The ice charts are based on Earth Observation (EO) data

(spaceborne optical and SAR images), reconnaissance flights (rarely), and ground truth data from ships, icebreakers and coastal ice stations. The ice chart production is performed mostly by subjective methods by updating previous chart with new input data. FIS also transmits digital satellite images to the operative Finnish and Swedish icebreakers daily in the ice season. (Seinä et al. 2006).

Optical satellite data have been used in FIS since 1968 (Seinä et al. 1997). Currently, optical satellite data from NOAA Advanced Very High Resolution Radiometer (AVHHR; since 1981) and NASA Terra/Aqua Moderate Resolution Imaging Spectroradiometer (MODIS, since 2005) sensors are used. Both sensors have visible and thermal infrared channels. The best spatial resolution of MODIS is 250 m and the resolution of AVHRR is 1.1 km. When a satellite orbit goes over the Baltic Sea, both AVHRR and MODIS images usually cover the whole Baltic Sea. Unfortunately, the use of optical images is heavily restricted by cloud cover and also by short days during the early and mid-winter.

The use of spaceborne SAR started in 1992 with ERS-1 SAR, first in experimental level and operationally in 1994 (Seinä et al. 1997). In Sweden and Germany operational use started already in 1992. The major advantages of SAR images compared to optical images are their independence on the amount of daylight and cloud cover, better resolution and better information content on sea ice cover, notably degree of ice deformation can be interpreted from the SAR images. The spatial resolution of ERS-1 SAR in operational use was 100 m and the image size 100 by 100 km. The small image size was the major drawback of the ERS-1 images; one image did not even cover the Bay of Bothnia. In 1998 RADARSAT-1 ScanSAR Narrow images replaced ERS-1/2 SAR images and since 2003 ScanSAR Wide images have been used. The RADARSAT-1 ScanSAR Wide images also have a resolution of 100 m in operational use, but their image size is around 500 by 500 km and, thus, one image covers e.g. the whole Bay of Bothnia or Gulf of Finland (the size of ScanSAR Narrow images is 300 by 300 km). Since 2004 also ENVISAT Wide Swath images (swath width 420 km) have been used to supplement RADARSAT-1 images. In 2006, the total number of RADARSAT-1 and ENVISAT images used by FIS was 163 and 82, respectively.

The SAR images are analyzed both visually and by automatic classification algorithms. FIMR has been developing classification algorithms since 1987. Current SAR products are high-resolution ice thickness chart (based on combination of SAR and ground truth data) and ice deformation chart (discrimination of various ice types). The SAR based ice thickness chart is delivered to the icebreakers. Classification algorithms for SAR images are reviewed in Chapter 4.5.

SAR images and products and FIS ice charts provide also information for the geophysical studies of the Baltic Sea ice. An example of FIS ice chart and SAR image for the same day is presented in Figures 2.2 and 2.3. Visual inspection of the SAR images shows locations of thin ice (black areas, i.e. low intensity of backscattered radar wave), deformed ice (bright areas, i.e. high intensity), location of ship channels and leads (bright thin curves in the image), and in this case clearly the location of the fast ice boundary. Backscattering intensity of open water depends highly on wind speed and fetch. It can vary from very low intensity (low wind speed) to very high (high wind speed). However, textural variation of intensity enables typically visual discrimination between open water (low texture) and deformed ice (typically high texture). Typically, even visual analysis of the SAR image gives more information of the sea ice cover than the FIS ice chart.

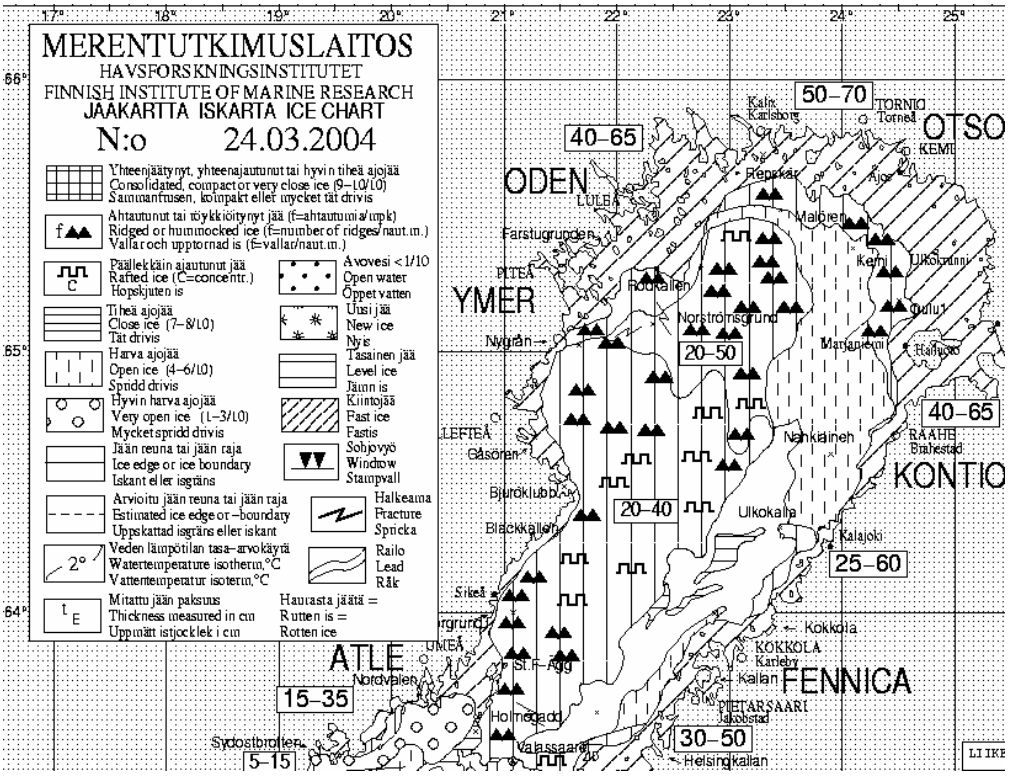

Figure 2.2 Finnish Ice Service ice chart on March 24, 2004.

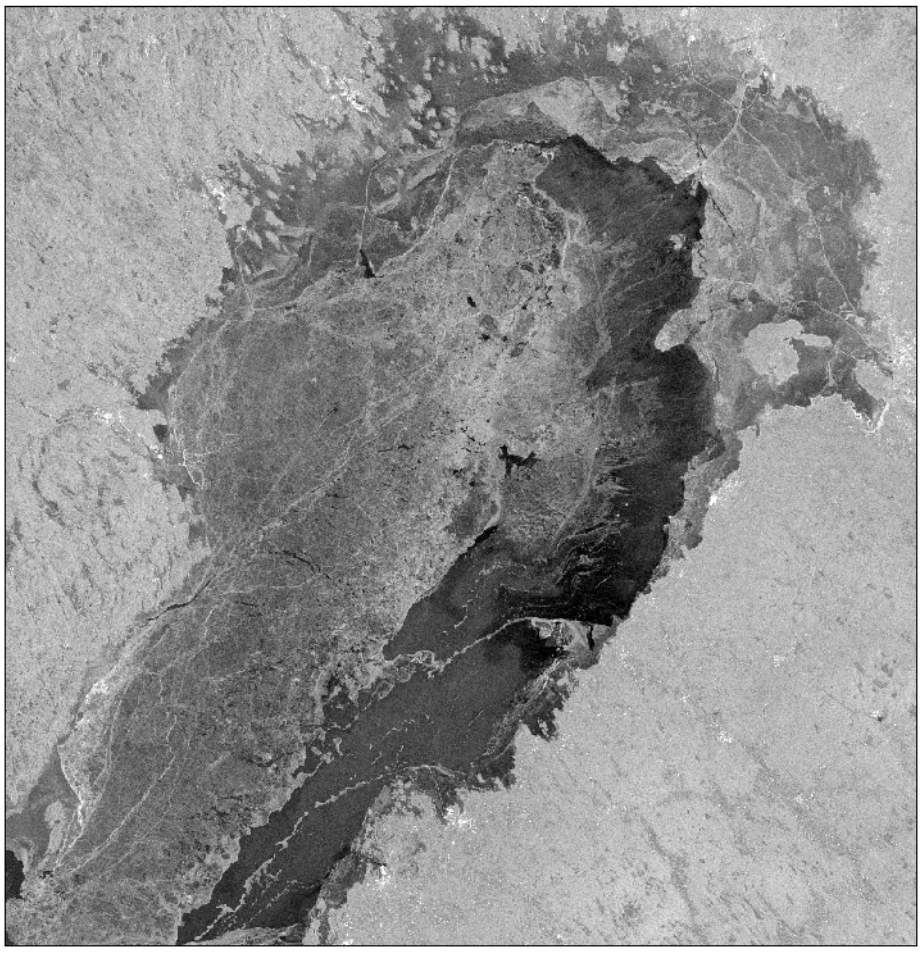

Figure 2.3 ENVISAT Wide Swath Mode image over the Bay of Bothnia on March 24, 2004, © European Space Agency. The image was rectified to the Finnish Uniform Coordinate System with 150 m pixel size.

3 Theoretical Background of Microwave Remote Sensing of Sea Ice

3.1 Backscattering Coefficient

Monostatic radar measurements (i.e. the same antenna is used in transmitting and receiving) of natural targets, like sea ice, are described using a quantity called backscattering coefficient σ° (Ulaby et al. 1982):

$$\sigma^{o}_{pq}(\theta_0) = \frac{4\pi R^2 \left\langle \left| E^s_p \right|^2 \right\rangle}{A \left| E^i_q \right|^2}, \tag{3.1}$$

where θ_0 is the radar incidence angle measured from vertical direction,

p, q are the received and transmitted polarizations, respectively; in remote sensing vertical (V) and horizontal (H) polarizations are mostly used,

E^s_p is the scattered field and E^i_q is the incident field,

A is the area illuminated by radar,

R is the range between target and radar.

Equation (3.1) shows σ° as the ratio of the statistically averaged total power backscattered by an equivalent isotropic scatterer to the product of the incident power density and the illuminated area (Ulaby et al. 1982). It is not the ratio of the total backscattered power to the incident power.

The area illuminated by a radar, i.e. the radar spatial resolution, is in the simplest case equivalent to the area illuminated by the 3 dB beamwidth of the antenna. In case of the SAR radars it is determined by the length of the synthetic aperture in azimuth direction (along flight track) and by radar pulse length in range direction (across track direction). The range R is usually measured by the radar instrument itself, typically by the time delay between a transmitted and a received radar pulse.

Measured σ° values are strongly modulated by the coherent fading phenomena. They are also corrupted by radar system noise. The effects of fading and noise on the measured backscattered power P are statistically modeled as (Rignot and Kwok 1993):

$$P = \left[\langle I \rangle T + \langle n \rangle\right] F, \tag{3.2}$$

where I is the backscattered power from the target,

n is the additive radar system noise power,

T is the texture random variable which represents the natural spatial variability of the backscattered power I, $E[T] = 1$,

F is the fading random variable characterized by a normalized χ^2-distribution with $2N$ degrees of freedom (N is the number on independent samples), $E[F] = 1$, $Var(F) = 1/N$.

The number of independent samples N in each single σ° value depends on the radar system parameters, e.g. on radar frequency bandwidth. N can be increased by spatial averaging of σ° data, but then data spatial resolution decreases.

The standard deviation of texture s_T is (Rignot and Kwok 1993):

$$s_T = \sqrt{\frac{\left(\mathrm{std}\left(\sigma^o\right)/\mathrm{mean}\left(\sigma^o\right)\right)^2 - 1/N}{1+1/N}}\left(1+\frac{1}{SNR}\right), \tag{3.3}$$

where SNR is the signal-to-noise ratio. If the target is homogeneous then s_T is zero, and variation in the measured average σ° (σ^o_M) is only caused by the random fading. Standard deviation of σ^o_M from a homogeneous target is (Ulaby et al. 1982):

$$\mathrm{std}(\sigma^o_M) = \frac{\langle\sigma^\circ\rangle}{\sqrt{N}}\left(1+\frac{1}{SNR}\right). \tag{3.4}$$

Measured σ° values are usually expressed in decibel scale:

$$\sigma^\circ[\mathrm{dB}] = 10\cdot\log_{10}(\sigma^\circ). \tag{3.5}$$

Standard deviation of σ° in dB scale is obtained from the Taylor-series expansion of σ° in dB-scale at an interval of about $\sigma^o = E\{\sigma^o\}$, which leads to (Pulliainen 1994):

$$\mathrm{std}\left(\sigma^o\right)[\mathrm{dB}] \approx \frac{10}{\ln 10}\frac{\mathrm{std}\left(\sigma^o\right)}{\mathrm{mean}\left(\sigma^o\right)}. \tag{3.6}$$

The simplest remote sensing radars measure the backscattered power only at one frequency and one polarization which is one of the following four linear polarization combinations: HH, VH, VV, HV. More advanced radars have two (dual-polarization radar) or all four (quad-polarization) polarization combinations. Typically dual polarization radars have one co- and one cross-polarization channel, e.g. HH and VH. Quad-polarized radars have basically one extra channel as in backscattering HV- and VH-polarized σ°'s are equal due to the reciprocity theorem. The most advanced radars, polarimetric radars, measure both amplitude and phase of the backscattered field at all four linear polarization combinations. The basics of radar polarimetry are presented in Chapter 3.2. Dual-, quad- and polarimetric radars may also operate at several frequency bands; a typical combination is C- and X-band or L- and C-band.

Theoretical backscattering models for sea ice are available in the literature, e.g. (Ulaby et al. 1982, 1986), (Fung 1994). These models are used to (1) study the total sea ice σ° and its σ° components (e.g. ice surface and volume scattering) as a function of various radar and sea ice geophysical parameters (e.g. incidence angle, ice surface roughness), (2) interpret the behavior of empirical sea ice σ° data; e.g. multi-incidence angle data or time series σ° data, and (3) develop classification algorithms for σ° data. The simplest models only model the co-polarized single scattering σ°, see e.g. (Fung 1994). More advanced models take into account multiple scattering events within the snow and ice surfaces and volumes. The multiple scattering is more difficult and laborious to model than the single scattering. The cross-polarized σ° in backscattering direction is caused only by multiple scattering events. In case of co-polarized σ°, the multiple scattering events may be negligible compared to the single scattering ones. Generally, single scattering models provide the identification and comparison of various scattering mechanisms, like ice surface and volume scattering, whereas multiple scattering models give only the total σ°, but are more accurate. In the following, a general single backscattering model for snow covered level sea ice is presented according to (Fung 1994). The model includes contributions from (see Figure 3.1):

1) snow surface
2) snow volume
3) snow bottom surface – snow volume interaction
4) sea ice surface
5) sea ice volume
6) sea ice bottom surface
7) sea ice bottom – sea ice volume interaction

The last two terms are optional depending whether the radar wave is assumed to reach the sea ice bottom surface or not.

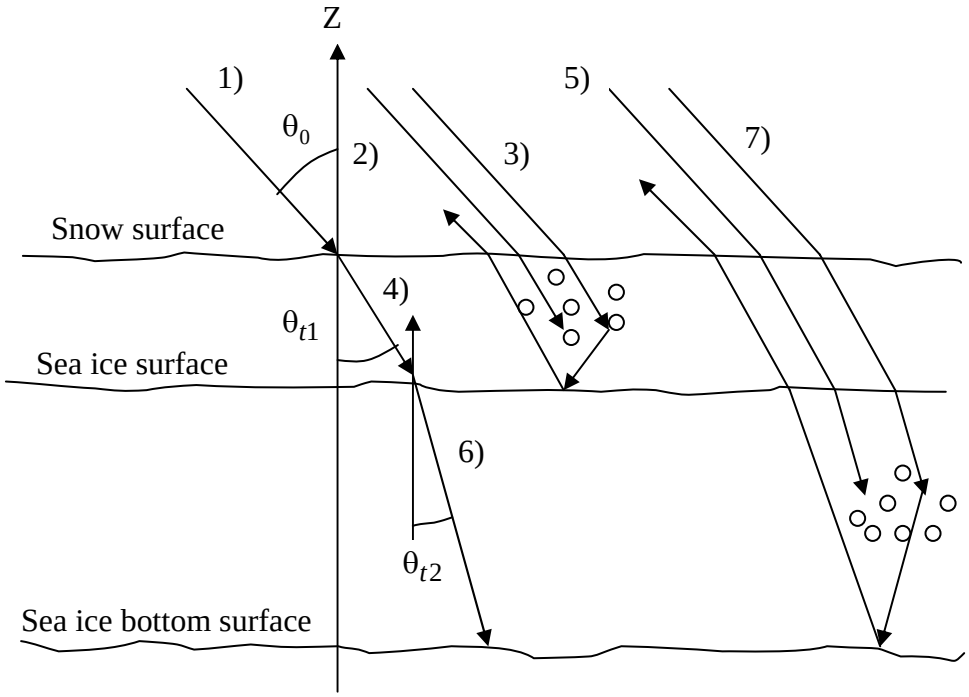

Figure 3.1 Backscattering mechanisms for snow covered level sea ice. The scattering paths correspond to the above mentioned terms. θ_0 is the radar incidence angle and θ_{t1} and θ_{t2} are the transmitted angles in snow and ice volumes, respectively.

The total backscattering coefficient for snow covered sea ice according to the first-order solution of the radiative transfer equation is (Fung 1994):

$$\sigma^o = \sigma^o_{ss} + \sigma^o_{sv} + \sigma^o_{ssv} + L_1^2 T_1^2 \frac{\cos\theta_0}{\cos\theta_{t1}} \left\{ \sigma^o_{is} + \frac{\cos\theta_{t1}}{\cos\theta_{t2}} \left(\sigma^o_{iv} + \sigma^o_{isv} + L_2^2 T_2^2 \sigma^o_{ws} \right) \right\}, \qquad (3.7)$$

where $\sigma^o_{ss}, \sigma^o_{is}, \sigma^o_{ws}$ are the snow surface, sea ice top and bottom surface backscattering coefficients,

σ^o_{sv} and σ^o_{iv} are the snow and sea ice volume backscattering coefficients,

σ^o_{ssv} and σ^o_{isv} are snow and sea ice surface-volume interaction scattering coefficients,

θ_{t1} and θ_{t2} are the transmitted angles in snow and ice volumes,

T_1 and T_2 are the Fresnel power transmission coefficients across snow and ice top surfaces,

L_1 and L_2 are one-way power loss factors through snow and sea ice layers:

$$L_x = \exp(-\kappa_{ex} d_x / \cos\theta_{tx}), \tag{3.8}$$

where subscript x is 1 or 2, κ_e is the volume extinction coefficient; κ_e = volume scattering coefficient κ_s + volume absorption coefficient κ_a,

d is the volume thickness.

The surface-volume interaction scattering coefficient is sum of two contributions: (1) first volume scattering followed by reflection at the bottom surface, and (2) first reflection at the bottom surface followed by volume scattering.

Transmission across top boundaries and reflection at bottom boundaries are accounted for using Fresnel power transmission (T) and reflection coefficients (R) (coherent case with plane surface) (Fung 1994). T and R are functions of snow and sea ice effective (bulk) dielectric constants (ε_r). The extinction coefficient κ_e is obtained either by a semi-empirical or pure empirical model or by calculating the absorption coefficient κ_a from the effective ε_r and the scattering coefficient κ_s using a theoretical volume scattering model.

The effective ε_r of sea ice can be understood in terms of a physical mixing theory which explains ε_r as a function of the permittivity of sea ice components: ice, gas and brine, and of the shape of the gas and brine inclusions. The effective ε_r of snow is a function ice, air and liquid water (if present) ε_r and the shape of the ice and water inclusions. This low-frequency approximation neglects the effects of scattering which means that the modeled ε_r is not dependent on the sizes of the inclusions. Simple low-frequency mixing models for snow and sea ice ε_r have been developed by combining theory and empirical ε_r data. Hallikainen et al. (1986) presents snow effective ε_r as a function of snow density and volumetric liquid water content (wetness). Hallikainen and Winebrenner (1992) show sea ice effective ε_r as a function of brine volume fraction which in turn is a function of sea ice density, salinity and temperature.

Surface backscattering components in (3.7) are functions of surface ε_r and surface roughness characterized by surface rms roughness s, correlation length L and autocorrelation function. Currently, the best choice for calculating surface backscattering is the integral equation method (IEM) model presented in (Fung et al. 1992, Fung 1994). The IEM model assumes scattering surface to be a Gaussian stationary random process, i.e. the properties of any given surface area are statistically identical to any other areas or to the whole. IEM has separate equations for single and multiple scattering contributions. The single scattering IEM model at co-polarization (simplest case) is (Fung et al. 1992, Fung 1994):

$$\sigma^{o}_{pp} = \frac{k^2}{2}\exp\left(-2\sigma^2 k_z^2\right)\sum_{n=1}^{\infty} s^{2n}\left|I^n_{pp}\right|\frac{W^{(n)}(-2k_x,0)}{n}, \tag{3.9}$$

where k is the wave number, $k_z = k\cos\theta_0$, $k_x = k\sin\theta_0$, and pp = HH- or VV-polarization,

$$I^n_{pp} = (2k_z)^2 f_{pp}\left(-k_z^2 s^2\right) + \frac{1}{2}(k_z)^n\left[F_{pp}(-k_x,0) + F_{pp}(k_x,0)\right], \tag{3.10}$$

where f_{pp} and F_{pp} are the Kirchhoff and the complementary field coefficients presented in Appendix 4B of (Fung 1994),

and $W^{(n)}$ is the Fourier transform of the nth power of the surface autocorrelation function $\rho(\xi,\zeta)$. If the surface is isotropic, then $W^{(n)}$ is:

$$W^{(n)}(-2k_x,0)=\frac{4}{2\pi}\int_0^\infty\int_0^\infty \rho(\xi,\zeta)^n\cos(-2k_x\xi)d\xi d\zeta\,. \tag{3.11}$$

Commonly used surface autocorrelation functions are Gaussian, exponential and transformed exponential functions (Fung 1994). For example, the Gaussian function and its $W^{(n)}$ are (Fung 1994):

$$\rho(\xi,\zeta)=\exp\left[-\left(\xi^2+\zeta^2\right)/L^2\right], \tag{3.12}$$

$$W^{(n)}(-2k_x,0)=\frac{L^2}{2n}\exp\left[-\frac{(-2k_xL)^2}{4n}\right]. \tag{3.13}$$

The validity limits of the IEM model are (Fung 1994):

$$\begin{aligned} ks &< 2\,, \\ ks &< 2\ (ks)(kL) < 1.2\sqrt{\varepsilon_r'}\,, \text{ Gaussian } \rho\,, \\ (ks)(kL) &< 1.6\sqrt{\varepsilon_r'}\,, \text{ non-Gaussian } \rho\,. \end{aligned} \tag{3.14}$$

The first limit is for the validity of the single scattering approximation and the second for approximating the local incidence angle in f_{pp} and F_{pp} with the radar incidence angle. f_{pp} and F_{pp} depend on the Fresnel reflection coefficients which in turn depend on the dielectric contrast.

Volume scattering in snow is caused by ice crystals. In sea ice volume scattering is modeled in literature either by brine pockets or by gas bubbles depending on the sea ice type. In dense new ice the brine pockets are assumed to be the source of volume scattering, whereas in older less dense, less saline ice types, like multiyear ice, the source is gas bubbles. For calculating volume scattering there are several models presented in literature. The simplest model is the Rayleigh single scattering model which assumes that the scatterers are very small compared with the incident wavelength and each scatterer is in the far field of others (Fung 1994). In this model the strength of volume scattering depends on the size of scatterers, volume fraction of scatterers (i.e. number of scatterers in unit volume) and on the scatterer ε_r contrast to the host media. The fraction of gas bubbles in sea ice depends, like brine volume fraction, on sea ice density, salinity and temperature. More advanced models allow close spacing between scatterers (i.e. scatterers are in the near field of each other) and take into account the shape of the scatterers, the correlation between the positions of the scatterers in the host medium and multiple scattering.

In summary, σ° of snow covered level sea ice depends on the following radar, snow and sea ice parameters when it is assumed that the scattering contribution from ice-ocean interface is negligible:

1. Radar parameters: frequency, incidence angle and polarization.
   - Incidence angle dependence of σ° comes mainly from the incidence angle dependence of the Fresnel reflection and transmission coefficients.
   - Frequency, i.e. radar wavelength, has an large effect on σ° as the surface and volume scattering components depends on the relative size of the roughness parameters and scatterer sizes on the wavelength.
   - The difference between co-polarizations HH and VV is mainly due to difference between the Fresnel reflection coefficients at H- and V-polarization in case of the surface scattering and due to the non-spherical scatterer shape in case of the volume scattering.
   - Differences between co- (HH and VV) and cross-polarization (HV or VH) are mainly due to the different dominating scattering mechanisms: single scattering at co- and multiple at cross-polarization.

2. Dielectric characteristics of snow and sea ice.
   - Bulk ε_r of snow and sea ice determine the volume absorption coefficient κ_a.

   2.1 Bulk ε_r of snow depends on
   - snow density
   - snow wetness
   - snow temperature, only in the case of dry snow

   2.2 Bulk ε_r of sea ice depends on
   - brine volume fraction which depends on
     - sea ice density
     - sea ice salinity
     - sea ice temperature
   - ε_r of a scatterer is a one of the parameters determining the volume scattering coefficient κ_s. Scatterers in snow are ice crystals. In sea ice they are either air bubbles or brine pockets.

   2.3 ε_r of ice crystal depends on
   - temperature

   2.4 ε_r of brine pockets depends on
   - brine salinity which depends on
     - parent sea water salinity
     - temperature

3. Geophysical characteristics of snow and sea ice.
   - Surface and volume backscattering components depend greatly on the following snow and sea ice parameters:

   3.1 Snow and sea ice small scale surface roughness characterized by surface rms roughness, correlation length and autocorrelation function (small scale roughness means here rms roughness values from few mm to few cm).

   3.2 Size and volume fraction of ice crystals in snow. Volume fraction depends on
   - snow density and wetness

3.3 Size and volume fraction of gas bubbles or brine pockets in sea ice. Volume fractions depend on
   - sea ice density, salinity and temperature

3.4 If sea ice is deformed, i.e. sea ice has also large scale surface roughness, like ice ridges, also the deformation features contribute to the level of σ°.

Theoretical backscattering models developed for the Baltic Sea level ice and deformed ice are reviewed in Chapter 4.3.

3.2 Radar Polarimetry

In the following only those topics of radar polarimetry relevant for the study conducted in this thesis are presented. Only basic polarimetric discriminants were studied in [P2].

A polarimetric SAR typically transmits H- and V-polarization alternately and receives the backscattered field at both H- and V-polarization, thus recording all combinations of these two linear polarizations: HH, VH, VV, HV. Both amplitude and phase of the scattered signal is measured. The measurements are represented by a complex backscattering matrix $\mathbf{S}$ which connects the received electric field to the transmitted field, e.g. (Touzi et al. 2004):

$$\vec{E}^{\,r} = [\mathbf{S}]\vec{E}^{\,t} = \begin{bmatrix} \vec{E}_H^{\,r} \\ \vec{E}_V^{\,r} \end{bmatrix} = \frac{e^{jkr}}{r} \begin{bmatrix} S_{HH} & S_{HV} \\ S_{VH} & S_{VV} \end{bmatrix} \begin{bmatrix} \vec{E}_H^{\,t} \\ \vec{E}_V^{\,t} \end{bmatrix}, \tag{3.15}$$

where r is the distance from the center of the illuminated area to the point of observation.

The unknown complex backscattered field is sampled in two orthogonal directions which completely characterize it. The backscattered field from a distributed target (e.g. sea ice) is a vector sum of waves with a variety of polarizations from numerous randomly positioned scatterers. The polarimetric SAR provides a measure of the mean field components of the resulting partially polarized wave in each image pixel, i.e. the measured $\mathbf{S}$ matrix for one pixel consists of the coherent superposition of the individual $\mathbf{S}_i$ matrices of all scatterers located within the pixel. In backscattering $S_{HV} = S_{VH}$ due to the reciprocity theorem and, thus, there are five independent parameters in $\mathbf{S}$: three amplitudes (at HH, HV and VV polarizations) and two phase parameters: co- and cross-polarization phase differences $\phi_{HH} - \phi_{VV}$ and $\phi_{HH} - \phi_{HV}$. Each element of $\mathbf{S}$ is a function of frequency, incidence angle and target electrical and physical properties. e.g. (Touzi et al. 2004, Lopez-Martinez et al. 2007).

The $\mathbf{S}$ matrix is only able to characterize the so-called coherent or pure scatterers. It cannot be employed to characterize, from a polarimetric point of view, the so-called distributed scatterers, i.e. natural remote sensing targets. This type of scatterers can be only characterized statistically due to the presence of fading noise. Since fading noise must be reduced, only second order polarimetric representations can be employed to analyze distributed scatterers. These second order descriptors are the average covariance $\langle \mathbf{C} \rangle$, coherency $\langle \mathbf{T} \rangle$ and Stokes $\langle \mathbf{M} \rangle$ matrices. All these matrices consist of linear combinations of the cross-products of the four basic elements of the matrix $\mathbf{S}$. These linear combinations and their correlations are closely related to the physical properties of the scattering medium. These matrices can be spatially averaged and can also be presented in the ground range coordinate system, whereas the $\mathbf{S}$ matrix is always presented in slant range and it cannot be averaged. $\langle \mathbf{C} \rangle$ is directly related to the system measurables whereas $\langle \mathbf{T} \rangle$ is closer related to the physical and geometrical properties of the scattering process, and thus allows a better and direct physical

interpretation. Multilook SAR data are generally provided under the $\langle \mathbf{M} \rangle$ or $\langle \mathbf{C} \rangle$ matrix format. For example, the $\langle \mathbf{C} \rangle$ matrix is, e.g. (Touzi et al. 2004, Lopez-Martinez et al. 2007):

$$\langle \mathbf{C} \rangle = \left\langle \begin{bmatrix} S_{HH}S_{HH}^* & \sqrt{2}S_{HH}S_{HV}^* & S_{HH}S_{VV}^* \\ \sqrt{2}S_{HV}S_{HH}^* & 2S_{HV}S_{HV}^* & \sqrt{2}S_{HV}S_{VV}^* \\ S_{VV}S_{HH}^* & \sqrt{2}S_{VV}S_{HV}^* & S_{VV}S_{VV}^* \end{bmatrix} \right\rangle . \tag{3.16}$$

In the following, various polarimetric discriminants are shortly described. They can be computed for every pixel in a polarimetric SAR image, but are often averaged over groups of pixels to reduce the effect of fading. The polarimetric discriminants are used for SAR image classification and interpretation of target geophysical properties and scattering mechanisms.

Total power or span in the backscattered field is, e.g. (Drinkwater et al. 1992):

$$Span = |S_{HH}|^2 + |S_{VV}|^2 + 2|S_{HV}|^2 . \tag{3.17}$$

Total power is also the sum the diagonal elements of $\langle \mathbf{C} \rangle$, $\langle \mathbf{T} \rangle$ and $\langle \mathbf{M} \rangle$ matrices.

The co-polarization ratio R_{co} is defined as, e.g. (Drinkwater et al. 1991):

$$R_{co} = \frac{\sigma^\circ{}_{HH}}{\sigma^\circ{}_{VV}} = \frac{|S_{HH}|^2}{|S_{VV}|^2} . \tag{3.18}$$

According to the IEM surface scattering model (Fung 1994) the co-polarization ratio depends on the surface roughness and the dielectric constant of surface. It is below 0 dB in the presence of pure top surface scattering and it decreases with increasing incidence angle. With a combination of top surface and volume scattering R_{co} is also below 0 dB, but now the incidence angle dependence decreases at large angles due to the dominating volume scattering. When the surface roughness or the strength of the volume scattering increases, R_{co} approaches 0 dB. However, the higher the dielectric constant of the surface is, the smaller is R_{co} due to the Brewster angle effect. R_{co} can be over 0 dB due to the either strong surface-volume interaction (Fung 1994) (e.g. there is scattering interaction between ice volume and ice-water interface) or double bounce scattering (i.e. dihedral corner reflection), e.g. (Lopez-Martinez et al. 2007). These scattering mechanisms raise HH-polarized scattering above VV-polarized one due to the Brewster angle effect.

The relation of the cross-polarized backscattering to the co-polarized one is characterized by the cross-polarization ratio R_{cr} or by the depolarization ratio R_{depol}, e.g. (Drinkwater et al. 1991, 1992):

$$R_{cr} = \frac{\sigma^\circ{}_{HH}}{\sigma^\circ{}_{HV}} = \frac{|S_{HH}|^2}{|S_{HV}|^2} , \tag{3.19}$$

$$R_{depol} = \frac{2\sigma^\circ{}_{HV}}{\sigma^\circ{}_{HH} + \sigma^\circ{}_{VV}} = \frac{2|S_{HV}|^2}{|S_{HH}|^2 + |S_{VV}|^2} . \tag{3.20}$$

These ratios are indicators of multiple scattering events which raise cross-polarized scattering relatively more than co-polarized scattering. Strong multiple scattering occurs when e.g. surface is very rough (Fung 1994).

The above mentioned discriminants can also be obtained with multichannel radars measuring only the intensities of the backscattered fields.

When the polarization state of the co- or cross-polarized signature is synthetically varied (polarization synthesis is explained e.g. in (Lopez-Martinez et al. 2007)) and the maximum and minimum intensities $P_{\max}$ and $P_{\min}$ are recorded, two statistics, the coefficient of variation γ and the fractional polarization f_p, can be calculated (Drinkwater et al. 1991):

$$\gamma = \frac{P_{\min}}{P_{\max}}, \tag{3.21}$$

$$f_p = \frac{P_{\max} - P_{\min}}{P_{\max} + P_{\min}}. \tag{3.22}$$

γ and f_p relate to the heterogeneity of the scattering mechanisms in the target and the fraction of polarized returns. High values of γ can be caused by a combination of multiple scattering, inhomogeneity in the scattering mechanisms within target, and a low signal-to-noise ratio. (Drinkwater et al. 1991).

The relative phase difference between co-polarized channels is obtained from, e.g. (Drinkwater et al. 1991):

$$\phi_{HH-VV} = \tan^{-1}\left(\frac{\mathrm{Im}\left(S_{HH}S_{VV}^{*}\right)}{\mathrm{Re}\left(S_{HH}S_{VV}^{*}\right)}\right). \tag{3.23}$$

If the surface is lossy, ϕ_{HH-VV} is negative, and further decreases with increasing incidence angle (Drinkwater et al. 1992). The higher the dielectric constant of the surface, the more rapid this decrease becomes. When the surface is very smooth, ϕ_{HH-VV} can be approximated by the Fresnel reflection coefficients. According to a theoretical backscattering model for thin ice (penetration depth is larger than ice thickness) by Winebrenner et al. (1995), there is an interference between up- and down-going waves in the ice layer resulting from scattering at the air-ice and ice-water boundaries which causes ϕ_{HH-VV} to oscillate as a function of ice thickness with a mean value of zero degrees. This interference effect may produce large values of ϕ_{HH-VV}. Also R_{co} oscillates as a function of ice thickness and is always below unity. If the scattering centers at HH- and VV-polarization are vertically separated then large ϕ_{HH-VV} values are also produced.

The correlation coefficient between co-polarized channels is, e.g. (Drinkwater et al. 1992):

$$\rho_{co} = \left|\frac{S_{HH}S_{VV}^{*}}{\sqrt{\left(S_{HH}S_{HH}^{*}\right)\left(S_{VV}S_{VV}^{*}\right)}}\right|. \tag{3.24}$$

If the magnitude of ρ_{co} is unity then backscattering is fully polarized; the co-polarized returns are perfectly correlated and the cross-polarized return is zero. An example is the backscattered wave received from an ideal trihedral corner reflector. ρ_{co} generally decreases with increasing incidence angle in sea ice that is predominantly surface scattering, and at an increasing rate in higher salinity ice (Drinkwater et al. 1992). The longer the radar wavelength, the lower is the sensitivity of ρ_{co} to surface or volume scattering effects. In presence of volume scattering low ρ_{co} values can be explained by two effects: ellipsoidal shape of scatterers (e.g. brine pockets in sea ice) and anisotropy due to the preferential

orientation of scatterers (e.g. vertical orientation of brine pockets) (Nghiem et al. 1995). When the penetration depth is larger than thickness (i.e. the interference effect is present) varying ice thickness within sample area produces ρ_{co} significantly less than one (Winebrenner et al. 1995). In general, the smaller ρ_{co} is, the greater the variance of ϕ_{HH-VV}, and the smaller f_p becomes.

3.3 Brightness Temperature

All physical objects emit thermal radiation in the form of electromagnetic waves. Under thermal equilibrium the absorption and emission of the object are equal, which means that the physical temperature of the object is constant. A perfect absorber and radiator is called a blackbody. Planck's radiation law gives the brightness of a blackbody, but at microwave frequencies the linear Rayleigh-Jeans law gives an good estimation (Ulaby et al. 1981). A physical object always radiates less than a blackbody at the same physical temperature. The ratio between the brightness of a real object and that of a blackbody is defined as emissivity e, which is dependent on the angular variables θ (measurement angle from vertical) and φ (azimuthal angle) (Ulaby et al. 1981). In passive microwave remote sensing, the power measured by a radiometer is expressed as brightness temperature $T_B(\theta,\varphi)$ (in Kelvin), which is the product of the emissivity of a target and its physical temperature T (Ulaby et al. 1981):

$$T_B(\theta,\varphi) = e(\theta,\varphi)\cdot T\ . \tag{3.25}$$

If the measurement target has azimuthal symmetry then T_B depends only on angle θ.

Radiometers typically measure T_B at both H- and V-polarization. Airborne and spaceborne radiometer systems also have several measurement frequencies. If surface temperature is simultaneously measured with T_B, then measured T_B values can be converted to emissivities which are more meaningful in comparison with target physical properties. However, this conversion is not always totally accurate as the surface temperature instruments, like infrared radiometers, measure only surface skin temperature, whereas T in (3.25) is the effective temperature for the layer from which the thermal radiation mainly emanates. The accuracy of the conversion is the better, the thinner this layer is.

Brightness temperature of snow covered level sea ice depends on the same sea ice physical parameters as the backscattering coefficient. Radiometer incidence angle changes measured T_B mainly through the Fresnel coefficients and the Brewster angle effect. Radiometer frequency (i.e. wavelength) changes measured T_B through the relative sizes of the roughness parameters and scatterers to the wavelength.

4 Previous Research in Microwave Remote Sensing of the Baltic Sea Ice

Investigations on the feasibility of microwave remote sensing for the Baltic Sea ice monitoring started in 1975 (Hallikainen 1992). The first research campaign was Sea Ice-75 organized jointly by Finland and Sweden. In this campaign first airborne radar (10 GHz side-looking airborne radar (SLAR)) and radiometer (0.6 and 5 GHz) measurements were conducted. It was followed in 1987 by the Bothnian Experiment in Preparation of ERS-1 (BEPERS-87) pilot study organized by Finland, Sweden and West Germany together (Leppäranta et al. 1992). This study included the first airborne SAR measurements over the Baltic Sea ice with a French X-band SAR. BEPERS-88 study included first airborne C-band SAR measurements conducted by Canada Centre for Remote Sensing (CCRS) and first C- and X-band helicopter-borne scatterometer measurements conducted by Laboratory of Space Technology of Helsinki University of Technology (Leppäranta and Thompson 1989). In the late 1980's the research work intensified for studying the use of the ERS-1 SAR images for the Baltic Sea ice monitoring. First ERS-1 images, and also the first spaceborne SAR images over the Baltic Sea ice, were acquired in winter 1992.

In the field of the Baltic Sea ice microwave remote sensing research Finland has been the most active country since the late 1980's, when counted by the number of projects and publications. Sweden was also very active up to around 1997; likely (and hopefully) there has just been temporary hiatus in the research work. In the other Baltic countries the research work has been limited. In the field campaigns organized by Finland and Sweden there have been occasionally scientists from other countries, like Germany, Russia, Canada, Great Britain and USA. The research projects in Finland have mostly been national, funded by Finnish Funding Agency for Technology and Innovation (TEKES) and Academy of Finland.

The main goal of the research projects has been to develop operational sea ice classification algorithms for spaceborne SAR data: ERS-1/2, RADARSAT-1 and ENVISAT Advanced SAR (ASAR). Besides this, the projects have also included (1) basic research in σ° signatures of sea ice, e.g. σ° statistics for various ice types and effect of snow wetness in the statistics, (2) theoretical modeling of σ° signatures, (3) field campaigns to gather ground truth data and σ° data with airborne and shipborne radars, (4) development of end-user software for interpretation and use of the sea ice products, and (5) various issues of data delivery to end-users at ships. Tasks (1)-(3) support the development and validation of the SAR classification algorithms.

Polarimetric SAR remote sensing of the Baltic Sea ice is still in infancy, mainly due to the very limited amount of data available thus far. The first, and so far the only, polarimetric SAR images over the Baltic Sea ice were acquired in 1995 by Danish airborne EMISAR radar (Dall et al. 1997).

Utilization of spaceborne microwave radiometer data for the Baltic Sea ice monitoring has been not been studied much. The main reason for this is the very coarse resolution of the radiometer data, e.g. in the AMSR-E data the resolution is from 56 to 6.4 km. The first study in using spaceborne radiometer data for determining the ice concentration in the Baltic Sea was conducted in 1986 (Hallikainen and Mikkonen 1986). The first airborne multifrequency radiometer (24/35/48/94 GHz) measurements for supporting the development of classification algorithms were conducted in 1990 (Hallikainen 1992).

In the following Sections previous studies in the various subjects of the microwave remote sensing of the Baltic Sea ice are reviewed. In the last Section those previous results relevant for this thesis are summarized.

4.1 Dielectric Constant of Sea Ice and Snow

Effective dielectric constant ε_r of the Baltic Sea ice has been studied empirically by Hallikainen (1983) and Hallikainen et al. (1988). Theoretical studies have not yet been conducted. Hallikainen (1983) measured in 1978 and 1979 ε_r of ice samples from the Gulf of Finland using frequencies 0.6 and 0.9 GHz. The salinity of the ice samples varied from 0.0 to 1.6‰ and temperature from -18 to -0.5ºC. The ε_r study by Hallikainen et al. (1988) was conducted in the Bay of Bothnia in 1987 at a frequency of 10 GHz. The salinity and temperature of the ice samples was from 0.0 to 1.0 ‰ and from -6.0 to -0.3ºC, respectively. These measurements have not been used to derive a general, wide frequency range Baltic Sea ice ε_r model.

Using the above mentioned measurements and data from many Artic Sea ice ε_r studies, Hallikainen and Winebrenner (1992) derived an empirical sea ice ε_r model where ε_r is only a function of relative brine volume fraction $v_b \le 70‰$:

$$\begin{aligned} &1\text{ GHz: } \varepsilon'_{rsi} = 3.12 + 0.009v_b,\ \varepsilon''_{rsi} = 0.04 + 0.005v_b, \\ &4\text{ GHz: } \varepsilon'_{rsi} = 3.05 + 0.0072v_b,\ \varepsilon''_{rsi} = 0.02 + 0.0033v_b, \\ &10\text{ GHz: } \varepsilon'_{rsi} = 3.0 + 0.012v_b,\ \varepsilon''_{rsi} = 0.0 + 0.010v_b\,. \end{aligned} \tag{4.1}$$

The equations do not explicitly take into account the effect of ice density upon the real part of ε_{rsi}. The volume fraction of brine is calculated from sea ice temperature, salinity and temperature using a method devised by Cox and Weeks (1983) and extended to the Baltic Sea ice low salinities and temperatures above -2ºC by Leppäranta and Manninen (1988).

Carlström and Ulander (1995) used the 4 GHz ε_{rsi} equation also at 5.3 GHz (frequency of ERS-1, RADARSAT-1 and ENVISAT ASAR) for the Baltic Sea ice, but they modified the constant term of the imaginary part to make it approach the measured values for fresh-water ice:

$$\text{Baltic Sea ice at 5.3 GHz: } \varepsilon'_{rsi} = 3.05 + 0.0072v_b,\ \varepsilon''_{rsi} = 0.001 + 0.0033v_b\,. \tag{4.2}$$

Effective ε_r of the snow cover on the Baltic Sea ice has not been studied and, thus, ε_r models for snow on land must be utilized. It is possible that ε_r for snow on land and on sea ice with equal density and wetness are somewhat different due to the strong wind packing of sea ice snow cover and occurrence of brine in snow on sea ice.

Real part of ε_r for dry snow is obtained from (Hallikainen et al. 1986):

$$\varepsilon'_{rds} = 1 + 1.9 \cdot \rho_{ds},\ \rho_{ds} \le 0.5\,\mathrm{g/cm^3} \tag{4.3}$$

and imaginary part below 13 GHz from (Tiuri et al. 1984):

$$\varepsilon''_{rds} = 1.59 \cdot 10^6 \left(0.52\rho_{ds} + 0.62{\rho_{ds}}^2\right)\left(f^{-1} + 1.23 \cdot 10^{-14}\sqrt{f}\right)\exp\left(0.036T_s\right), \tag{4.4}$$

where ρ_{ds} is dry snow density, f is frequency and T_s is snow temperature in degrees Celsius.

For wet snow, ε_r is calculated using a semi-empirical Debye-like model (Hallikainen et al. 1986):

$$\varepsilon'_{rws} = A + \frac{Bm_v^x}{1+\left(f/f_0^2\right)}, \qquad \varepsilon''_{rws} = \frac{C\left(f/f_0\right)m_v^x}{1+\left(f/f_0^2\right)}, \tag{4.5}$$

where m_v is volumetric liquid water content of snow in percent (wetness),

$A = 1.0 + 1.82\rho_{ds} + 0.02A_1 m_v^{1.015} + B_1$, $B = 0.073A_1$, $C = 0.073A_2$,

$x = 1.31$, $f_0 = 9.07$ GHz, $A_1 = A_2 = 1.0$ and $B_1 = 0$ when $f < 15$ GHz.

4.2 Geometric Properties of Sea Ice

For theoretical modeling of level ice σ° the following statistics of the ice surface roughness are needed: rms surface roughness, surface correlation length and the form of the surface autocorrelation function. If the contribution of snow surface σ° is estimated to be significant then the same statistics are also needed for the snow surface. For σ° modeling of sea ice deformations, like ice ridges, also a geometrical surface structure model of ice is required. In the case of σ° modeling of a deformed ice field in scale of large SAR pixels (e.g. 100 by 100 m) a spatial model for occurrence of deformations, e.g. spatial density of ice ridges, is furthermore needed. These statistics and models also help to interpret measured σ° signatures. Of the deformed ice types, surface structure and spatial statistics of ice ridges have been measured and modeled so far. The most extensive study on the ice ridge spatial statistics has been conducted by Lensu (2003). The results of this study are not reviewed here as they have not yet been utilized in the classification of SAR images and theoretical σ° modeling.

4.2.1 Ice surface roughness

The most extensive study so far on the Baltic Sea ice surface roughness has been conducted by Manninen (1997a). She measured in four field campaigns in 1992-1994 surface roughness of sea ice in the following three scales: small scale; profile length 1 m, horizontal resolution 1 mm, medium scale; length 5 m, resolution 5 cm, and large scale; length 50 or 100 m, resolution 50 cm. Measured ice types ranged from very smooth level ice to very rough rubble fields. Small scale roughness measurements were also conducted on ice ridge blocks. Analysis of the measurements indicated a dependence of the surface rms roughness s and correlation length L on the measurement length l. This is a property of fractal profile and it turned out that a suitable method to describe the dependence of s and L on l in the ice surface profiles is the fractional Brownian motion (fBm). fBm itself is a non-stationary process, but its increments are stationary.

The functional dependence of s of the fBm on the measurement length l has a power-law form (Church 1988):

$$\ln(s) = a + b\ln(l) \tag{4.6}$$

and L is linearly dependent on l (Church 1988):

$$L = k_0 l\,. \tag{4.7}$$

The coefficient a is related to the actual profile level, whereas b describes the variation of the profile with spatial frequency. The value of a depends on the unit used for l and s. The coefficients k_0 and b are functions of the fractal dimension D of the surface (Church 1988):

$$k_0 = \frac{2(2-D)^2}{(9-4D)},\ b = 2 - D. \tag{4.8}$$

Consequently, there is a simple relationship also directly between s and L:

$$L = k_0 \exp(-a/b) s^{1/b}. \tag{4.9}$$

Using linear regression analysis the coefficients k_0, a and b were calculated for all measured small, medium and large scale profiles. On all scales s obeyed fBm behavior quite well; the median of the correlation coefficient for the linear regression was above 0.9 in all cases. L was not as clearly of the fBm type. Although the correlation between k_0 and b is obvious on all cases, it is not strong enough to enable elimination of one of these three coefficients. The general similarity of the small, medium and large scale results clearly revealed the fractal-like, i.e. multiscale surface roughness, nature of the Baltic Sea ice surfaces. (Manninen 1997a).

It was difficult to find any representative average values of k_0, a and b for different ice types. However, in the large scale the relationship between a and b and the interdependence of (4.9) as a function of l in the s-L space reveals different ice types to some degree, for example, the smoother the ice, the smaller is a for equal values of b. The relationship of k_0 and b does not distinguish any ice types. (Manninen 1997a).

In practice, (4.6) and (4.7) cannot be expected to be valid to infinity. However, it is probable that s and L increase to maximum values characteristic of the ice type in question and then saturate. (Manninen 1997a).

The small scale s increases with time due to wind, snow accumulation, and varying temperature. Ice blocks of old ridges are typically slightly rougher than surrounding flat ice areas. Typically dry thin snow layer decreases the small scale roughness, whereas wet snow sticks to the ice surface easily and over time produces typically anisotropic small scale roughness on the ice. The surface roughness is typically larger parallel to the direction of the predominant wind. Ice blocks in ridges have typically only moderately anisotropic surfaces. In the medium and large scale, snow fills deep pits of deformed ice and, thus, s of the snow surface is typically smaller than that of the ice surface. The snow and ice surfaces are correlated, but only at a coarse level. (Manninen 1997a).

The s and L values presented by Manninen (1997a) are consistent with values reported in other Baltic Sea ice roughness studies for 1 m and 10 m profiles, e.g. (Johansson 1988, Carlström and Ulander 1995). However, the other researchers did not analyze the dependence of s and L on l.

Carlström and Ulander (1995) and Dierking et al. (1999) measured ice surface roughness with a laser profiler which acquired 1 m profiles. After low-pass filtering of the profiles, horizontal resolution was 2 mm and rms elevation error was 0.5 mm. It was assumed that the measured profiles are from a wide-sense stationary surface, i.e. s and L do not depend on the measurement location and l. For each profile, the autocorrelation function (ACF) was calculated using standard signal processing algorithms, including mean and trend removal. ACF's of several profiles from the same surface were averaged to reduce statistical

fluctuations. Exponential ACF was found to be an adequate model for the measured average ACF.

Dierking et al. (1997) developed a surface roughness model for an area of refrozen brash ice in order to interpret ship based scatterometer measurements. The roughness model was based on surface profile data measured with a laser profiler. In total eight 9-meter long profiles were measured in two lines running in radial direction from the scatterometer position. The horizontal and vertical resolutions of the profiles were 20 mm and 3 mm, respectively. As the profiles revealed considerable changes in the surface roughness, the area of the scatterometer measurements was regarded to be nonstationary. For estimation of the magnitude of roughness variations over the area illuminated by the scatterometer, the profiles were divided into 4.5 m long segments which were assumed to represent surfaces with wide-sense stationary roughness, i.e. the measurement area was approximated to consist of adjacent patches of stationary roughness. From the roughness spectra of the segments, two classes were distinguished: 'smooth' and 'rough' class. Segments grouped into a certain class were within the ±2 standard deviation interval around the mean class spectrum. The form of the surface ACF needed in the theoretical σ° models was assumed to be:

$$\rho(x) = \exp\left(- x^2 \Big/ \sqrt{x^2 L_e^2 + L_g^4}\right), \tag{4.10}$$

where L_e and L_g are the exponential and Gaussian correlation length, respectively. If $L_g << L_e$ this ACF model describes a surface consisting of large structures which are correlated exponentially with scale length of L_e, and superimposed small scale structures (rms roughness at maximum few centimeters) with a Gaussian correlation function of scale length L_g.

The calculation of ACF includes mean and trend removal in the surface profile data. This affects the shape of the resulting ACF because means and trends from individual segments of finite length are used instead of the population mean and trend of the infinite data series. A consequence of this is that s and L are smaller than the corresponding values of the population (s_∞ and L_∞). The decrease of segmentwise s and L depends on the ratio L/l. For example, for the class 'rough' s and L of a 4.5 m long segment were 22 mm and 0.25 m, respectively, compared to s_∞=28 mm and L_∞=0.46 m. In case of a 9 m segment, s was 25 mm and L was 0.34 m. Therefore, the ideal profiling length for class "rough," should be longer than 10 m in order to measure roughness parameters which are close to s_∞ and L_∞. However, this is impractical in the field work and, additionally, profiles may not be stationary over the long lengths.

In summary, there are three possibilities for describing the surface roughness of the Baltic Sea ice: (1) Surface roughness is stationary over large areas, e.g. in a SAR pixel of 100 by 100 m. s and L do not depend on l. However, in empirical data the dependence is present if the ratio L/l is not small enough. (2) Surface roughness is stationary over small surface patches which have different roughness spectra (i.e. s and L values). Roughness is nonstationary over large areas. (3) Surface has multiscale roughness which can be characterized by the fBm process. s and L always depend on l, regardless of how large l is. Case (1) can used with traditional surface backscattering models, like the IEM model, which assume stationary surface. Likewise is Case (2), if the stationary surface patches are equal or larger than the area of the illuminated by the radar. Case (3) is not valid with the traditional scattering models and, thus, its use requires either modifications to these models or development of entirely new models. Manninen's (1997a) results obtained with a large surface roughness data set suggested strongly that Case (3) is valid for the Baltic Sea ice.

4.2.2 Surface structure of ice ridge

Ice ridges in the Baltic Sea have been studied intensively in the past, but the main emphasis has been in the large scale properties of the ridge sail and keel (Manninen 1996a). For theoretical modeling of σ°, a surface structure model of an ice ridge is required. Models for the surface structure have been developed in (Carlström and Ulander 1995) and (Manninen 1992).

Model by Carlström and Ulander (1995)

Carlström and Ulander (1995) modeled an ice ridge as an ensemble of equally sized circular ice disks on a horizontal plane surface. This was based on the hypothesis that the circular scattering pattern of the disk may be interpreted as an ensemble average of the scattering from an ice block with arbitrary shape that is randomly rotated around the normal of its major facet. The physical parameters of the disk are the radius and thereby the area of the disk facet, disk thickness and superimposed small scale roughness (rms-roughness from 1 mm to few centimeters), and the 2-D joint probability density function (pdf) of the disk facet slopes in the horizontal x- and y-directions. The model was simplified by assuming the slope pdf to be azimuthally isotropic and, thus, it can be obtained from 1-D profile measurements of ice ridges which yield an 1-D surface slope distribution. For the measured profiles, the Cauchy pdf can be used to represent the distribution of the ice disk slopes:

$$p(z'_x) = \frac{m}{\pi} \frac{1}{\left(m^2 + z'^2_x\right)}, \tag{4.11}$$

where z'_x is the surface height derivative in the x-z plane and m is the half-value point of the Cauchy pdf.

The 2-D isotropic pdf for the ice disk surface slopes is now:

$$p(z'_x, z'_y) = \frac{m}{2\pi\left(m^2 + z'^2_x + z'^2_y\right)^{3/2}}, \tag{4.12}$$

where z'_y is the surface height derivatives in the y-z plane.

The size and slope angle of the disk are assumed to be independent in the model. The model does not include large scale topography parameters of ice ridges, like width and height of the ice ridge.

Model by Manninen (1992)

Manninen (1992) developed a 3-D geometrical structural ice ridge model based on ridge geometry and ice block size and orientation statistics. The main idea of the model is to calculate an incidence angle distribution for the cross sectional surface of an ice ridge.

The general shape of the triangular cross-section of the ice ridge sail is defined by the proximal and distal slope angles θ_p and θ_d, sail height h_r and porosity p ($0< p <1$). The ice blocks in the ridge sail are assumed to be rectangular polyhedrons. Each ice block is described with the three Euler angles: horizontal rotation angle φ, vertical rotation angle θ, and angle ψ describing the rotation of the main facet around its normal vector, and with three dimensions: length a and width b of the main facet and thickness h of the ice block. Other parameters needed are the vertical distance h_f between the radar and ice level, the radar incidence angle θ_0 at the proximal edge of the ridge sail, and the radar azimuth angle φ_0 between the radar look direction and the normal of the ridge direction (for description of the model see Figures 2 and 3 and Table 1 in (Manninen 1992)).

The calculation of the Euler angles and the dimension parameters is presented in (Manninen 1993, 1994). A summary of the calculation process is available in (Manninen 1996a, pp. 12-14). Needed ice ridge ground truth measurements are described in (Manninen 1996b, p. 147).

Manninen (1996b) conducted ground truth measurements of ice block size, shape and orientation for several ice ridges in four field campaigns in 1991-1994. This data was used to study statistics of the Euler angles and dimension parameters. In 1993, also general shape of an ice ridge was studied. The general cross-section of an ice ridge was defined by a sequence of slices comprising two joining triangles (see Fig. 4. in (Manninen 1996b)).

Measured ridge shape parameters were the slope angles and lengths of the ridge sail along the ridge. The results showed that the slope angle and length do not seem to obey log-normal or normal distribution very well. The height and the height difference of the two sides were normally distributed. The two cross-sectional triangles were generally not similar, only their sail heights had a clear correlation. The slope angle did not depend strongly on the other three slope parameters (width, height and length). A slight negative correlation existed between the slope width and the slope angle, indicating that steepest slopes corresponded to the narrowest sails. The average slope angle was equal for both sides. This was expected, as the ice blocks on both sides of the ridge were formed from the same ice field and had similar piling properties.

According to the ice block measurements, the average measured vertical inclination θ_m of the individual ice block main facets was about equal in both sides of a ridge. However, the two sides were different from each other when the orientation of the main facets was described with Euler angles θ and φ. Thus, the vertical process of deformation affected both sides in roughly the same way, whereas the horizontal rotation of the ice blocks was different. Although the shape of the main facets varied very much, the orientation of the side facets versus the main facet was typically very close to orthogonal. Consequently, the approximation of the ice block polygons by rectangular polyhedrons is very good, if the main facets can be matched well with rectangles. As triangular facets were rare, it was usually possible to find a good rectangular approximation for the main ice block facets. The Euler angles and dimensions of the ice blocks could be described with normal pdfs. Empirical distributions were typically very wide, e.g., standard deviations were from 20º to 70º. The correlations between the six parameters were almost nonexistent. Only the length a and the width b had a slight positive correlation. It was noted, that the two sides of a ridge should be treated statistically separately.

Manninen (1996b) emphasized that 3-D modeling of ridges is essential, since the total side facet area visible to the radar is typically at least as large as the total main facet area. The assumption that the main facets alone represent the ridges well is not directly justified.

4.3 Theoretical Backscattering Models

Theoretical modeling of level ice σ° has been studied by the models presented in literature by Carlström and Ulander (1995) and Dierking et al. (1997, 1999). They compared modeled σ° values to measured ones. Dierking et al. (1997) also modeled textural variation (s_T) of σ°. Input data to the σ° models were obtained from ground truth measurements. Manninen (1997b) developed the IEM model by Fung (1994) to be applicable to surfaces with multiscale surface roughness (fractal-like surfaces). σ° models for ice ridges have been developed by Carlström and Ulander (1995) and Manninen (1992). In their σ° models they used different surface structure models of ice ridges. The model by Carlström and Ulander (1995) was further developed by Carlström (1997). The ice ridge σ° models are also applicable for other deformation features which consist of ice blocks with dimensions several times larger than the radar wavelength.

4.3.1 Level ice

σ° modeling studies by Carlström and Ulander (1995) and Dierking et al. (1999)

Carlström and Ulander (1995) formulated a σ° model for level ice based on the first-order solution of the radiative transfer equation. The model included six scattering components: snow, ice and ice-ocean surface scattering, volume scattering from air bubbles in ice, surface-volume interaction scattering in ice and transmitted scattering from ice surface to ice volume and then reflection at ice-ocean interface. The first five components are illustrated in Figure 3.1. Surface scattering was modeled with the IEM model and volume scattering with the Rayleigh model. The transmitted surface scattering was modeled with the small perturbation model (Ulaby et al. 1982).

Using the radar parameters of ERS-1 SAR (frequency 5.3 GHz, VV-polarization, incidence angle 23º), the effect of ice salinity on the different scattering components was investigated. For other sea ice parameters typical values based on the ground truth measurements during two field campaigns in the Bay of Bothnia in 1992 were used; e.g. ice thickness was 30 cm. The air bubble diameter was set to 2 mm which yields an high estimate for the volume scattering contribution. The results showed that dominating contributions from the ice-ocean interface are obtained only when ice salinity S <0.1‰. For S >0.2‰ all scattering components due to the ice-ocean interface can be neglected. Scattering from dry snow surface was always negligible.

The scattering model was also compared with ERS-1 SAR derived σ° values for level ice. In this comparison the scattering model was simplified to include only scattering contributions from ice surface and volume. This model is very sensitive to the air bubble diameter, which made it difficult to validate it with measured σ° values. The air bubble diameter was set to 1 mm. When the ice surface rms roughness s >1.5 mm and S >0.5‰, which is typical for pack ice, the model showed that ice surface scattering is totally dominating. The model predicted and ERS-1 σ° values differed less than 2 dB. When s <1 mm and S <0.1‰, the model clearly underestimated the measured σ° values. Carlström and Ulander (1995) concluded that ice surface scattering is typically the dominant scattering mechanism for level pack ice for the ERS-1 SAR radar parameters. Sub-surface scattering (e.g. ice volume and ice-ocean interface scattering) is significant only when S <0.5‰ which is typical for level landfast ice at the bottom of the bays in the Bay of Bothnia and the Gulf of Finland.

Dierking et al. (1999) conducted ship based scatterometer measurements of smooth level ice in the Bay of Bothnia in April 1995. The scatterometer was operated at 1.25, 2.6, 5.4 and 10 GHz (L-, S-, C- and X-band) and at HH- and VV-polarization. The incidence angle ranged from 20º to 60º in steps of 5º. Various snow and sea ice parameters, including ice surface roughness and ice volume properties, were acquired during the field work. Measured σ° values were compared to predictions of a theoretical σ° model based on the first-order solution of the radiative transfer equation (Fung 1994). The model included scattering contributions from ice surface, ice volume and ice-ocean interface. The ice bulk was divided into two layers and, thus, into two volume scattering components, because of the observed change of the average S from 0.1‰ to 0.4‰ at a depth of about 0.15 m. The thickness of the lower layer was between 0.25-0.65 m in the model. Surface scattering between the two ice layers was not considered. Surface and volume scattering of dry snow layer with an average thickness of 5 cm, as well as the absorption loss in the snow, were neglected. Also surface-volume and interface-interface scattering interactions were ignored. Ice volume scattering from air bubbles was modeled with the Rayleigh model, ice surface scattering with the IEM model and ice-ocean interface scattering with the geometric optics approximation (Ulaby et al. 1982). The latter model was selected because the impulse radar measurements of the ice thickness indicated large, slow variations which suggest an undulating ice-ocean interface with a large rms surface slope.

When the dielectric contrast in the ice-ocean interface is determined by the average ε_r of the lower ice layer and the sea water, as in (Carlström and Ulander 1995), the modeled σ° values were much too large. A good correspondence with the measured σ° values was obtained when it was assumed that there is a thin bottom layer above the ice-ocean interface with ε_r of 5.5-j0.6. This was considered as a realistic assumption, because near the ice-ocean interface, v_b increases drastically and, thus, also ε_r, and the radar wave is strongly attenuated before it reaches the ice-ocean interface.

At X-band modeled and measured σ° values compared well at most incidence angles. The modeling results indicated that volume scattering from the upper ice layer dominated. Ice surface scattering was significant only at small incidence angles (<30º). At C-band, the ice surface scattering was the main scattering source up to an incidence angle of 45º at HH-polarization and up to 55º at VV-polarization. At larger incidence angles, ice volume scattering became significant. Also at S-band, the ice surface was the strongest scattering source. Contributions from the ice volume were negligible, but depending on ice thickness, scattering from ice-ocean interface may have contributed noticeably to the total σ°. At C- and S-band the measured co-polarization ratio was close to one even at larger incidence angles, whereas the predicted ratio was about +3 dB at 60º. This discrepancy could be due to volume inhomogeneities in the ice which are not accounted for in the volume scattering model and due to the surface and volume multiple scattering effects. At L-band, the measured σ° values could be explained by scattering from the ice-ocean interface.

In summary, these studies indicated that at C-band co-polarization (RADARSAT-1, ENVISAT ASAR) ice surface scattering typically dominates when the incidence angle is less than 45º and snow cover is dry. If the ice surface is very smooth and salinity S <0.5‰ then scattering from ice-water interface and ice volume are significant.

σ° and s_T modeling study by Dierking et al. (1997)

Dierking et al. (1997) conducted ship based scatterometer measurements over an area of refrozen brash ice. The scatterometer operated at 5.4 GHz with HH- and VV-polarization. The incidence angle was varied from 20º to 65º in steps of 5º. For each incidence angle, data at 14 different azimuth directions separated by 5º were measured. The scatterometer data were processed to the mean σ° values, 95% confidence limits of σ°, std of texture (s_T) (see (3.3)), and the standard deviation of the estimated s_T at each incidence angle. Two ERS-1 SAR-derived mean σ° and s_T values were also obtained. These measured data were then compared with theoretical σ° and s_T models. For modeling σ° and s_T a roughness model for the study area was developed based on the surface profile measurements. Surface roughness was assumed to be stationary over small surface patches divided into ‘smooth’ and ‘rough’ classes (see Chapter 4.2.1). The size of the patches equaled roughly the area illuminated by the scatterometer antenna.

Theoretical ice surface σ° modeling for the two roughness classes was conducted using the IEM model. As the thin snow cover was dry its scattering contribution was neglected, as was the ice volume scattering. There was good correspondence between measured and theoretical σ° values at VV- and HH-polarization for class “rough” except at incidence angles of 35º and 40º and at incidence angles ≥60º. The theoretical σ° values obtained for class “smooth” were much lower than the measured averages. Thus, the magnitudes of the roughness parameters were in the range of class “rough” for a large areal fraction of the study area, whereas only a few single smooth patches were imbedded in the rougher surface matrix which did not influence the measured mean σ°.

As the estimated roughness parameters depend on the segment length l, it was investigated how changes in the surface parameters due to a varying l affect the predicted values of σ°. With l values from 1.12 to 9 m, it was found out that the difference between σ°'s calculated with $l < \infty$ and $l = \infty$ increased with decreasing l and with increasing incidence angle. However, the difference was generally low; at maximum around 2.5 dB and less than 1 dB for $l \geq 4.5$ m. Considering the confidence intervals of the measured σ°, it was concluded that the changes in the predicted σ° values due to different segment lengths are acceptable if $l >> \lambda$.

The expected received power and s_T in the presence of two surface roughness classes I ('rough') and II ('smooth') were modeled as:

$$P = (1 - f)P_I + fP_{II}, \tag{4.13}$$

$$s_T = \frac{f(1-f)(P_{II} - P_I)^2}{(fP_{II} + (1-f)P_I)^2} \tag{4.14}$$

where f is the area fraction of the class II, P_I and P_{II} are backscattered power of classes I and II, respectively. Simulations of s_T were carried out using theoretical σ°'s for P_I and P_{II} (σ° is proportional to P) and varying f from 0.0 to 0.4. The simulated s_T was larger at HH- than at VV-polarization, and with increasing incidence angle s_T increased to a maximum at 35º (VV-polarization) and 60º (HH-polarization), respectively, and then decreased at larger incidence angles. Consequently, SAR images acquired at HH-polarization and at the mid-to-large incidence angle range are the most sensitive to surface roughness inhomogeneities. From the measured s_T values, f estimates were evaluated by searching the minimum of deviations between the measured and theoretical s_T. The largest f values were obtained at 35º (f =0.45) and 40º (f =0.30). With these f estimates, the modeled σ° values were within the confidence intervals of the measured data.

In the ERS-1 SAR images the study area did not exhibit any intensity variations due to surface roughness inhomogeneities. It is possible that the length scales of roughness variations were smaller than the ERS-1 SAR resolution, and that the variations were distributed homogeneously on larger scales. Additionally, according to the s_T simulations the ERS-1 SAR has relatively low sensitivity to the surface roughness variations.

In general, the above method for simulating σ° and s_T for an inhomogeneous sea ice area is a valuable tool for sea ice SAR image studies, but it requires the areas within the SAR pixels to have wide-sense stationary surface roughness.

IEM σ° model for surface with multiscale roughness (Manninen1997b)

Manninen (1997b) modified the IEM model in (3.9) to be applicable to surfaces with multiscale surface roughness (continuous roughness spectrum) by replacing the single scale autocorrelation functions with multiscale ones. For example, the isotropic multiscale Gaussian ρ and its $W^{(n)}$ are:

$$\rho(\xi, \zeta) = \frac{1}{2}(1+2b)\left(\frac{\xi^2 + \zeta^2}{k_0^2 x_0^2}\right)^{1/2+b} \Gamma\left(-\frac{1}{2} - b, \frac{\xi^2 + \zeta^2}{k_0^2 x_0^2}\right), \tag{4.15}$$

$$W^{(n)}(-2k_x, 0) = \frac{k_0 x_0}{-2k_x} \int_0^\infty \left[\frac{1}{2}(1+2b)x^{1+2b}\Gamma\left(-\frac{1}{2} - b, x^2\right)\right]^n J_1(-2k_x k_0 x_0 x)dx, \tag{4.16}$$

where b and k_0 are coefficients in (4.6) and (4.7), x_0 is the maximum distance (the length of the surface profile), Γ is the incomplete gamma function and J_1 is the Bessel function of the first kind. Equation (4.16) can only be solved using numerical integration. The best accuracy is obtained with the Euler's method.

The multiscale autocorrelation functions fitted always better experimental small, medium and large scale functions for various Baltic Sea ice types (for description of scales see Chapter 4.2.1) than the single scale functions. Additionally, coefficients b and k_0 obtained from the medium and large scale measurements produced reasonable autocorrelation functions for the small scale cases.

The inclusion of roughness scales smaller than that corresponding to the maximum L may also lead to smaller values of $W^{(n)}$, although the opposite case is more typical at larger distances. Though the interference of various scales is sometimes slightly destructive, increasing s (or x_0) usually increases multiscale σ°. The multiscale σ° increases more strongly with increasing x_0 than the single scale σ° (ordinary IEM), and surpasses it for many ice types already in an area having a diameter of about 50 m. The difference between the single and multiscale σ° values is naturally smallest for the smoothest ice surfaces.

It is difficult to decide what x_0 to use for an area illuminated by the radar. In principle, the whole illuminated area should be taken into account, but usually it is thought that the roughness scale close to the radar wavelength is the most important. However, currently there is no rule on how to choose the value of x_0. The maximum value of x_0 is limited by the IEM validity limits which for the exponential surface correlation are:

$$x_0 < \left(\frac{0.3k_0}{\sqrt{2}\exp(a)} \right)^{\frac{1}{b-1}}, \tag{4.17}$$

$$x_0 < \left(\frac{1.6\sqrt{\varepsilon_r'}}{k^2 \exp(a) k_0} \right)^{\frac{1}{b+1}}. \tag{4.18}$$

In most cases the latter condition is more restrictive for the Baltic Sea ice, which has small ε_r, than the former one. According to the measured ice surface profiles, it seemed that in many cases, especially for either heavily ridged ice or very smooth ice, IEM could be applied to areas comparable, for example, to the resolution of ERS-1 SAR, if the local incidence angle in the Fresnel reflection coefficients can be approximated with a better value than the radar incidence angle. It was concluded that the multiscale IEM model is not yet applicable to large pixels of very rough surfaces with small ε_r, like the Baltic Sea ice.

This multiscale IEM model has not yet been validated with empirical σ° data or with moment method calculations. Neither it has been used in the studies by other researchers. Other multiscale IEM models have been presented in the literature, e.g. a model by Mattia and Le Toan (1999) who derived the model starting from the scattered field equations. Also in this model the choice of the maximum distance is problematic.

4.3.2 Ice ridges

Model by Carlström and Ulander (1995) and Carlström (1997)

Carlström and Ulander (1995) developed an ice ridge σ° model using their surface structure model of the ice ridges (see Chapter 4.2.2). The model is based on the incoherent (power) summation of the scattering contributions from discrete circular ice disks. First, an expression

for the mean scattering cross section σ of a single disk is derived, then σ° is obtained from an ensemble average of the scattering from a large number of disks with random sizes and tilt angles. Carlström and Ulander (1995) modeled only the coherent and incoherent scattering of the major (front) facet the disk. Carlström (1997) further developed the model by adding the coherent and incoherent scattering of the circular side facet, incoherent scattering from the back facet and shadowing functions of the major and side facets. Only co-polarized backscattering is considered in the model and the difference between HH- and VV-polarization is neglected. Also volume scattering, multiple scattering within the ice disks and between the disks and effect of snow cover are neglected.

The total σ° of a large number of disks is (Carlström 1997):

$$\sigma^\circ = S_m\left(\sigma^\circ_{mc} + \sigma^\circ_{mi}\right) + S_s\left(\sigma^\circ_{sc} + \sigma^\circ_{si}\right), \tag{4.19}$$

where S_m and S_s are the shadowing functions for the major and side facets, respectively, σ°_{mc} and σ°_{mi} are the coherent (specular) and incoherent (diffuse) σ° of the major facet and σ°_{sc} and σ°_{si} are the corresponding components for the circular side facet.

The coherent and incoherent σ°'s are obtained as ensemble averages of the radar cross sections, e.g.:

$$\sigma^\circ_{mc} = \frac{\langle \sigma_{mc} \rangle}{\langle A_h \rangle}, \tag{4.20}$$

where A_h is the projection of the ice disk on the horizontal plane.

For a dielectric circular plate (major facet of the ice disk) with a radius much larger than the radar wavelength, the coherent backscattering cross section σ for near-normal incidence is obtained from the physical-optics approximation (Ruck 1970) (see eq. (2) in (Carlström 1997)). If the penetration depth in the ice disk is larger than the disk thickness then there is also a coherent reflection on the far side of the disk (or back facet). Since the disk thickness may be considered a random variable, phase interactions between the front and back facets will average out and the mean reflectivity is given by the incoherent model for a dielectric slab (Ulaby et al. 1986). The incoherent σ is the sum of the surface scattering contributions from the front and back facets of the ice disk according to a layer scattering model (Fung 1994). For the coherent σ of the circular side facet, high frequency approximation for a circular cylinder of finite length is used (Ruck 1970). The incoherent σ of the side facet is estimated by numerical integration of σ° with the IEM model over the circular side facet with a varying local incidence angle.

When calculating σ°_{mc}, σ°_{mi}, σ°_{sc} and σ°_{si} it is assumed that the disk major facet area A and the facet slope angle are independent and the corresponding ensemble averages are computed independently. The slope angle is described by an isotropic 2-D joint pdf, see (4.12). For this pdf, the mean projected area becomes (Carlström and Ulander 1995):

$$\langle A_h \rangle = \frac{A}{1+m}. \tag{4.21}$$

Now the mean scattering contribution from major facets ($\sigma^\circ_{mc} + \sigma^\circ_{mi}$) is independent of the disk area. Hence, the model is valid also for a distribution of disk sizes provided that the disks are large enough for the physical optics σ to be valid. Additionally, the slope pdf must be slowly varying compared to the scattering pattern of the disk. The side facet scattering, however, is dependent of the relation between thickness and area of the disks.

Modeled C-band σ° values at low incidence angles are dominated by scattering from the major disk facets. At large incidence angles, scattering is reduced by shadowing, while an increased contribution is obtained from the side facets. However, for incidence angles below 45º, both shadowing and side facet scattering can be ignored with little error.

Carlström (1997) compared the model with the numerical moment method computations at C-band. The results showed good agreement when the imaginary part of the dielectric constant of ice was higher than 0.03-0.1. For lower attenuation in the disks, the backscatter model was found to underestimate the scattering, especially for large incidence angles. This is likely due to multiple scattering within the disks.

The model was also compared with ice ridge σ° values extracted from the ERS-1 SAR images. The input data to the model consisted of ground truth measurements of seven ice ridges in 1993 and 1994. The observed σ° values could be explained by the model when taking into account an uncertainty in the model computations of ±1.5 dB due to the dielectric loss factor. In the range of the observed ERS-1 σ° values, the model sensitivity to the surface slope parameter m was small, whereas the sensitivity to the dielectric loss was larger. The model result was dominated by coherent scattering from the major facets, whereas incoherent scattering from small scale roughness (rms-roughness from 1 mm to few centimeters) was important only when m was small (m <0.2).

Model by Manninen (1992)

When the scatterers are smaller than the radar spatial resolution, each measured σ° is correlated to an ensemble average of σ°'s corresponding to the individual incidence angles along the ridge sail. Based on this, Manninen (1992) derived an ice ridge σ° model using her 3-D geometrical structural ice ridge model which provides local incidence angle (θ_i) pdfs of ice ridges. Incoherent HH-, VV- and cross-polarized σ°'s for the three facets of a rectangular polyhedron were calculated either with the small perturbation model (Manninen 1992) or with the IEM model (Manninen 1996b). Total coherent (specular) σ° of ice ridge can also be derived in order to compare it to total incoherent σ°. Volume and multiple scattering and the effect of snow cover are neglected.

The θ_i pdf is obtained by assuming that at every ridge slope point there is a distribution of ice block facet orientations defined by the pdfs of the ice block Euler angles. At first, incidence angle θ_i pdfs for the three ice block facet types (bh, ah, ab; a and b are the length and width of the main facet and h is the block thickness) on the proximal and distal sides of the ridge are obtained as histograms with a chosen bin width. The three facet types together produce the θ_i pdfs for either side of the ridge. The proximal and distal distributions are then combined to get the total θ_i pdf of the ridge (see equations (1)-(11) in (Manninen 1992)). As there is no correlation between the Euler angles and dimensions of the ice blocks, their pdfs can be assumed to be independent in the θ_i pdf calculations. Now only the mean values of the ice block dimensions are needed and the Euler angle ψ affects only the θ_i pdfs of the minor facets. The shadowing effect of individual ice blocks in not included in the model, but it affects the results only if certain block orientations are mode probable to be shaded than other orientations. When the radar incidence angle is greater than 0º, as is the case always for SAR, only those major block facets that have the same azimuth angle as the radar wave can produce direct specular reflections. With this 3-D ice ridge structural model, the probability of specular reflection is much lower than with a 2-D model.

Manninen (1996b) calculated the θ_i pdfs for a ridge measured in the Bay of Bothnia in 1992. Calculations were conducted using the ERS-1 SAR incidence angle θ_0 of 23º. The obtained incidence angles tended to be naturally larger in the distal than in the proximal side. Part of

the distal side was shaded when the azimuth angle φ_0 between the radar look direction and the normal of the ridge direction was close to 0º. The pdf's were smoothest on either side of the sail, when φ_0 was equal to the average value of the Euler angle φ. There was a clear peak in the pdf's of the main facets at about the value of θ_0, because the Euler angle pdfs were so broad. Similarly, there was a corresponding small peak in the side facet bh pdf at about 90º-θ_0. Because the pdfs of the Euler angles were so broad, there were no major differences between the two sides of the ridge or the different φ_0 values. Ground truth data for other ridges produced similar total θ_i pdfs as in this example, which was due to the broad pdfs of the Euler angles. Although θ_0 dominates the local θ_i pdf's and φ_0 also has a clear effect, these features are quite similar for all ridges and do not depend very much on the exact geometrical shape of the ridges.

With the 3-D geometrical model for an ice ridge, the average value for the backscattering coefficient $\langle \sigma^\circ_s \rangle$, $s = p$, d, at an individual point on the proximal (p) and distal (d) slope of an ice ridge is:

$$\langle \sigma^\circ_s \rangle = \frac{\iiint [\sigma^\circ(\theta_1)bh + \sigma^\circ(\theta_2)ah + \sigma^\circ(\theta_3)ab] f_{1s}(\theta) f_{2s}(\varphi) f_{3s}(\psi) d\theta d\varphi d\psi}{\iiint (bh + ah + ab) f_{1s}(\theta) f_{2s}(\varphi) f_{3s}(\psi) d\theta d\varphi d\psi}, \tag{4.22}$$

where $f_{1s}(\theta)$, $f_{2s}(\varphi)$ and $f_{3s}(\psi)$ denote the separate pdf's for the Euler angles and $\sigma^\circ(\theta_i)$ is the backscattering coefficient of a facet with incidence angle θ_i.

If ice ridge σ° is compared to level ice σ°, it has to be calculated at a certain slope point and related to its projection area at the horizontal plane. As the ice blocks of a ridge sail partly overlap, the total projection area is not simply the sum of individual projection areas. This is taken into account by modifying the denominator of (4.22), see (Manninen 1992, eq. (14) and (15)). Finally, the σ° values at various slope points are integrated. The results for the proximal and distal sides are then combined to give the total average incoherent σ° per unit horizontal area of a ridge:

$$\langle \sigma^\circ_t \rangle = \frac{\tan\theta_d \langle \sigma^\circ_p \rangle + \tan\theta_p \langle \sigma^\circ_d \rangle}{\tan\theta_p + \tan\theta_d}. \tag{4.23}$$

The coherent (specular) σ° of an ice block facet is obtained with the σ° for a dielectric rectangular plate (Ulaby et al. 1982). The total coherent σ° is approximated as:

$$\langle \sigma^{\mathrm{o}}_{ct} \rangle = \sum_{i=1}^{3} \int_0^{\pi/2} \sigma^{\mathrm{o}}_{ci}(\theta_i) f_{si}(\theta_i) d\theta_i. \tag{4.24}$$

Calculation of the total coherent σ° is numerically very demanding since the σ° function for the rectangural plate is steeply peaked.

With all calculated θ_i pdf's of different ice ridges, the incoherent total σ° was a few dB larger than the total coherent σ° (Manninen 1992, 1996b). Additionally, the general behavior of the total σ° was dominated by surface scattering at both co- and cross-polarization. These results were obtained with a rather coarse resolution of 2º for the incidence angle distributions, but likely a finer resolution would not increase the importance of the coherent σ°. The qualitative similarity of co- and cross-polarized σ°'s supports the idea that the coherent σ° is not the dominant one, as the cross-polarized σ° has no coherent component.

The incoherent σ° depends mostly on the ice block surface roughness, secondly on the block ε_r and the least on the ridge geometrical parameters (e.g. Euler angle pdf's). The σ° contrast between level ice and ice ridge is the largest at cross-polarization. For all measured ridges the average φ was closer to 0º than 90º which yields slightly larger σ° when radar is viewing across the ridges than it is viewing along them.

Using their 2-D ice ridge σ° model, Carlström and Ulander (1995) concluded that the coherent component of the total σ° is typically the dominant one. According to Manninen (1996a), this was based on the wrong assumption that 2-D joint pdf of the ice block facet slopes is azimuthally isotropic, i.e. that it is possible to obtain the slope pdf from just 1-D profile measurements of ice ridges (surface profiles yield the slope values of lines projected on the ice blocks, but these do not present the inclination of the actual ice block surfaces). Generally, both models are too complicated for inversion of ice ridge parameters from SAR data and they can be mainly used to study the effect of various parameters on coherent and incoherent σ° components.

4.4 Backscattering Signatures

Empirical backscattering signature studies of the Baltic Sea ice have been previously conducted using (1) helicopter-borne scatterometer data (Hyyppä and Hallikainen 1992, Hallikainen and Toikka 1992, Similä et al. 2001), (2) airborne SAR images (Kemppainen 1989, Carlström 1990, Sun et al. 1992, Dierking and Askne 1998), and (3) ERS-1 SAR images (Dammert et al. 1994, Lundin 2001). The scatterometer data were acquired in 1988, 1990 and 1991 with the HUTSCAT (Helsinki University of Technology Scatterometer) C- and X-band quad-polarization scatterometer. The airborne SAR images were acquired with SAR systems operating at L-, C- and X-bands during BEPERS-87/88 (Bothnian Experiment in Preparation of ERS-1) and EMAC-95 (European Multisensor Airborne Campaign) campaigns. Some of the airborne SAR systems did not have cross-polarization measurement capability. The amount of L-band data is very small and most of it were acquired with the polarimetric EMISAR radar. Backscattering signature studies using RADARSAT-1 and ENVISAT SAR images have not yet been published.

Below, the main results of the C- and X-band σ° signature studies with non-polarimetric radars are first discussed. This is followed by a review of studies on the L- and C-band polarimetric discriminants and the comparison of σ° data with weather data.

4.4.1 C- and X- band signatures

The mean σ° at all C- and X-band polarizations increases with increasing ice deformation and decreases with increasing incidence angle θ_0 (Kemppainen 1989, Hyyppä and Hallikainen 1992, Hallikainen and Toikka 1992, Dammert et al. 1994). The contrast between open water and level ice is around 3 dB higher at C-band VV- than at VH-polarization (Carlström 1990), whereas that between deformed ice and level ice is at VH-polarization even 10 dB higher (Carlström 1990, Hyyppä and Hallikainen 1992). Mean σ° for ice ridges showed considerable azimuthal angle dependence at X-band co-polarization; it was 3 dB higher across ice ridges that along them (Hyyppä and Hallikainen 1992).

The standard deviation of texture s_T (see (3.3)) was on the average the largest for ridged ice and the smallest for jammed brash barrier (Dammert et al. 1994). For level ice types the variation of s_T was large. s_T decreased when snow wetness increased. For deformed ice types the mean s_T was generally higher at VH- than at VV-polarization (Carlström 1990).

In all previous studies ice type discrimination results with a single channel σ° were usually poor. In Hyyppä and Hallikainen (1992) and Hallikainen and Toikka (1992) cross-polarized

σ° provided better results than co-polarized σ° and their combination gave the best results. Sometimes even all ice types (total number from three to six) were discriminated. The results of the ice type discrimination usually improved with increasing θ_0 (Carlström 1990, Hallikainen and Toikka 1992). According to (Hyyppä and Hallikainen 1992) and (Hallikainen and Toikka 1992) X-band provides slightly better discrimination results than C-band. In (Carlström 1990) and (Sun et al. 1992) combined use of mean and standard deviation of σ° did not increase the number of discriminated ice types, although the separation between some ice types increased a little. However, in (Dammert et al. 1994) a total of seven ice type classes in the ERS-1 data had more or less clearly separated signatures in the mean σ° vs. s_T coordinates under dry snow condition. Under wet snow conditions only smooth level ice and ridged ice were discriminated. General classification rules for several ice seasons based on the mean σ° vs. s_T would only be able to discriminate three (level ice, deformed ice, very deformed ice) and two (level ice, deformed ice) ice classes under dry and wet snow condition, respectively. Open water leads were not discriminated from sea ice.

The BEPERS-88 C-band SAR and the ERS-1 SAR results for the mean σ° are generally in agreement with the previous HUTSCAT results. The differences are most likely due to the different ice type definitions and the small data amounts.

More complex statistical analysis of the C-band HH-polarization σ° signatures acquired with HUTSCAT was conducted in (Similä et al. 2001). There a hierarchical Bayesian model for the estimation of ice surface roughness was constructed. Using the Markov Chain Monte Carlo (MCMC) methodology the posterior distribution of the central model parameter related to surface roughness was numerically approximated. The results provided by the statistical model showed good agreement with a video-based ice type classification, and their geophysical interpretation is possible. It was also demonstrated how using the determined posterior distribution it is possible to examine such questions as given the scatterometer measurements, how many highly deformed ice fields exceeding the specified diameter is encountered when moving along a line, and what is the uncertainty of the obtained estimate. Also some suggestions to extend the method for SAR images were given.

4.4.2 L- and C-band polarimetric discriminants

The first and so far the only polarimetric SAR images over the Baltic Sea ice were acquired in 1995 by Danish airborne EMISAR radar (Dall et al. 1997). EMISAR and the image data set are described in Chapter 5.1.4 (the same data set was also used in [P2]).

Dierking and Askne (1998) studied polarimetric discriminants using one L- and one C-band image acquired in March 1995 in the Bay of Bothnia. The polarimetric data were in the multi-looked covariance matrix format. The following five ice classes were visually identified in the images: dark, average and bright level ice, moderately deformed ice (fragments of level ice are present), and heavily deformed ice (no embedded level ice). Altogether 150 windows of size 441 pixels were randomly distributed over these ice types. Backscattering coefficients, co- and depolarization ratio ($R_{co} = \sigma^\circ_{VV} / \sigma^\circ_{HH}$ in here, R_{depol}) and phase difference ϕ_{HH-VV} were then calculated using the average covariance matrix elements of the windows.

At L-band VV-polarization (HH- and VH-polarizations not discussed) dark and bright level ice patches were well separated from the average level ice with the level of σ°. At C-band the data points of the three level ice classes partly overlapped. According to a single backscattering model (contributions from ice surface, ice volume and ice-water interface backscattering was dominated by the ice-water interface at L-band, and by the ice surface at C-band. At L-band R_{co} for level ice types was around 1.0, whereas at C-band R_{co} was larger than 1.0 and increased with increasing θ_0 (roughly from 1.2 to 1.6). At both bands R_{depol} was

rather constant at around 0.1. Both R_{co} and R_{depol} did not separate the three level ice types. Level ice ϕ_{HH-VV} at C-band varied from -10º to +10º and at L-band from 0º to 30º. At both bands ϕ_{HH-VV} increased slightly with increasing θ_0. The observed ϕ_{HH-VV} at C-band was explained with dominating ice surface scattering and the L-band one by an anisotropic character of the ice layer close to the ice-water interface.

The σ° contrast between level ice and deformed ice types was much larger at L-band than at C-band. Additionally, at L-band the contrast at cross-polarization was clearly larger than at co-polarization. R_{co} and R_{depol} revealed no differences between the deformed ice types. At L-band R_{co} was from 0.8 and 1.0 and at C-band from 0.7 to 1.1. R_{co} values smaller than one may indicate the dominance of double bounce or coherent scattering from ice blocks. At C-band R_{depol} was around the same (0.1±0.05) for level and deformed ice types, but at L-band it was larger (0.2) for deformed ice. This indicated that multiple scattering processes within deformed ice were stronger at L-band. At L-band ϕ_{HH-VV} was scattered around zero and at C-band it was from -10º to +5º.

4.4.3 Comparison between backscattering signatures and weather data

Lundin (2001) compared σ° values derived from ERS-1 SAR time series with air temperature from a coastal weather station. The SAR data set consisted of 17 images acquired over the northern part of the Bay of Bothnia during January 13 - April 7, 1994. Based on the image and air temperature (T_a) data, the time series was divided into two phases; the cold phase (T_a <-1ºC), covering the first 16 images (up to March 26), and the warm phase (T_a >0ºC) consisting of the last image. Nineteen test sites of various ice types were selected on fast ice area. Time series of the mean σ° values of these test sites were then compared with T_a. The results indicated a decreasing σ° trend with increasing T_a under cold conditions. Very rough ice (average slope -0.03 dB/1ºC) was slightly more sensitive than smooth ice (-0.02 dB/1ºC) to a T_a change. In case of the smooth ice, it was speculated that the ocean heat flux through the relatively thin Baltic Sea ice increases snow moisture near the ice surface when air temperature increases, leading to an increased absorption of the SAR signal. The surface temperature of deformed ice possibly adjusts more easily to the ambient air temperature than smooth ice due to the larger ice thickness and deformed ice structure which reduces ocean heat flux to the ice surface. From cold to warm phase σ° for all ice types clearly decreased due to the decrease in ice surface scattering. The decrease was larger for rough ice than for smooth ice as wet snow cover makes rough ice areas look much smoother.

In connection with operational use of SAR images it has been observed that under warm conditions (temperature > 0ºC; snow cover is wet) the overall SAR intensity and texture are much reduced compared to those under cold conditions.

4.5 Sea Ice Classification by Spaceborne SAR Images

Studies conducted on the classification of the spaceborne SAR images of the Baltic Sea started in the early 1990's as the ERS-1 satellite was launched and have been continued since then. The performed studies can be divided into following subjects: (1) classification of ice types, (2) open water – sea ice discrimination, (3) sea ice thickness estimation, and (4) sea ice dynamics. Most of this research work has been conducted by Finnish Institute of Marine Research (FIMR). FIMR's major goal has been to develop operational Baltic Sea ice products which are easy to use and informative for end-users. Currently, operational sea ice products based on RADARSAT-1 ScanSAR and ENVISAT ASAR Wide Swath Mode images are provided by FIMR.

4.5.1 Classification of various ice types

Already the pilot studies with airborne SAR data indicated that the SAR intensity value alone is not sufficient to discriminate between different ice types, e.g. (Kemppainen 1989). Hence, additional ways to describe the sea ice SAR signature properties have been tried in the studied classification schemes. In (Similä and Helminen 1995) the wavelet transform was utilized to characterize the local statistics typical for different ice deformation categories. The distribution of wavelet coefficients was modeled using the mixture of three normal distributions. The class parameters were estimated applying a stochastic version of the expectation-maximization (EM) algorithm. The ice chart was formed with the maximum likelihood classification. This leaded to an operative sea ice classification algorithm for the ERS-1 SAR data when the open water identification based on the blockwise autocorrelation was added (Similä 1996). The accuracy of the results was assessed by visual interpretation and with comparison to the FIS ice charts. The small coverage of the ERS-1/2 SAR images (100 km by 100 km) was a problem which was overcome by the RADARSAT-1 ScanSAR images. These images became the most important sea ice information source in the Baltic Sea and generated an extensive sea ice mapping research work.

Karvonen (2004) developed a method for segmentation and classification of the Baltic Sea ice SAR images, based on Pulse Coupled Neural Networks (PCNN's). The segmentation method includes an automated training, based on decomposing the total pixel value distribution into a mixture of normal class distributions. The algorithm has especially been developed, trained and tested using logarithmic scale Radarsat-1 ScanSAR Wide images (delivered by KSAT in Tromso, Norway) with 100 m pixel size.

Prior the segmentation an incidence angle correction, specifically designed by Karvonen et al. (2002) for the Baltic Sea ice SAR images, is applied. This correction is based on the results of [P3]. The estimation of the class parameters and boundaries, i.e. the training phase, is based on the assumption of the mixture of normal distributions and the EM algorithm. The contextual information used in the classification/segmentation step is provided by the PCNN scheme. Currently, the algorithm has been trained for dry snow conditions only. The number of classes is fixed to six based on the number of modes in the total data distribution. This figure approximately corresponds to the number of sea ice classes in [P1] and also approximately to the number of classes that can be distinguished from SAR images based on backscattering. The classes are manually assigned to various ice types by comparing the classified SAR image to the FIS ice chart and original SAR image. The geophysical interpretation of the classes is basically just that the degree of deformation (surface roughness) increases as the class mean intensity increases. Fast ice areas, with lower surface roughness and thus lower backscatter than thinner deformed ice areas, can cause misclassification of the thicker fast ice to the thinner smooth ice classes. However, this can be corrected (1) by using a fast-ice recognition algorithm (Karvonen and Similä 1999) and (2) the location of the fast ice typically does not change rapidly. Fast ice is a seventh class in the final classification.

The segmented SAR image is also an input image for open water – sea ice discrimination algorithm, see below. Typically the SAR-based sea ice features computed by FIMR algorithms are segment-wise rather than pixel-wise, because fading corrupts pixel-wise intensity values.

Carlström and Ulander (1995) presented a semi-empirical inversion model for estimating sea ice surface rms roughness s from σ° values in the ERS-1 SAR images. The model is based on the assumption that σ° is only dependent on s and the radar incidence angle θ_0, when snow cover is dry. For σ° values below around -12 dB which are typical for level ice, s is estimated with a theoretical σ° model consisting of ice surface and volume scattering components (see Chapter 4.3.1). For ice volume parameters and ice surface correlation length

averages of measured values are adapted. The maximum value of s with the level ice model is 5 mm. For deformed ice with σ° values over -10 dB, s is estimated with an empirical relation between σ° and s and θ_0. This model yields s values over 15 mm. The gap between the level and deformed ice models (s from 5 to 15 mm) is bridged by linear interpolation in log-log space. The standard deviation between the measured s and the model estimate was approximately ±50%. The main limitations of the inversion model are that snow cover must be dry, s must be larger than 1 mm, and ice salinity above 0.2‰ for ice surface scattering to be dominant. Thus, for low salinity fast ice the inversion model overestimates s.

4.5.2 Open water – sea ice discrimination

Usually there is more structural information in the pixel patterns originating from sea ice fields than in the pixel patterns over open water. The latter ones are often relatively structureless, depending, however, on wave conditions and currents. This observation can be quantified using the spatial autocorrelation measure (Similä 1994). There the classification accuracy in the open water – sea ice discrimination was determined for a limited ERS-1 SAR image set (100 m resolution) when the pixel block size is increased and the autocorrelation threshold is kept fixed (0.2). In that data set almost no ice area was classified into open water when the block size increased enough (15 by 15 pixels or larger) and few open water areas, well below 10 %, were classified as ice. The proposed classification scheme consisted of intensity values with the autocorrelation measure being a part of the contextual information. The classification maps were obtained using the ICM algorithm.

Using the autocorrelation as a discriminant an operative and thoroughly validated algorithm to separate ice and open water in the RADARSAT-1 ScanSAR images was developed by Karvonen et al. (2005). The SAR image to be classified is first segmented with the PCNN algorithm (Karvonen 2004), and the autocorrelation is computed for the segments rather than for pixel blocks. The autocorrelation of a segment is the mean of the local autocorrelation over the segment. The segmentation is further refined by a segmentation based on local autocorrelation. The size distribution of the resulting segments varies highly depending on the ice conditions, the range being from 1 km^2 to several thousand km^2. The largest segments occur in the open water areas. The algorithm first uses a lower threshold to define whether a segment certainly contains open water (autocorrelation smaller than threshold) or not, and then tests the adjacent segments to the open water segment for the upper threshold and, if the values are less than the upper threshold, the open water area is expanded by these segments. Only one such expansion pass is performed. Finally, a filtering step is performed, and open water segments with a size less than a given size threshold are set to ice, unless they are long and narrow, corresponding to typical shape of leads.

The algorithm performance under both dry and wet snow conditions was evaluated by comparing the results with the RADARSAT-1 ScanSAR Wide images to the FIS digitized ice charts, in which the sea ice information is based on human interpretation of multiple data sources, including remote sensing data. The algorithm agreed with the location of open water and ice in the ice charts with about 90% and 80% accuracy, respectively. Especially large open water areas were very well distinguished. The validation confirmed that autocorrelation is not very sensitive to ocean wave conditions and radar incidence angle.

Lundin (2001) studied the derivation of the Baltic Sea ice concentration from Radarsat-1 ScanSAR Narrow images, based on the local mean backscatter threshold between open water and sea ice (Dokken et al. 2000). The threshold is a linear function between θ_0 and pixel intensity and it is determined from manually extracted water and ice pixel values typical for different areas. The exact location of the threshold is fine tuned by minimizing the number of the misclassified manually chosen pixels. Based on the threshold each 50 by 50 m pixel is given the value of ice or water. Sea ice concentration is then estimated by averaging classified

pixels over a chosen pixel block. Typically, new ice is non-separable from calm open water due to its low backscatter intensity. Another ice type which does not differ in mean backscatter from a calm water surface, is smooth level ice mostly situated within the fast ice zone. In order to prevent misclassification, the land fast ice is masked by the 10 m bathometry data that is assumed to cover the main part of the land fast ice areas. Furthermore, large open water areas with high backscatter due to wind induced roughness are manually masked. Under wet snow condition it is more difficult to discriminate between open water and ice pixels.

4.5.3 Sea ice thickness estimation

Karvonen et al. (2003) developed an algorithm for sea ice thickness estimation by refining the sea ice thickness information present in a daily digitized FIS ice chart using RADARSAT-1 ScanSAR Wide and ENVISAT ASAR Wide Swath images. The SAR based ice thickness maps in 500 m resolution are provided operationally and are available for users shortly after the SAR data are received.

First, an incidence angle corrected SAR image (Karvonen et al. 2002) is segmented with a slightly modified isodata clustering algorithm. After segmentation each SAR segment is compared to the segments in the ice thickness map. If over 50% (current limit) of a SAR segment is covered by one thickness segment, this thickness segment is extended to cover the whole SAR segment, otherwise the thickness segment remains unchanged. This step defines anew the boundaries of a thickness segment. Then the thickness values are linearly mapped such that the minimum thickness is mapped to correspond to the minimum SAR segment intensity mean and the maximum thickness to correspond to the maximum SAR segment intensity mean inside the same thickness map segment. This procedure is typically applied to a thickness map and a SAR image originating from the same day, producing a map called a refined ice thickness map. If only an ice chart from previous day is available then this procedure can be utilized to give an estimate for the current ice thickness distribution. The estimation works well if only minor changes in the ice conditions between the SAR acquisition and the ice thickness chart have occurred. However, changes in ice conditions can be radical due to the dynamic nature of drift ice fields. Errors produced by ice movement are reduced by masking off open water areas in the refined ice thickness map using the open water – sea ice discrimination map.

Karvonen et al. (2004) compared Radarsat-1 ScanSAR Wide image data pixel values, FIS ice thickness charts and the refined thickness charts to sea ice thickness measurements with a helicopter-borne electromagnetic induction (EM) based sensor. The EM sensor operated by Alfred Wegener Institute and the ice thickness measurement principle are described e.g. in (Haas 2006). The EM data resolution is around 30-40 m and the spatial sampling rate is 3 to 4 m. For level ice the accuracy of the EM thickness measurements is about 10 cm (Haas 2006). For ridged ice the accuracy is weaker due to water appearing between ice blocks, resulting in a systematic underestimation bias. However, almost always the occurrence of an ice ridge can be detected.

The data sets were acquired in February 2003 in the Bay of Bothnia and in the Gulf of Finland. Based on the EM data, sea ice was coarsely divided into three categories: level ice by thermal growth (thickness less than 50 cm), rafted ice (50-100 cm), and ridged ice (>100 cm). Additionally, there was also open water category. The dynamic range of the SAR pixel values was first divided into 15 equal-sized bins. Then, given a fixed bin, a conditional distribution of the three ice thickness categories was computed. It was observed that the fraction of small ridges (rafted ice) remained relatively constant (about 30%) independent of the SAR pixel value. On the other hand, the area covered by large ridges grew almost linearly from 0-10 % at very low pixel values to 90-100 % at the highest values. The fraction of level ice decreased from 70% at low pixel values to less than 10 % at high values. Only weak correspondence was observed when comparing the data sets pixel by pixel, i.e. the correlations between the

SAR data or the operational ice charts and the EM data were relatively low. This ambiguity is partly due to ice movement between the SAR data acquisition and EM measurements, and possible registration inaccuracies between the data sets. Furthermore, quite different ice conditions can give similar σ° signatures [P1]. Comparisons of the data sets indicated that the refined thickness chart shows better the local mean ice thickness than the original thickness chart. In summary, based on a sample of SAR intensity values, it is possible to assign a crude estimate of the ice type distribution for the ice field from which this scattering originates. This assignment requires a priori knowledge about the order of ice thickness.

Similä et al. (2006) developed an algorithm for direct derivation of the ice thickness from the SAR images in order to include information about the degree of ice deformation into the SAR refined thickness charts. A SAR image is first segmented, and then an ice thickness distribution is assigned to each segment. The algorithm was developed using EM data and four ENVISAT ASAR alternating polarization precision (APP) images at HH- and VV-polarization acquired in March 2005 in the Bay of Bothnia under dry snow conditions.

The segmentation of the APP images is performed using both HH and VV channels. First, both channels are filtered using anisotropic diffusion filtering, and then a 2-D k-means clustering for all the pixel pairs is performed. A post-filtering operation joins all the segments whose size is less than a threshold to neighboring segments. Finally, segment mean images for the filtered segmentation are computed for both channels.

The total ice thickness distribution is estimated by assigning an ice thickness distribution f_k to each σ° (in dB), rounded to the nearest integer. The segment-wise ice thickness distribution is formed as a mixture of different conditional densities f_k, where the densities are weighted by the relative occurrences of each σ° value in the segment. These procedures require construction of a conditional ice thickness distribution given a certain σ° value, i.e., it is assumed that if a given σ° value occurs the thickness of the underlying ice field is assumed to vary according to the corresponding f_k. Validity of this approach essentially depends on how representative the EM data set is. The ice thickness distribution is modeled as a mixture distribution of two components. One component describes the thickness distribution in the level and rafted ice areas which thickness less than 100 cm, the other component describes thickness distributions for the rest of the thickness values (mainly ridged ice). The proportion between level/rafted ice and ridged ice is controlled by a mixture parameter, which describes the relative fraction of ridged ice and is a linear function of σ°. In the March 2005 data set, the shape of the total thickness distribution varied strongly with the σ° value (see Fig. 2 in (Similä et al. 2006)).

In the whole March 2005 data set, the measured and estimated marginal ice thickness distributions were quite close to each other. This indicated that the training data set for f_k was large enough to cover most of the ice conditions present in the test area. The largest differences between measured and estimated values occurred in areas where the σ° values were high (low) but the EM data indicated thin (thick) ice. The proposed approach predicts too large (small) ice thickness in these cases. The segment-wise thickness distribution estimates usually had the same form as the measured ones. The largest errors occurred in the areas where the backscattering strength constantly remained relatively high (above -14 dB) but the EM measurements indicated thin ice.

4.5.4 Sea ice dynamics

Sea ice dynamics can be observed from time series of SAR images by tracking spatial displacements of geometric features like large ice floes, ice floe edges and large ice ridges. So far few studies have been conducted for the Baltic Sea ice. The most recent results were presented by Leppäranta et al. (1998). They estimated sea ice dynamics from three ERS-1

SAR image pairs acquired in February and March 1994 with either 3 or 6 day time interval using an optical-flow algorithm presented in (Sun 1996). The algorithm has two steps: (1) derivation of the first-order motion vectors which are related to rigid motion (translation and deformation) and which describe the large-scale displacement of the ice pack, and (2) derivation of the higher-order motion or the deformation which is due to non-rigid motion (for details see (Sun 1996)). Before analysis, the SAR images were averaged to pixel size of 400 by 400 m. In all three SAR image pairs the estimation of the mean ice velocity fields was successful. Air temperature was well below 0ºC in all cases suggesting that the snow cover on ice was dry, i.e. the main backscattering source was the ice surface. The total error in the displacements was around 0.9 km. The actual displacements were an order of magnitude larger.

The observed ice velocities showed a considerable stiffening of the ice pack as the minimum ice thickness increased from 10 to 30 cm. This is due to the change in the character of ice deformation under compression from rafting to ridging. An analysis of the SAR based ice velocity fields with a numerical ice dynamics model based on the viscous-plastic ice rheology allowed estimations of the compressive strength of the ice and the ratio of compressive strength to shear strength. It was concluded that a SAR repeat cycle of 3 days is good for updating an ice dynamics model but for detailed ice-dynamics investigations a data frequency of once per day is preferable.

4.6 Sea Ice Classification by SAR Interferometry

Dammert et al. (1998) studied the use of SAR interferometry (InSAR) for remote sensing of the Baltic Sea ice. Before describing their results, the basics of the InSAR are briefly presented.

InSAR is a technique where at least two SAR images acquired over the same target with slightly different radar positions are combined into an interferogram which contains information on target geophysical properties. For a stable surface, the phase of the interferogram is related to the large scale topography, e.g. (Graham 1974, Zebker and Goldstein 1986). For a large unstable surface, consistent displacements of that surface also affect the phase, and thus multiple SAR images can be used to detect surface changes over larger areas. The interferogram is produced by multiplication of the two complex SAR images (either one is conjugated), pixel by pixel, and then the phase is extracted. The equation for the interferometric phase in repeat-pass InSAR after correction for the phase difference for the flat Earth (surface reference) is (Dammert et al. 1998):

$$\Delta\varphi = \frac{4\pi B_n}{\lambda R \sin\theta_0}\Delta h + \frac{4\pi}{\lambda}\Delta\eta + \phi_{noise} + 2\pi n\,, \tag{4.25}$$

where B_n is the baseline normal to the line of sight, R is the average satellite-to-surface distance, Δh represents the topographic height relative the reference surface, $\Delta\eta$ represents a small temporal movement of large objects between the image acquisitions in the radar look direction, and ϕ_{noise} is the phase noise due to temporal changes of scatterers and radar system noise. There is a general 2π ambiguity associated with all phase measurements. In general, measurements of both surface elevations and small displacements are possible with repeat-pass InSAR. $\Delta\eta$ can be either horizontal, vertical or a combination of both. The sensitivity to the surface topography increases with the baseline while the sensitivity to surface movements is independent of it. Thus, repeat-pass InSAR with a small baseline is good for surface displacement maps.

InSAR technique provides also a measure of the interferometric coherence, i.e. the degree of correlation between two images (Born and Wolf 1980):

$$\gamma = \frac{E\left\{S_1 S_2^*\right\}}{\sqrt{E\left\{\left|S_1^2\right|\right\} E\left\{\left|S_2^2\right|\right\}}}. \tag{4.26}$$

The coherence image is formed by replacing the ensemble averages with spatial averages in (4.26). The coherence γ is related to volumetric scattering effects and changes of scatterers between acquisitions, i.e. volume and temporal decorrelation, e.g. (Gatelli et al. 1994). The temporal decorrelation can be caused by two things, movements of scatterers and changes of scatterers. With only small random movements of the scatterers, it is possible to interpret γ as a measure of such movements. If the volume decorrelation is insignificant, as is the case for the thin Baltic Sea ice, then γ is determined by the temporal variation of the dominating scatterer (e.g. ice surface scattering), and thus it can be used to characterize the backscattering properties of different ice types. (Dammert et al. 1998).

Dammert et al. (1998) acquired three ERS-1 SAR images on 24, 27 and 30 March, 1992, over the Bay of Bothnia under dry snow conditions. Three interferograms and three coherence images were calculated from the SAR images. All interferograms had a relatively small baseline, and thus low sensitivity for ice topography and good for ice displacement maps. The resolution of the interferograms is at best 1 mm for relative surface displacements. A 40 km by 40 km area from the northern Bay of Bothnia, containing mainly landfast ice, was selected for detailed studies.

For low salinity smooth fast ice, a decreasing γ trend with increasing $\sigma°$ was observed. For this ice type the total $\sigma°$ is a combination of ice surface and ice-ocean interface scattering (Carlström and Ulander 1995). With $\sigma°$ increasing due to the ice-ocean interface scattering there is a possibility of multiple coherent scattering between the ice surfaces, which increases the sensitivity to temporal changes, yielding smaller γ. For rougher ice areas with dominating ice surface scattering γ varied relatively little. Also snow cover seemed to retain γ over these ice areas.

Discontinuities in the interferograms showed slip lines in deformation of the fast ice zone. Smoother transitions were due to ice topography and deformation, but the interferogram structure suggested that a significant part of the phase shift must have been due to horizontal ice deformations. With this assumption, it was possible to calculate horizontal deformation maps of the fast ice. These maps show where strains occur in the ice pack and can be valuable in prediction of ice ridging and opening of new leads. It is possible, however, that some very local topographics effects over ice ridges also exist in the interferograms. Assuming that the phase shift over the ridge originates just from the ridge topography, it is possible to measure the ridge height.

It is possible to apply a geophysical interpretation of the horizontal ice deformation maps. Small horizontal shifts result as a response of the ice to stresses which are below the plastic yield limit (ice field starts to drift). The stresses may be caused by winds, currents and sea level tilt. When the stresses are below the plastic yield limit, the displacements are elastic strains or viscous creeps within meters or so. The transition of when and how the (nearly) stationary ice starts to drift is a major problem in sea ice mechanics. With the horizontal ice deformation maps it is possible to study the nearly stationary state (for details see (Dammert et al. 1998)). In this case study, the ice was nearly stationary as the stresses were below the yield limit. Two ice floe compressions were observed and the strains were believed to be viscous.

Dammert et al. (1998) suggested that InSAR data are very valuable for theoretical σ° modeling and sea ice mechanics studies.

4.7 Sea Ice Properties with Radar Altimetry

Radar altimeters can measure the surface elevation of the sea ice sheets. These data can be converted to an estimation of sea ice freeboard, which together with estimated ice density and snow load on sea ice provide estimations of sea ice thickness and mass. Combined with ice movement from other EO data, like consecutive SAR images, net sea ice volume and area fluxes are obtained. Empirical data on sea ice thickness, mass and fluxes are very important for sea ice climatology, dynamics and thermodynamics studies. Naturally, sea ice thickness data is also important for ship navigation.

So far the spatial resolution of spaceborne radar altimeters has not been really adequate for sea ice studies, but Cryosat-2, to be launched in March 2009, will fill the resolution criteria (the launch of CryoSat on October 8, 2005, failed). Cryosat-2 combines conventional pulse-limited altimeter hardware with new synthetic aperture and interferometric signal processing (Drinkwater et al. 2004). These new features will allow CryoSat-2 to systematically monitor changes in the sea ice thickness when snow load and ice density estimations are available. The capability of CryoSat-2 to estimate the Baltic Sea ice thickness will be very likely lower than for the Arctic and Antarctic sea ice due to the dynamic nature and small freeboards of the Baltic Sea ice.

A few radar altimetry studies of the Baltic Sea ice have been conducted. Ulander and Carlström (1991) analyzed Geosat altimeter data acquired over the Baltic Sea ice during the BEPERS-88 field campaign. The purpose was to find out the main backscatter mechanism (coherent/incoherent) for radar echoes scattered from sea ice at normal incidence angle by comparing Geosat data to a theoretical backscattering model. Retrieval of sea ice thickness was not studied. Geosat was Ku-band (wavelength 2.2 cm) pulse-limited altimeter. The altimeter footprint had a diameter of 1.7 km and the diameter of the first Fresnel zone ($\sqrt{2H\lambda}$) was 190 m.

The coherent σ° was modeled with (Brown 1982), (Ulander 1987):

$$\sigma^\circ_{coh} \approx \left|R(0)\right|^2 F^2 \frac{H}{c\tau} \exp\left(-4k^2 s^2\right) \tag{4.27}$$

and the incoherent σ° with (Ulander 1987):

$$\sigma^\circ_{incoh} \approx 0.3F\left|R(0)\right|^2 \frac{H}{c\tau}, \tag{4.28}$$

where $R(0)$ is the Fresnel reflection coefficient, τ is the compressed radar pulse length, H is the altimeter altitude, c is the speed of light, and F is the fractional area coverage of the flat dielectric mirrors over the first Fresnel zone.

Sea ice surfaces can be considered rough at Ku-band. To produce a truly coherent (specular) reflection, the surface must have height variations less than $\lambda/10$ over the first Fresnel zone. In the incoherent model, the surface is considered to be inhomogeneous with a small area fraction consisting of flat patches with rms height less than $\sim\lambda/10$ and extending over a few meters. The patches are assumed to be horizontal, but the patch height distribution is not restricted. For simplicity, the patches are assumed to be circular.

The Geosat data were classified into four ice types based on interpretation of an airborne SAR imagery: smooth and rough young ice, thin ice and deformed ice. Both young and thin ice types had altimeter echo waveforms which were narrow peaked and approached the system

impulse response. With the mean and std statistics of σ° all four ice types were quite well discriminated. Based on the inversion of F from (4.27) and (4.28) it was not possible determine whether the backscatter mechanism was coherent or incoherent. With the coherent model the estimates for F are very sensitive to the value of s. Comparison between empirical and simulated Geosat data for a frozen lead indicated that the normal incidence σ° was caused by incoherent scattering. It was hypothesized that the incoherent backscatter originates from many flat and horizontal patches on the inhomogeneous ice surface.

The first, and so far the only, attempt of measuring sea ice freeboard in the Baltic Sea using altimeter data is discussed in (Ulander 1991). The altimeter data were acquired with Geosat over heavily deformed ice in March 1988. The height of the level young and thin ice was used as a reference level. The height profile was smoothed over 4.7 km of data with a resulting rms height error of 11 cm over level ice (see Figure 6 in (Ulander 1991)).

4.8 Brightness Temperature Signatures

The feasibility of using UHF (300 MHz – 3 GHz) and low frequency microwave radiometers for determining the ice thickness of the Baltic Sea ice has been investigated in (Tiuri et al. 1976, 1978) and (Hallikainen 1983) (a summary is in (Hallikainen 1992)). At UHF and low microwave frequencies low salinity Baltic Sea ice is a nonscattering, low-loss medium, and thus the phase coherence of the electromagnetic waves propagating in the sea ice layer is preserved. Due to coherent wave reflections within the ice layer, the brightness temperature T_B oscillates strongly as a function of ice thickness h_i. A local maximum in T_B is predicted for the nadir angle when h_i is an odd number of quarter wavelengths and a local minimum when h_i is an integral number of half wavelengths. Thus, the relationship between T_B and h_i is not unambiguous and retrieval of h_i from T_B data is not straightforward. According to theoretical T_B modeling, T_B has the highest sensitivity to the ice salinity (Hallikainen 1983).

The measured T_B at 610 MHz (helicopter-borne radiometer) as a function of h_i was observed to follow closely the theory. At a higher frequency of 5 GHz, T_B saturated for small ice thicknesses and it is determined primarily by the dielectric properties and surface roughness of the snow and sea ice layer (case of incoherent scattering). The T_B results at 610 MHz suggested that, due to the smoothing effects in T_B data caused by antenna beamwidth and moving helicopter, h_i can be determined with a single channel radiometer with reasonable accuracy. The accuracy of the h_i retrieval can be increased by using either a broadband UHF radiometer or a multichannel radiometer. The use of broadband radiometers is not possible due to the presence of man-made noise sources, like television transmitters. In the multichannel radiometer system, the frequencies must be selected properly in order to achieve an unambiguous relation between T_B and h_i. With a UHF radiometer system having frequencies 530, 780 and 930 MHz an accuracy of ±20 cm was obtained when the local variations in the ice salinity, surface temperature and snow thickness were approximately known (Hallikainen 1983).

Kurvonen and Hallikainen (1996) investigated T_B signatures acquired in the Bay of Bothnia in February and March 1992 with a helicopter-borne radiometer system operating at frequencies 24, 34, 48 and 94 GHz, V-polarization only. The incidence angle was 45º. The T_B data were assigned to the following surface types: open water, new ice, close pack ice (crushed ice and slush, not solid) and compact pack ice. The dataset included three different snow cover conditions: dry snow, wet snow and refrozen snow. For the dry snow condition 24 GHz data were not available.

Under dry snow and refrozen snow conditions the mean T_B for compact pack ice decreased with increasing frequency (around 20 K from 34 to 94 GHz). This was very likely due to high volume scattering in the snow cover at 94 GHz. For snow-free close pack ice the mean T_B, on the contrary, increased with increasing frequency (around 10 K). This was also the case for new ice under dry snow condition (increase 15 K), but under refrozen snow condition new ice was covered by a frost layer, and the mean T_B now decreased from 24 to 94 GHz (around 10 K). Under wet snow condition only close and compact pack ice were measured and their mean T_B values increased slightly (<10 K) from 24 to 94 GHz. The mean T_B values for the two ice types were very close to each other and close to their physical temperatures which was around 0ºC. The mean T_B for open water always increased considerably (even 80 K) with increasing frequency. For compact pack ice the standard deviation of T_B was clearly larger at 94 GHz than at lower frequencies due to the large variation of snow depth on compact pack ice.

For classification of the surface types a combination of high-frequency (94 GHz) and low-frequency (24 or 34 GHz) channel provided the best results. The higher frequency is sensitive to dry and refrozen snow, so it is useful for the detection of pack ice and fast ice, which are usually covered by snow. The problem with the high frequency channel is that the T_B of pack ice and fast ice may be equal to that of open water, if there is the right amount of dry or refrozen snow on the ice. Hence, a lower frequency channel is needed to detect open water in all weather conditions. It is also useful for detection of new ice if it is covered by snow or frost. Discrimination of ice types is, however, quite poor when the snow cover is wet.

4.9 Sea Ice Classification by Spaceborne Radiometer and Scatterometer Images

Ice concentration mapping in the Baltic Sea using spaceborne radiometer was first studied by Hallikainen and Mikkonen (1986) with Nimbus 7 Scanning Multichannel Microwave Radiometer (SMMR) data (SMMR operated in 1978-1987). Ice concentration mapping using the Special Sensor Microwave Imager (SSM/I) data (available since 1987) with the NASA Team algorithm (Cavalieri et al. 1984, 1991) has been studied by Grandell and Hallikainen (1994) and Grandell et al. (1996). The latter also derived the Baltic Sea ice concentration from ERS-1 Wind Scatterometer data and compared the results with the SSM/I concentration maps. Baltic Sea ice studies with the NASA Advanced Microwave Scanning Radiometer (AMSR-E) data (available since 2002) have not yet been published. Before reviewing the results, the NASA Team algorithm is briefly described.

The NASA Team algorithm was originally developed for the Nimbus-7 SMMR data (Cavalieri et al. 1984) and has subsequently been modified for the SSM/I data as well (Cavalieri et al. 1991). The algorithm is based on the assumption that a data pixel consists of a mixture of open water and two ice types. In the Arctic Oceans, the two ice types have been identified with help of additional information from field and airborne observations to be first-year (FY) and multiyear sea ice (MY) (Comiso et al. 1997). The algorithm uses data from three SSM/I channels; 19H, 19V and 37V, processed into 25 by 25 km grid cells, and it is based on two independent variables; polarization ratio PR and gradient ratio GR. These variables are defined as (Cavalieri et al. 1984):

$$PR = \frac{T_B(19\mathrm{V}) - T_B(19\mathrm{H})}{T_B(19\mathrm{V}) + T_B(19\mathrm{H})}, \tag{4.29}$$

$$GR = \frac{T_B(37\mathrm{V}) - T_B(19\mathrm{V})}{T_B(37\mathrm{V}) + T_B(19\mathrm{V})}. \tag{4.30}$$

PR generally distinguishes between open water and ice, with open water having higher PR values. GR generally distinguishes between the two ice types, with higher GR values corresponding to FY. The advantage of using ratios instead of brightness temperature differences is that they are largely independent of ice temperature differences (Cavalieri et al. 1984). The V-polarized GR is particularly used because at 37 GHz layering in the dry snow cover strongly influences the horizontally polarized brightness temperatures, but leaves the vertical polarization largely unchanged due to the Brewster angle effect (Mätzler et al. 1984).

From PR and GR the FY and MY concentrations (C_{FY} and C_{MY}) are calculated with the following equations (Cavalieri et al. 1991):

$$C_{FY} = \left(a_0 + a_1 PR + a_2 GR + a_3 PR \cdot GR\right)/D\,, \tag{4.31}$$

$$C_{MY} = \left(b_0 + b_1 PR + b_2 GR + b_3 PR \cdot GR\right)/D\,, \tag{4.32}$$

where:

$$D = c_0 + c_1 PR + c_2 GR + c_3 PR \cdot GR\,. \tag{4.33}$$

The total sea ice concentration is the sum of the first-year and multiyear ice concentrations:

$$C_T = C_{FY} + C_{MY}\,. \tag{4.34}$$

The coefficients a_i, b_i and c_i are functions of a set of nine brightness temperatures. These brightness temperatures, referred to as algorithm tie points, are observed SSM/I brightness temperatures over areas of known ice-free ocean, FY, and MY for each of the three SSM/I channels. The tie points can be either global (Arctic or Antarctic) or regional (e.g. Baltic Sea).

The algorithm includes a simple weather filter in order to eliminate spurious ice concentrations due to weather related effects at polar latitudes (Cavalieri et al. 1991). The filter sets the ice concentration to zero for all pixels with $GR \geq 0.05$ (currently, there are also other weather filters). This threshold also eliminates ice concentrations below 15%.

Grandell and Hallikainen (1994) studied the determination of the Baltic Sea ice concentration using the SSM/I data acquired over the Sea of Bothnia and Bay of Bothnia from beginning of November 1990 to the end of May 1991. The NASA team algorithm tie points for open water and FY were adjusted for the Baltic Sea. The MY tie point was kept as it is for the Arctic Oceans which meant that the algorithm was used for mapping only the total ice concentration. The tie points for the Baltic Sea and Artic Oceans are presented in Table 4.1. The open water tie points are larger for the Baltic Sea than for the Arctic Oceans, especially at 19.35 GHz H-polarization. No explanations for this difference were given. The SSM/I-derived ice concentrations were compared to the FIS ice charts and the correlation was over 0.80 for the best test areas. However, the time period for the correlation study was quite short and the correlations were mostly based on either 0% or 90 to 100% ice concentration values. The effect of the tie points selection was also studied and it was observed that the Arctic tie points gave concentration values 10 to 20% too small with respect to the ground truth and, thus, the selection of the Baltic Sea tie points should be performed with care.

Grandell et al. (1996) compared Baltic Sea ice coverages derived from the SSM/I and ERS-1 C-band Wind Scatterometer data to each other. The data sets were acquired over the whole Northern Baltic Sea during the winters of 1992-1996. The SSM/I sea ice concentrations were derived using the specific Baltic Sea tie points of Grandell and Hallikainen (1994). The ERS-1 Wind Scatterometer has three antennas looking 45º forward (fore beam), across track (mid beam), and 45º backwards (aft beam) with respect to the satellite track. The data are processed

Table 4.1 Tie points of the NASA Team algorithm for the Arctic Oceans (Cavalieri et al. 1991) and the Baltic Sea (Grandell and Hallikainen 1994).

SSM/I channel	Open water		First-year ice		Multiyear ice
	Arctic	Baltic Sea	Arctic	Baltic Sea	Arctic and Baltic Sea
19.35 H	100.8 K	114.4 K	242.8 K	225.0 K	203.9 K
19.35 V	177.1 K	184.2 K	258.2 K	251.8 K	223.2 K
37.0 V	201.7 K	207.6 K	252.8 K	241.7 K	186.3 K

into a 25 km grid. Each pixel is imaged with three different azimuthal viewing directions and with two incidence angles (one for mid-beam and another for both fore and aft beams). An algorithm for sea ice detection was developed based on the anisotrophy index (Wismann et al. 1996):

$$\phi(\theta) = \frac{\left|\sigma^\circ(\theta_{forebeam}) - \sigma^\circ(\theta_{aftbeam})\right|}{\left|\sigma^\circ(\theta_{forebeam}) + \sigma^\circ(\theta_{aftbeam})\right|} \tag{4.35}$$

and the slope index (Gohin 1995):

$$SL(\theta) = -\frac{\left\{\sigma^\circ(\theta_{midbeam}) - \frac{1}{2}\left[\sigma^\circ(\theta_{forebeam}) + \sigma^\circ(\theta_{aftbeam})\right]\right\}}{\theta_{midbeam} - \frac{1}{2}\left(\theta_{forebeam} + \theta_{aftbeam}\right)}, \tag{4.36}$$

where linear values of σ° are used for calculating $\phi(\theta)$ and values in dB for $SL(\theta)$. $\phi(\theta)$ is a basic discriminant for determining whether the pixel in question is open water (high $\phi(\theta)$) or ice. However, open water may in some cases have low $\phi(\theta)$ values (e.g. calm ocean). $SL(\theta)$ describing incidence angle behavior of σ° helps to discriminate open water from sea ice. For sea ice, the incidence angle dependence of σ° is a linear function, but for open water σ° decreases rapidly at small incidence angles, before reaching a linear response. The thresholds for $\phi(\theta)$ and $SL(\theta)$ for discriminating open water and sea ice are: open water $\phi(\theta) > 0.16$ and $SL(\theta) > 0.45$; sea ice $\phi(\theta) \le 0.16$ and $SL(\theta) \le 0.45$. The scatterometer algorithm yields only a open water – sea ice classification image, i.e. pixels have either 0% or 100% ice concentration.

The results with the SSM/I data indicated that a coastline effect, which occurs when part of the mainlobe and/or sidelobe footprint of the radiometer antenna is over land in addition to open water or sea ice, contaminates the ice concentration estimates up to 50 km (two pixels) from the coastline. The sea ice area extent has to rise above a “noise” level in order to be distinguishable from the coastline effect. The magnitude of the “noise” level depends strongly on the selection of the concentration value used for determining the ice edge contour. Only in 1994 and 1996 winter was severe enough for the sea ice extent to rise above this “noise” level. For the Wind Scatterometer data, the coastline effect was smaller, the contamination limit was closer to one pixel (25 km). The weather filter of the NASA team algorithm worked well in the open water areas of the Baltic Sea, while mixed and ice pixels were left uncorrected. The scatterometer algorithm, however, did not appear to need any weather corrections. Therefore, mixed pixel estimates, i.e. definition of the ice edge, could be enhanced by combined use of the Wind Scatterometer and SSM/I data. The temporal

estimates of the total ice coverage with the Wind Scatterometer data corresponded to roughly those with the SSM/I data.

In general, these two studies indicated that the SSM/I data provide an estimation of the Baltic Sea ice coverage, but the coastline contamination effect and low spatial resolution limits its usability due to the small size of the Baltic Sea (this also applies for the AMSR-E data).

4.10 Summary

In the following, the main results of the previous studies relevant for this thesis are summarized.

Geometric properties of the Baltic Sea ice and theoretical σ° modeling

- Baltic Sea ice has a fractal-like multiscale surface roughness, i.e. surface rms roughness s and correlation length L depends on the measurement length. Snow cover on deformed ice decreases s as snow fills deep pits of deformed ice. In contrast, snow cover on level ice typically increases s due to wind redistribution of snow and snow melt-refreeze cycles. (Manninen 1997a).
- At C-band co-polarization (RADARSAT-1, ENVISAT) ice surface scattering is typically dominating when θ_0 is less than 45º and snow cover is dry. If ice surface is very smooth and salinity S <0.5‰, which is typically the case for level fast ice, the scattering from ice-water interface and ice volume are significant. (Carlström and Ulander 1995, Dierking et al. 1999).
- At X-band co-polarization volume scattering from the upper ice layer dominates under dry snow condition. The ice-ocean interface is the main scattering source at L-band. (Dierking et al. 1999).
- The main scattering component of ice ridge σ° at C-band co-polarization is the coherent scattering (specular reflection) from ice block major facets according to (Carlström and Ulander 1995, Carlström 1997), whereas according to (Manninen 1992, 1996b) it is the incoherent surface scattering from ice blocks. This difference is due to the different ice ridge surface structure models used.
- The ice ridge σ° depends on the most on the ice block surface roughness, secondly on the block ε_r and the least on the ridge geometrical parameters. The theoretical σ° contrast between level ice and ice ridge is the largest at cross-polarization. σ° is larger when radar is viewing across the ice ridge than it is viewing along it. (Manninen 1992).

Backscattering signatures at C- and X-band

- The mean σ° at all C- and X-band polarizations increases with increasing ice deformation and decreases with increasing θ_0 (Kemppainen 1989, Hyyppä and Hallikainen 1992, Hallikainen and Toikka 1992, Dammert et al. 1994).
- The σ° contrast between open water and level ice is around 3 dB higher at C-band VV- than at VH-polarization (Carlström 1990), whereas that between deformed ice and level ice is at VH-polarization even 10 dB higher (Carlström 1990, Hyyppä and Hallikainen 1992).
- s_T at C-band HH-polarization is on the average the largest for ridged ice and the smallest for jammed brash barrier. s_T decreases when snow wetness increases. For deformed ice types the mean C-band s_T is generally higher at VH- than at VV-polarization. (Carlström 1990, Dammert et al. 1994).
- s_T at C-band HH-polarization is typically larger than that at VV-polarization (obtained with data for brash ice). s_T at HH-polarization is the most sensitive to surface roughness inhomogeneities at the mid-to-large incidence angle range. (Dierking et al. 1997).

- Ice type discrimination results with a single channel $\sigma°$ are usually poor. Cross-polarized $\sigma°$ provides better results than co-polarized $\sigma°$ and their combination gives the best results. The ice type discrimination usually improves with the increasing θ_0. X-band provides slightly better discrimination results than C-band. (Carlström 1990, Hyyppä and Hallikainen 1992, Hallikainen and Toikka 1992).
- Combined use $\sigma°$ and s_T increases ice type discrimination, especially under dry snow condition. Open water leads are not discriminated from sea ice with $\sigma°$ and s_T. (Dammert et al. 1994).
- $\sigma°$ decreases with increasing air temperature under cold conditions. Very rough ice is slightly more sensitive than smooth ice to a air temperature change. From cold to warm condition $\sigma°$ for all ice types decreases. The decrease is larger for rough ice than for smooth ice as wet snow cover makes rough ice areas look much smoother. (Lundin 2001).

Polarimetric discriminants at L- and C-band

- L- and C-band co- and depolarization ratios ($R_{co} = \sigma^o_{VV} / \sigma^o_{HH}$ in here) do not separate different level ice types. L-band R_{co} is close to one, whereas C-band R_{co} is over one and increases with increasing θ_0. At both bands R_{depol} is around 0.1. Level ice ϕ_{HH-VV} at C-band varies from -10º to +10º and at L-band from 0º to 30º. ϕ_{HH-VV} increases slightly with increasing θ_0 at both bands. The observed ϕ_{HH-VV} at C-band can be explained with dominating ice surface scattering and at L-band by an anisotropic character of the ice layer close to the ice-water interface. (Dierking and Askne 1998).
- L- and C-band R_{co} and R_{depol} do not discriminate deformed ice types. At L-band R_{co} is from 0.8 and 1.0 and at C-band from 0.7 to 1.1. R_{co} values smaller than one may indicate the dominance of double bounce or coherent scattering from ice blocks. According to larger R_{depol} at L- than at C-band multiple scattering processes within deformed ice are stronger at L-band. At L-band ϕ_{HH-VV} for deformed ice is scattered around zero and at C-band it is from -10º to +5º. (Dierking and Askne 1998).

Brightness temperature signatures

- Under dry snow and refrozen snow conditions the mean T_B for snow covered ice types decreases with increasing frequency due to increase of snow volume scattering. Standard deviation of T_B increases with increasing frequency if there are large variations in snow thickness. Under wet snow condition mean T_B values for snow covered ice types are close to each other. (Kurvonen and Hallikainen 1996).
- For classification of the surface types a combination of high-frequency (94 GHz) and low-frequency (24 GHz) channels provides the best results. The high frequency channel is sensitive to dry and refrozen snow, so it detects snow covered ice types. The low frequency channel detects open water in all weather conditions. Discrimination of ice types is rather poor when the snow cover is wet. (Kurvonen and Hallikainen 1996).

Determination of the Baltic Sea ice coverage with spaceborne radiometer data

- The SSM/I data provides an estimation of the Baltic Sea ice coverage, but the coastline contamination effect and low spatial resolution limits its usability. The sea ice area extent has to rise above a “noise” level in order to be distinguishable from the coastline effect. Algorithms for the Arctic Sea must be modified for the Baltic Sea ice conditions. (Grandell and Hallikainen 1994, Grandell et al. 1996).

5 Investigation of Backscattering Signatures of the Baltic Sea Ice

For supporting development of operational classification algorithms for SAR images, the following investigations on active microwave remote sensing of the Baltic Sea ice were conducted: (1) statistics of C- and X-band backscattering signatures [P1], (2) statistics of L- and C-band polarimetric discriminants [P2], (3) incidence angle dependence of σ° in RADARSAT-1 SAR images [P3], (4) dependence between standard deviation and measurement length for σ° signatures and its usability in sea ice classification [P4], and (5) dependences between SAR σ° time series and results of a thermodynamic snow/ice model [P5]. Below, radars and data sets used in [P1]-[P5] and general sea ice and snow cover classes used are first presented, followed by discussions of the research methods and main results with comparisons to previous studies, when appropriate.

5.1 Radar Instruments and Data Sets

5.1.1 HUTSCAT scatterometer

The HUTSCAT (Helsinki University of Technology Scatterometer) is a helicopter-borne non-imaging frequency modulated - carrier wave (FW-CW) scatterometer operating simultaneously at frequencies 5.4 GHz (C-band) and 9.8 GHz (X-band) and all four linear polarizations (Hallikainen et al. 1993). HUTSCAT was designed and constructed during 1987-1990 by Laboratory of Space Technology of TKK. The main parameters of HUTSCAT are presented in Table 5.1. HUTSCAT measures the backscattered power as a function of measurement range at a resolution of 0.68 m. At each channel 20 backscattered power spectra per second are measured. Simultaneously with the backscattering measurements, the target is recorded by a video camera, and DGPS-coordinates (differential GPS) of the flight track are saved. A typical flight altitude is 100 m and the flight speed is 25 m/s. Internal and external calibration are used to eliminate short-term and long-term variations in the backscattered power level. Internal calibration is conducted by a delay line which connects transmitted power to the receiver. External (absolute) calibration is achieved with active radar calibrators and corner reflectors. The backscattered power spectra data are converted to absolute σ° values using internal, external and range calibration coefficients.

HUTSCAT measurements over the Baltic Sea ice were conducted in 1992-2003 during seven ice research campaigns, see Table 5.2. The two research campaigns in 1992 were part of the international PIPOR (A Programme for International Polar Oceans Research) ERS-1 project. The campaigns in 1993 and 1994 were part of the Finnish OSIC (Operational Sea Ice Charting using ERS-1 SAR images) ERS-1 pilot project. The campaigns in 1995 and 1997 were carried out within the framework of the ESA EMAC (European Multisensor Airborne Campaign) and EU IMSI (Integrated Use of New Microwave Satellite Data for Improved Sea Ice Observation) projects, respectively. The campaign of 2003 was part of the national ESSI (ENVISAT and the Baltic Sea Ice Conditions) project. R/V Aranda operated by FIMR was the base for the HUTSCAT and ground data measurements in 1992-1997. In 2003, the base was Marjaniemi pilot station in Hailuoto Island in the Bay of Bothnia.

HUTSCAT measurements were conducted along selected test lines that included various ice types. A typical length of each test line was tens of kilometers. The measurements were conducted at incidence angles of 23 and 45 degrees. Both angles are within the incidence angle range of RADARSAT-1 ScanSAR (20º to 50º). The 23-degree angle is within the incidence angle range of both ERS-2 SAR (19.5º to 26.5º) and ENVISAT ASAR Wide Swath Mode (WSM) images (16º to 43º), and the 45-degree angle is only two degrees larger than the maximum incidence angle of ENVISAT WSM. The ground truth measurements included ice

Table 5.1 The main parameters of the HUTSCAT scatterometer (Hallikainen et al. 1993, Hyyppä et al. 1999).

Parameter	Value
Center frequency	5.4 and 9.8 GHz
Modulation	FM-CW
Sweep bandwidth	230 MHz
Polarization	HH, HV, VV, VH
Measurement range	20 to 160 m
Range resolution	0.68 m
Incidence angle	0° to 45° of nadir
Antenna effective two-way 3 dB beamwidth	4.7° (large), 6.7° (small) (5.4 GHz) [1)] 4.4° (9.8 GHz)
Antenna polarization isolation	26.0 dB (large), 22.5 dB (small) (5.4 GHz) [1)] 28.5 dB (9.8 GHz)
Relative $\sigma°$ 90% confidence interval	±0.3 dB (5.4 and 9.8 GHz)
Absolute $\sigma°$ 90% confidence interval	±1.0 dB (5.4 GHz HH, VH) ±0.6 dB (5.4 GHz VV) ±0.7 dB (9.8 GHz)
Noise equivalent $\sigma°$	< -25.0 dB (5.4 GHz HH) < -28.5 dB (5.4 GHz VV) < -46.5 dB (5.4 GHz VH) < -21.0 dB (9.8 GHz HH) < -24.5 dB (9.8 GHz VV) < -48.0 dB (9.8 GHz VH)

1) Small 5.4 GHz antenna (diameter 40 cm) was used in 1992 and large antenna (diameter 75 cm) from 1993 onward.

and snow characteristics (e.g. snow depth, snow density and wetness profiles) and they were conducted mainly near R/V Aranda (1992-1997) or Marjaniemi pilot station (2003). Weather data were provided by the R/V Aranda weather station (1992-1997) or Finnish Meteorological Institute (FMI) Marjaniemi weather station (2003).

Here $\sigma°_{VH}$ (the first letter denotes the incident polarization and the second the scattered polarization) was chosen to represent cross-polarized $\sigma°$ because at the VH channel the noise floor is 3 dB lower than at the HV channel.

HUTSCAT data were assigned into various surface type classes described in Chapter 5.2 by video imagery. Only the sections of the measurement lines fulfilling the following requirements were accepted for further data analysis: (1) identification of ice type was reliable, and (2) section length as measured by the video imagery was more than 10 s, which corresponds to a distance of 250 m. The decision of the surface type is more reliable, when the imagery is ‘averaged’ over reasonable lengths. Accuracy of the video classification was estimated by comparing two classification results for a single measurement line (length 60 km). The classifications were conducted one year apart by the author. Eighty per cent of the two classifications matched each other. The total amount of HUTSCAT data corresponds roughly to a distance of 1000 km. Seventy-seven per cent of the data were assigned into

various surface types. The ground truth data provided further classification of HUTSCAT data into dry, moist and wet snow cover wetness classes, see Chapter 5.2.

Table 5.2 HUTSCAT scatterometer datasets for the Baltic Sea ice.

Campaign and date	Position of R/V Aranda	Inc. angles [deg]	Air temp. [°C]	No. of ice types	Snow coverage and thickness	Snow class
PIPOR-92A 10 Feb	Bay of Bothnia 65° 31’ N, 24° 21’ E	23, 45	+0.4	4	Snow coverage on level ice 20-50%. Shallow snow accumulations behind ridges and blocks.	Wet snow/ Wet ice
PIPOR-92A 11 Feb	Bay of Bothnia 65° 31’ N, 24° 21’ E	23	-1.0	3	Mean thickness less than 10 cm.	Wet snow
PIPOR-92A 14 Feb	Bay of Bothnia 65° 18’ N, 23° 47’ E	23	-12.0	7	Mean thickness less than 10 cm.	Moist snow
PIPOR-92B 12 Mar	Bay of Bothnia 65° 24’ N, 23° 35’ E	23, 45	-1.4	3	Ice was only partly covered with snow.	Moist snow
PIPOR-92B 15 Mar	Bay of Bothnia 65° 25’ N, 23° 35’ E	23	-3.4	7	Ice was covered by a roughly 10 cm even snow layer. Large areas of ice were flooded. Areas with thicker ice were unflooded.	Moist snow
PIPOR-92B 18 Mar	Bay of Bothnia 65° 25’ N, 23° 35’ E	23	+0.1	5	Ice was covered by a roughly 10 cm even snow layer. Wind had mixed up new and old snow.	Wet snow
PIPOR-92B 20 Mar	Bay of Bothnia 65° 25’ N, 23° 35’ E	23	-1.1	6	Snow had melted from less rough ice areas. Snow remained in more deformed areas.	Wet snow/ Wet ice
PIPOR-92B 21 Mar	Bay of Bothnia 65° 25’ N, 23° 36’ E	23, 45	-6.5	4	Ice was mostly snow-free and snow surface was hard with crust.	Dry snow/ Dry ice
OSIC-93 23 Feb 25 Feb 28 Feb	Bay of Bothnia 65° 15’ N, 24° 14’ E	 23 45 23	 -13.3 -5.3 -5.2	 3 2 2	Deformed ice covered with few cm thick old snow layer and with drift snow layer (0-20 cm). Level ice covered with salty hoarfrost.	Dry snow
OSIC-94 23 Mar	Sea of Bothnia 62° 18’ N, 20° 27’ E	23, 45	-0.2	4	Level ice almost snowfree. Shallow snow accumulations behind ridges and blocks.	Wet snow/ Wet ice
OSIC-94 26 Mar	Gulf of Finland 59° 56’ N, 25° 24’ E	23, 45	-4.6	6	Partly frozen 2-3 cm thick slush layer on level ice. Up to 50 cm thick snow accumulations in ridges.	Moist snow
EMAC-95 4 Apr 6 Apr	Bay of Bothnia 65° 12’ N, 24° 14’ E	23, 45	-6.7 -0.4	4 7	Mean snow thickness 10-40 cm. Occasionally a thin slush layer underneath the snow cover.	Moist snow
IMSI-97 21 Mar 23 Mar	Bay of Bothnia 65° 16’ N, 23° 58’ E 64° 13’ N, 22° 24’ E	23, 45	-10.6 -7.1	5 5	Level ice covered by a very thin loose new snow layer. Some snow in ridges and on rough ice areas.	Dry snow/ Dry ice
ESSI-03 13 Feb 14 Feb 18 Feb	Near Marjaniemi pilot station	23, 45	-4.3 -10.0 +2.1	1 2 3	Average snow thickness on level fast ice 26 cm.	Dry snow Dry snow Moist snow

The HUTSCAT data were averaged to a resolution of either 12.5 m [P4] or 25 m [P1], [P3]. At a typical flight speed of 25 m/s this corresponds to averaging 10 or 20 consecutive σ° values together. These resolutions were chosen to match coarser resolution spaceborne SAR data and at the same time to keep the sample sizes of some ice types large enough for a reliable estimation of the statistical parameters. Averaged data have around 50 (12.5 m) or 100 (25 m) independent samples in each σ°. The standard deviation of fading is then below

0.62 or 0.43 dB. For SDI, HDI and FBI a large amount of data exist under all snow conditions (see Chapter 5.2 for ice type definitions). For NI and RLI data exist under dry and moist snow condition only. Under moist and wet snow condition there is small amount of data for LBI. Only in two field campaigns the number of samples for open water leads is large enough.

For the estimation of s_T with (3.3), averages of the instrument noise equivalent backscattering coefficient (σ°_N) and N are needed. For HUTSCAT σ°_N depends considerably on the measurement range which means that its accurate estimation is usually very difficult. Therefore, s_T is in [P1] estimated just by the normalized standard deviation (standard deviation divided by mean) which is further converted to dB values using (3.6). When N is 100 in each σ°, the difference between s_T and normalized standard deviation is smaller than 0.1, if SNR is larger than 10 dB.

5.1.2 RADARSAT-1

RADARSAT-1 SAR operates at 5.3 GHz (C-band) with HH-polarization. It has several operation modes with different image sizes and resolutions. In [P3], RADARSAT-1 ScanSAR Narrow images acquired over the Bay of Bothnia in 1998-2000 are used. The ScanSAR Narrow mode operates with a combination of two (ScanSAR Narrow A; SNA) or three antenna beams (SNB). The main difference between the two image types is their incidence angle range, 19 to 39 degrees for SNA and 30 to 46 degrees for SNB (RSI 2000). The ScanSAR Narrow images were received and processed by the KSAT in Tromsø, Norway. The images delivered by KSAT were in ground range projection with a 50-m pixel spacing. At FIS the images were rectified to the Universal Transverse Mercator (UTM) projection with a 100 m pixel spacing using an algorithm described in (Herland and Berglund 1995). The land areas in the images were masked off. The backscatter intensity in the images is coded with an 8-bit logarithmic scale. Backscattering coefficients are derived using:

$$\sigma^{\circ} = \left(\frac{B^P}{G} \right)^2 \sin(\theta_0), \tag{5.1}$$

where P is the 8-bit pixel value (0-255), B is the logarithmic scale (1.024), G is the logarithmic gain factor (0.16).

KSAT did not provide absolute calibration of the ScanSAR Narrow images. The nominal radiometric uncertainty within any image or between any two images is at maximum 3 dB according to the header files accompanying the image data. Ground to slant range distance conversion coefficients needed to calculate θ_0 for every pixel using a method described in (Shepherd 1998) were neither provided. Thus, θ_0 was calculated with the following method: first, the incidence angles are calculated for the nearest and most distant range pixels using image geometry and satellite orbit parameters obtained from the image header files and, second, the incidence angles for other pixels are interpolated in the UTM projection with one degree accuracy.

For studying the θ_0 dependence of the statistical properties of σ° in [P3] a special selection method of the ScanSAR Narrow images was needed. First, image pairs over the Bay of Bothnia were selected from a large number of images acquired during February-April in 1998-2000 using air temperature data from three Finnish coastal weather stations; Valassaaret, Ulkokalla and Hailuoto, see Figure 5.1. The air temperature was required to be either below or above 0°C at least one day before the acquisition of the first image and also between the times of the acquisition of both images. Secondly, the image pairs were classified either to dry snow or wet snow condition. The two images of an image pair provide σ° data at two different incidence angles for exactly the same areas for statistical analyses. The SAR

images of the pairs were typically acquired 1.5 days apart at different orbits, one at descending orbit around 05:00 UTC and the other at ascending orbit around 16:00 UTC. This orbit combination provided a large range of the θ_0 difference values between the two images. The total number of image pairs is 28, with 21 for dry snow and 7 for wet snow condition. Nine pairs were acquired in 1998 and 7 and 12 in 1999 and 2000, respectively.

Two consecutive SAR images were first matched using the land mask; then a linear regression model between the pixel coordinates of the two images was determined using bright spots (e.g., stationary ships, heavily deformed ice areas) in the images. The accuracy of this matching procedure is estimated to be one to two pixels.

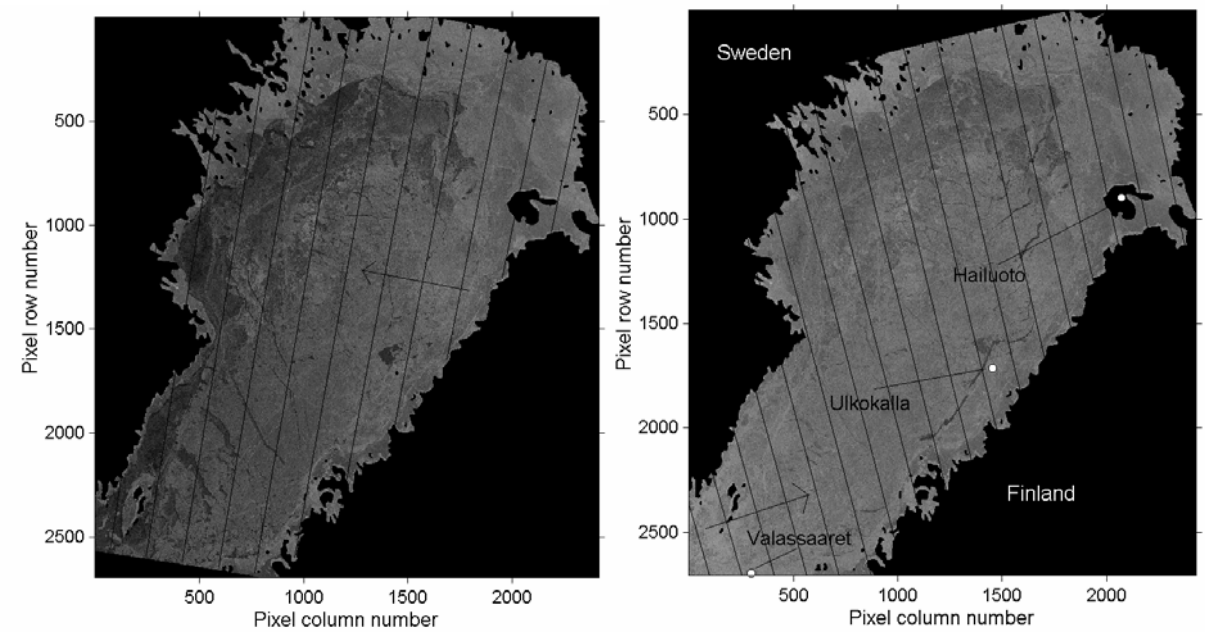

Figure 5.1 A RADARSAT ScanSAR Narrow image pair over the Bay of Bothnia. (a) SNB type acquired on March 17, 2000 (04:50 UTC) at descending orbit. (b) SNA type acquired on March 18, 2000 (15:51 UTC) at ascending orbit. The arrow in the image indicates the SAR look direction. The three FMI coastal weather stations used in [P3] are shown in (b). The incidence angle values in the images are shown with one degree boundaries.

5.1.3 ENVISAT ASAR

ENVISAT ASAR operating at 5.331 GHz has several single and dual polarization operating modes. In [P4] and [P5], image mode precision (IMP), alternating polarization precision (APP) and Wide Swath Mode (WSM) images are used. The APP and IMP modes have seven different swath types, denoted as IS1 to IS7, with different incidence angle ranges. All images used here were delivered in ground range projection. Some characteristics of the image types are described in Table 5.3.

SAR images were processed to σ° values using the ESA's BEST-software and then rectified to the Finnish Uniform Coordinate System (northing and easting in meters) with either 25 m [P4] or 30 m [P5] pixel size for the APP and IMP images and with 150 m pixel size for the WSM images. The correlation between neighboring pixels of the rectified images is negligible.

In [P4], two IMP images at HH-polarization and two APP images at HH/HV-polarization acquired over the northern part of the Bay of Bothnia in February 2003 are used, see Table 5.10. The images were classified into dry snow and moist snow conditions using field campaign data.

Table 5.3 Some characteristics of the ENVISAT ASAR APP, IMP, and WSM images (Closa et al. 2003, Meadows and Wright 2003a, 2003b; Rosich et al. 2004).

	APP	IMP	WSM
Pixel size	12.5 by 12.5 m	12.5 by 12.5 m	75 by 75 m
Azimuth resolution	27.65±0.86 m	22.07±0.43 m	108.13±3.5 m
Range resolution	range dependent on average 26 m	range dependent on average 25 m	range dependent on average 120 m
Equivalent number of looks	2	3.61	around 16
Absolute accuracy	±0.49 dB	±0.41 dB	±0.63 dB
Noise equivalent σ°	-28 to -22 dB	-26 to -21.5 dB	-25 to -22 dB

For comparisons of σ° time series with results of a thermodynamic snow/ice model in [P5], 21 IMP images (February 3 to March 16, 2004) and eight WSM images (March 8 to April 7, 2004) were acquired over the Bay of Bothnia, see Table 5.4. All images have HH-polarization. The local acquisition time was either between 10:40-12:15 (descending orbit) or 21:25-22:53 (ascending orbit). The time interval between acquisition of two SAR images varied from one to eight days.

Table 5.4 ENVISAT ASAR data set for [P5]. Time period is from February 3 to April 7, 2004. The number for the ENVISAT data indicates the swath type (IS1-IS7) of an IMP image. 'W' means a WSM-image.

Date	2.3	4	5	6	7	8	9	10	11	12	13	14	15	16	17	18	19
ENVISAT	7	2		7		1		4							1	3	
Date	20	21	22	23	24	25	26	27	28	29	3.1	2	3	4	5	6	7
ENVISAT	1	2	7		1	6	3		5	4		4			3	6	
Date	8	9	10	11	12	13	14	15	16	17	18	19	20	21	22	23	24
ENVISAT	W						1	6	4		W	W					W
Date	25	26	27	28	29	30	31	4.1	2	3	4	5	6	7			
ENVISAT			W			W							W	W			

5.1.4 EMISAR

EMISAR is a fully polarimetric L-band (1.25 GHz) and C-band (5.3 GHz) SAR operated by Technical University of Denmark (Christensen et al. 1998). In 1995 EMISAR was flown on the Gulfstream G3 aircraft of the Royal Danish Air Force. EMISAR has a resolution of 2 by 2 m and an image size of 9.6 (range) by 13 (azimuth) km in slant range. The incidence angle varies in the images from 40º to 60º, being around 54º at the image centers. EMISAR deliverables are the full resolution single look scattering matrix data in the slant range projection with 1.5 by 1.5 m pixel size and the multilooked covariance matrix data in the pseudo ground range projection with 5 by 5 m pixel size.

In the EMAC-95 campaign, EMISAR acquired data on March 22 and 23, and May 2 and 3 over four 9 by 9 km test sites in the Bay of Bothnia (Dall et. al 1997). In 1995, EMISAR operated only at one frequency band at a time and changes between C-band and L-band required a landing of aircraft to reconfigure the SAR for the other frequency. In [P2], L- and C-band scattering matrix images acquired in March over one test site are studied. The ice situation on this test site was typical for normal winter.

5.2 Sea Ice and Snow Cover Wetness Classes

HUTSCAT data were assigned by video imagery into surface type classes presented in Table 5.5. The ice type classes are based on the ice type classification described in Section 2.2 (classification ways "surface structure" and "stage of ice development and ice thickness") and on the classification used operationally for the FIS ice charts (see Figure 2.2). Here a surface type 'open water leads' (OW) is used instead of 'open water' because all measured open water areas were leads typically few kilometers across. The ice type classes are as follows: Nilas (NI) is a general term for recently formed ice which is usually less than 10 cm thick. It is same as the class 'new ice' in the FIS ice chart. Nilas is not divided into sub-groups, because their identification in video imagery is very difficult and also because it does not pose any problems for ship navigation. Smooth level ice (SLI) is almost unaffected by deformation, only cracking or finger rafting may occur. Rough level ice (RLI) has protruding ice blocks and floe edges and low uneven surface areas and it has typically broken and frozen several times. SLI and RLI belong to classes 'level ice' and 'fast ice' of the FIS ice chart. Slightly deformed ice (SDI) consists of ice ridges, uneven surfaces and level ice areas, the sizes of which are usually larger than 100 m pixel in SAR images. The average size of level ice areas in highly deformed ice (HDI) is usually smaller than the pixel size, and the proportion of level ice areas is smaller than in SDI, i.e. the degree of deformation is higher. Discrimination of SDI from HDI in video imagery is often difficult and subjective. Both SDI and HDI represent the class 'ridged or hummocked ice" of the FIS ice chart. In addition, SDI also represents the classes "rafted ice' and 'consolidated compact ice'. Loose and frozen brash ice (LBI, FBI) are accumulations of ice fragments not more than 2 m across. Their surface is usually very rough in scales of below few tens of centimeters. The FIS ice chart class 'windrow' belongs to the LBI class.

From the EMISAR images windows representing NI, level ice (LI), SDI and HDI ice types were visually selected [P2]. LI is a combination of the HUTSCAT SLI and RLI classes.

For ENVISAT data in [P4], following three ice types classes are used: LI, deformed ice (DI) and highly deformed ice (HDI). The classes were visually assigned for different test areas. The LI class corresponds to SLI in the HUTSCAT data. DI is a mixture of the HUTSCAT RLI and SDI classes whereas HDI is a mixture of SDI and HDI classes. Nilas was not present in the SAR images.

Test sites on fast ice representing LI and DI were visually selected on the RADARSAT-1 image pairs [P3]. It was not possible to identify visually different level ice and deformed ice sub-types and, thus, only these two broad ice type classes were used.

Table 5.5 Baltic Sea ice type classes assigned for the HUTSCAT data.

Main group	sub Group	Abbr.	Effect on ship navigation
Open water leads	None	OW	None
Nilas	None	NI	None
Level ice	Smooth level ice	SLI	Depends on thickness
	Rough level ice	RLI	
Deformed ice	Slightly deformed ice	SDI	Slows down or blocks navigation
	Highly deformed ice	HDI	Usually blocks navigation
Brash ice	Loose brash ice	LBI	Depends on thickness
	Frozen brash ice	FBI	

As discussed earlier, snow cover wetness has a large effect on the statistics of the sea ice σ°. Therefore, all HUTSCAT data in [P1], [P3] and [P4], EMISAR data in [P2] and ENVISAT data in [P4] were further classified using ground truth data into the following snow cover wetness categories: (1) dry snow (volumetric wetness ≈ 0%), (2) moist snow (wetness < 1%) and (3) wet snow (wetness > 1%). According to (Hallikainen et al. 1986) the penetration depth of radar wave in snow decreases rapidly as a function of snow wetness for wetness values below 1%. The decrease is much slower as the wetness is above this value, see Figure 5.2. For the RADARSAT-1 data in [P3], only dry snow and wet snow classes were used. For ENVISAT data in [P5], where a detailed study between σ° and snow and sea ice properties was conducted, the wetness percentage limit between moist and wet snow classes was increased to 2%. This was based on the theoretical σ° modeling of snow covered level ice using the first-order solution of the radiative transfer equation in (3.7) (Fung 1994). After this increase the ice surface scattering is smaller than the snow surface scattering under wet snow condition when snow cover is thin (thickness at minimum around 10 cm). It is believed that using this new wetness limit in the other journal articles, would not have caused significant changes in the results.

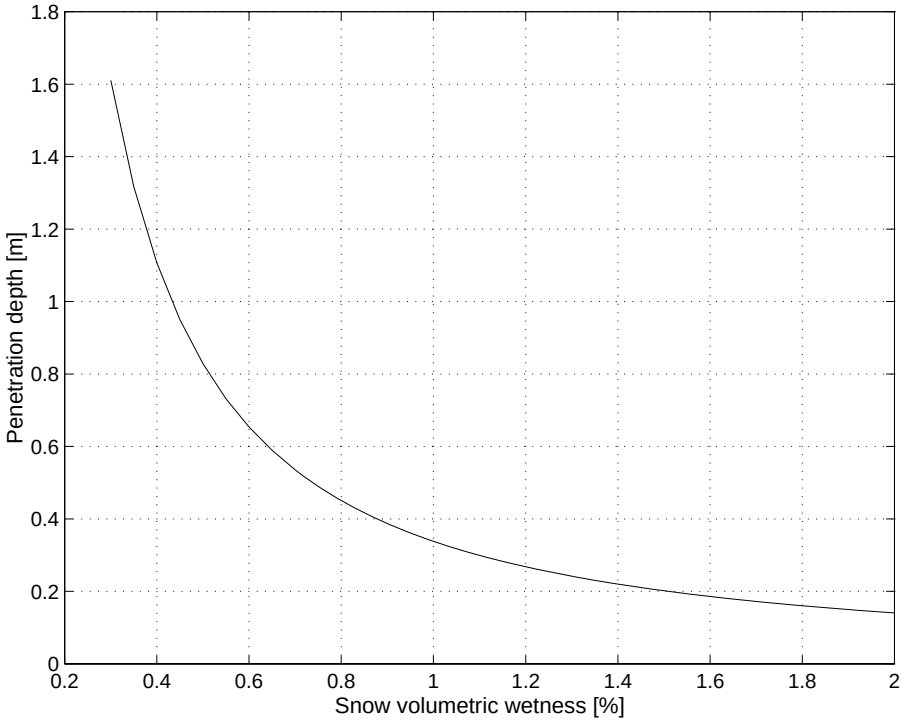

Figure 5.2 Penetration depth in snow as a function of snow wetness (Hallikainen et al. 1986). The frequency is 5.3 GHz and incidence angle is 0º. Snow density is 0.2 g/cm^3. Scattering in snow is ignored.

5.3 C- and X-band Backscattering Signatures

Empirical statistics on backscattering signatures of various ice types are of general interest and they can also be utilized in the classification of the SAR images. For example, they could provide a simple limit for the level of σ° above which ice is most likely deformed ice. Therefore, statistics of C- and X- band σ° signatures for various ice types was investigated in [P1] using the HUTSCAT data acquired in 1992-1997 (Table 5.2) and averaged to a resolution of 25 m. Before statistical analyses, the HUTSCAT data were divided into large and small data sets. A large data set consists of all measurements conducted on a single day or during the same field campaign. The different large data sets of a same snow cover wetness

class were typically not combined because the mean σ° for the same ice type typically varies substantially from one data set to another due to the different local ice and snow cover characteristics. Small data sets were formed by moving step by step an interval of nine σ° values over the HUTSCAT data. Here the different single measurement lines for a surface type were not combined because, if the mean levels of σ° for separate lines are very different, their combination yields erroneous statistics.

For the large data sets the following statistical parameters were calculated: means, 90% confidence intervals and probability density functions (pfd's) for 5.4 and 9.8 GHz HH-, VV- and VH-polarized σ° and co- and cross-polarization ratios (R_{co} and R_{cr} in (3.18) and (3.19)). The pdf's were also used to conduct maximum likelihood classification of the surface types. The means and stds were calculated only when the number of samples was at least ten. For the 90% confidence intervals and pdf's at least 20 samples were required. The pdf's were estimated with the Parzen method (Therrien 1987) using a Gaussian kernel function with a std of 1.0 dB which was large enough to filter out small random like fluctuations in the shape of the pdf, but still small enough to preserve large scale details. For the small data sets the mean and std (3.6) of σ° were calculated.

5.3.1 Mean and 90% confidence interval of σ°

Examples of the means and 90% confidence intervals of 5.4 and 9.8 GHz σ° under dry and wet snow condition are presented in Figures 5.3 and 5.4. The results show that the mean σ° (σ°_M) usually increases when the degree of ice deformation increases. Theoretically σ° increases when the surface rms roughness s, the size or the fraction of the volume scatterers increases (Fung 1994). According to (Manninen 1997a) s is usually larger for deformed ice than for level ice. Additionally, very likely various kinds of deformation features, like ice ridges, generate more volume and multiple scattering than NI and LI. Generally, σ°_M decreases with increasing θ_0. The difference between the σ°_M values at the angles of 23 and 45 degrees depends on ice type, snow condition and data set. The difference is usually larger at co- than at VH-polarization. The dependence between C-band HH-polarization σ°_M and θ_0 is further studied in [P3]. No clear dependence between σ°_M and the snow wetness condition was observed. This is due to the different local ice and snow characteristics in different large data sets of the same snow condition, which give rise to large variations for σ°_M of the same ice type.

The range of the σ°_M values (maximum minus minimum σ°_M) is on average of the same order under dry and moist snow condition and noticeably larger than under wet snow condition. When the snow cover is wet, it attenuates or even totally blocks backscatter from underlying sea ice, yielding small range of σ°_M, as the surface of the snow cover is usually smoother than that of sea ice (Manninen 1997a). At HH- and VV-polarization the range of σ°_M is on average equal and mostly smaller than at VH-polarization.

The 90% interval of observed σ° values is on average the largest for NI and deformed ice types and the smallest for brash ice types. This can be explained by the definitions of these ice types. SDI and HDI consist of various kinds of level and deformed areas, whose σ°_M levels are likely very variable. NI is a common definition for all different new ice types less than 10 cm thick, which may have highly variable levels of σ°_M. Brash ice has usually very rough surface, but it is also very homogeneous in overall geometry. The 90% intervals for deformed ice types are on average the largest under dry snow and the smallest under wet snow condition which indicates that the attenuation of wet snow reduces the spatial variation of σ° compared

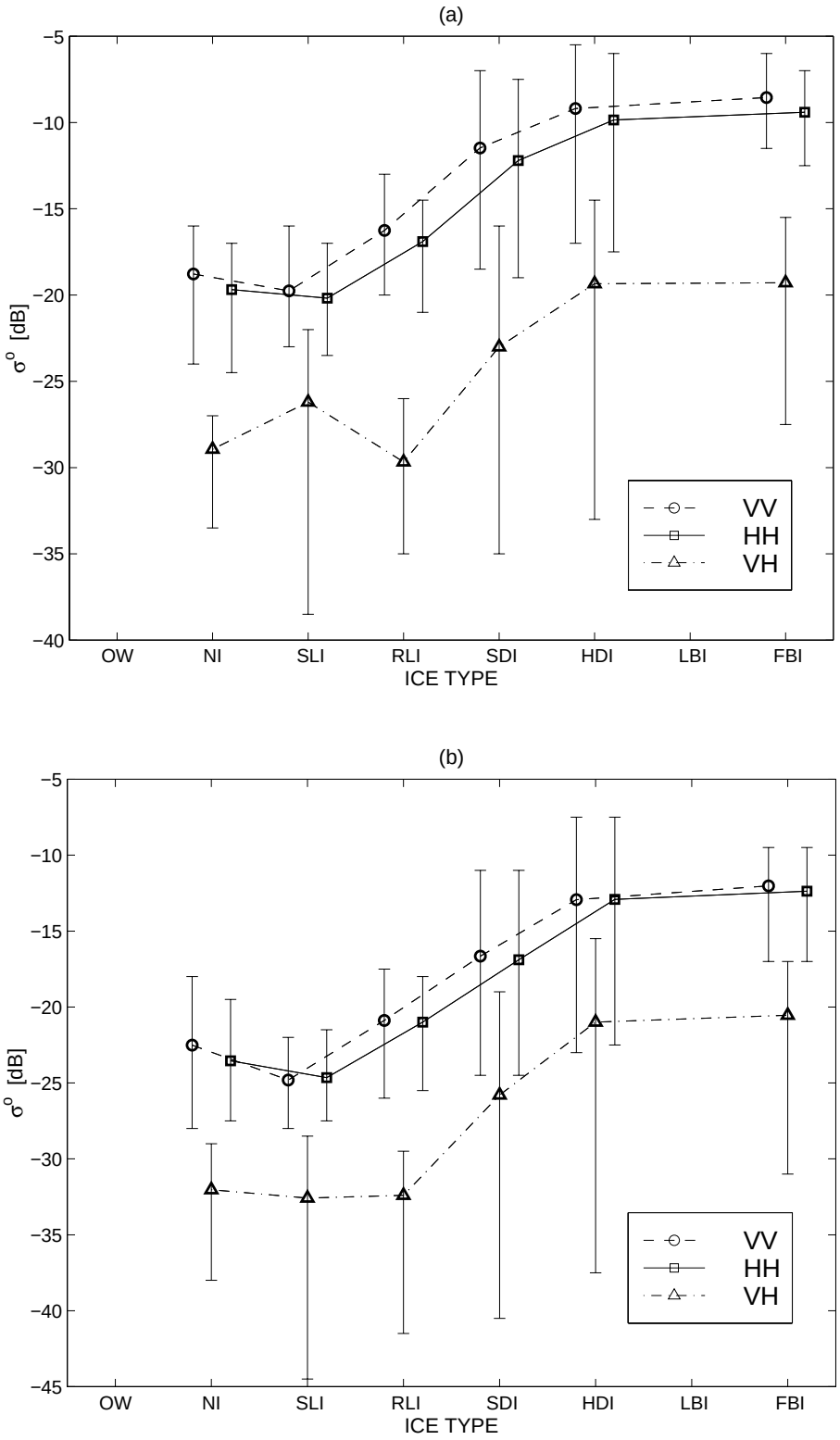

Figure 5.3 Mean and 90% confidence interval of σ° for various ice types using the IMSI-97 dry snow data averaged to a resolution of 25 m: (a) 5.4 GHz at an incidence angle of 23º, (b) 5.4 GHz at 45º, (c) 9.8 GHz at 23º and (d) 9.8 GHz at 45º.

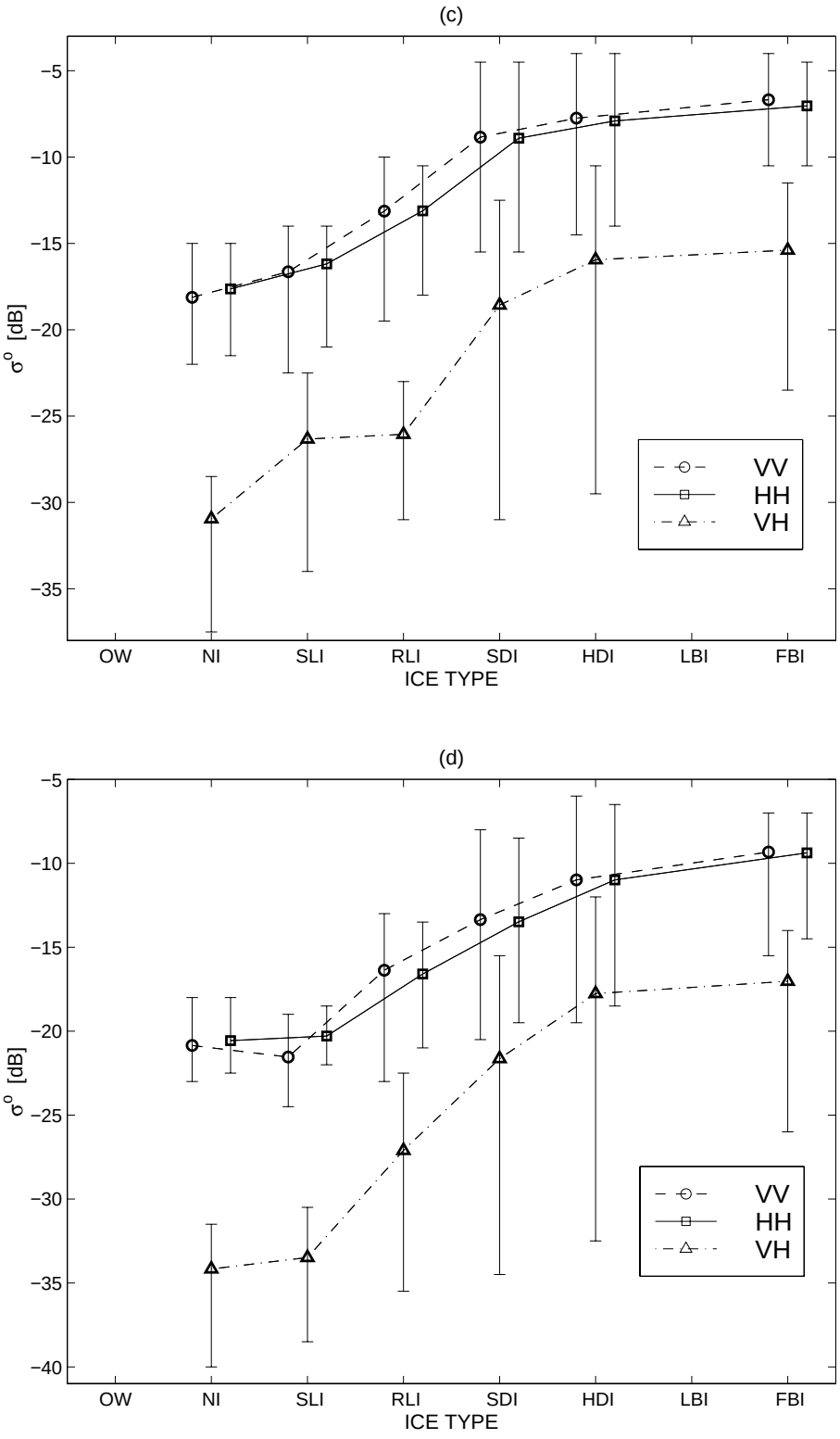

Figure 5.3 Continues.

to dry and moist snow conditions. At VH-polarization the 90% intervals under dry and moist snow conditions are typically larger than at co-polarizations.

The differences between the statistics of the VH- and co-polarized σ° are due to the different dominating scattering mechanisms and unequal σ° contrasts between LI and DI at these polarizations. The VH-polarized σ° is due to the multiple surface and volume scattering and co-polarized σ° mainly due to the single scattering events (Fung 1994).

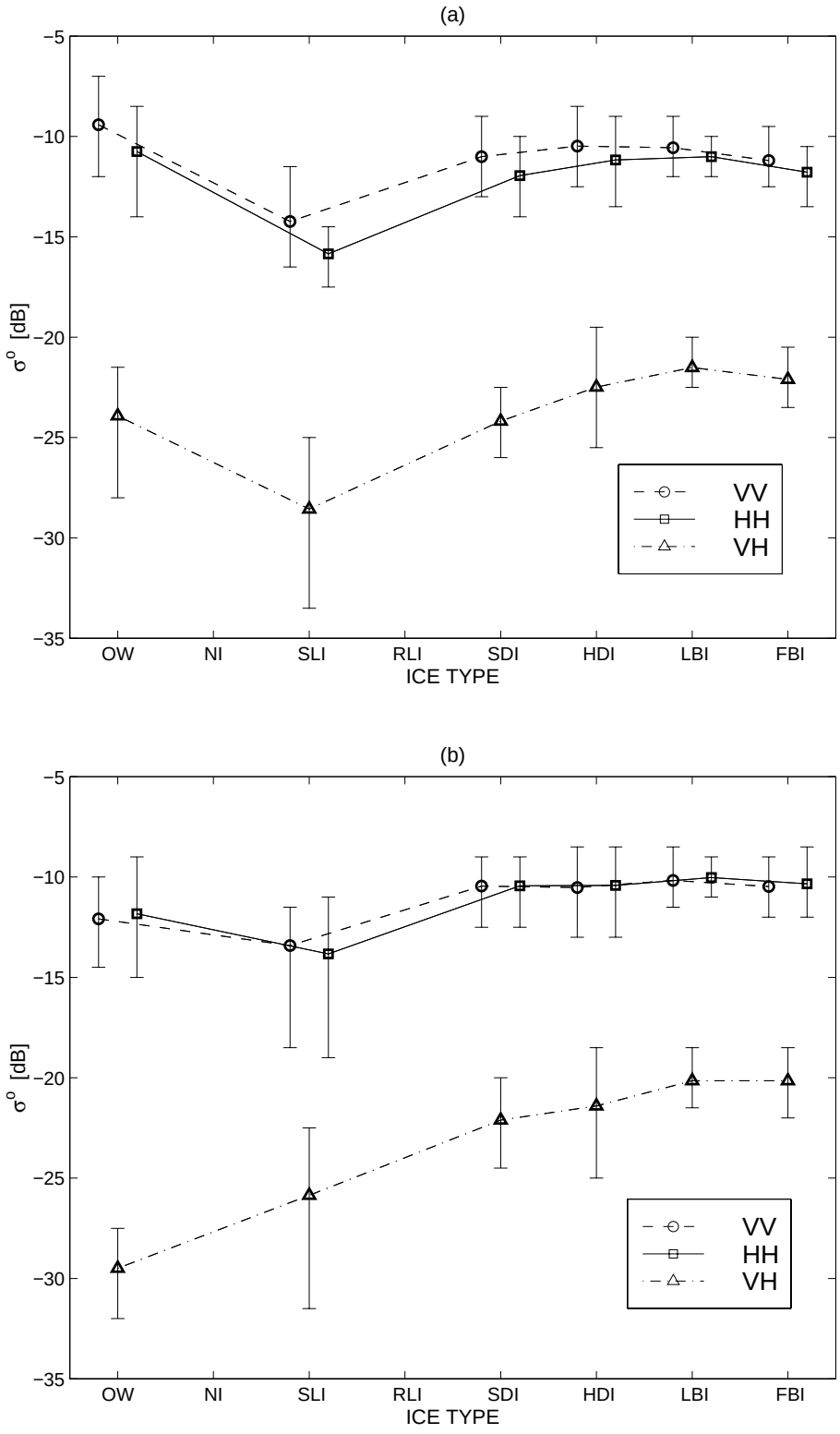

Figure 5.4 Mean and 90% confidence interval of σ° for various ice types using the PIPOR-92B wet snow data acquired on February 20, 1992. The data were averaged to a resolution of 25 m: (a) 5.4 GHz at an incidence angle of 23º and (b) 9.8 GHz at 23º. No data were acquired at an incidence angle of 45º.

5.3.2 Probability density function of σ°

Examples of the estimated pdf's for 5.4 GHz HH- and VH-polarized σ° under dry and moist snow condition are shown in Figures 5.5 and 5.6. The shapes of the pdf's at VV- and HH-polarization are typically very similar. For OW, NI, level ice and brash ice types the shapes of the pdf's are from close to the Gaussian pdf to very asymmetrical and irregular, depending on data set and channel. The pdf can also be asymmetrical, if the mean σ° is close to the HUTSCAT noise floor. Under dry and moist snow condition the shapes of the pdf's for SDI and HDI are both usually irregular but have different skewness. The pdf for SDI has usually longer upper than lower tail whereas for HDI the relation is opposite, because SDI has more low backscatter level ice areas than high backscatter deformed ice areas contrary to HDI. Under wet snow condition the pdf's are close the Gaussian pdf as wet snow reduces the contrast between level and deformed ice. The calculated pdf's are used in maximum likelihood classification experiments in Chapter 5.3.4.

5.3.3 Co- and cross-polarization ratios

R_{co} and R_{cr} for the IMSI-97 dry snow data are shown in Figure 5.7. The mean R_{co} for various ice types at 5.4 GHz and angle of 23º is mostly below 0 dB (min -2.0 dB), which likely indicates that the ice surface scattering dominates at C-band co-polarizations when θ_0 is small, as was suggested in (Carlström and Ulander 1995, Dierking et al. 1999). At 45º and at 9.8 GHz also mean R_{co} values above 0 dB for all ice types commonly exist. In some cases these cannot be explained by the effect of the radar noise floor, and theoretical modeling of R_{co} would be needed to find explanations. The range of the mean R_{co} values for all surface types is quite small, below 2 dB at 23º and below 4.5 dB at 45º.

The mean R_{cr} usually decreases with increasing ice deformation and is larger for OW than for various ice types. Deformed ice types with very rough surfaces and various kinds of large deformation features probably generate on average more multiple surface and volume scattering than NI and level ice types, yielding low R_{cr}. From 23º to 45º the mean R_{cr} mostly decreases because the θ_0 dependence of σ° is usually stronger at HH- than at VH-polarization. The range of the mean R_{cr} is always larger than that of the mean R_{co}. Usually the 90% interval of R_{cr} is the largest for NI and deformed ice types and the smallest for RLI, which generally follows the behavior of the 90% interval for σ°.

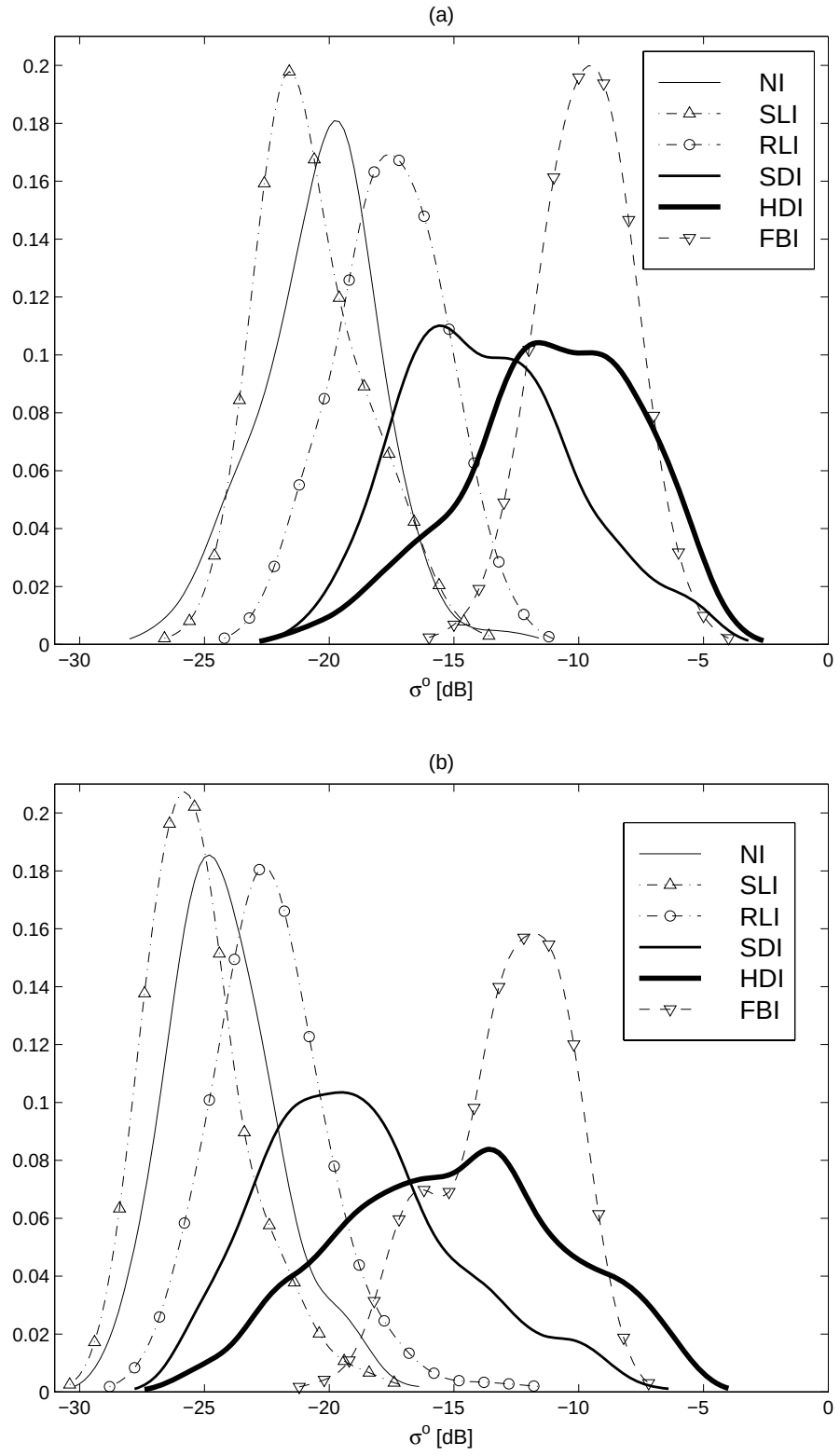

Figure 5.5 Probability density functions of 5.4 GHz HH- and VH- polarized σ° for various ice types using the IMSI-97 dry snow data. The data were averaged to a resolution of 25 m. HH-polarization at incidence angles of (a) 23º and (b) 45º. VH-polarization at (c) 23º and (d) 45º.

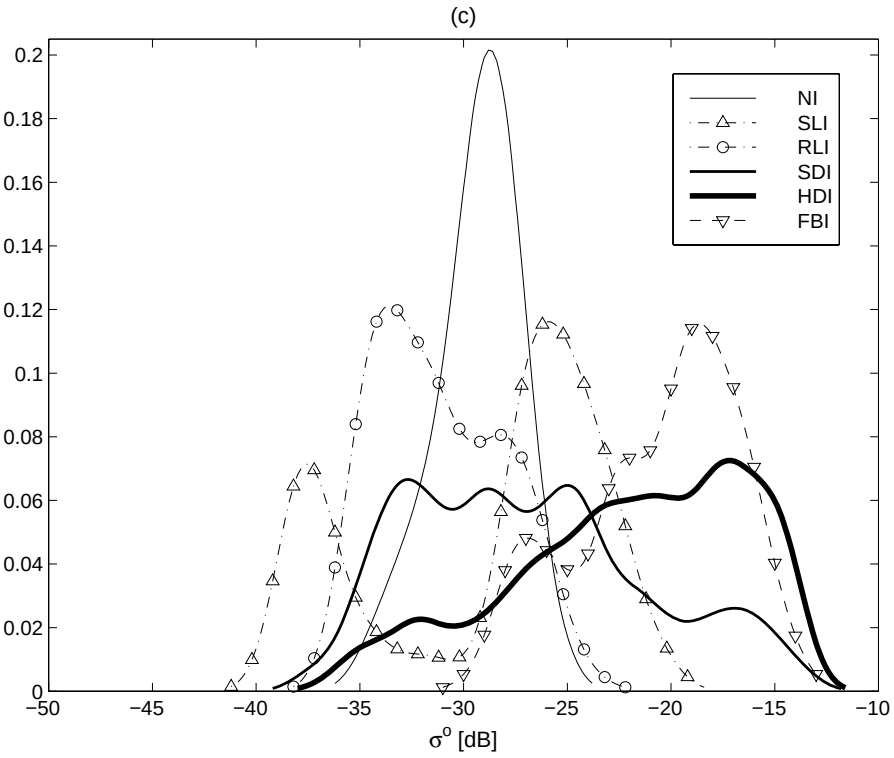

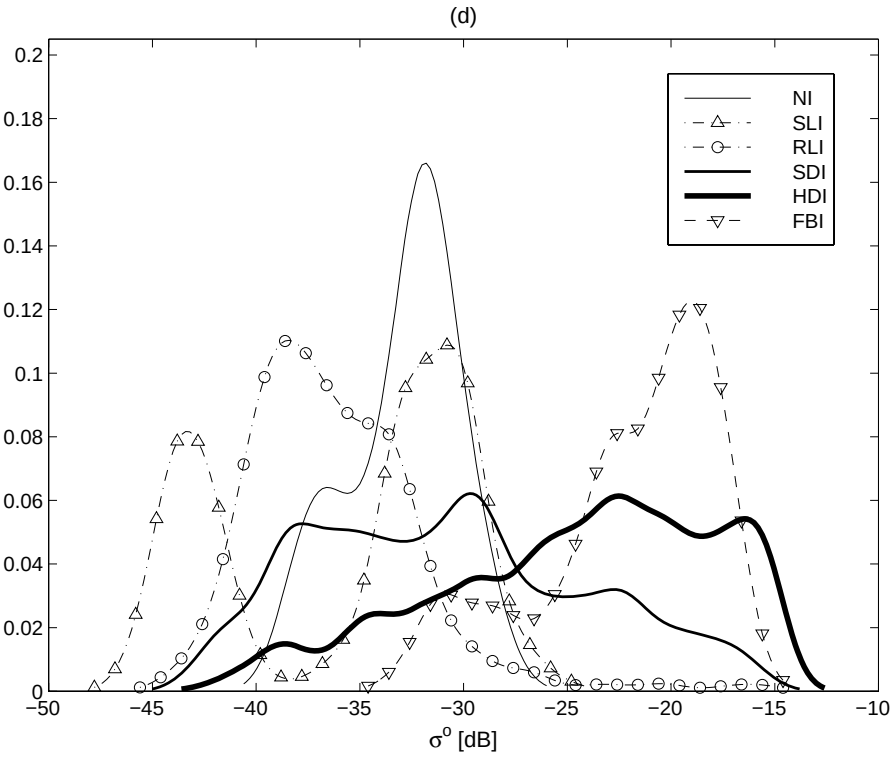

Figure 5.5 Continues.

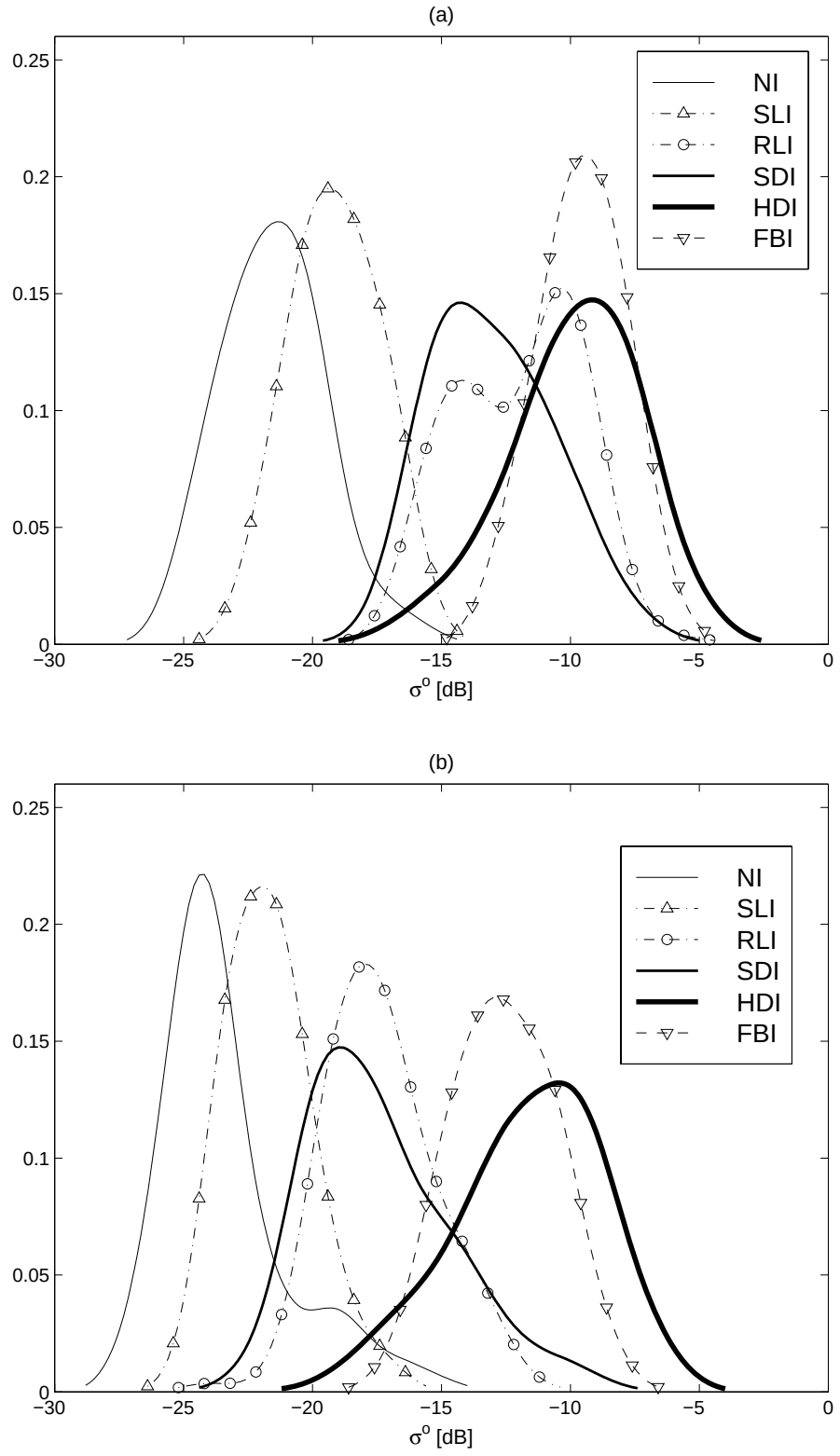

Figure 5.6 Probability density functions of 5.4 GHz HH- and VH- polarized σ° for various ice types using the EMAC-95 moist snow data. The data were averaged to a resolution of 25 m. HH-polarization at incidence angles of (a) 23º and (b) 45º. VH-polarization at (c) 23º and (d) 45º.

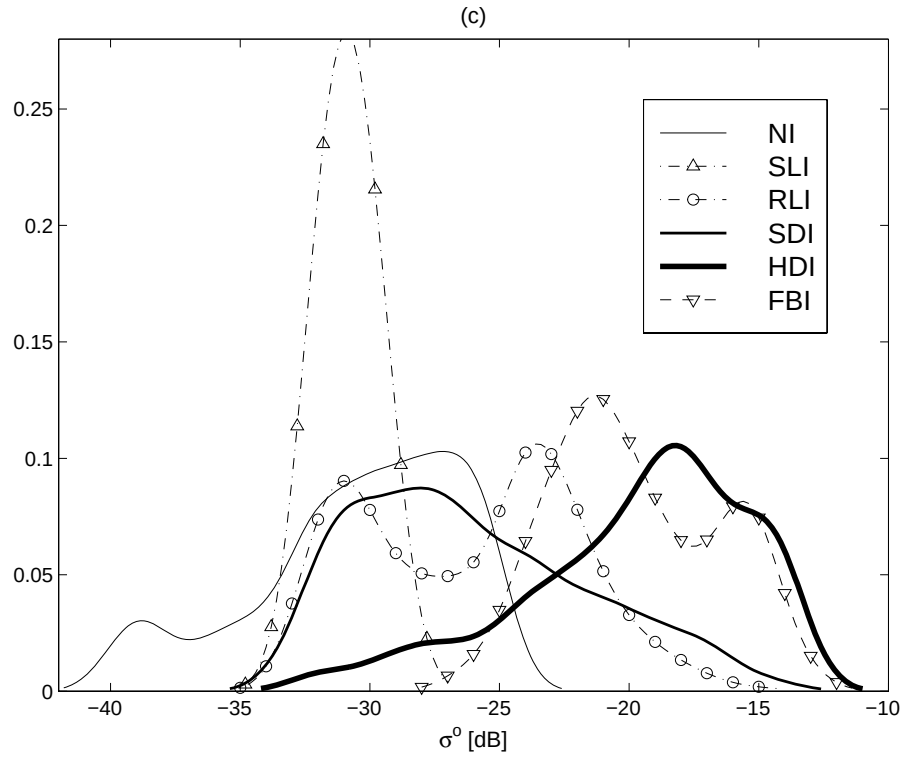

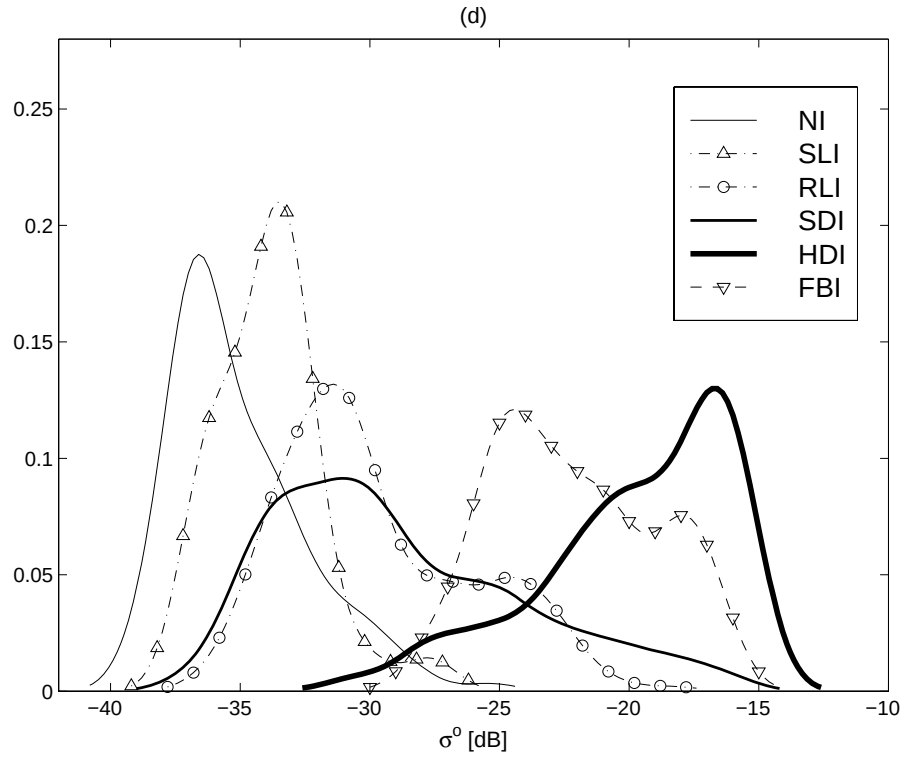

Figure 5.6 Continues.

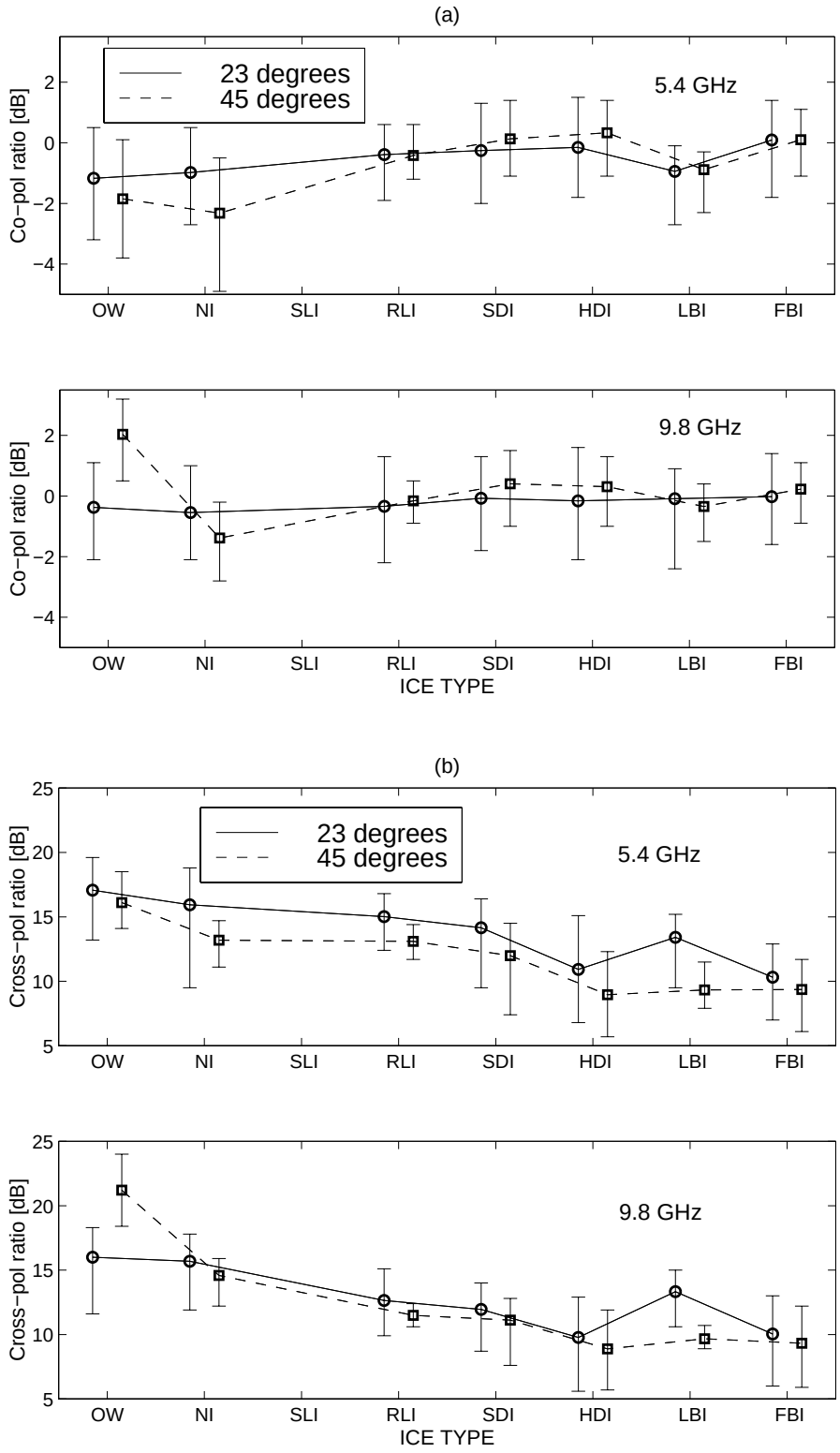

Figure 5.7 Mean and 90% confidence interval of (a) co- and (b) cross-polarization ratios for various ice types using OSIC-94 moist snow data acquired on March 26, 1994. The data were averaged to a resolution of 25 m.

5.3.4 Maximum likelihood classification of surface types

Before conducting maximum likelihood classifications, unsupervised principal component analysis was carried out in order to find out the number of main dimensions (dimensionality) for different multichannel combinations. Here the dimensionality is defined as the number of principal components that contain at least 90% of the variance of the dataset. According to the

results the dimensionality is usually one and at maximum two for various two- to six-dimensional combinations of the channels. The two-dimensional combinations of the channels can be further reduced to one-dimensional channel ratios. All wet snow data sets had to be excluded from the classifications due to the small data amount for most of the ice types. The same data were used for the classification and estimation of the pdf's.

The mean accuracy of the classification is in all cases quite poor, only between 0.17-0.68. For OW and all ice types the discrimination accuracy varies very much from one data set to another, even from 0.0 to 1.0 for some ice types. With all single channels, the mean classification accuracy is around 0.50 which indicates that there are no noticeable differences in the classification capability between co- and VH-polarized channels and frequencies 5.4 and 9.8 GHz. For R_{co} and R_{cr}, the mean accuracy is even lower. In summary, it is not possible to reliably distinguish various ice types and OW in C- and X-band SAR images only by an automatic intensity-based classification. However, only discrimination of NI and SLI from deformed and brash ice types would be useful for the SAR image interpretation, but the HUTSCAT data sets indicate that ice conditions under which these ice types are not discriminated are common. Discrimination of the surface types is further studied in the next Section using mean and std of σ°.

5.3.5 Mean and standard deviation

Mean and std of σ° for small data sets describe the local spatial variation of σ° (nine HUTSCAT σ° values corresponds those from a 3x3 window in a SAR image), and thus knowledge on their statistics is useful for SAR image classification studies. The mean std is usually the largest for deformed ice types and the smallest for either NI, SLI or FBI. At VH-polarization this difference between the ice types is larger than at co-polarizations. At HH- and VV-polarization both the mean standard deviations and the 90% intervals are roughly equal suggesting that at these polarizations the textural variations of σ° are on average equal. For deformed and brash ice types the mean std at VH-polarization is under dry and moist snow condition always larger than at co-polarizations, but under wet snow condition no consistent difference is present. The snow cover condition has a clear effect on the mean std for deformed ice types; they are the largest under dry snow condition and the smallest under wet snow condition. The observed properties of the mean and the 90% interval of std can be explained similarly as in the case of the 90% interval of σ°. Due to the small range of mean std values and large 90% intervals, std does not discriminate unambiguously any surface type. The discrimination results are worse than those with mere σ°.

Mean and std of σ° were used together to investigate discrimination of surface types. The discriminations between the surface types were evaluated visually using 90% confidence ellipses calculated with the principal component analysis for all dry snow and for all moist snow data sets separately, see Figure 5.8. Visual inspection indicates that it is possible at all polarizations to set a cut-off level for mean σ° below which the surface type is either OW, NI or SLI. Another cut-off level can be set to discriminate FBI and DI from other ice types. An area of high mean and std of σ° corresponds SDI or HDI. This works better at VH- than at co-polarizations. At 45º the ellipses are typically slightly more separated from each other than at 23º, but the difference between 5.4 and 9.8 GHz is small. Generally, the derivation of a coarse classification table based on the mean and std seems to be possible, but its usefulness in SAR image classification is likely quite poor.

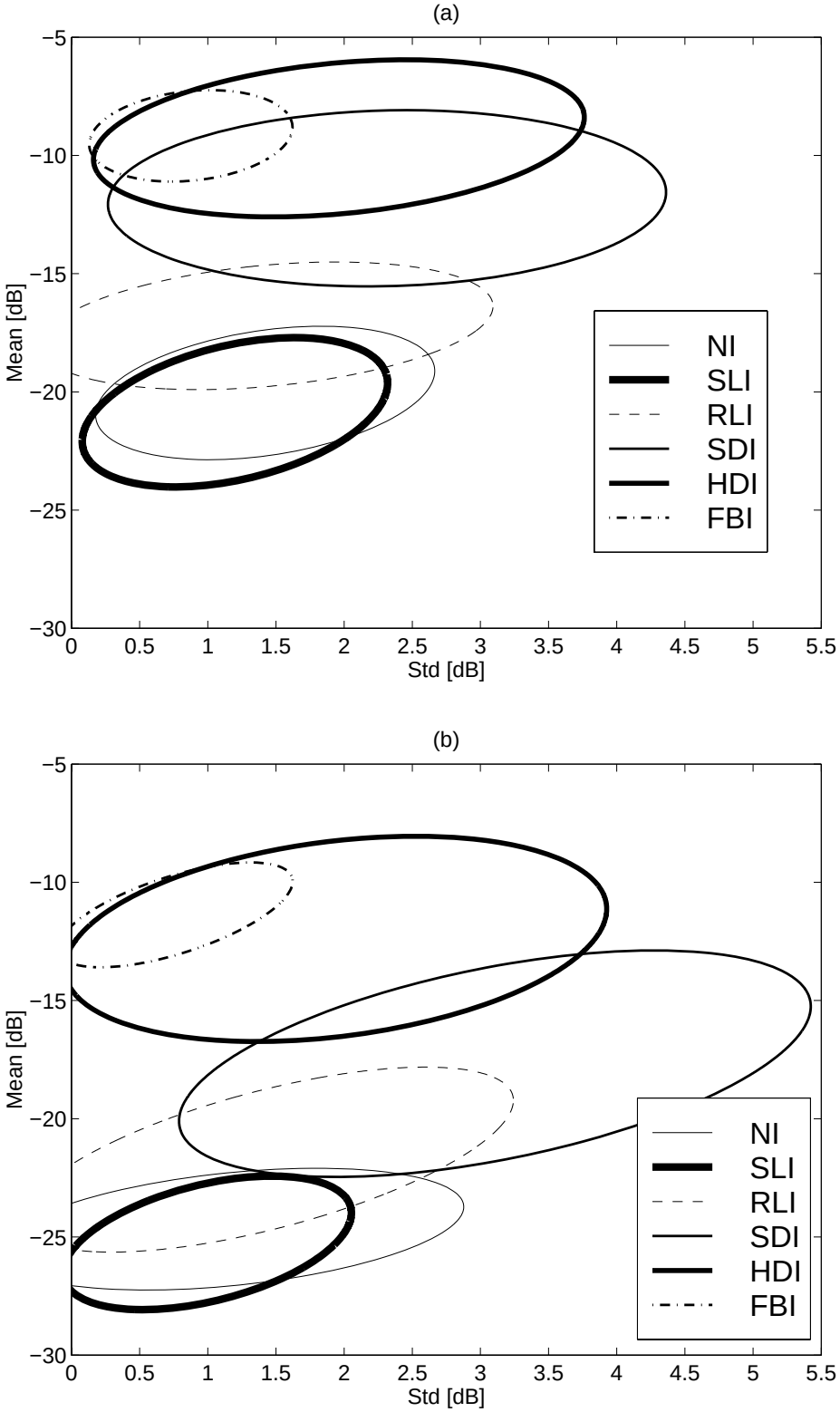

Figure 5.8 Mean and standard deviation of nine 5.4 GHz HH- and VH-polarized σ° for various surface types using all dry snow data sets averaged to a resolution of 25 m. HH-polarization at incidence angles of (a) 23º and (b) 45º. VH-polarization at (c) 23º and (d) 45º. The ellipses represent 90% confidence limits.

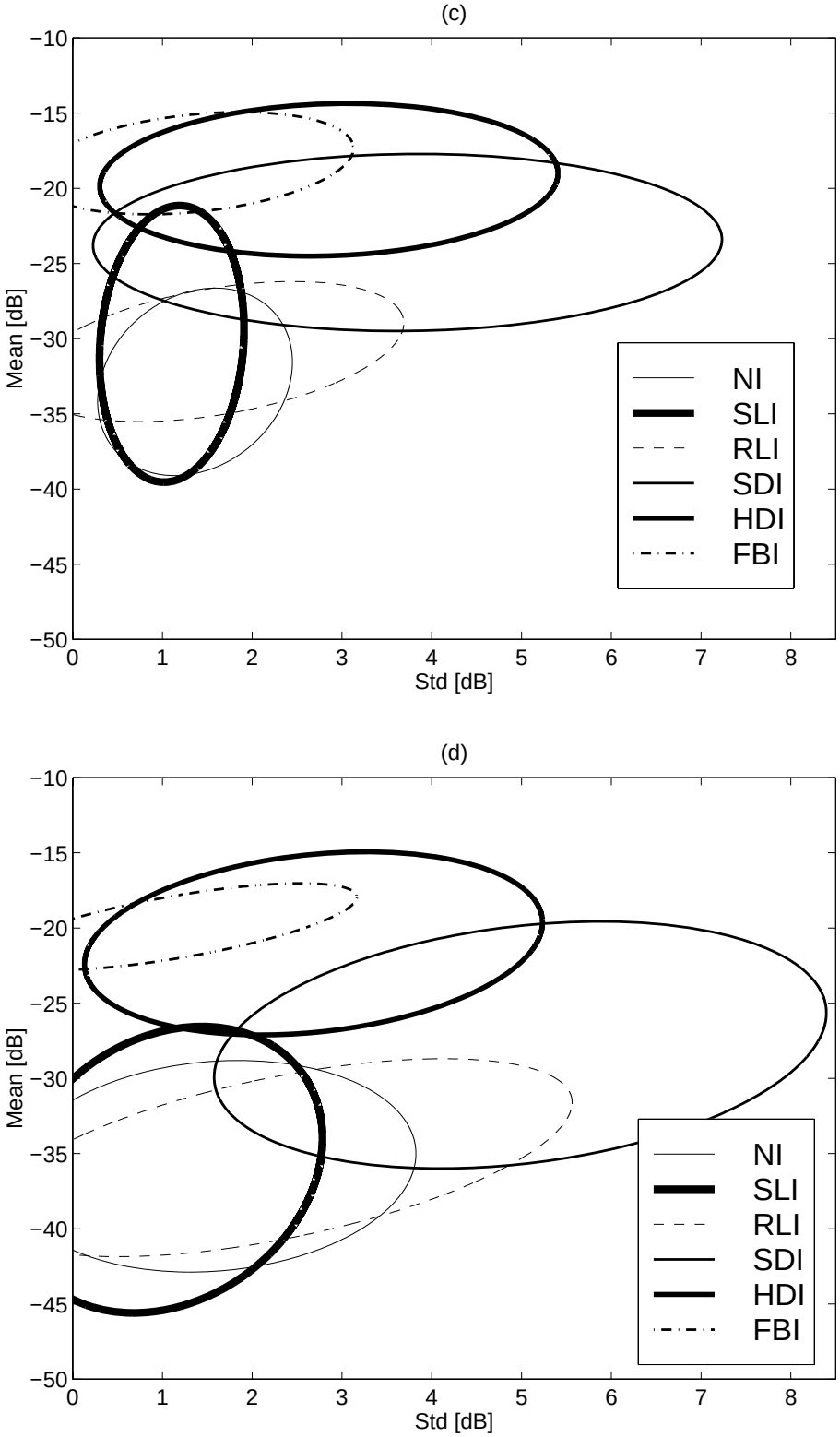

Figure 5.8 Continues.

5.3.6 Backscattering contrast between ice deformations and level ice

The large scatter of σ° values for SDI and HDI suggests that ice deformations and level ice areas in a deformed ice field have highly distinct levels of σ°. To study if this is the case, two 1000 m long test lines of highly deformed ice measured under dry and wet snow conditions are plotted in Figures 5.9 and 5.10. The data for the test lines were averaged to the 12.5 m resolution. The figures show that the average contrast between level and deformed ice areas is

the highest for VH-polarization and practically non-existent for R_{co}. The contrasts are noticeably larger for the dry snow than for the wet snow test line which is due to the radar wave attenuation in wet snow. The frequency dependence of the contrast is noticeable only in the dry snow test line at VH- and co-polarizations; the contrast is 2 to 5 dB higher at 5.4 than at 9.8 GHz. This is likely due to stronger volume scattering at 9.8 GHz. When the incidence angle increases from 23º to 45º only the contrast at 5.4 GHz VH-polarization for the dry snow test line clearly increases (about 3 dB). However, at 45º the co-polarized σ° values for level ice areas are increased by the HUTSCAT noise floor. Generally, the 5.4 GHz VH-polarized σ° at 45º is the best variable to discriminate level and deformed ice areas in a deformed ice field.

The small average value of R_{cr} for deformed ice areas suggests that multiple surface and/or volume scattering is considerable in various kinds of deformation features. Carlström and Ulander (1995) suggested that the main scattering mechanism at C-band VV-polarization in ice ridges is specular reflections from the major facets of the ice blocks, whereas Manninen (1992, 1996b) suggested that it is the incoherent surface scattering from ice blocks at both co- and cross-polarization. The results here suggest that Manninen's conclusion is the right one as low R_{cr} is (likely) not possible when specular reflections are dominating at co-polarizations.

The high contrast between level ice and ice deformations at VH-polarization may indicate a possibility to discriminate them in fine resolution VH-polarized SAR images (resolution from 5 to 10-20 m). At coarser resolutions (e.g. 100 m) it may be possible to relate the magnitude of the VH-polarized σ° to the degree of ice deformation. The development of a such model would require some quantitative information on ice deformation (e.g. laser profiling of ice surface).

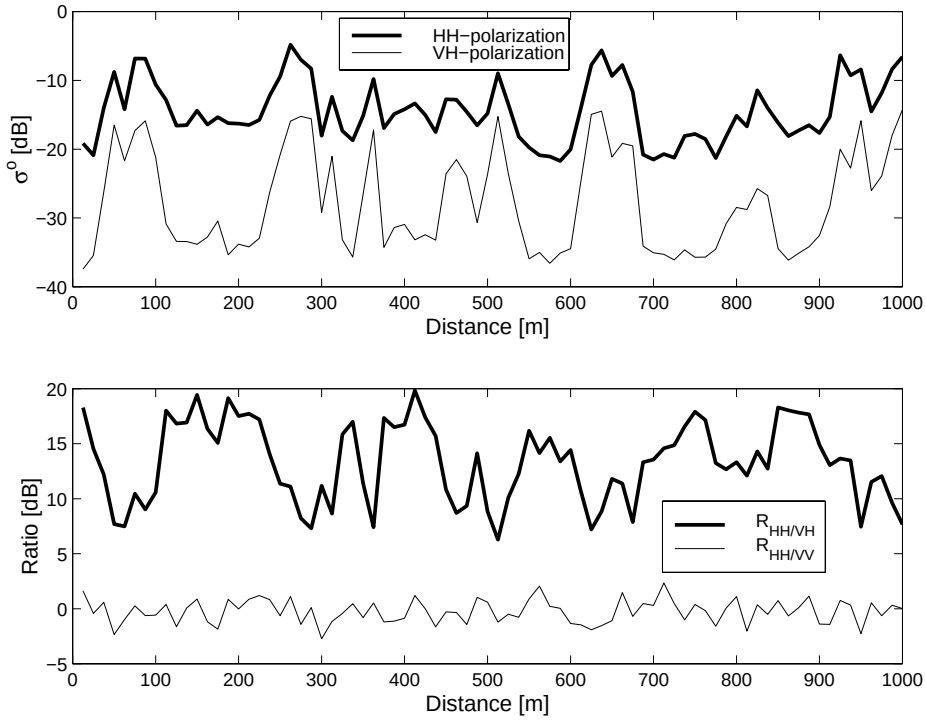

Figure 5.9 5.4 GHz HH- and VH-polarized σ°, R_{co} and R_{cr} as a function of distance for a highly deformed ice test line of the IMSI-97 dry snow/ice data. The data were averaged to a resolution of 12.5 m. The incidence angle is 23º.

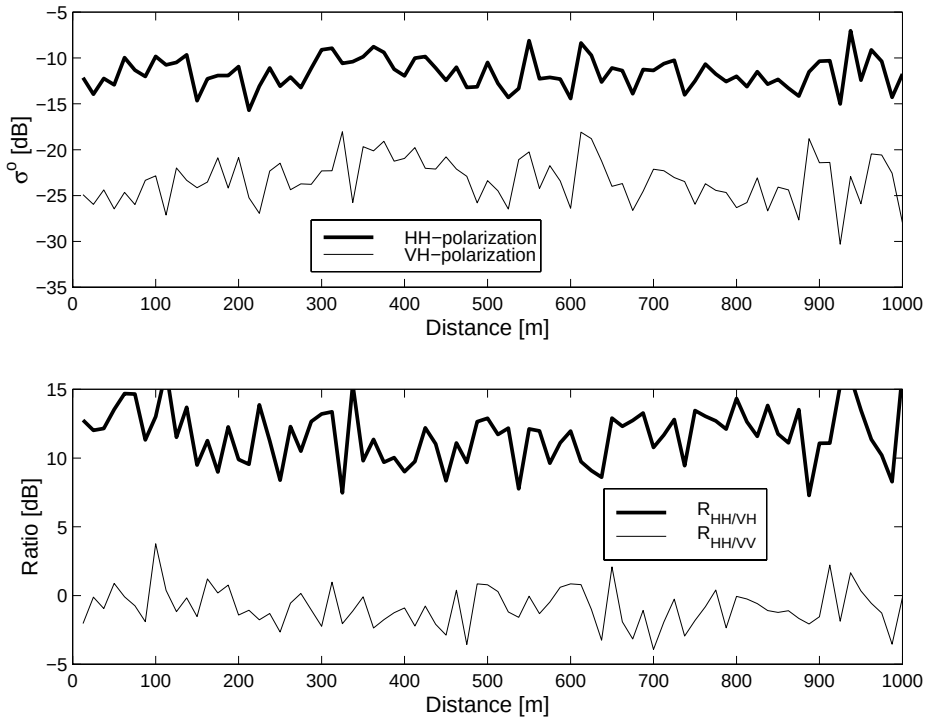

Figure 5.10 5.4 GHz HH- and VH-polarized $\sigma°$, R_{co} and R_{cr} as a function of distance for a highly deformed ice test line of the OSIC-94 wet snow data acquired on March 23, 1994. The data were averaged to a resolution of 12.5 m. The incidence angle is 23º.

5.3.7 Comparison with previous results

Generally, the HUTSCAT results for the behavior of the mean and standard deviation of $\sigma°$ as a function of e.g. ice deformation agree with the previous studies. However, here std of $\sigma°$ is on average equal at HH- and VV-polarization, but this was not case in (Dierking et al. 1997) where s_T at HH-polarization was typically somewhat larger. This disagreement is likely due to different spatial resolutions; 25 m here and around 4.5 m in (Dierking et al. 1997), and data amounts. The main disagreements are related to the surface type discrimination. According to (Hyyppä and Hallikainen 1992, Hallikainen and Toikka 1992) X-band provides slightly better classification results than C-band. Here the automatic classification results at C- and X-band were roughly equal. Dammert et al. (1994) reported that even seven ice type classes can have more or less separated signatures in the mean $\sigma°$ vs. s_T space under dry snow condition, but here this is not the case under any snow wetness condition. These disagreements may partly be due to the differences in the definitions of the ice type classes. Small amounts of data in most of the previous studies may also have reflected in the results. Additionally, Dammert et al. (1994) used much larger areas than here to calculate the mean $\sigma°$ and s_T which likely diminished the local large variation of $\sigma°$ leading to clearly separated ice type signatures.

5.3.8 Summary

For the SAR image classification studies, the HUTSCAT results can be summarized as:

(1) It is not possible to reliably discriminate open water and various ice types in C- and X-band SAR images only by their level of σ°, R_{co} or R_{cr}. Very likely just visual interpretation of SAR images gives better results than automatic intensity-based classification.

(2) Using a large number of SAR images it is possible to derive a coarse classification table based on the mean and standard deviation of σ° for small windows, but its usefulness for SAR image classification is likely poor, because the signatures for various ice types are usually close to each other.

(3) The high σ° contrast at VH-polarization under dry snow condition between level and deformed ice areas in a deformed ice field suggests a possibility to discriminate them in fine resolution SAR images (resolution < 10-20 m). At coarser resolutions it may be possible to relate the magnitude of VH-polarized σ° to the degree of ice deformation.

(4) Snow wetness has a large effect on the σ° statistics. Notably, when snow cover is wet then the σ° contrasts between various ice types are smaller than in dry snow case.

(5) The following combination of the radar parameters: C-band, VH-polarization and an incidence angle of 45º, provides slightly better ice type discrimination accuracy than any other combination.

5.4 L- and C- Band Polarimetric Discriminants

Artic Sea ice classification studies with airborne and Space Shuttle SIR-C polarimetric SAR data have clearly indicated that better ice type classification is possible with polarimetric data than with only single channel data, e.g. (Scheuchl et al. 2004). RADARSAT-2 to be launched in 2007 will provide C-band polarimetric data over narrow 25 km wide swaths. These data are not suitable for operational monitoring of the Baltic Sea ice, but they will allow thorough investigation of the backscattering signatures and mechanisms of various ice types. In order to fully utilize the forthcoming spaceborne polarimetric data, it is good to conduct preliminary studies with airborne data.

Polarimetric discriminants for various ice types were investigated in [P2] using one L-band and one C-and EMISAR image. The L-band image was acquired when snow cover was dry, whereas at the time of the C-band acquisition the snow cover was somewhat moist. The image data were in the slant-range scattering matrix format. In [P2] also the polarimetric discriminants for the Baltic Sea and Artic Sea ice types were compared to each other and image classification experiments were conducted, but they are not discussed here. Exactly the same images were studied in (Dierking and Askne 1998), but there the data were in the multi-looked covariance matrix format.

The statistics of the following polarimetric discriminants: co-polarization correlation coefficient ρ_{co}, co- and cross- polarization ratios R_{co} and R_{cr}, phase difference ϕ_{HH-VV} and coefficient of variation γ, were calculated by extracting 27 large windows from the images. Each window was divided into subsets of 40 by 40 pixels (60 by 60 m), denoted as coarse pixels which simulated pixel size of possible spaceborne wide swath polarimetric data. For each coarse pixel averages of the polarimetric discriminants were computed. The large windows represented one of the following ice types: NI (4 coarse pixels), LI (200), SDI (89) and HDI (152).

At C-band the mean R_{co} is mostly smaller than one; from 0.32 for NI to 1.04 for HDI, whereas at L-band it is larger than one; from 1.00 to 1.27. R_{co} decreases with increasing θ_0 at C-band, but at L-band there is slight increase. The C-band observations are consistent with a theoretical backscattering model for ice surface scattering. The explanation for L-band R_{co} values over one is currently uncertain. The average R_{cr} increases with increasing ice deformation at C-band (from 5.9 to 10.5), but at L-band it decreases (from 8.9 to 4.9). The C-band behavior is contrary to the C-band HUTSCAT results in [P1]. The low C-band R_{cr} values for NI and LI could be due to the influence of the EMISAR noise floor.

The mean γ is smaller at C- (from 0.08 to 0.20) than at L-band (from 0.23 to 0.42). The larger γ is, more there is multiple scattering or heterogeneity in the scattering mechanism within the target. The wavelength at L-band is so large (24 cm) that strong multiple scattering within the ice volume is unlikely. Possible sources for multiple scattering are ice surface and/or ice-water interface (when rough), ice floe edges and ice ridges. Further work is needed to find out the exact sources.

The mean ϕ_{HH-VV} at C-band is very close to 0º, but at L-band it is clearly negative for NI and LI (-29º and -23º) and slightly negative for deformed ice types (max -9.5º). If the surface is lossy, ϕ_{HH-VV} is negative with increasing negative difference with increasing θ_0 (Drinkwater et al. 1992). However, realistic values of ε_r for sea ice cannot explain the observed values for NI and LI at L-band. Large values of ϕ_{HH-VV} are caused by the interference between up- and down-going waves in the ice layer resulting from scattering at the air-ice and ice-water boundaries (Winebrenner et al. 1995). ϕ_{HH-VV} oscillates as a function of ice thickness with a mean value of 0º. Also R_{co} oscillates as a function of thickness and is always below unity, which is contradictory to the observed values.

The mean L-band ρ_{co} is quite low and variable within the ice types (from 0.28 to 0.67). At C-band mean ρ_{co} is roughly equal for all ice types (from 0.72 to 0.80). Low L-band values cannot be explained by dominating surface scattering. In the presence of volume scattering, ρ_{co} is low due to the ellipsoidal scatterers or preferential orientation of scatterers (anisotropy) (Nghiem et al. 1995). Occurrence of strong volume scattering at L-band within the ice layer is not likely. When the penetration depth is larger than thickness (i.e. the interference effect is present) varying ice thickness within sample area produces ρ_{co} values significantly less than one (Winebrenner et al. 1995). In theory, the smaller ρ_{co} is, the greater the variance of ϕ_{HH-VV} and the larger γ becomes. The L-band observations follow this behavior to some degree.

The observations for R_{co} are roughly equal in (Dierking and Askne 1998) and [P2]. This is also the case for ϕ_{HH-VV} with the exception that at L-band there is sign difference in level ice ϕ_{HH-VV} values. For level ice the dominant scattering mechanism at C-band is very likely the ice top surface scattering as was the case in (Carlström and Ulander 1995) and (Dierking et al. 1999). At L-band the scattering process seems to be more complicated: (1) If double-bounce scattering is dominating then $R_{co} = \sigma^{o}_{HH} / \sigma^{o}_{VV}$ is over one as observed, but then ϕ_{HH-VV} and ρ_{co} should be very large, and this was not the case. (2) The interference effect resulting from scattering at the air-ice and ice-water boundaries can produce quite large ϕ_{HH-VV} and low ρ_{co} as observed here, but R_{co} is always less than one, which was not the case. (3) Coherent

scattering also produces R_{co} values over one, but then ρ_{co} should be very large. In conclusion, further work in needed to find out the dominating scattering mechanisms at L-band in this data set.

5.5 Incidence Angle Dependence of C-band HH-polarization σ°

For operational monitoring of the Baltic Sea ice RADARSAT-1 ScanSAR Wide and ENVISAT Wide Swath images at HH-polarization are currently used. Both images have large incidence angle (θ_0) range, RADARSAT-1 from 20º to 49º and ENVISAT from 16º to 43º. Successful implementation of the SAR classification algorithms is complicated due to this large θ_0 variation which causes significant changes in σ° level and contrast. To quantify and to allow compensation, at least partly, the θ_0 dependence of three statistical parameters: the mean σ°, standard deviation and autocorrelation coefficient of texture (s_T and ρ_T) (Rignot and Kwok 1993), of the C-band HH-polarized σ° signatures were investigated in [P3] using RADARSAT ScanSAR Narrow image pairs. During the time of this study these images were used for operational sea ice monitoring. These images have a θ_0 range either from 19º to 39º (SNA type image) or 30º to 46º (SNB). HUTSCAT data were also used to study the θ_0 dependence of the mean σ°. The main reason for using the HUTSCAT data was its good classification to a total of seven different ice types using video imagery, whereas it was feasible to classify the RADARSAT-1 data only to two ice types, and thus the HUTSCAT results present a good comparison dataset for the RADARSAT-1 ones.

The dependence between the mean σ° and θ_0 in the HUTSCAT data was derived from the difference between the mean σ° dB-values at angles of 23º and 45º divided by the angle difference of 22 degrees, i.e. the dependence was assumed to be linear in dB-scale and described by a slope in dB/1º units. The results are in Table 5.6. The mean slope values were also derived for all ice types except for NI as for it the mean slope did not seem to be meaningful. The results show that the slope depends on the ice type and has quite large variation for each ice type caused by variable ice conditions in the data sets. The average slope is the smallest (from -0.10 to -0.19 dB/1°) for HDI and FBI and the largest (from -0.20 to -0.31 dB/1°) for SLI and RLI. The small average slope FBI and HDI is very likely due to their large surface roughness (Manninen 1997a) and more varying local incidence angles. Theoretically (IEM σ° model (Fung 1994)) the slope decreases with increasing surface roughness. The data amount is too small to reliably determine the dependence between the average slope and snow condition, but it is possibly the largest one under wet snow condition.

From the RADARSAT-1 ScanSAR image pairs, windows of size 1.1 by 1.1 km (11 by 11 pixels) representing either LI or DI in fast ice areas of the Bay of Bothnia were visually selected. Windows were not selected over NI; although it can be stationary between the image acquisitions, its thickness and surface characteristics may change considerably during that time. The chosen size of the window was a compromise between the requirement of a large window for accurate calculation of the statistical parameters and a small window for keeping the ice area within the window as homogeneous as possible. The windows of an image pair provides θ_0 difference ($\Delta\theta_0$) and σ° difference ($\Delta\sigma^\circ$) pairs from exactly the same areas. Within one image pair the range of the $\Delta\theta_0$ values varies from 11 to 30 degrees. The azimuthal viewing angle difference between the windows is around 140 degrees. The number of selected windows (n) in one image pair for each ice type varies from 118 to 1359, and the average is around 470.

Table 5.6 The slope of the incidence angle dependence (dB/1°) of the mean 5.4 GHz HH-polarized σ°'s of the various Baltic Sea ice types using the HUTSCAT data sets acquired at incidence angles of 23 and 45 degrees.

Data Set	Snow Class	NI	SLI	RLI	SDI	HDI	LBI	FBI
21 Mar 1992	Dry					-0.13		-0.06
21 Mar 1997	Dry	-0.17	-0.18	-0.19	-0.22	-0.14		
23 Mar 1997	Dry		-0.21	-0.23	-0.17	-0.18		-0.14
Mean	Dry	-	-0.20	-0.21	-0.20	-0.15		-0.10
12 Mar 1992	Moist				-0.10	-0.14		
26 Mar 1994	Moist	-0.21		-0.22	-0.18	-0.11		-0.14
4 Apr 1995	Moist			-0.21	-0.21	-0.06		
6 Apr 1995	Moist	-0.07	-0.12	-0.19	-0.14	-0.08		-0.13
Mean	Moist	-	-	-0.21	-0.16	-0.10		-0.14
10 Feb 1992	Wet		-0.28		-0.17	-0.16		-0.15
23 Mar 1994	Wet		-0.33		-0.27	-0.22	-0.16	
Mean	Wet	-	-0.31	-	-0.22	-0.19	-	-0.15

As the scatter plots of $\Delta\sigma^\circ$ vs. $\Delta\theta$ indicated in most cases a very linear relationship between $\Delta\sigma^\circ$ and $\Delta\theta$ for both ice types, the following linear regression model was assumed:

$$\Delta\sigma^\circ \sim N\left(b_0 + b_1\Delta\theta_0, \sigma^2\right). \tag{5.2}$$

This model provided much better coefficients of determination (r^2) than using only windows of a single SAR image, i.e. the linear regression of the mean σ° on θ_0. This is demonstrated in Figure 5.11. The better accuracy can be explained by the fact that mean σ° values at different incidence angles from exactly the same areas were used for the model fitting.

The mean $\Delta\sigma^\circ$ vs. $\Delta\theta_0$ for level ice and deformed ice under dry snow condition is shown in Figures 5.12 and 5.13 using data sets yielding the best and the worst r^2. A summary of the results using 21 image pairs for dry snow and 7 pairs for wet snow condition is presented in Table 5.7. The contribution of the fading to the results is very small as the std of mean σ° is below 0.16 dB.

The RADARSAT-1 derived average slopes under dry snow condition are very close to HUTSCAT ones, but under wet snow condition they are somewhat larger. However, more HUTSCAT wet snow data would be needed to verify the difference. The RADARSAT-1 results also show correlation between the slope of the linear σ° incidence angle dependence and the ice type. Under both dry snow and wet snow condition the average slope is larger for LI than for DI which is in agreement with the HUTSCAT results. Thus, the contrast between LI and DI increases with increasing θ_0. The average slope is somewhat larger under wet snow than under dry snow condition. When snow cover is wet the dominant scattering source is the snow top surface which is usually smoother than the ice surface (Manninen 1997a). The dielectric constant ε_r of the scattering surface also has an effect on the σ° incidence angle dependence (Fung 1994). For wet snow the imaginary part of ε_r (ε_r'') is larger than for low salinity dry ice surface. The smoother the surface or the larger ε_r'', the more rapidly σ° drops off with increasing θ_0 (Fung 1994).

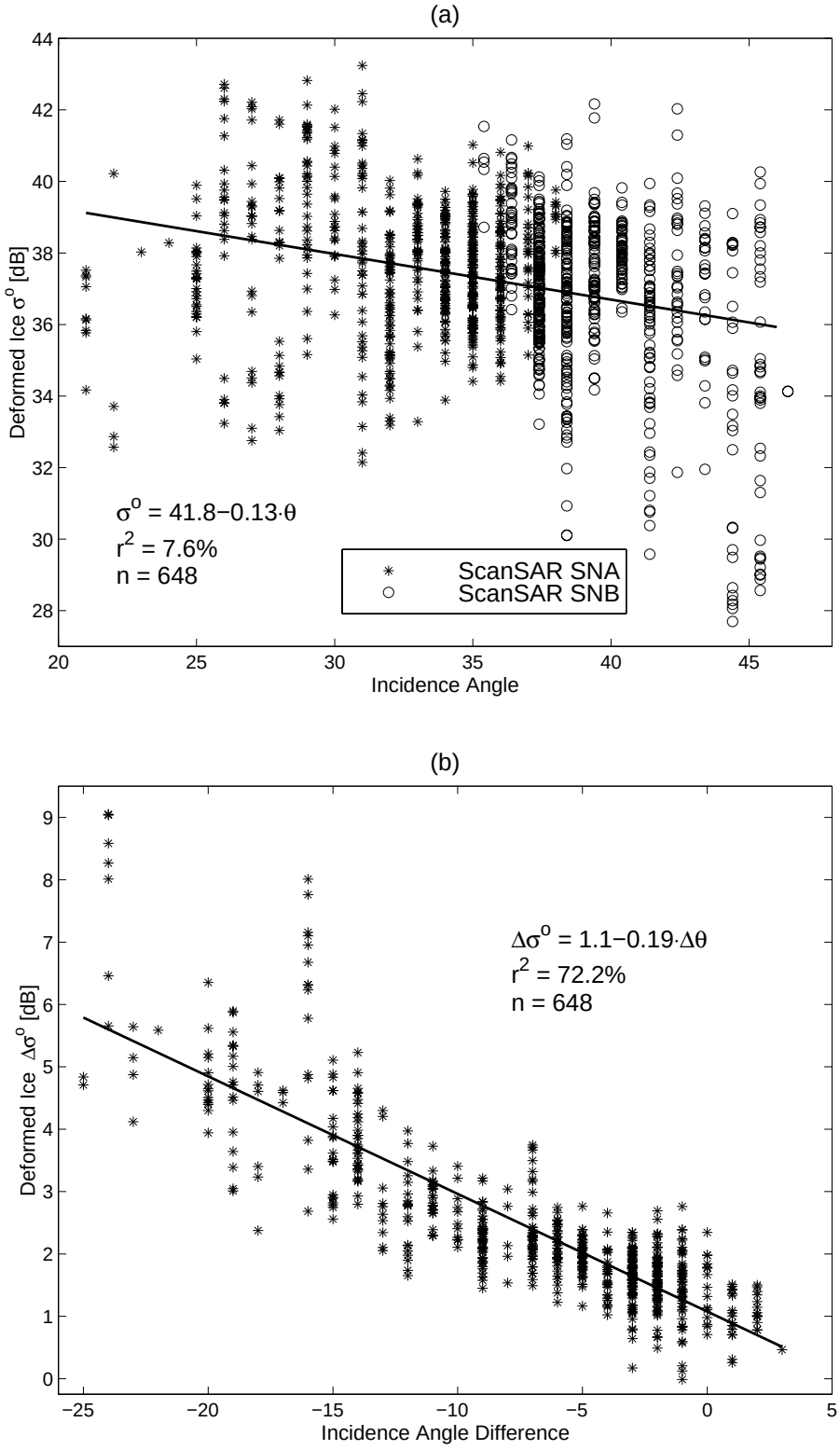

Figure 5.11 (a) Observed mean σ° vs. θ_0 and (b) mean $\Delta\sigma^\circ$ vs. $\Delta\theta_0$ for deformed ice using 11 by 11 pixel windows selected from SNB and SNA RADARSAT images acquired on February 22 and 23, 2000, respectively, under dry snow condition. The dB-scale in (a) is arbitrary. The relative calibration difference between the SNA and SNB images is compensated in (a).

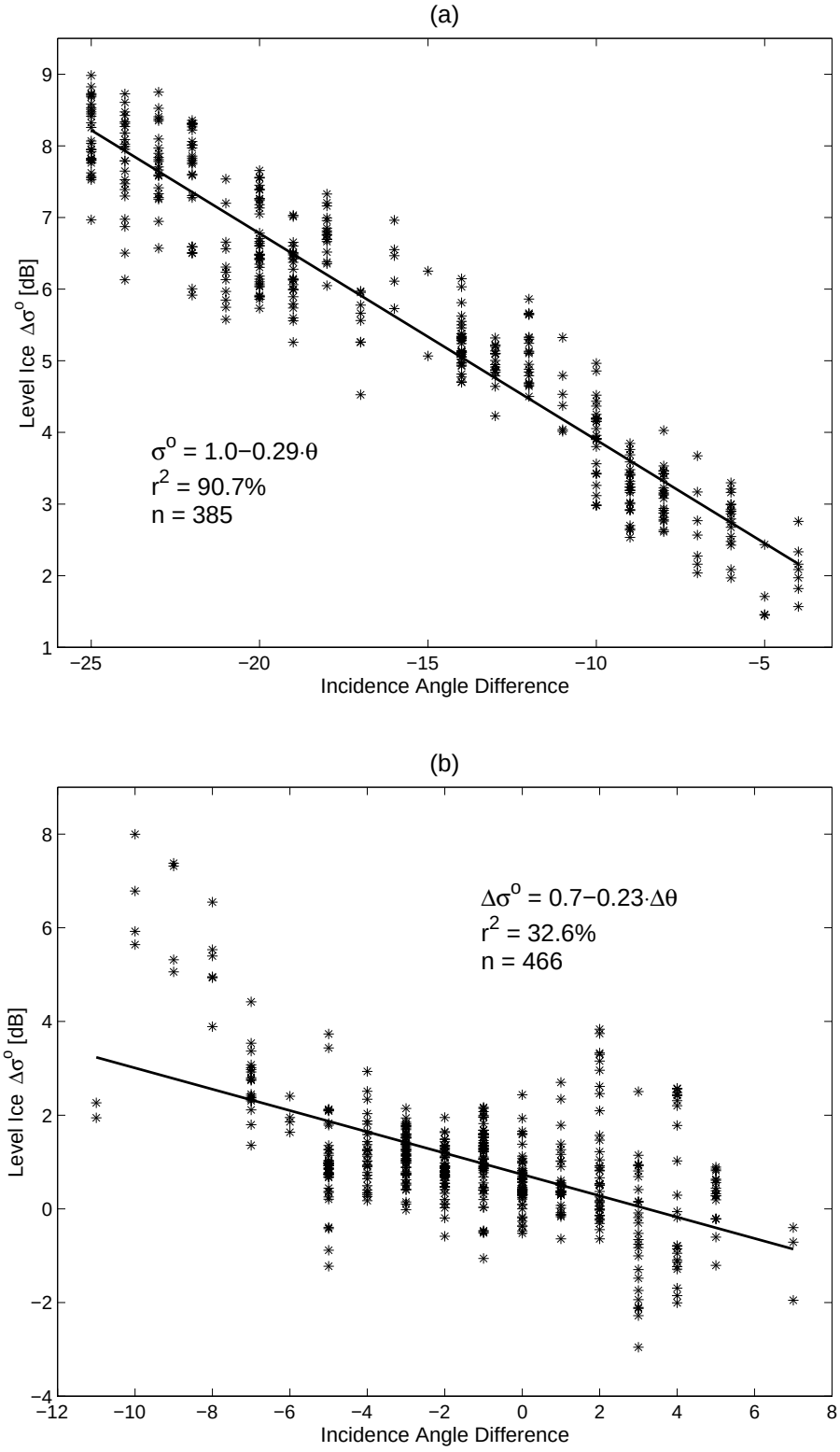

Figure 5.12 Observed mean $\Delta\sigma^\circ$ vs. $\Delta\theta$ for level ice under dry snow condition. (a) The best coefficient of determination (90.7%) using the RADARSAT image pair acquired on March 8 and 10, 1998. (b) The worst coefficient of determination (32.6%) using the RADARSAT image pair acquired on February 6 and 7, 1999.

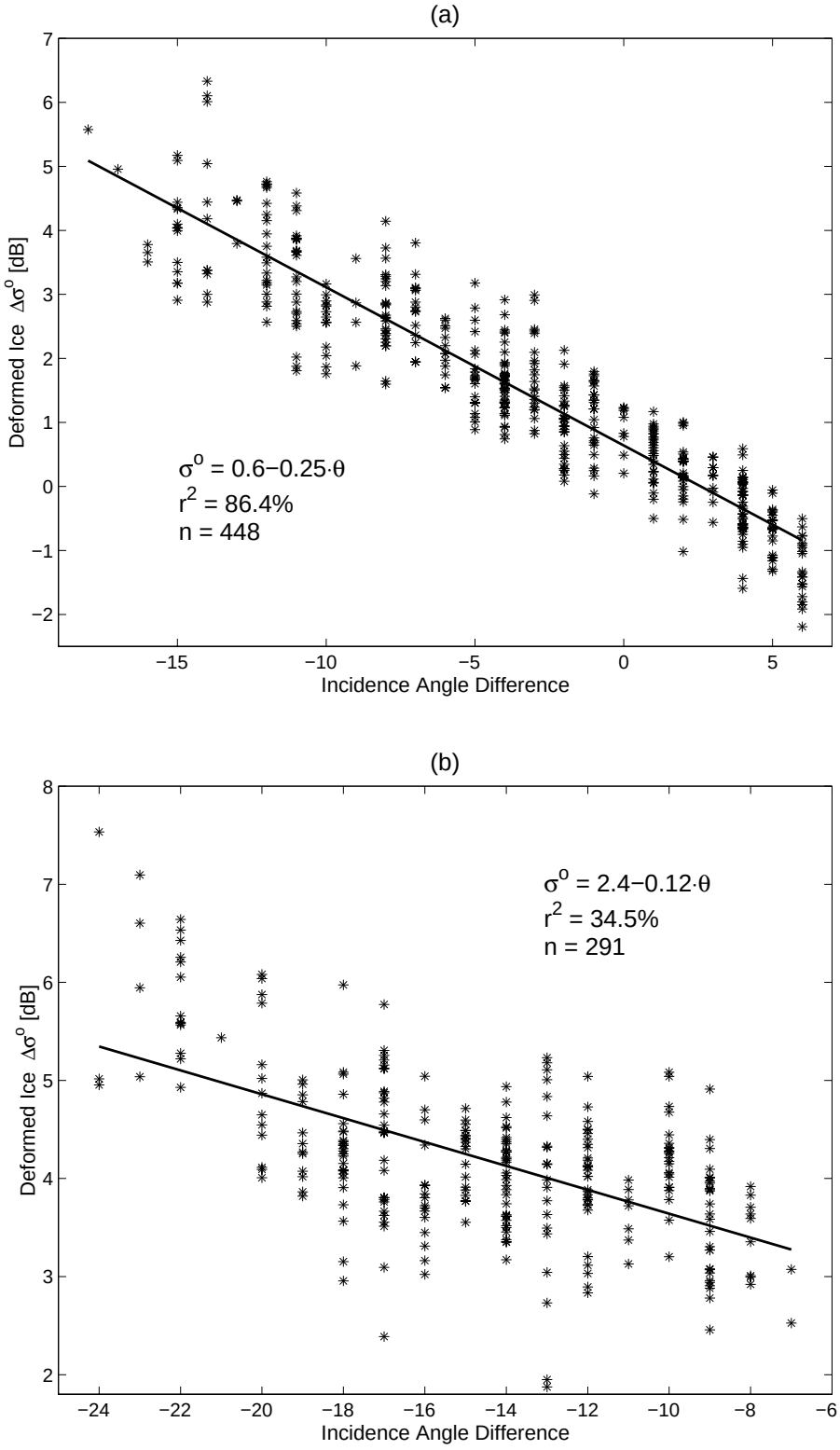

Figure 5.13 Observed mean $\Delta\sigma^\circ$ vs. $\Delta\theta$ for deformed ice under dry snow condition. (a) The best coefficient of determination (86.4%) using the RADARSAT image pair acquired on March 5 and 7, 1998. (b) The worst coefficient of determination (34.5%) using the RADARSAT image pair acquired on March 6 and 7, 2000.

Table 5.7 The results of the linear regression between the mean $\Delta\sigma^\circ$ and $\Delta\theta_0$ using the RADARSAT-1 ScanSAR Narrow data.

Ice Type	Snow Class	Number of	Slope term b_1 [dB/1°]				r^2 [%]		
		Image Pairs	Mean	Std	Min	Max	Mean	Min	Max
LI	Dry	21	-0.25	0.04	-0.19	-0.34	79.9	32.6	90.7
DI			-0.21	0.04	-0.12	-0.30	70.2	34.5	86.4
LI and DI			-0.23	0.05	-0.12	-0.34	75.1	32.6	90.7
LI	Wet	7	-0.34	0.08	-0.19	-0.46	59.9	18.8	75.2
DI			-0.27	0.08	-0.16	-0.37	48.6	29.4	71.3
LI and DI			-0.31	0.08	-0.16	-0.46	54.3	18.8	75.2

The ranges of slope values are also large with the RADARSAT-1 data, the difference between the maximum and minimum values is nearly 0.3 dB/1°. This is due to different specific ice conditions during acquisitions of SAR image pairs and due to the sometimes inaccurate classification of data into two ice types without any ground truth. All wet snow image pairs are from the melting period of sea ice in spring when ice melting constantly modifies ice and snow characteristics. Additionally, air temperature data may not always accurately indicate whether snow wetness has been unchanged between the acquisition of the image pair and one day before the acquisition of the first image. A thermodynamic snow/ice model would better estimate the snow cover wetness class.

r^2 varies substantially under both snow conditions. Under dry snow condition the average r^2 is nevertheless quite high, 79.9% for LI and 70.2% DI, whereas under wet snow condition it is somewhat lower, 59.9% and 48.6%, respectively. However, in many image pairs with small r^2 the likelihood of the linear σ° incidence angle dependence is visually confirmed, and the small r^2 is due to the large scatter of data. Additionally, according to a t-test the linear regression was significant in ever image pair (P-value always 0.00). As DI data have large scatter caused by various kinds of deformed ice features and azimuthal look angle dependence of ice ridge σ°, r^2 is typically lower for DI than for LI.

In general, the RADARSAT-1 and HUTSCAT results agreed with each other and they were also supported by theoretical backscattering model calculations (for details see [P3]): the more deformed ice the smaller the slope, and the higher moisture content of ice or snow the larger the slope.

In case of s_T and ρ_T it was very difficult to find accurately any kind of relationship between s_T or ρ_T and $\Delta\theta$, due to the very large scatter of data points. Consequently, a thorough linear regression study of the data was not conducted. The average change of s_T or ρ_T as a function of θ_0 is very small, but for individual windows the change can be significant with either a positive or negative trend.

Using the RADARSAT-1 results for the σ° incidence angle dependence Karvonen et al. (2002) developed an incidence angle correction algorithm for the ScanSAR images. It is used in the FIMR's operational SAR classification algorithms (see Chapter 4.5).

5.6 Dependence between Standard Deviation and Measurement Length for C-band σ°

Surface roughness measurements of various Baltic Sea ice types have indicated fractal-like nature of the ice surface (Manninen 1997a). In general fractal-like nature of the surface roughness has been observed for many natural surfaces, e.g. for cultivated soil in (Yordanov and Guissaird 1997, Davidson et al. 2000). This gave an idea to study whether this fractal-like nature extends from a property of sea ice roughness to a property of σ°. Empirical studies performed for several SAR data sets measured over many natural targets suggest that this could be the case, e.g. (Manninen and Ulander 2001). The aim of [P4] was to determine if the rms variation of the Baltic Sea ice σ° data depends on the length of measurement l, and if it does, then assess its usability for SAR image classification. The study was conducted using the HUTSCAT data acquired in 1992-2003 and two ENVISAT IMP images at HH-polarization and two APP images at HH/HV-polarization acquired over the northern part of the Bay of Bothnia in February 2003 (see Table 5.10).

5.6.1 Theoretical background

The continuous self-similar Gaussian process $B_H(t)$, indexed by a Hurst parameter H ($0 < H < 1$), which has the fractional Gaussian noise (fGn) as its stationary increment process, is called fractional Brownian motion (fBm), e.g. (Beran 1994). Due to the Gaussianity, the process $B_H(t)$ is fully specified by the expected value and the covariances. Based on the value of H the corresponding fBm can be classified into three different categories (Beran 1994(. If $H \in (1/2, 1)$, then the associated increment process fGn is long-range dependent (positive correlation between increments far apart), if $H = 1/2$ the associated increment process consists of independent, identically distributed (IID) normal variables (the ordinary Brownian motion), and if $H \in (0, 1/2)$, the increment process shows only short-range dependence (negative correlation between two successive increments). For a fBm profile the fractal dimension D is defined as $D = 2 - H$.

Due to their inherent nature, fractals are analyzed by multiscale methods, e.g. box counting method and wavelet analysis (Mallat 1989). For image data, local fractal dimension (LFD) has been used as a feature in texture classification in many studies, e.g. (Chen et al. 1993, Ewe et al. 1997, Gambine et al. 2004). Typically LFD is estimated in windows around each data pixel. Usually suitable window sizes for LFD estimation are defined experimentally, as compromises between desired classification resolution and precision of the estimates. In several studies, comparisons of the estimates to fractal images with known D have been made, and it seems that the estimates are typically not very accurate, e.g. (Chen et al. 1993).

In [P4] D is estimated using the power-law form functional dependence of standard deviation σ of a fBm profile on the measurement length l described by (4.6) (Church 1988). Here the coefficient b of (4.6) equals H. Different correlation structures of the increment processes in fBm result in different growing rates of σ as a function of l.

Even for a stationary process with single scale autocorrelation function (ACF) the sample σ increases with increasing l if the samples are positively correlated. This is demonstrated by the expression for the sample variance s^2 of n correlated measurement X_i with the same finite variance σ^2 (Beran 1994):

$$E\left(s^2\right) = E\left(\frac{\sum_{i=1}^{n}\left(X_i - \overline{X}\right)^2}{n-1}\right) = \sigma^2\left(1 - \frac{\delta_n(\rho)}{n-1}\right), \tag{5.3}$$

where the bias term is the sum of the pairwise correlations: $\delta_n(\rho) = \frac{1}{n}\sum_{i \neq j}\rho(i, j)$.

If the correlations far apart decrease to zero, the bias term in (5.3) becomes negligible when l is long enough. In these situations σ increases with increasing l, the exact form of increase depending on the prevailing correlation structure.

5.6.2 Analysis methods

σ as a function of length l is calculated from profile data in the following steps: (1) A profile is divided into disjoint segments with a fixed length giving n segments per profile. (2) A window of length d is slid through a segment by one sample steps. In every allowed window position σ is computed. This yields m distinct σ values for every segment. (3) m values of σ are averaged for each segment separately. (4) The steps (2) and (3) are repeated when d increases from the minimum to the maximum length. (5) For each segment (4.6) is fit using d as the explaining variable. This yields n sets of regression coefficients (a, b) for each profile. The coefficient b yields information how the large and small scale variations occur in a given segment. This information cannot be extracted from σ or ACF statistics because they are calculated only at one fixed length. If the fractal-like property holds, the proposed approach would give new information about the nature of the local oscillation structure of signal statistics.

The accuracy of the calculation method for revealing the true nature of the dependence of σ on l was studied in three disparate cases using simulated data sets. The first data sets consisted of simulated fBm profiles, with H values of 0.1, 0.3, 0.5, 0.7 and 0.9. At each H value ten profiles of length 1024 points were simulated using the freeware Fraclab-software in Matlab (Fraclab). The second data set was single scale Gaussian and exponential ACF profiles. Their length was 1000 points, σ was fixed to 5 points and profile correlation length L had values of 5, 50 and 100. Ten profiles were simulated at each L value. These profiles exhibit functional dependence between σ and l, if the profile length is relatively short with respect to L. The third data set was profiles of random fading with length of 1000 points. Fading with 10 and 50 independent samples (N) was also added to the fBm and single scale ACF profiles to simulate radar measurements. The first figure of N is a rough estimate for the ENVISAT data, and the second one for the HUTSCAT data.

D was estimated using both full length profiles and separate segments with length of 20, 40, and 60 points. Segment-wise analysis emulates analysis of the radar data, where segment length of 40 points is used. For a single profile it produces a large number of D estimates which are all averaged together. In case of the fBm profiles, these D estimates are compared to those obtained with the Fraclab (calculates regularization dimension (Roueff and Véhel 1998)).

Before the analysis, the minimum and maximum length for d ($d_{\min}$ and $d_{\max}$) in Step (4) must be chosen. $d_{\min}$ was chosen to be five profile points. When d increases, the amount of sample estimates of σ decreases and their average is subject to greater random variation. The choice for $d_{\max}$ depends on how much random variation is allowed. In (Manninen 2003), $d_{\max}$ was chosen empirically to be 60% of the segment length. After testing with various limits it was concluded that the 60% limit is also appropriate here.

The magnitude of b variation for a segment of 40 points from fBm profiles without and with fading is illustrated in Figure 5.14 using probability density functions (pdf). In case of the original fBm profiles the pdfs at different values of D have a very wide support and overlap with each other and, thus, accurate separation between the profiles with different D values is not possible. However, the empirical mean values and modes of the b values preserve the theoretically correct ordering as a function of D. Therefore, a single b value is a meaningful discriminant. After fading is added to the fBm profiles, the pdfs with different theoretical D are wide and totally mixed with each other, making classification of the segments based on a single b value impossible. However, the average b values shown in Table 5.8. are still clearly larger than the average b of 0.02 for random fading.

The main results of the analyses with different types of profiles can be summarized as follows: (1) The analysis method can reliably detect whether σ in short profile segment increases with increasing l according to (4.6) if this is theoretically the case. (2) There exist non-fractal profiles which on short intervals exhibit the same kind of power-law dependence between σ and l as a fBm realization. (3) Using only short segments of profile data, it is not possible to determine if a profile is truly fractal-like. (4) If the textural variation of the sea ice σ° follows fBm behavior, then the analysis method, using small segments of the measured σ° data, would yield quite constant slope term b regardless of D for the ice type σ° texture and, thus, very poor classification of ice types. However, the average b would be clearly larger than that for an IID process. (5) If σ° texture follows behavior of a profile with Gaussian or exponential ACF, then short segments would yield average b with only small range of values as function of texture L. The average b would again be larger than for the IID process. (6) Finally, if the variation of the sea ice σ° data is an IID process, then within the small segments the linearity between $\ln(\sigma)$ and $\ln(l)$ would be very weak and the average b very close to zero.

Table 5.8 Estimated average fractal dimension D and coefficient of determination of (4.6) for fBm profiles. Fading characterized by 50 independent samples.

Theoretical D	Segment n=40	
	Without fading	With fading
1.9	1.89 0.86	1.92 0.82
1.7	1.76 0.93	1.88 0.88
1.5	1.60 0.96	1.87 0.85
1.3	1.45 0.98	1.88 0.83
1.1	1.29 0.99	1.92 0.75

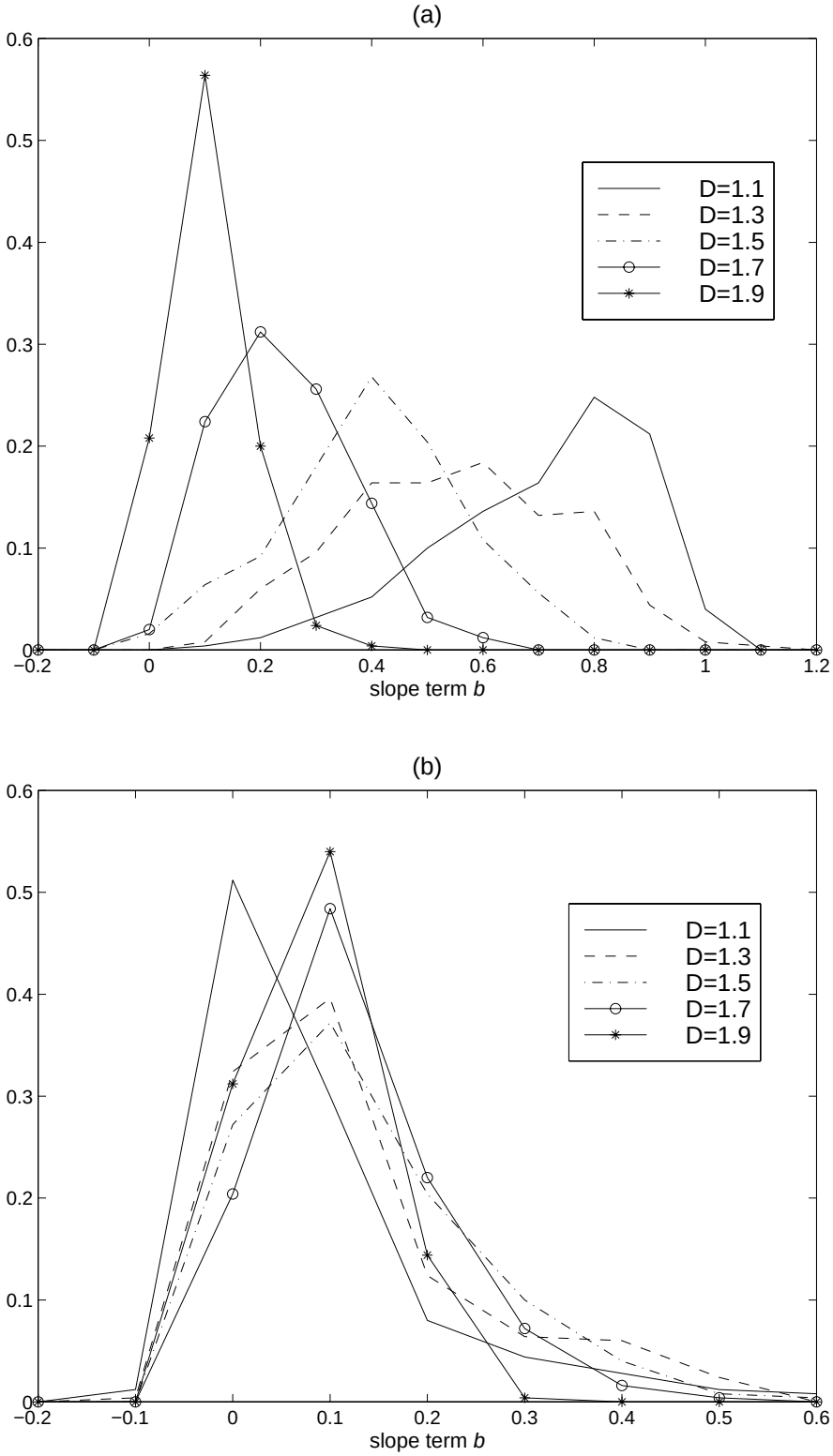

Figure 5.14 PDFs for the slope term b of (4.6) estimated from the 40-point segments of ten fBm profiles (a) without and (b) with random fading process. Theoretical D is from 1.1 to 1.9. The bin width is 0.1 in the pdfs. Number of b coefficients at each D value is 250.

Analysis of HUTSCAT and ENVISAT Data

For the HUTSCAT data classified to dry, moist and wet condition and averaged to a resolution of 12.5 m, the segment length in (4.6) was chosen to be 40 consecutive σ° values, which corresponds to the measurement length of 487.5 m. The chosen segment length is a compromise between a long segment for a large number of points in (4.6) and a short segment

applicable for informative classification. The number of segments for an ice type varies from 4 to 105.

Rectangular areas representing LI, DI, and HDI were visually selected from each rectified ENVISAT SAR image. A typical area of a rectangle was 15 km^2. Within each rectangle, 10 windows of size 40 x 40 pixels (1000 x 1000 m) were selected at random locations. The average number of windows for each ice type is around 140. Equation (4.6) was calculated as in the case of the HUTSCAT data, but the average σ was calculated separately for horizontal and vertical direction and then these two estimates were averaged together as no noticeable anisotropy was detected. The segment length of 40 σ° values corresponds to a measurement length of 975 m.

5.6.3 HUTSCAT results

A clear linear dependence between $\ln(l)$ and $\ln(\text{std}(\sigma^\circ))$ was typically observed in the HUTSCAT σ° segments of various ice types. The average coefficient of determination r^2 for all data is 0.84, and for only 23% of the total of 3096 segments r^2 is below 0.80. An example of statistics for r^2 and b is presented in Table 5.9. Dependence between $\ln(l)$ and $\ln(\text{std}(\sigma^\circ))$ for those segments where r^2 has its maximum or minimum value for each ice type is shown in Figure 5.15 at HH- and VH-polarization. When the measurement lines of various ice types are used in their full length (max 60% length 6.5 km, average 650 m) in (4.6), the average r^2 is still high, 0.84 and there is no correlation between r^2 and the measurement length. This suggests an increase of $\text{std}(\sigma^\circ)$ as a function of l up to a distance of at least a few kilometers.

Table 5.9 Statistics for the coefficient of determination r^2 and regression coefficient b of (4.6) using 5.4 GHz HH-polarization HUTSCAT scatterometer data acquired at an incidence angle of 23 degrees under dry snow condition.

	NI	SLI	RLI	SDI	HDI	FBI
Data amount	13	29	21	27	105	19
Average r^2	0.89	0.84	0.82	0.92	0.83	0.79
std r^2	0.15	0.19	0.27	0.08	0.23	0.25
Average b	0.150	0.118	0.147	0.177	0.141	0.093
std b	0.107	0.113	0.155	0.113	0.100	0.083

The statistical confidence of the obtained b values was estimated using the variation coefficient (vc) of $\text{std}(\sigma^\circ)$ and applying t-test to the following hypothesis : H0: $b = 0$; H1: $b > 0$; risk level 0.05. The average vc for windows of length from 5 ($d_{\min}$) to 24 pixels ($d_{\max}$) decreases roughly exponentially from 0.65 to 0.20. The hypothesis H0 is rejected for 92% of the total b values. It is concluded that: (1) the obtained b values typically have high statistical confidence; (2) b values are not considerably influenced by limited sample sizes for the average $\text{std}(\sigma^\circ)$, and (3) the large stds of b shown in Table 5.9 are due to the large statistical variability of the individual segments.

Comparison between HUTSCAT results and those for the simulated profiles suggested that σ° as a function of l for sea ice cannot be described completely either by fractal, single scale ACF or random process of IID variables. The dependence is likely a more complicated process.

The average b is usually the largest for SDI (from 0.094 to 0.250) and the smallest for FBI (from 0.067 to 0.174). These averages are clearly larger than the values obtained for profiles

of random fading. In case of a fBm profile, the smaller b is, the more uniformly and densely distributed are the significant changes in the profile. FBI is has very homogeneous surface structure, and thus its σ° has typically small textural variations without any large scale patterns, resulting a small b value. Whereas in the case of SDI, the overall level of the σ° may remain low (or high) on a relatively long interval before a large jump. The large scale variation for SDI induced by the ridging intensity variation is greater than the local variation due to the small scale roughness and fading, yielding a large b. HDI exhibits also variation between ridged ice and LI as SDI, but the fraction of ridged ice is consistently high, and thus, the large scale variation of σ° is smaller than for SDI.

There are no systematic differences on the average b values between HH- and VV-polarizations. Under all snow conditions the average b at VH-polarization for SDI, HDI and FBI is consistently larger; on the average by 33%, than at co-polarizations. At VH-polarization the σ° contrast between LI and DI is larger than at co-polarizations [P1] yielding increased large scale textural variation of σ°.

When θ_0 increases from 23º to 45º, the average b at co-polarizations for SDI and HDI always increases, on the average by 30%. For level ice areas in a deformed ice field, the magnitude of decrease of σ° with an increasing θ_0 is larger than for deformed ice areas, which produces more pronounced large scale variation of σ° at angle of 45º [P3]. At VH-polarization both increasing and decreasing trends exist, likely due to the smaller σ° incidence angle dependence [P1].

Under wet snow condition the average b is always smaller than under dry and moist snow condition; the relative difference to dry snow condition is around 75%. This can be explained by the reduction of the spatial variation of σ° due to the smooth wet snow surface. It is noted that the effect of snow cover should be studied by measuring the same ice field under various snow wetness conditions. This is possible with the ENVISAT data.

When the data resolution decreases, textural variations of σ° are more and more averaged, but the effect of fading is decreasing. Thus, the large scale σ° oscillations become more pronounced and the average b increases, up to some resolution limit. The effect of the resolution was studied by calculating average b values also at a resolution of 25 m for a distance of 487.5 m. From resolution of 12.5 m to 25 m, the average b increases in almost all cases. The increase is the smallest for SDI and HDI (average 13%) and the largest for SLI and FBI (average 56%) which have smaller textural variations than other ice types, and, thus, when the fading decreases they become more visible.

The distribution of the b and a values is so large that unambiguous ice type discrimination is not possible, which is understandable as the ice roughness variation and, thus, also the σ° variation constitute a continuum instead of distinctly separable classes (Manninen 1997a). On the basis of Figure 5.16, the DI types (HDI, SDI, FBI) are as well separated from LI areas as by using only mean and std of σ°. Generally, both methods perform equally well for the HUTSCAT data when the window size is relatively large (40 pixels). The disadvantage of using the std values is that they are fixed for a certain distance. The results here suggest that there are two uncertainties in the estimation of std for σ° data: (1) uncertainty due to the sampling size, and (2) std depends on the measurement length. Hence, an accurate comparison with corresponding std values of different studies does not seem to be possible if the distance used for their determination is not equal.

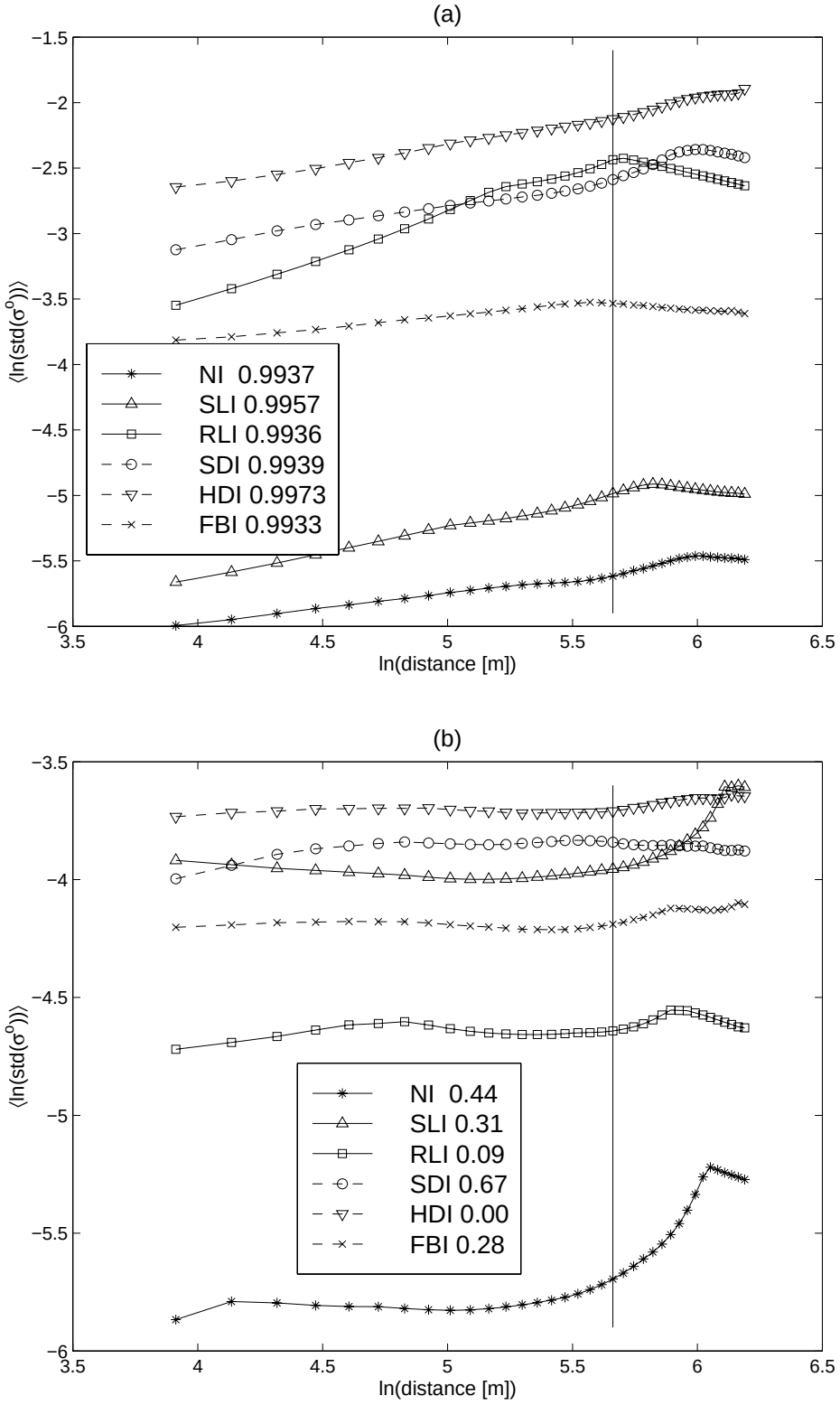

Figure 5.15 The dependence between $\ln(l)$ and $\ln(\mathrm{std}(\sigma^\circ))$ for various ice types using the HUTSCAT 5.4 GHz dry snow Baltic Sea ice data. (a) and (c) the strongest, and (b) and (d) the weakest dependence at HH- and VH-polarization, respectively. The section length is 40 σ° values (distance of 487.5 m). The incidence angle is 23º. The maximum and minimum r^2 for each ice type are given. The vertical line shows the maximum distance used in (4.6) according to the 60% rule.

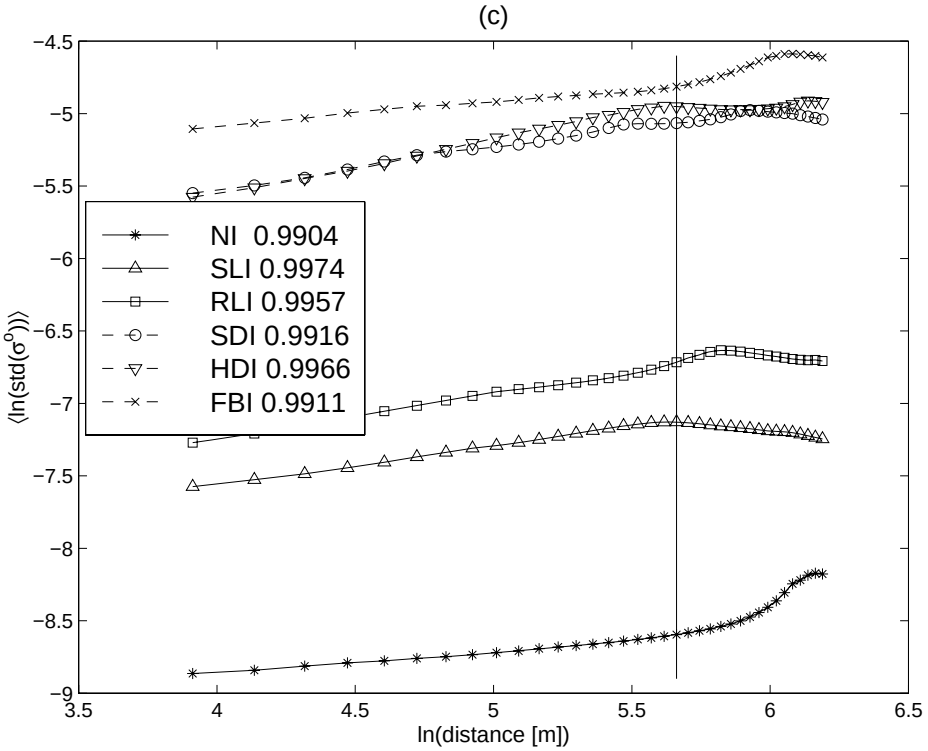

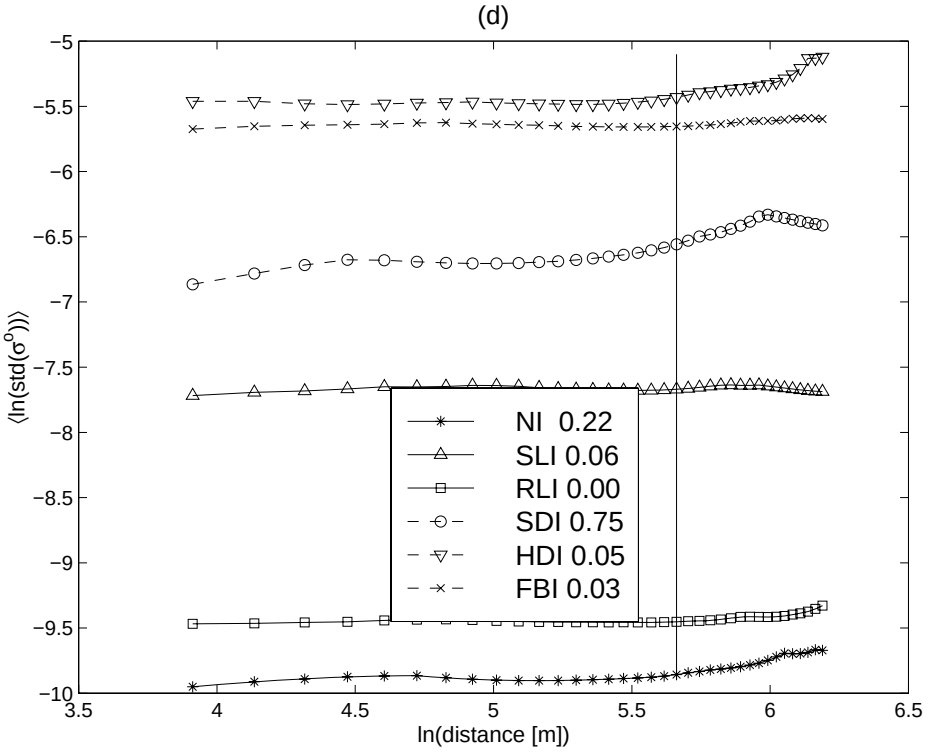

Figure 5.15 Continues.

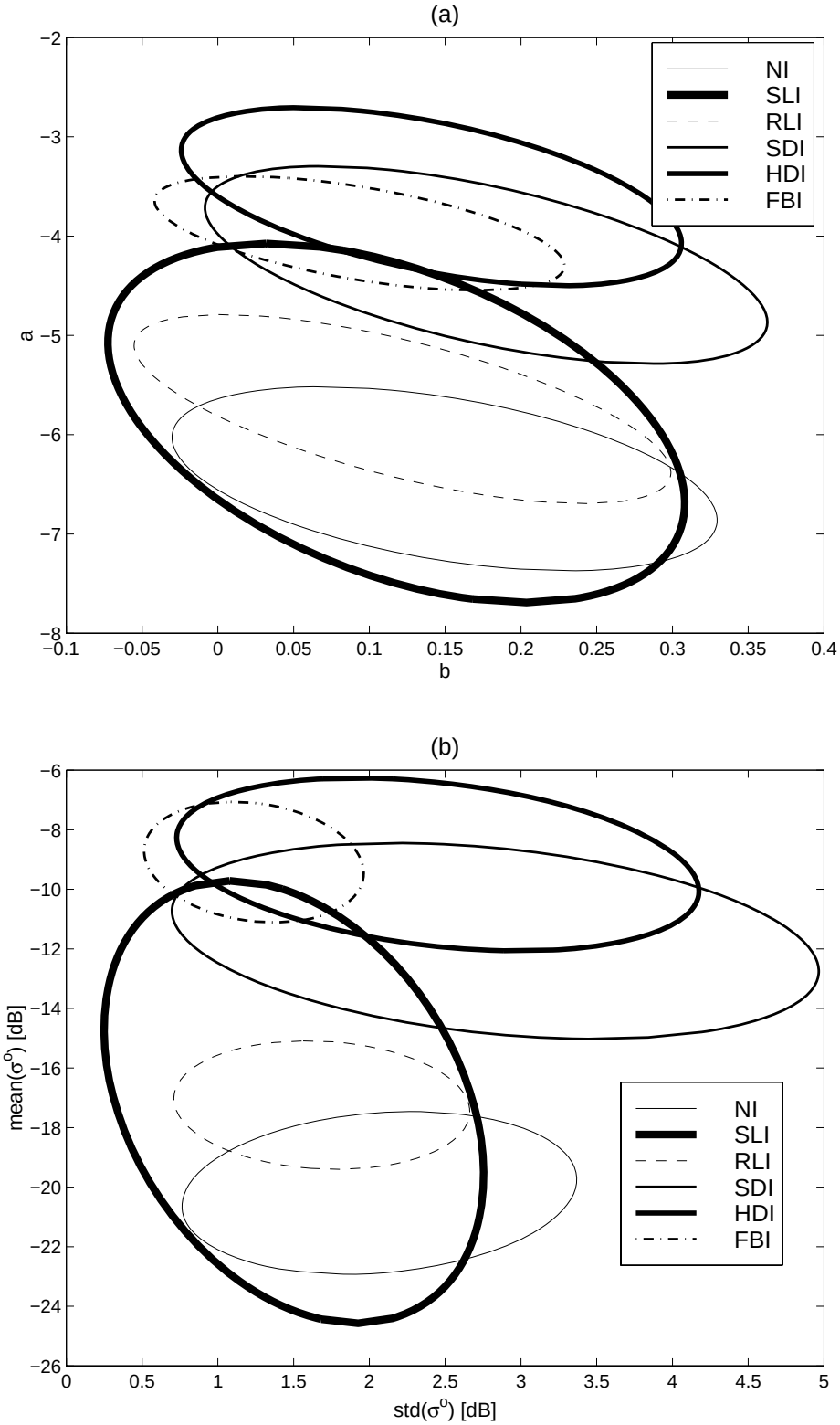

Figure 5.16 Variation of (a) regression coefficients a and b of (4.6) and (b) the mean and std for a section of 40 σ° values of various ice types using the HUTSCAT 5.4 GHz HH-polarization dry snow Baltic Sea ice data. The incidence angle is 23º. Ellipses represent 90% confidence limits.

5.6.4 ENVISAT results

The average r^2 for all data is very high (0.98), and only 6.2% of the total of 2460 r^2 values is below 0.95. The average r^2 is larger than in the HUTSCAT data due to the very large amount of distinct std(σ°) values available for averaging in the ENVISAT data. An example of the dependence between $\ln(l)$ and $\ln(\text{std}(\sigma^\circ))$ for the ENVISAT data in shown Figure 5.17. For LI, DI, and HDI, the average b varies from 0.058 to 0.144, see Table 5.10. These averages are larger than that of around 0.03 for random fading. The hypothesis, H_0: $b = 0$; H_1: $b > 0$, is always rejected with risk level 0.05 and, and vc is on the average around 0.6 at $d_{\min}$ and decreases to 0.3 at $d_{\max}$, indicating high statistical confidence of the calculated b values.

The average b always increases with increasing ice deformation (89% on the average). At HV-polarization, the average b for HDI is always slightly larger (23% on the average) than at HH-polarization. The effect of snow wetness was studied with the SAR images of February 16 and 19 acquired over the same ice field. Under dry snow condition, the average b at HH-polarization is always a little larger (on the average 13%) than under moist snow condition. This suggests that a smooth moist snow cover reduces the large scale textural variation of σ°.

Table 5.10 Statistics for the regression coefficient b of (4.6) using ENVISAT SAR data acquired in the Bay of Bothnia in February 2003.

Date	Image Swath	Polari-zation	Inc. Angle	Snow Cover	Data Amount			Average *b*			Std *b*		
					LI	DI	LI	LI	DI	HDI	LI	DI	HDI
14 Feb	IMP IS3	HH	28.6-30.9	Dry	140	140	130	0.058	0.107	0.113	0.010	0.037	0.025
15 Feb	APP IS6	HH	39.1-42.6	Dry	110	150	150	0.061	0.100	0.122	0.010	0.025	0.025
		HV						0.066	0.090	0.144	0.008	0.025	0.037
16 Feb	IMP IS1	HH	15.3-20.5	Moist	110	150	150	0.060	0.087	0.103	0.011	0.022	0.024
19 Feb	APP IS2	HH	19.6-24.7	Dry	110	150	150	0.070	0.099	0.111	0.010	0.023	0.024
		HV						0.074	0.094	0.142	0.016	0.027	0.040

Equation (4.6) was also studied using a window of size 80 x 80 pixels (2000 x 2000 m) for the SAR image of February 15. The average r^2 decreases only very slightly when the window size increases. The average b for LI and HDI decreased on the average 26% and 19%, respectively. This decrease could indicate that the dependence of σ° is changing as a function of the spatial frequency.

A typical increase of std(σ°) in dB-scale with increasing N x N window size was investigated using the ENVISAT image of February 14. The average std(σ°) for LI increased from 1.87 dB for the 5 x 5 window to 1.96 dB for the 20 x 20 window. For HDI, the corresponding values are 2.34 and 2.73 dB. For LI, the increase is subtle, but for DI types it is noticeable.

In general, the ENVISAT results and their explanations are identical to the HUTSCAT ones. The differences are likely due to the different number of independent samples and different ice type definitions. The discrimination capability of the coefficient pair (a, b) is comparable to that of mean and std of σ° when the window size is 1000 m. An example of the b coefficient and std(σ°) calculation for whole SAR image is shown in Figure 5.18. Both b and std(σ°) images have lower values for LI than for DI, also different kind of edges, like ship channels, are seen in the images.

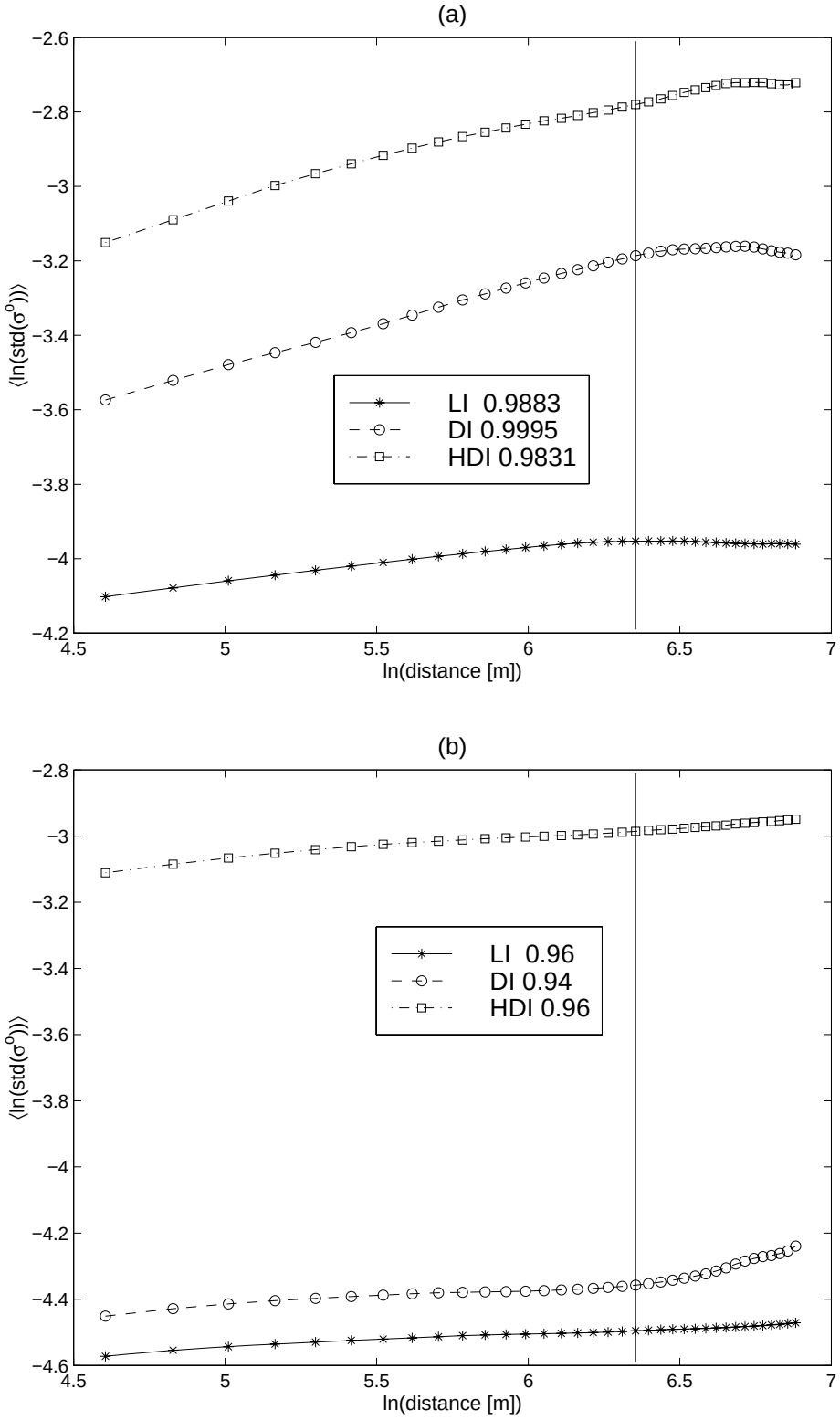

Figure 5.17 Strongest (a) and weakest (b) dependence between ln(l) and ln(std(σ°)) for three ice types using ENVISAT HH-polarization data acquired over the Bay of Bothnia in February 14, 2003. The section length is 40 σ° values (distance of 975 m). The pixel size in the ENVISAT data is 25 m. The maximum and minimum r^2 for each ice type are given. The vertical line shows the maximum distance used in (4.6) according to the 60% rule.

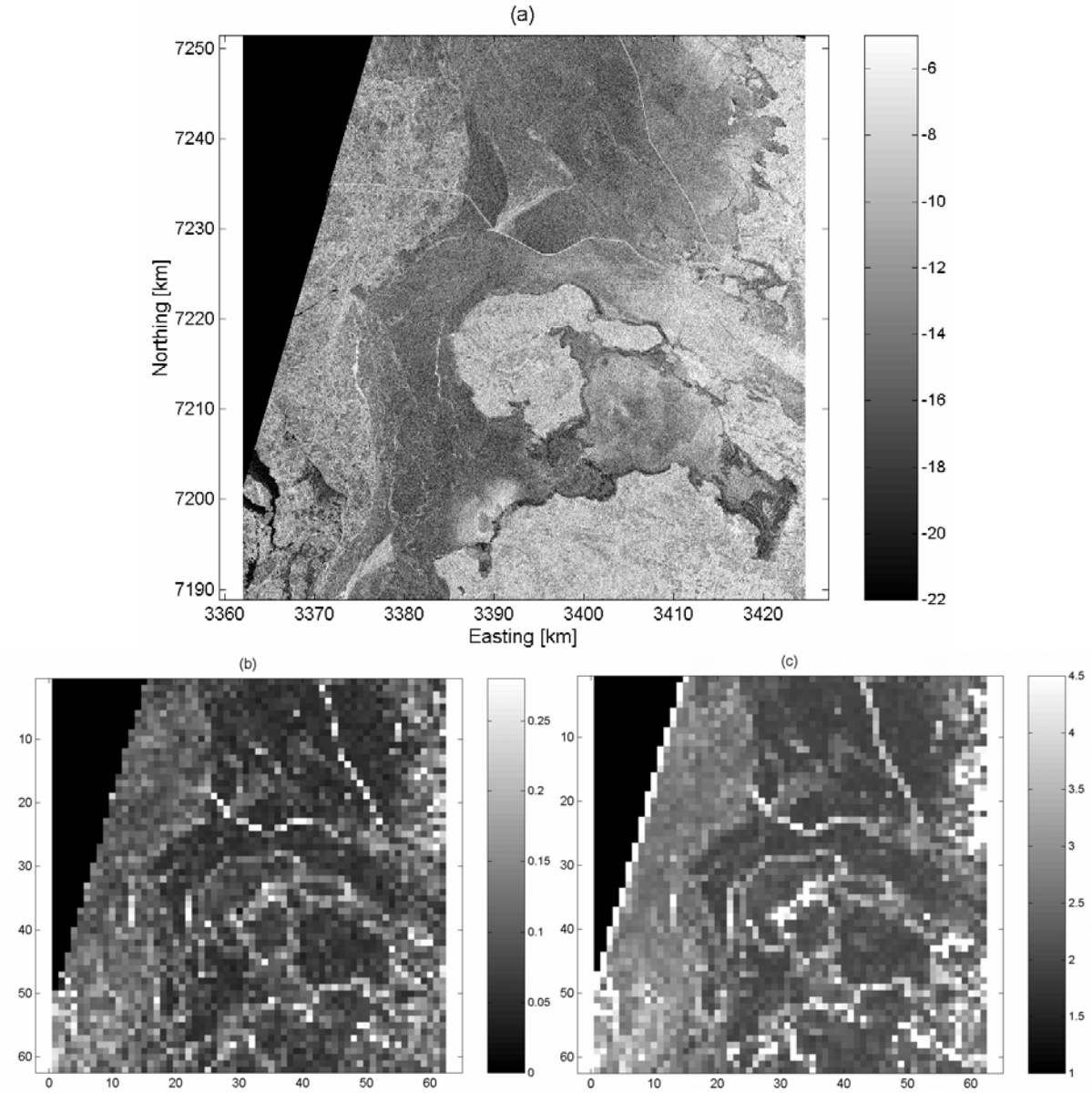

Figure 5.18 (a) ENVISAT HH-polarized IMP SAR image acquired on February 14, 2003. The SAR image was rectified to the Finnish Uniform Coordinate System with a 25 m pixel spacing. (b) the b coefficient of (4.6) and (c) std of σ° in dB calculated using a window of 40 by 40 pixels.

5.6.5 Summary on classification of ice types

The scatter in the values for b and a in both HUTSCAT and ENVISAT data is so large that unambiguous ice type discrimination is not possible either using one of them alone or both together. DI types were mostly discriminated from other ice types, but this discrimination was not essentially better than that obtained with just the mean and std of σ°. It is possible that a relation exists between b computed from the surface profile of large scale sea ice deformation, i.e., the slope term for $\ln(l)$ versus ln(std(surface height)), and b computed from the σ° profile. This assumption could only be studied with quantitative ground truth data describing ice surface topography. The use of parameters b and a instead of std and mean is preferred due to the scale-invariant comparability with the results of other studies obtained with different calculation window sizes and with radar instruments of different resolutions. Generally, the dependence of std(σ°) on l could be utilized in the SAR classification, e.g., by designing a classifier which uses multiple different window sizes as a feature vector.

5.7 Comparison between σ° Time Series and Thermodynamic Snow/Ice Model

FIMR has developed classification algorithms for identification of different ice types and open water and for estimation of sea ice thickness in the SAR images. Interpretation of the classification results is often difficult, because the algorithms utilize mainly the image structure and little or even no geophysical information are utilized. The classification results should very likely improve with the addition of this information. Additionally, the current knowledge on how changing weather and sea ice conditions change σ° of various ice types is very limited, only the effect air temperature (Lundin 2001) and coarse snow wetness classes [P1] on σ° has been studied so far.

For the Arctic Sea ice, SAR σ° time series have been compared with thermodynamic parameters of sea ice in several studies. The sea ice targets in these studies were landfast smooth first-year ice (FY) and multiyear ice (MY) in the Canadian Arctic Archipelago. An overview of several studies conducted with ERS-1 and RADARSAT-1 data is presented in (Barber et al. 2001). In a few studies a thermodynamic model of sea ice has been coupled with a theoretical σ° model (Barber and Thomas 1998, Barber and Nghiem 1999). The main results are: (1) Typical time evolution of C-band HH- and VV-polarization σ° has been determined for FY through seasonal periods of freeze-up, winter, early melt, melt onset and advanced melt. The temporal evolution of FY σ° is strongly linked to ice thermodynamics (Barber et al. 2001). (2) In FY, the melt onset is denoted by a rapid increase in σ°. When snow wetness increases to 1-3%, the large brine-wetted snow grains in the basal layer likely contribute a significant volume scattering term to σ°. As wetness further increases, but is still within the pendular regime, snow surface scattering becomes also significant (Barber et al. 2001). (3) Net shortwave energy flux explains a statistically significant portion of the observed seasonal variation of FY σ° (Barber et al. 1995). (4) Inversion of surface albedo from RADARSAT-1 data over FY is possible throughout the melt season (from early to advanced melt) (Hanesiak et al. 2001). (5) Dependence of σ° on snow thickness was found over smooth thick FY (Barber and Thomas 1998, Barber and Nghiem 1999). There is a increase in σ° from a cold snow (< -13ºC) to a warm snow (> -6ºC) case during winter season caused by the thermal modification of brine volumes in snow and sea ice. The amount of σ° increase is weakened as the snow cover becomes thicker.

Due to the differences between the Artic and Baltic Sea ice discussed in Chapter 1, these results may not be directly valid for the Baltic Sea ice. Therefore, in [P5] a time series of C-band HH-polarized σ° of the Baltic Sea land-fast level ice were compared with the results of a 1-D thermodynamic snow/ice model. The objectives of the study were: (1) to study how the model results of sea ice thermodynamics help to understand the changes in the σ° time series, and (2) to find out which thermodynamic parameters mainly cause the σ° changes. The study period began in the middle of the winter, February 3, 2004, and ended in the early melt season, April 7, 2004. The σ° time series were obtained from ENVISAT SAR images (Table 5.4). The snow/ice model results were validated and fine-tuned using ground truth data and MODIS-derived ice surface temperature.

5.7.1 One-dimensional thermodynamic snow/ice model (HIGHTSI)

The full model descriptions for a 1-D high-resolution thermodynamic snow/ice model (HIGHTSI) are given in (Launiainen and Cheng 1998, Cheng et al. 2003). The model is targeted for process studies, e.g., to resolve the evolution of snow/ice temperature profile and snow/ice thickness. Integration of the partial-differential heat conduction equation of snow and ice layers serves as the numerical core of the model. The surface temperature is solved from a detailed surface heat/mass balance equation, which defines the upper boundary conditions for the model, and is also used to determine if surface melting occurs. The solar

radiation penetrating through the surface is parameterized, making the model capable to quantitatively calculate sub-surface melting (Launiainen and Cheng 1998, Cheng et al. 2003). The surface albedo is parameterized according to (Pirazzini et al. 2006). Atmospheric stratification is taken into account in the calculation of the turbulent air-ice heat and moisture fluxes. A heat and mass balance at the ice bottom serves as the lower boundary condition of the model. Snow-to-ice transformation via both superimposed ice and snow-ice formation is taken into account. The evolution of snow properties, such as snow density and heat conductivity, are modeled. A high spatial resolution of the model (e.g., 20 layers in the snow and 20 in the ice) ensures that the response of the snow/ice temperature regime to the absorption of solar radiation near the surface is correctly resolved. The model has been successfully validated against observations in the Baltic Sea (Launiainen and Cheng 1998, Cheng et al. 2003, Cheng et al. 2001).

The following HIGHTSI output variables are used for the interpretation of the σ° time series: snow thickness h_s, superimposed ice thickness h_{si}, snow and ice surface temperatures T_s and T_i. Currently, the HIGHTSI model does not estimate the vertical profile of the volumetric wetness of snow. During the on-set of melting, the melt water is assumed to percolate without delay to the snow-ice interface. Depending on the local heat flux divergence, the melt water is then partly or entirely transformed into superimposed ice. Nevertheless, weather history and snow melting events are used to estimate whether snow cover is dry (volumetric wetness 0%), moist (wetness < 2%) or wet (wetness > 2%) (see Section 5.2 for details).

5.7.2 Test sites and data sets

The ENVISAT IMP and WSM data sets for the study are presented in Table 5.4. Using an ENVISAT IMP SAR image acquired on February 10, 2004, five test sites on landfast level ice were selected near Marjaniemi weather station on Hailuoto Island in the Bay of Bothnia, see Figure 5.19. The size of these test sites is 510 by 510 m. The distance from test sites 1-5 to Marjaniemi ranges from 2 to 6 km. Two test sites were selected at a FIMR's weekly ice and snow thickness measurement station south of Hailuoto Island, 13 km from Marjaniemi.

An average σ° time series was constructed in the following way: (1) Mean σ° values in each SAR image for the seven test sites were calculated. The size of the test sites in the IMP and WSM images was 17 by 17 and 3 by 3 pixels, respectively. (2) The σ° time series for the seven test sites were averaged together. The average σ° time series is represented by the mean and std of σ° and the average θ_0 at each sampling time. This average time series is considered better for analysis than the individual seven time series, as the test sites were selected visually without any ground truth and, also, the HIGHTSI results are representative in a scale comparable to the test region, without a possibility to resolve spatial differences between the individual test sites. The std of σ° is from 0.28 to 1.28 dB indicating that the ice conditions at the test sites were not exactly the same. The effect of fading in the time series is negligible. The mean σ° values are at least 2 dB above the noise equivalent σ°.

Besides variation in sea ice properties, variation of θ_0 causes changes in the average σ° time series. Under dry and wet snow conditions, level ice σ° decreases on average 0.25 dB/1º and 0.34 dB/1º with increasing θ_0, respectively [P3]. In the data set used here, the variation induced by θ_0 can be up 7 dB. To diminish the incidence angle effect, the σ° time series was first divided into three sub-series, where the σ° values are from two or three adjacent ENVISAT IMP swath types combined with WSM σ° values, which are within the θ_0 ranges of the sub-series, see Table 5.11. Next, the σ° values in the sub-series were scaled to average θ_0's of the series using only the correction factor for dry snow condition. Small θ_0 range of the three sub-series allows the use of single correction factor with little error (max error only

around 0.5 dB under wet snow condition). This way it is possible to find out σ° changes due to the changing sea ice properties. The statistical character of the θ_0 scaling procedure was taken into account by increasing the imagewise std of σ° values by 0.16 dB in the subseries 1 and by 0.20 dB in the subseries 2 and 3, when identifying statistically significant changes between the consecutive σ° values. The three different average σ° time series are shown in Figure 5.20.

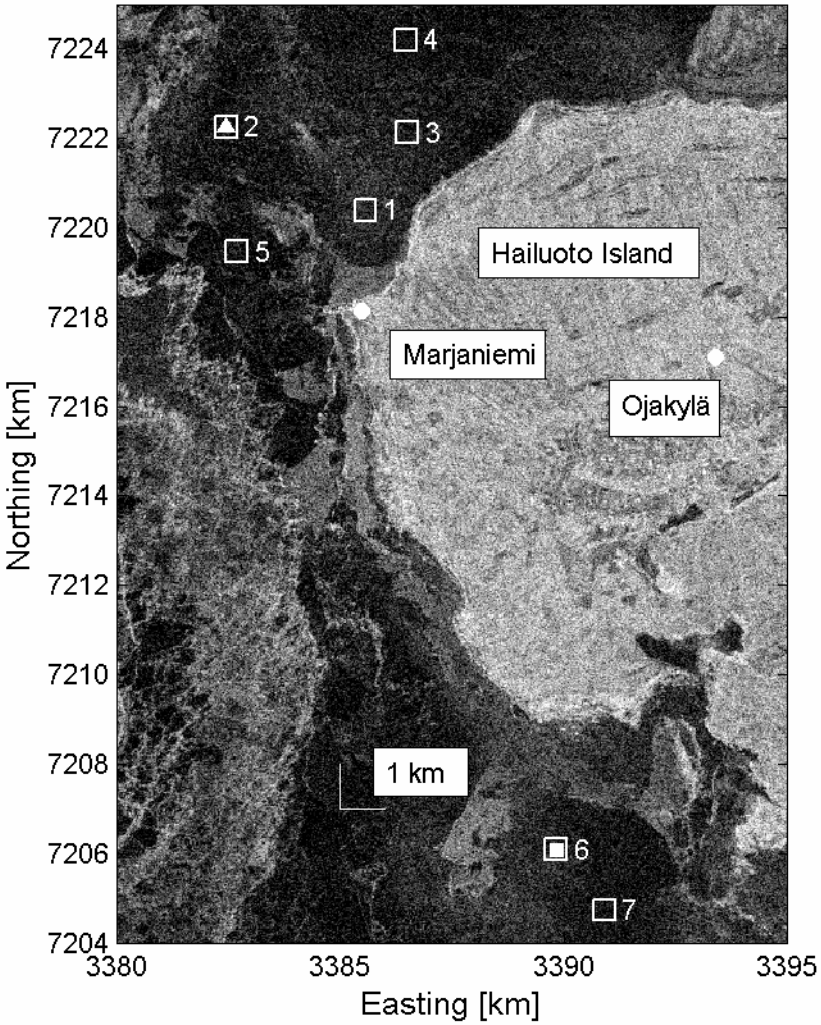

Figure 5.19 Test sites and ground truth data locations; the test sites were selected over landfast level ice near Hailuoto Island in the Bay of Bothnia. Symbols are: '□' = test site, '●' = weather station, '■' = FIMR's weekly ice and snow thickness measurement station, '▲' = surface temperature location in the MODIS data. The SAR image was rectified to the Finnish Uniform Coordinate System (northing and easting in kilometers).

Table 5.11 Average ENVISAT SAR derived time series of σ° for landfast level ice near Hailuoto Island in the Bay of Bothnia.

IMP Swaths	Start	End	IMP Samples	WSM Samples	Total Samples	Inc. Angle	Mean Inc. Angle
IS1, IS2	4 Feb	30 Mar	7	1	8	16.3 - 23.6	19.5
IS2, IS3, IS4	4 Feb	27 Mar	9	3	12	23.5 - 34.1	29.2
IS5, IS6, IS7	3 Feb	7 Apr	7	4	11	35.9 - 44.9	40.2

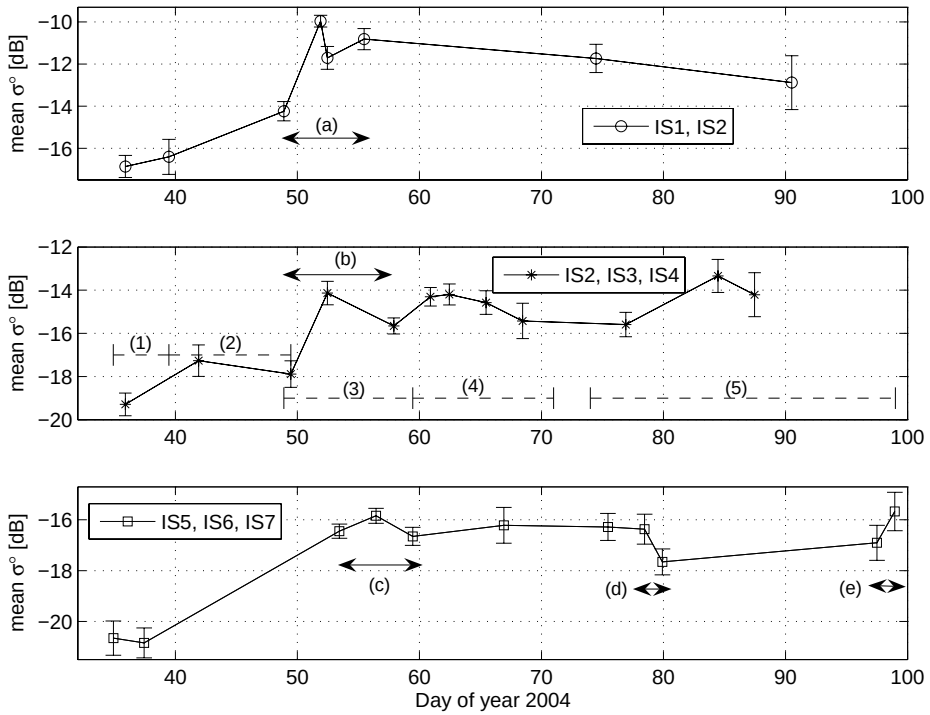

Figure 5.20 Average ENVISAT IMP and WSM SAR σ° time series for landfast level ice near Hailuoto Island. The time series were obtained using σ° data for seven test sites. The three different time series are denoted with the IMP swath types used in their construction. Vertical errorbars indicate ±1 standard deviation variation of σ°. Numbers (1)-(5) indicate the five different main phases in the time series and letters (a)-(e) are the parts selected for detailed qualitative analysis.

The turbulent air-snow fluxes in the HIGHTSI model were calculated on the basis of wind speed, air temperature, and relative humidity observations at the FMI Hailuoto Marjaniemi weather station. The short-range (3-12 h) forecasts of the European Centre for Medium-Range Weather Forecasts (ECMWF) were used for the downwelling solar shortwave and thermal longwave radiative fluxes at the snow surface. The Hailuoto Ojakylä daily observations on precipitation provided the source term for the snow depth; in case of missing data, the ECMWF precipitation forecasts were applied. All the forcing data were linearly interpolated to the model time step of 1 h.

MODIS based snow/ice surface temperature was calculated using the procedure described in (Hall et al. 2004) under clear-sky conditions. Totally 19 daytime and 10 nighttime temperature estimates for the test site 2 (Figure 5.19) were obtained for the study period.

5.7.3 HIGHTSI results

The correlation coefficient between the HIGHTSI and MODIS results for T_s is 0.90, and there are only six cases with the absolute error of HIGHTSI exceeding 5 K. These cases occurred in cold conditions mostly with a low wind speed. In such conditions, the modeling of surface temperature is liable to errors, because the theoretical basis for the parameterization of the turbulent surface fluxes may break down (Mahrt 1999). The HIGHTSI estimation for T_s is clearly better than the ECMWF one, which include 14 cases with the absolute error exceeding 5 K. This demonstrates a benefit that HIGHTSI can bring compared to ECMWF for the interpretation of the SAR data.

A comparison of the modeled snow thickness and conceptual snow temperature regimes (isothermal with T_s = 0 ºC in the white areas) is shown in Figure 5.21. The FIMR weekly (on sea ice) and FMI daily (on land) snow thickness measurements are used as references. The agreement between the model results and FIMR observations varies in time. It is reasonably good during the early continuous snow accumulation (before day number (DN) 40) and the later event of snow melt after DN 90. From DN 70 to 80, the melting trend of modeled results was coherent with the observations, but large differences are apparent between DN 48 and 62. However, the FIMR weekly data have poor temporal resolution and it is affected by wind drift, which can generate large spatial variations reducing its representativeness. Although the snow cover was much thicker at land than on the sea ice, the observed and modeled temporal evolution agreed well. In summary, HIGHTSI can well catch up the snow surface heat balance and melt events.

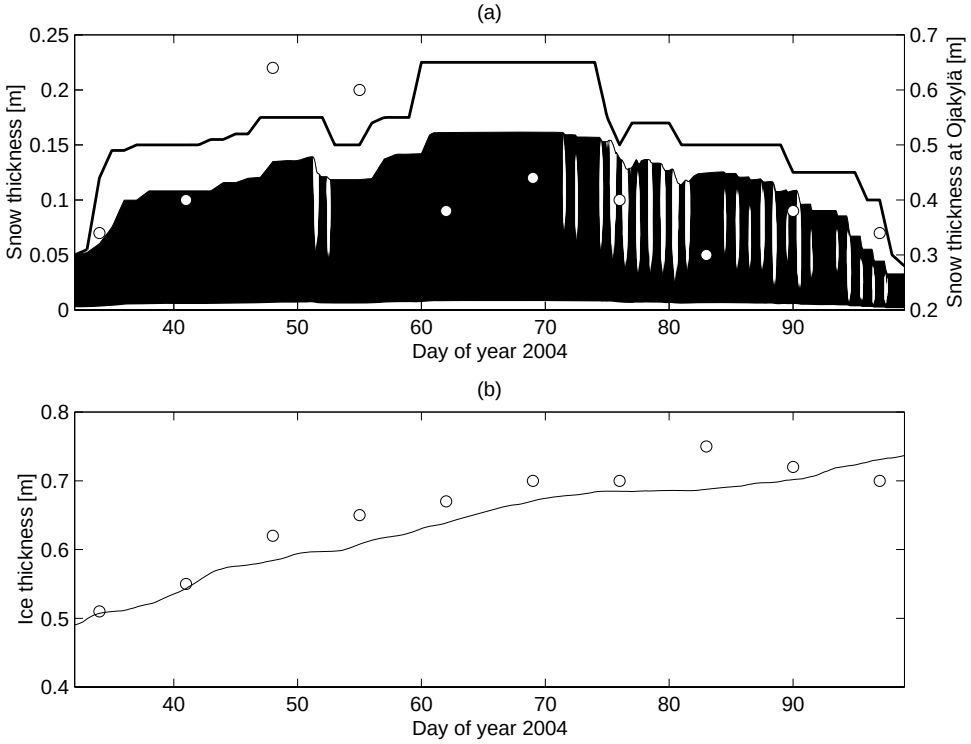

Figure 5.21 (a) Time series of modeled snow thickness and active melt regions (white areas) in the snow pack. The FIMR weekly snow thickness observations at the test site 6 (Figure 5.19) are marked by circles, and the thicker line indicates the snow thickness measured on land at FMI Hailuoto Ojakylä station. (b) The modeled total ice thickness (solid line) and FIMR weekly measurement (dots).

The modeled total ice thickness compares well with the FIMR weekly measurements (Figure 5.21). During the whole period, there was about 5 cm of ice growth to the ice bottom. The rest of the growth was due to superimposed ice. The small discrepancies between observed and modeled results maybe due to errors in the heat balance at the ice bottom.

5.7.4 General evolution of σ°

In the study period, from February 3 to April 7, 2004, with the help of HIGHTSI results, five different main phases (phases 1-5) were identified in the three σ° time series, denoted here as ts12, ts234 and ts567 (see Figure 5.20). The phases are discussed in detail in [P5]. During the entire two-month study period, there was an increasing σ° trend. The range of the mean σ°

values was up to 7 dB, indicating a very large variation for level ice σ°. As the ice season proceeded with multiple melt-refreeze cycles, there were very likely increases in superimposed ice thickness, snow pack stratification, snow grain size, density and surface roughness. This yielded an increase in snow volume and surface scattering and also a rougher snow-ice interface enhancing the ice surface scattering. In the rather limited σ° data set, the variation of σ° was strong on two occasions, DNs 48-60 and 79 onwards in response to the change of ice conditions. During the general melting period, DN 74 onwards, the standard deviations of σ° were always rather large, indicating large variations in the surface conditions between the seven test sites, perhaps due to spatial variations in snow melt.

As the winter weather conditions in the Baltic Sea are highly variable, both during a single ice season and between consecutive years, it is not possible to establish a typical level ice σ° trend through the ice season. In this data set σ° increased on a seasonal scale with increasing shortwave energy flux, as in (Barber et al. 1995). However, the short-time oscillation of net shortwave energy did not produce any detectable σ° oscillation. In the Baltic Sea, it is reasonable to study what kind of σ° changes are typically observed when weather changes, e.g., from cold to warm, and how the ice season history is typically reflected in the changes.

5.7.5 σ° time series vs. HIGHTSI analysis

The effect of a value of a HIGHTSI variable on the value of σ° depends on the previous states of snow and ice surface layer. Hence, a proper statistical analysis would require the use of some stochastic process with a memory property, e.g., an autoregressive process. However, due to the sparseness and limited amount of the σ° data, only a linear relationship between a modeled variable and the σ° values was tested using correlation analysis. The 90 % confidence intervals for the correlation coefficient were constructed using the nonparametric bootstrap method (Davidson and Hinkley 1997). For all variables tested at least one of the three confidence intervals, one interval for each time series, covered the zero value for the correlation coefficient. Hence, no single HIGHTSI variable explained a statistically significant amount of the observed σ° variation when a linear dependence model was assumed. It is noted that the three different time series exhibited slightly different σ° patterns, but it is impossible to determine if these differences are real or just due to the sparse sampling.

For studying qualitatively the relationships between the σ° changes and HIGHTSI variables, significant changes in the σ° time series were first identified using the Welch t-test (Welch 1938). Based on the test results five intensively sampled periods were chosen, marked as periods (a)-(e) in Figure 5.20. The most interesting σ° behavior occurred in periods (a)-(c), between DN 48.89-59.45. During this time period the SAR data coverage was the most frequent. As an example of the σ° vs. HIGHTSI qualitatively analysis, periods (a) and (b) are discussed below. In periods (d) and (e), the variables produced by the HIGHTSI model cannot be directly linked to the observed σ° changes. Detailed ground truth, combined with theoretical σ° modeling, would have been needed. It is noted that the following figures of σ° change are not absolute values due to the incidence angle scaling.

In period (a) (part of ts12), from DNs 48.89 to 51.90, σ° first increased by 4.3 dB. HIGHTSI results suggested that the 13 cm thick snow cover on DN 48.89 was dry. T_s increased from -14.2 to 0.0 ºC and T_i from -1.5 to -0.7 ºC. T_s was 0 ºC during a period of 15 hours before DN 51.90, i.e., snow was melting and snow thickness h_s decreased by 1.4 cm. On DN 51.90, the thin snow cover was likely moist or even wet. On DN 48.89 backscattering from snow covered level ice was very likely dominated by ice surface scattering. The large increase of σ° from DN 48.89 to 51.90 could be due to a strong combination of moist snow surface and volume scattering and ice surface scattering, i.e., the thin snow pack was not yet so wet that it

totally prevented scattering from the ice surface. The contribution of snow cover on σ° is reflected in the large decrease of the SAR image contrast in deformed ice areas (observed visually) from DNs 48.89 to 51.90, see Figure 5.22. An increase of snow wetness reduces σ° difference between level ice and deformed ice leading to a decrease in contrast.

From DNs 51.90 to 52.46, σ° decreased by 1.7 dB. On DN 52.46, there was actual sub-surface melting going on in the snow pack, while DN 51.90 represented night conditions with refreezing of the melt water from the previous day. Hence, the snow pack was much more wet on DN 52.46, and snow surface and volume scattering, therefore, strongly dominated. Increased snow absorption very likely decreased ice surface scattering to an insignificant level. This could explain the observed decrease in σ°. The image contrast is worse on DN 52.46 than on 51.90 (Figure 5.22). During DNs 52.46-55.47, σ° increased by 0.9 dB. Weather got colder with T_s decreasing to -12.6 ºC and T_i to -2.0 ºC. There was no change in h_s, but h_{si} increased by 1.2 cm. Snow wetness most probably decreased to zero and, thus, ice surface scattering dominated. The slight increase of σ° from wet snow condition on DN 52.46 to dry snow condition on DN 55.47 suggests that ice surface was now rougher due to the formation of superimposed ice than wet snow surface on DN 52.46. The contrast is clearly better on DN 55.47 than on 52.46 (Figure 5.22).

In period (b) (part of ts234), σ° increased by 3.8 dB from DNs 49.46 to 52.46. On DN 49.46, snow cover was dry (T_s -14.4ºC and T_i -1.8ºC) and then its properties were changing like in period (a), resulting in wet snow cover on DN 52.46. This indicates that wet snow surface and volume scattering on DN 52.46 was larger than ice surface scattering under dry condition on DN 49.46. During 5.5 days, DNs 52.46-57.90, σ° decreased by 1.5 dB. T_s and T_i went through a decreasing-increasing cycle ending at -6.2 and -1.3 ºC, respectively. h_s increased by 2.1 cm due to precipitation on DNs 56 and 57, and h_{si} increased by 1.8 cm due to refreezing during cold weather. The snow cover changed from wet to dry. The dominating ice surface scattering on DN 57.90 was larger than ice surface scattering on DN 49.46, possibly due to an increase in ice surface roughness produced by an increase of h_{si}. In period (a), an σ° increase was observed when snow cover changed from wet to dry (DNs 52.46-55.47), but here, σ° decreased during the same snow cover change (DNs 52.46-57.90). The reason for this discrepancy is uncertain; only clear differences between these two incidents are an increase of snow thickness on DNs 56-57, smaller temperatures on DN 57.90, and 10-degrees difference in the incidence angle. This discrepancy demonstrates complexity of σ° changes as a function of sea ice condition.

5.7.6 Comparison with previous results

In a previous Baltic Sea ice study (Lundin 2001), it was observed that σ° decreases with increasing air temperature under cold conditions (air temperature < 1 ºC), but this study did not take into account changes in snow and ice thickness and temperature due to the changing weather conditions and, notably, σ° data were not used in the sampling time order it was acquired.

For the Artic Sea FY it has been observed that σ° increases with increasing snow wetness when wetness is within the pendular regime (phenomena at melt onset) (Barber et al. 2001). This σ° increase was also observed here for landfast level ice with a thin snow cover. For the Artic FY, the increase is likely due to the large brine-wetted snow grains in the snow basal layer and wet-snow surface scattering (Barber et al. 2001). In the case of the Baltic Sea ice, the basal snow layer is almost non-saline, and the σ° increase with increasing wetness is possibly due to the strong combination of moist/wet snow surface and volume scattering and ice surface scattering.

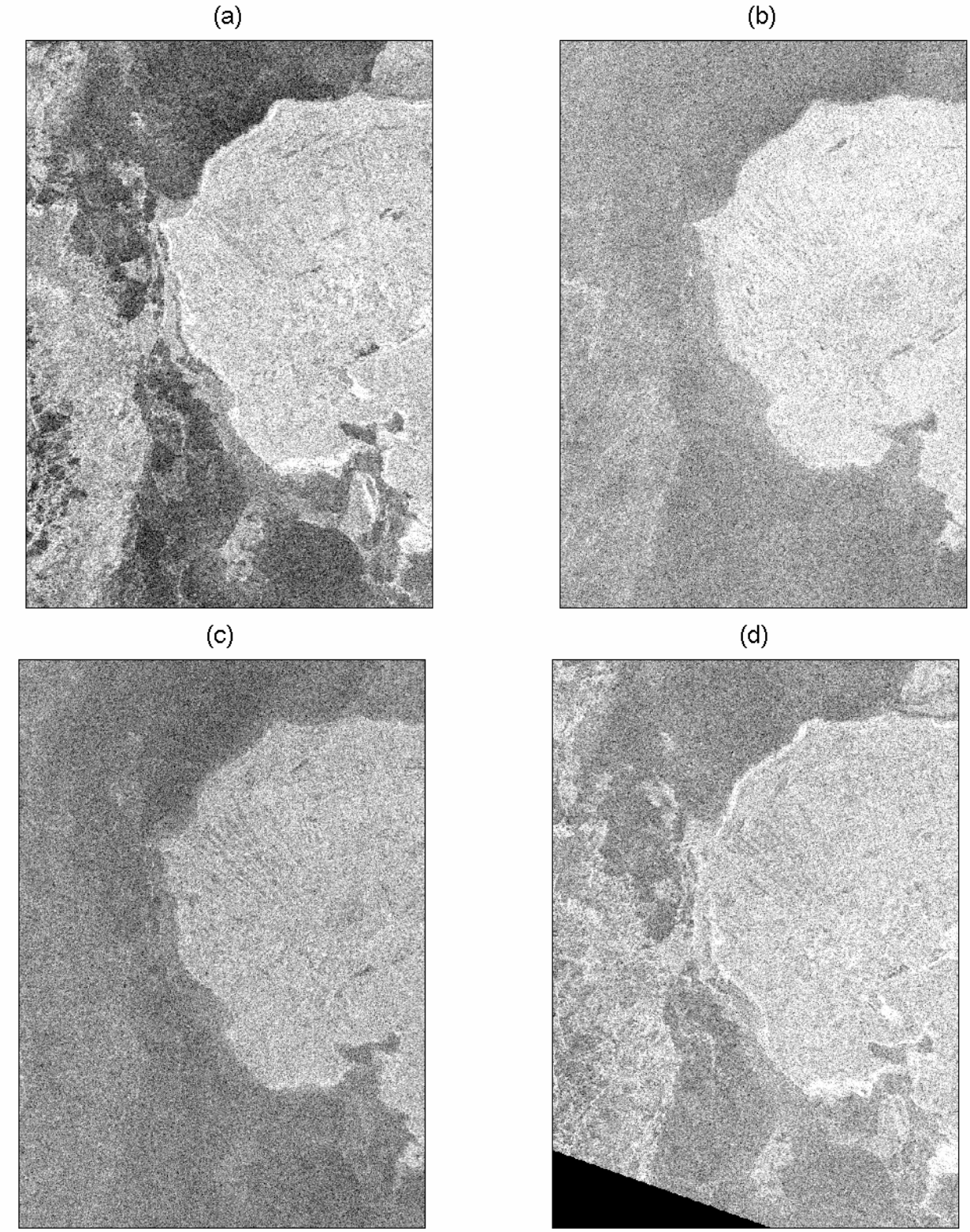

Figure 5.22 ENVISAT IMP HH-polarization SAR images acquired over the study area on (a) DN 48.89 (February 17) with incidence angle θ_0 of 16.4º, (b) DN 51.90 (February 20) with θ_0 of 21.2º, (c) DN 52.46 (February 21) with θ_0 of 23.5º, and (d) DN 55.47 (February 24) with θ_0 of 18.8º. The SAR series demonstrates the effect of snow wetness (increases from (a) to (c) and then decreases from (c) to (d)) to the image contrast. σ°, in the images, is expressed in dB-scale from -20 to -5 dB (black to white).

5.7.7 Significance of the results for SAR image interpretation

Generally, the HIGHTSI output variables greatly helped to interpret the behavior of the Baltic Sea level ice σ° with changing ice and weather conditions. There were some cases where detailed ground truth combined with theoretical σ° modeling, would have been needed for interpretation of the σ° trends. Quantitative analysis between the σ° trends and the HIGHTSI variables indicated that no single HIGHTSI variable explained a statistically significant amount of the observed σ° variation when a linear dependence model was assumed. The importance of the snow metamorphic state for the σ° behavior was emphasized in (Barber et al. 2001). Here, the state of the snow layer could not be extracted from any single HIGHTSI variable or variable combination. It was hypothetically determined by examining the evolution of snow layer over a longer time period.

There is a large variation of level ice σ° with changing weather conditions. It is likely linked to snow cover wetness, formation of superimposed ice, which changes ice surface roughness, snow stratification due to snow melt-freeze cycles, and snow accumulation and melting, which change snow surface roughness. The σ° variation complicates visual and automatic classification of the SAR images as, for example, under dry snow condition, the level ice σ° is smaller than under wet snow condition, and increasing snow cover wetness decreases contrast between level ice and deformed ice. Thus, for good automatic classification, the algorithms must be tuned for different ice and snow conditions. The HIGHTSI model could act as an indicator of various ice and snow conditions and, combined with SAR data, provide an empirical database describing typical relationships between σ° and changing sea ice properties for algorithm development.

6 Investigation of Passive Microwave Signatures of the Baltic Sea Ice

Spaceborne radiometer data acquired with the SSM/I and AMSR-E instruments is not currently used for operational monitoring of the Baltic Sea ice. The main reason for this is the coarse spatial resolution of the data, e.g. in the AMSR-E data the resolution is from 56 to 5.4 km, and the coastline contamination effect (sea ice extent has to rise above a "noise" level in order to be distinguishable from the coastline effect) (Grandell et al. 1996). However, ice concentration maps based on radiometer data could help to validate classification algorithms of the SAR images by providing an independent data set on sea ice conditions. Additionally, time series of ice concentration maps, showing temporal evolution of ice extent, could be used in geophysical studies. Grandell and Hallikainen (1994) and Grandell et al. (1996) have showed that SSM/I data and the NASA Team algorithm (Cavalieri et al. 1984, 1991), after modification of the tie points, provide an estimation of the Baltic Sea ice concentration, but further research is still needed before above mentioned uses of the radiometer data are fully feasible. It is possible that new algorithms especially suited for the Baltic Sea ice conditions are needed.

In order to support development of ice concentration algorithms for the spaceborne radiometer data, the following investigations were conducted in [P6] using airborne radiometer data: (1) behavior of the brightness temperature (T_B) and polarization ratio (PR) as a function of ice type and frequency, (2) correlation between different radiometer channels and the number of main dimensions for multichannel datasets, (3) discrimination of open water leads from sea ice and classification of various ice types using various combinations of radiometer channels or PR and spectral gradient (GR) ratios, and (4) suitability of the SSM/I data with the NASA Team and Bootstrap ice concentration algorithms for mapping the Baltic Sea ice. The effect of snow cover wetness on most of these tasks was also investigated. Below, the HUT radiometer system and the data sets are first described, followed by discussion of the main results of tasks (1)-(4).

6.1 HUTRAD Radiometer and Data Sets

Laboratory of Space Technology of Helsinki University of Technology (TKK) measured T_B signatures of various Baltic Sea ice types and open water leads in March, April and May 1995 during the EMAC-95 campaign and in March 1997 during the IMSI campaign with the airborne non-imaging HUTRAD microwave radiometer system.

In the EMAC-95 campaign, HUTRAD consisted of the following eight channels: 6.8 GHz (H- and V-polarization), 10.65 GHz (H and V), 18.7 GHz (H and V), 24 GHz (V) and 34 GHz (V). In early 1996 the 24 and 34 GHz radiometers were replaced by a new non-imaging high-frequency subsystem, which has 23.8, 36.5 and 94 GHz receivers with H- and V-polarization. All radiometers have been designed and constructed by Laboratory of Space Technology of TKK. The radiometers were mounted onboard a twin-engine Short SC-7 Skyvan aircraft owned by TKK. The radiometers looked backwards along the flight track. The nominal incidence angle of all radiometers was 50 degrees, but the true incidence angle depended slightly on the pitch angle of the aircraft and was between 46 and 50 degrees. The main technical characteristics of HUTRAD are presented in Table 6.1. The radiometer measurements were conducted at an altitude of 300 m and the flight speed was 57 m/s. The target was recorded with a video camera, and the DGPS-coordinates of the flight track were saved with the radiometer data. All radiometers were calibrated before and after each measurement flight with a liquid nitrogen-cooled cold calibration target and a hot calibration target in ambient temperature. Due to temporary spatial limitations in the aircraft in during the

EMAC-95 campaign, the channels 6.8 and 10.65 GHz could not be used simultaneously on board the aircraft.

Table 6.1 Technical characteristics of the HUTRAD non-imaging radiometers (Kurvonen and Hallikainen 1996, Hallikainen et al. 1998).

	6.8 GHz	10.65 GHz	18.7 GHz	23.8 GHz	36.5 GHz	94 GHz	24[1)] GHz	34[1)] GHz
Radiometer type	Dicke	Dicke	Dicke	Dicke	Dicke	Total power	Dicke	Dicke
Polarization	H & V	H & V	H & V	H & V	H & V	H & V	V	V
Incidence angle	50°	50°	50°	50°	50°	50°	50°	50°
Bandwidth (MHz)	310	120	750	750	400	2000	650	650
Integration time (s)	0.5	0.5	0.5	0.5	0.5	0.5	0.2	0.2
Sensitivity (K)	0.25	0.6	0.35	0.20	0.30	0.50	1.6	1.2
Antenna 3 dB beamwidth	5.0°	3.2°	3.7°	4.0°	4.0°	3.0°	5.4°	4.2°
Footprint (m), altitude 300 m	41 by 64	26 by 41	30 by 47	33 by 51	33 by 51	24 by 38	44 by 69	34 by 53

1) Not in use since late 1995.

The radiometer data sets are shown in Table 6.2. Using video imagery the data were assigned to OW and seven ice types, see Table 5.5. The minimum length of a data section for a surface type was chosen to be 10 s which corresponds approximately to a distance of 550 m. 68% of the EMAC-95 data were successfully assigned into different surface types. For the IMSI-97 datasets measured on March 20 and 23, 1997, the corresponding figures are 59% and 77%, respectively. The ground truth data provided further classification into dry, moist and wet snow classes.

Based on the quality control of the radiometer data, the IMSI datasets at 6.8, 10.65 and 94 GHz were rejected from the analysis. This was due to a failure in the temperature control of the receivers, then still in the phase of undergoing flight tests. Also part of the 18.7 GHz data measured on March 20, 1997, had to be rejected for the same reason.

The measured T_B values were not converted to emissivities due to the lack of the surface temperature data. The T_B data used here also contain the reflected down-welling apparent atmospheric T_B:

$$T_{B,atmos}(f,\theta) = T_{B,atmos\downarrow}\left(1 - e(f,\theta_0)\right), \tag{6.1}$$

where $T_{B,atmos\downarrow}$ is the down-welling apparent atmospheric T_B, e is surface emissivity, and f is frequency. A statistical model for $T_{B,atmos\downarrow}$ in Finland is (Pulliainen et al. 1993):

$$T_{B,atmos\downarrow} = \alpha_{\downarrow}(t) T_s \left(1 - t\right), \tag{6.2}$$

where $\alpha_{\downarrow}$ is the approximate atmospheric profile factor for determining the effective downwelling temperature $\alpha_{\downarrow} T_s$, T_s is surface temperature and t is atmospheric transmissivity. At the used frequencies the effect of the atmosphere is the largest at 23.8 GHz;

for example, when t has extreme values of 0.74 and 0.92 which it exceeds 95% and 15% of time, respectively, and T_s is 273 K, then $T_{B,atmos}$ is 68 K and 21 K, respectively. For the Baltic Sea ice types mean emissivities are not available. According to Eppler et al. (1992) typical emissivities for Arctic Sea dark nilas at 37 GHz V- and H-polarization are 0.81 and 0.77 (no data at 23.8 GHz were given). The corresponding values for Arctic first-year ice are 0.96 and 0.91. These emissivities suggest that the contribution of $T_{B,atmos}$ in the measured T_B data is nearly five times higher for very young Baltic Sea ice types than for deformed ice types, but the absolute value of $T_{B,atmos}$ is nevertheless mostly less than 16 K.

Table 6.2 Airborne microwave radiometer measurements of the Baltic Sea ice.

Campaign and date	Radiometer data (GHz)	Measurements	Surface types	Air temp. (°C)	Snow cover characteristics	Snow class
EMAC-95 22 Mar 1995	6.8, 10.65, 18.7: V and H	Four 9 by 9 km test sites in the Bay of Bothnia.	OW, NI, RLI, HDI, FBI	-3.8	Mean thickness < 10 cm. Snow cover consisted of refrozen snow and light new snow.	Dry snow
EMAC-95 5 Apr 1995	6.8, 10.65, 18.7: V and H 24 V	Four 9 by 9 km test sites in the Bay of Bothnia.	OW, RLI, SDI, HDI, FBI	-4.5	Mean thickness 10-40 cm. Old snow at the bottom, new snow in the middle and 2 cm thick layer of frost snow on the top.	Moist snow
EMAC-95 3 May 1995	6.8, 10.65, 18.7: V and H 24, 34 V	Two 9 by 9 km test sites in the Bay of Bothnia.	OW, RLI, HDI	+0.6	Thickness 0-10 cm. Snow very coarse grained.	Wet snow
IMSI-97 20 Mar 1997	18.7, 23.8, 36.5: V and H	Two lines in the Bay of Bothnia. Total length 490 km.	OW, NI, SLI, RLI, SDI, HDI, FBI	-5.5	LI covered only by a very thin loose new snow layer. Some snow on the ridges and in rough ice areas.	Partial dry snow cover
IMSI-97 23 Mar 1997	18.7, 23.8, 36.5: V and H	Two lines in the Bay of Bothnia. Total length 200 km.	NI, SLI, RLI, SDI, HDI, FBI	-9.0	LI covered by few millimeters of loose snow. Snow packed to the ridged and rough ice areas.	Partial dry snow cover

6.2 Polarization Ratio Signatures

In [P6] mean and 90% confidence interval statistics of T_B and polarization ratio PR:

$$PR = \frac{T_B(f,V) - T_B(f,H)}{T_B(f,V) + T_B(f,H)} \tag{6.3}$$

were studied as a function of frequency and ice deformation, but as only PR statistics are important for the NASA Team type algorithms, only the results for PR are discussed here. Statistics of T_B data for 18.7 and 36.5 GHz V-polarization channels used in the Bootstrap ice concentration algorithm (Comiso 1995, Comiso et al. 1997) are discussed in Chapter 6.4.

The mean and 90% confidence intervals of PR values for various ice types under three different snow conditions are presented in Figure 6.1. Under partial dry snow cover and dry snow cover conditions the mean PR decreases (min 0.03 and max 0.10) at all frequencies with increasing ice deformation. Under moist snow condition PR also decreases (from RLI to FBI), but at maximum only 0.02. In the NASA Team algorithm, the 19.35 GHz PR for the first-year ice and multiyear ice tie point is 0.031 and 0.045, respectively (Cavalieri et al.

1991). The first-year ice tie point for the Baltic Sea is 0.056 (Grandell and Hallikainen 1994). In the NASA Team algorithm modified for mapping thin ice in the Arctic seasonal sea ice zones, the average PR at 19.35 GHz for new ice and young ice is 0.150 and 0.08, respectively (Cavalieri 1994). According to these figures a change of 0.01 in the average PR can be considered significant.

PR decreases (max 0.04) with increasing frequency under partial dry snow condition, where the frequency range of the polarization ratio data is from 18.7 to 36.5 GHz. Under other snow cover conditions monotonous frequency behavior of PR was not observed. In these cases, PR is typically the largest at 10.65 GHz in the frequency range from 6.8 to 18.7 GHz. The small amount of dry, moist and wet snow data may be reflected in the results.

The observed behavior of PR is consistent with the sea ice emission model by Fung (1994); when surface roughness, i.e. ice deformation, increases V-polarized T_B stays roughly equal whereas H-polarized T_B increases considerably and, thus, PR decreases. The effect of surface roughness increases with increasing frequency. PR also decreases with decreasing ice surface ε_r which is a function of ice salinity. For NI ε_r is larger than for older ice types. An increase of snow optical depth, either by increase of frequency, snow thickness, scatterer (ice crystals) size or volume fraction, depolarize more the sea ice emission leading to a decrease in PR (Fung 1994). Empirical PR data sets for the Artic Sea ice have also shown that PR decreases with increasingly thick ice types (Cavalieri 1994). This decrease is due to changes in ice surface roughness and salinity, and also likely due to accumulation of snow cover.

6.3 Discrimination of Open Water and Various Ice types

Before studying the discrimination between various surface types in the radiometer data sets, correlation and principal component analysis (PCA) were carried out in order to find out any dependencies between the radiometer channels and the number of main dimensions of the multichannel datasets. If two channels are highly correlated, they are not independent and are hence redundant. The number of the main dimensions plus one is the amount of sea surface types whose fractions in every spaceborne radiometer data pixel can be unambiguously determined (Rothrock et al. 1988). PCA was conducted using unsupervised method because of its ability to describe all forms of variance in the data; not only are the differences between the mean frequency spectra of surface types taken into account, but so are the variances in their signatures (Wensnahan et al. 1993). Here the dimensionality is defined as the number of principal components that contain at least 90% of the variance of the dataset. The correlation matrices were calculated using all radiometer data, whereas PCA was conducted using only the data classified to surface types. The dimensionality was not calculated for the wet snow dataset due to the small number of surface types, only three.

PCA indicated that the number of main dimensions for partial, dry snow and moist snow datasets is only one. The first principal component contained from 96.6% to 98.8% of the total variance. Correlations between different channels were high, from +0.86 to +1.0. Therefore, in the experiments of surface type discrimination it is meaningful to use at maximum a combination of two channels or ratios (PR, GR) at a time. The result also suggests that only concentration of two Baltic Sea surface types, open water and sea ice in general (all ice types together), can be resolved from the spaceborne radiometer data in the frequency range from 6.8 to 36.5 GHz. However, more airborne radiometer data and also spaceborne radiometer data are needed to confirm this.

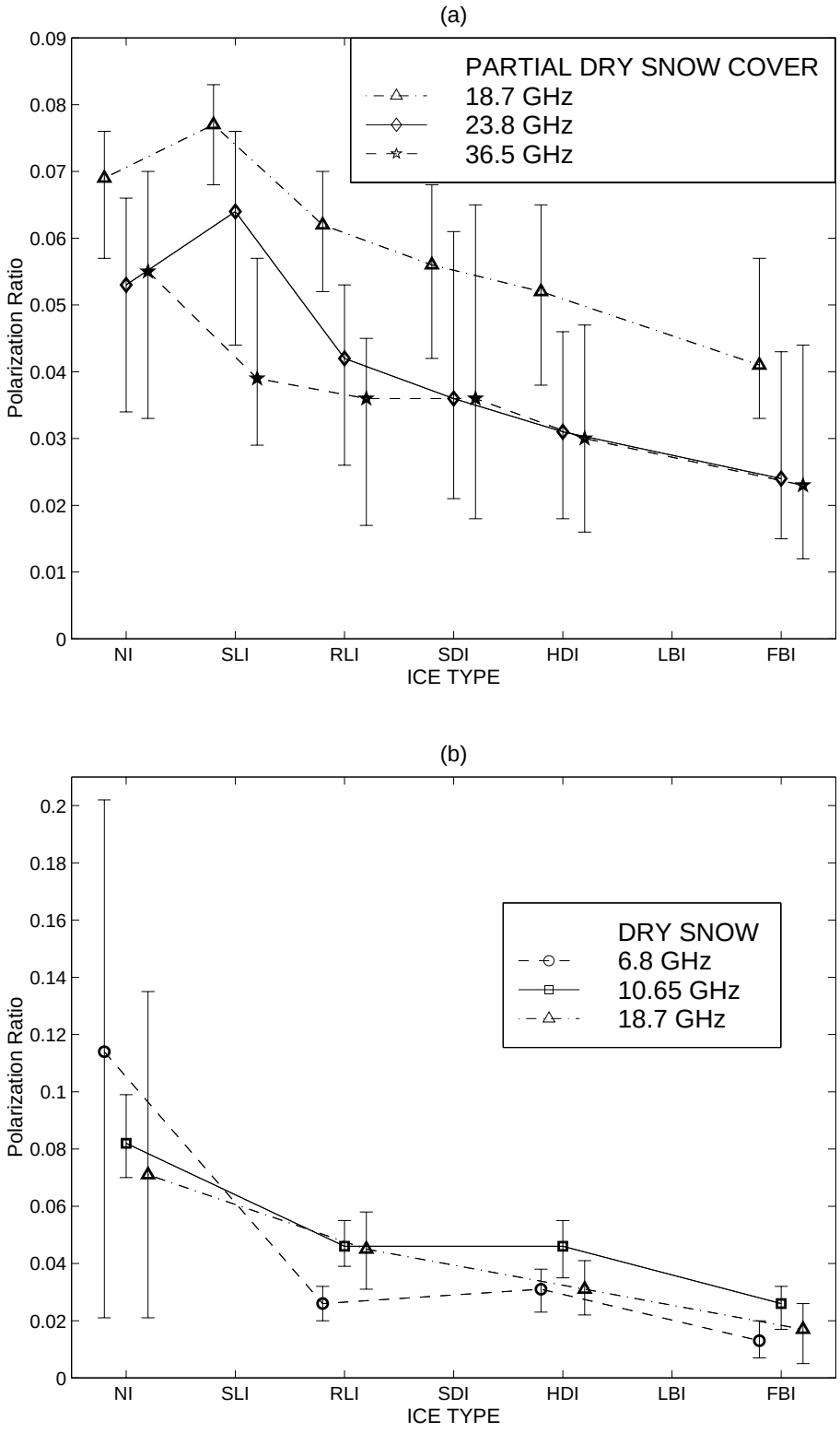

Figure 6.1 Mean and 90% confidence interval of polarization ratio for various ice types using (a) the IMSI-97 partial dry snow cover data, (b) the EMAC-95 dry snow cover data, and (c) the EMAC-95 moist snow cover data.

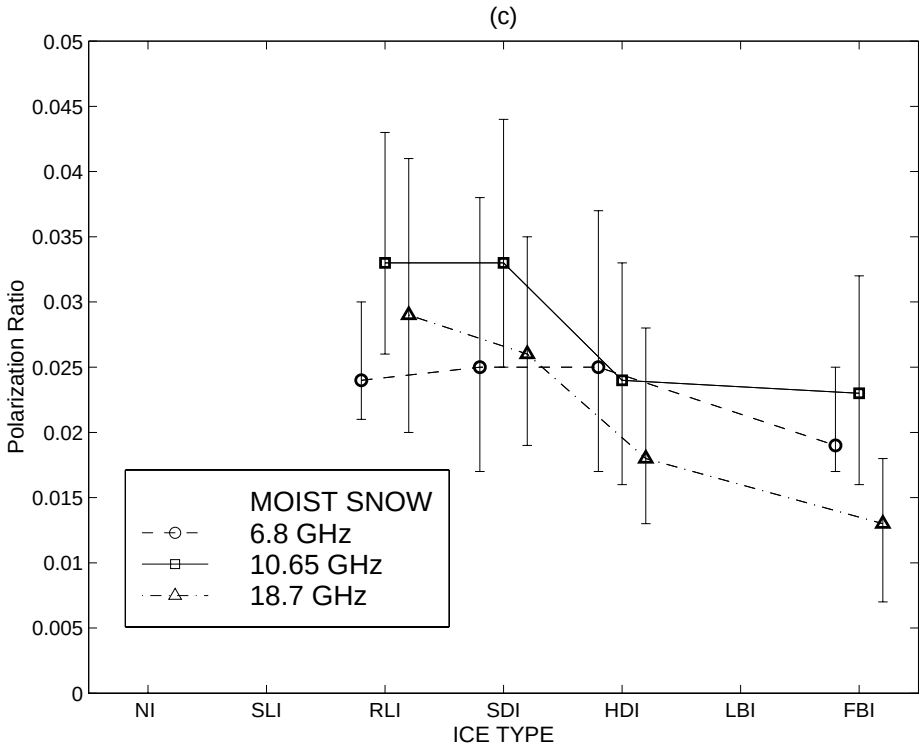

Figure 6.1 Continues.

Open water leads can be distinguished from all sea ice types using only single channel data in the frequency range 6.8 - 36.5 GHz, either V- or H-polarization, regardless of the wetness of snow cover. This is due to the large T_B contrast between water and ice. The calm and foam-free sea surface increased the contrast. No open water areas outside the ice pack, where the sea surface can be very rough, were measured.

The best variables for discriminating various ice types under different snow conditions are shown in Table 6.3. The gradient ratio GR there is defined as:

$$GR = \frac{T_B(f_2, P) - T_B(f_1, P)}{T_B(f_2, P) + T_B(f_1, P)}, \tag{6.4}$$

where f_1 and f_2 are frequencies ($f_1 < f_2$) and P is either H- or V-polarization. The best ice type classification result was achieved under dry snow condition, see Figure 6.3. The mean GR is clearly negative for RLI most likely due to the large amount of volume scattering in thick snow cover, which separates it from HDI. Under moist and partial dry snow cover conditions (Figure 6.2), the unambiguous classification of all ice types is not possible. Under wet snow condition only two ice types were measured and they were discriminated reliably. Principal components calculated from different combinations of T_B channels or ratios did not yield better results than those in Table 6.3. Only in the partial dry snow cover case the data amount is so large that the classification results can be considered statistically very reliable.

The comparison of the classification results to those in (Kurvonen and Hallikainen 1996) is not meaningful as the high-frequency 94 GHz data which provided good results there was not available here and, besides, the number of different ice types in their study was quite low.

Table 6.3 Classification of the Baltic Sea ice types using airborne radiometer data.

Snow Class	Data Source	No of Ice Types	Radiometer Data [GHz]	Best Algorithm [GHz]	Classification Results
Partial dry snow cover	IMSI-97	6	18.7, 23.8, 36.5	[1)] PR 18.7 and GR 18.7/36.5 V-pol	Ice types are not distinguished.
Dry snow cover	EMAC-95 22 March	4	6.8, 10.65, 18.7	PR 10.65 and GR 10.65/18.7 V-pol	Ice types are distinguished reliably.
Moist snow cover	EMAC-95 5 April	4	6.8, 10.65, 18.7, 24 V	[1)] PR 18.7 and GR 18.7/6.8 V-pol	Frozen brash ice distinguished from other ice types. No data for new ice was available.
Wet snow cover	EMAC-95 3 May	2	6.8, 10.65, 18.7, 24 V, 34 V	[1)] PR 6.8 and GR 6.8/34 V-pol	Only rough level ice and highly deformed ice were measured. These ice types are distinguished reliably.

1) Additionally, several different combinations of polarization and gradient ratios produced practically equivalent classification.

Even though the ice types are discriminated in the fine resolution airborne radiometer data, the determination of the ice type concentrations from the coarse resolution spaceborne data is most likely not possible, because the mean signatures for various ice types are very close to each other. This conclusion is supported by the results of PCA analysis.

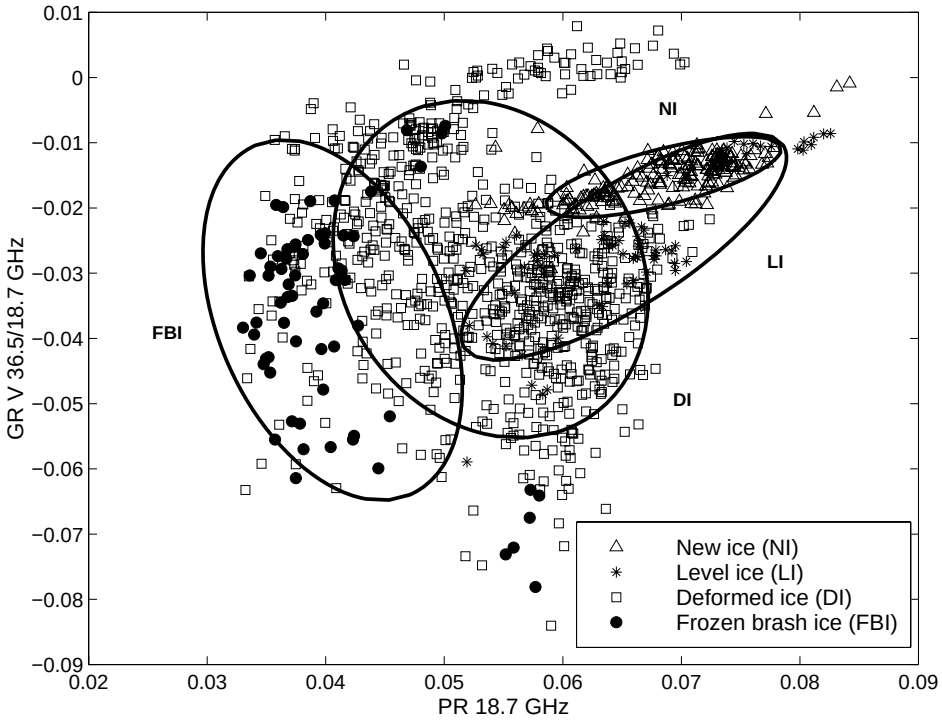

Figure 6.2 Polarization ratio at 18.7 GHz versus V-polarization gradient ratio between frequencies 36.5 and 18.7 GHz for various ice types using the IMSI-97 partial dry snow cover data. The data were averaged to a resolution of 200 m. The ellipses represent 90% confidence intervals.

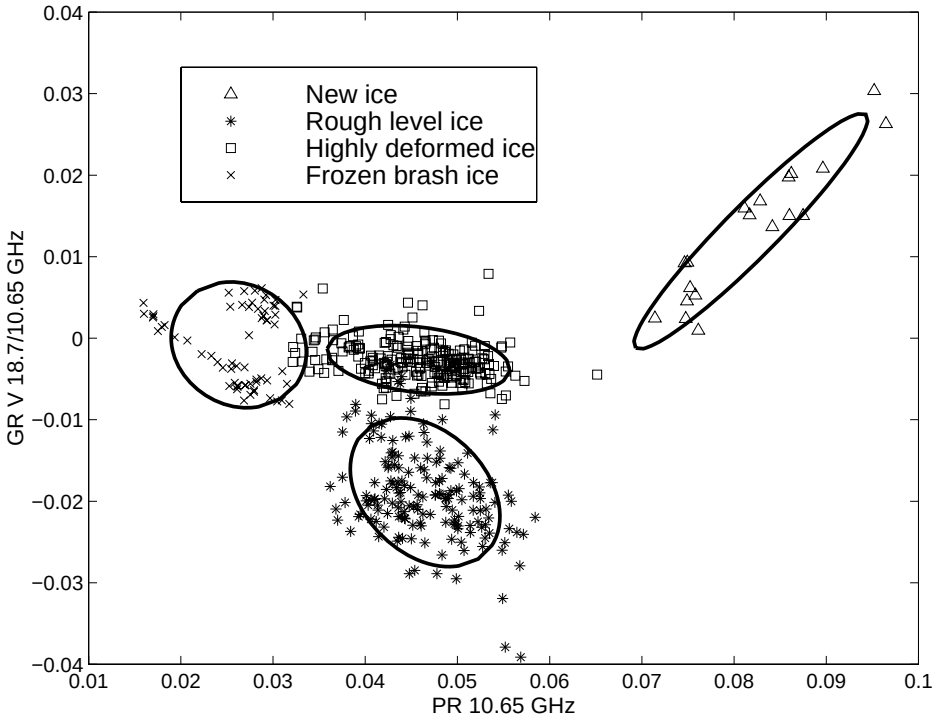

Figure 6.3 Polarization ratio at 10.65 GHz versus V-polarization gradient ratio between 18.7 and 10.65 GHz for various ice types using the EMAC-95 dry snow data. The data were averaged to a resolution of 100 m. The ellipses represent 90% confidence intervals.

6.4 Applicability of the NASA Team and Bootstrap Ice Concentration Algorithms

The NASA Team algorithm is described in Chapter 4.9. The Bootstrap algorithm (Comiso 1995, Comiso et al. 1997) for the Arctic seasonal ice regions where first-year ice dominates employs 19.35 and 37.0 GHz V-polarization T_B channels for determination of the total sea ice concentration. The algorithm uses the fact that in scatter plots 19V vs. 37V open water points tend to cluster around a point and different regions of the Arctic tend to form separate clusters along a line of a given slope. The basis of the algorithm in shown Figure 6.4(a). A data point at location I along line AD, which passes through the clusters of various ice types, is assumed to represent 100% ice cover of the same ice type as at point B. Point O is close to the lowest T_B for open water. Data points along line OI represent different concentrations of this ice type. The line AD and point O in Figure 6.4(a) were plotted using values for the Arctic seasonal ice zones (Comiso et al. 1997). They are empirical parameters similar to the tie points of the NASA Team algorithm.

Applicability of the SSM/I data with the NASA Team and Bootstrap algorithms for the Baltic Sea ice mapping was evaluated using the partial snow cover data. This is the only data set that has channels equivalent to those used in the algorithms. The data were averaged to a spatial resolution of 100 m. All open water measurements were conducted at an incidence angle of 46º whereas measurements for various ice types were conducted at angles of 46º and 50º.

A scatter plot of 36.5 GHz V-polarized T_B versus 18.7 GHz V-polarized T_B using data classified to surface types is shown in Figure 6.4(a). The signatures of various ice types are not grouped to distinct clusters; rather, they form a single large cluster. The large scatter of T_B values is very likely due to fine spatial resolution, 100 m, of the airborne radiometer data. At the resolution of the gridded SSM/I data, 25 km, the fine scale emissivity variations

average out, and the T_B signatures of the same ice type are likely very close to each other. To see if this is the case, the resolution of the SSM/I data was simulated by representing each surface type with the mean and standard deviation of T_B, see Figure 6.4(b). The mean T_B values of various ice types are now very close to each other; the ranges of the means are only 11 and 20 K at 18.7 and 36.5 GHz, respectively. The standard deviations are also very small, below 12 K. This is in agreement with the formulation of the Bootstrap algorithm where it is assumed that different regions of the Arctic tend to form separate clusters along a line AD, and the Baltic Sea is roughly one such region. The mean T_B for open water leads differ largely from the open water point for the Artic, but this is expected due to the calm and foam-free surface of the leads, and the difference in the incidence angle (HUTRAD 46º for open water vs. SSM/I with 53º). Based on the Figure 6.4, it seems that the Bootstrap algorithm also is suitable in the Baltic Sea after adjusting point O and line AD using SSM/I and AMSR-E data acquired in different ice conditions, e.g. dry/wet snow condition.

A scatter plot of the 18.7 GHz PR versus V-polarization GR between 36.5 and 18.7 GHz is illustrated in Figure 6.5(a). These ratios are used in the NASA Team algorithm. Figure 6.5(a) shows also the NASA Team algorithm triangles using the Arctic tie points (Cavalieri et al. 1991) and the Baltic Sea tie points (Grandell and Hallikainen 1994). As expected, the Baltic Sea tie points agree better with the airborne $PR-GR$ signatures than the Arctic tie points. The signatures of various ice types are scattered over a large area and, thus, again only derivation of the total ice concentration is possible. The large scatter is probably again due to the very fine resolution of the airborne data. The poor resolution of the SSM/I data was again approximated by the means and standard deviations, Figure 6.5(b). The mean $PR-GR$ values are very close to the Baltic Sea first-year ice tie point and the standard deviations are small. The results suggest that at least under partial dry snow condition it is not possible to modify the NASA Team algorithm to map concentrations of new ice (i.e. thin ice) and all other ice types combined in the Baltic Sea as has been done in the Arctic seasonal ice areas (Cavalieri 1994). Like the results of Grandell and Hallikainen (1994) and Grandell et al. (1996), Figure 6.5 also suggests that the NASA Team algorithm is suitable for determination of the Baltic Sea total ice concentration. However, the values of the tie points should be studied with SSM/I or AMSR-E data sets of different ice conditions. It is possible that the algorithm triangle can be replaced with a single line connecting the tie points for open water and 100% ice concentration.

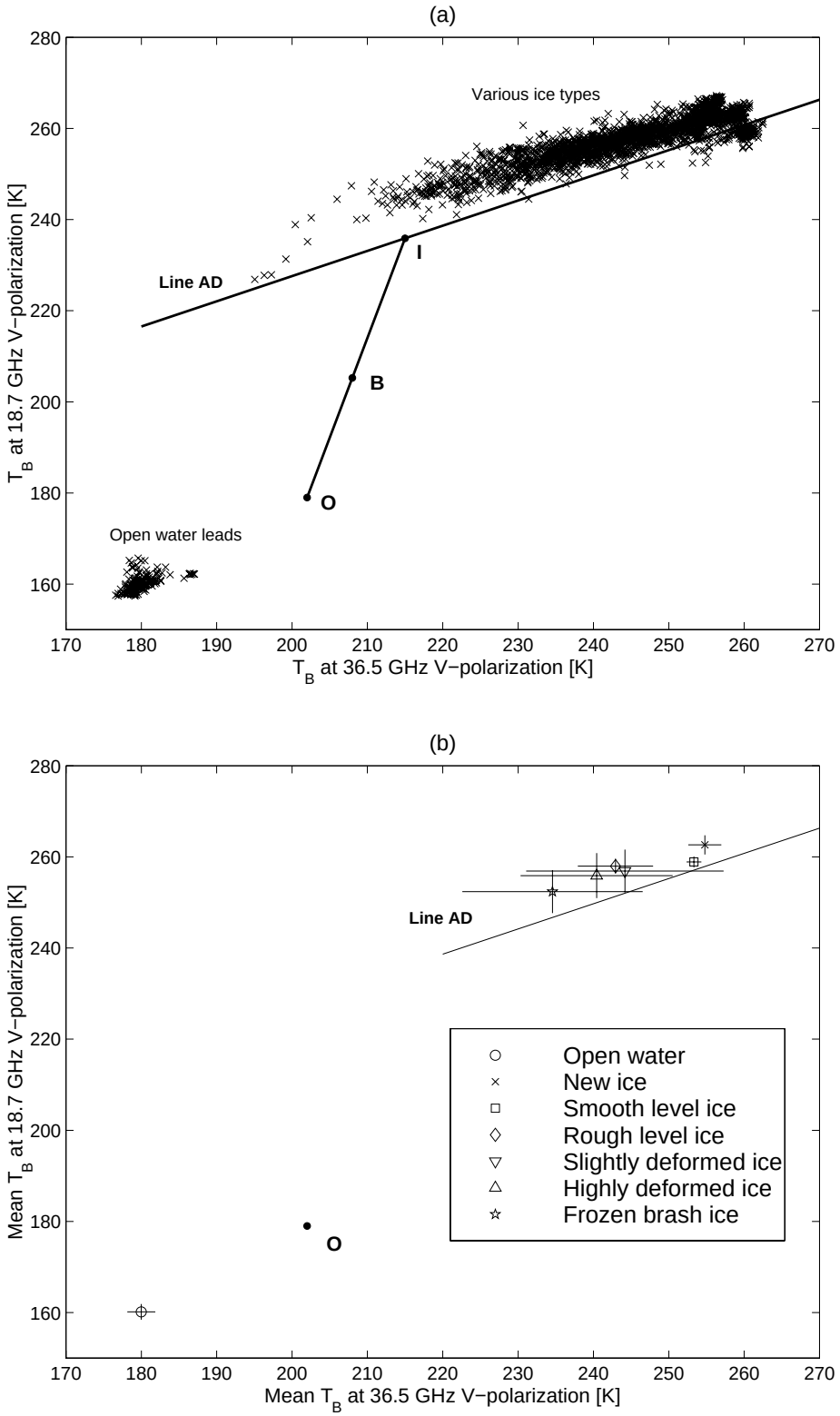

Figure 6.4 36.5 GHz V-polarized versus 18.7 GHz V-polarized brightness temperatures for various surface types using the IMSI-97 partial dry snow cover data. (a) Scatter plot using the data averaged to a resolution of 100 m. For explanation of line AD and symbols B, I, and O see text. (b) Mean and ±1 standard deviation confidence intervals of the brightness temperatures.

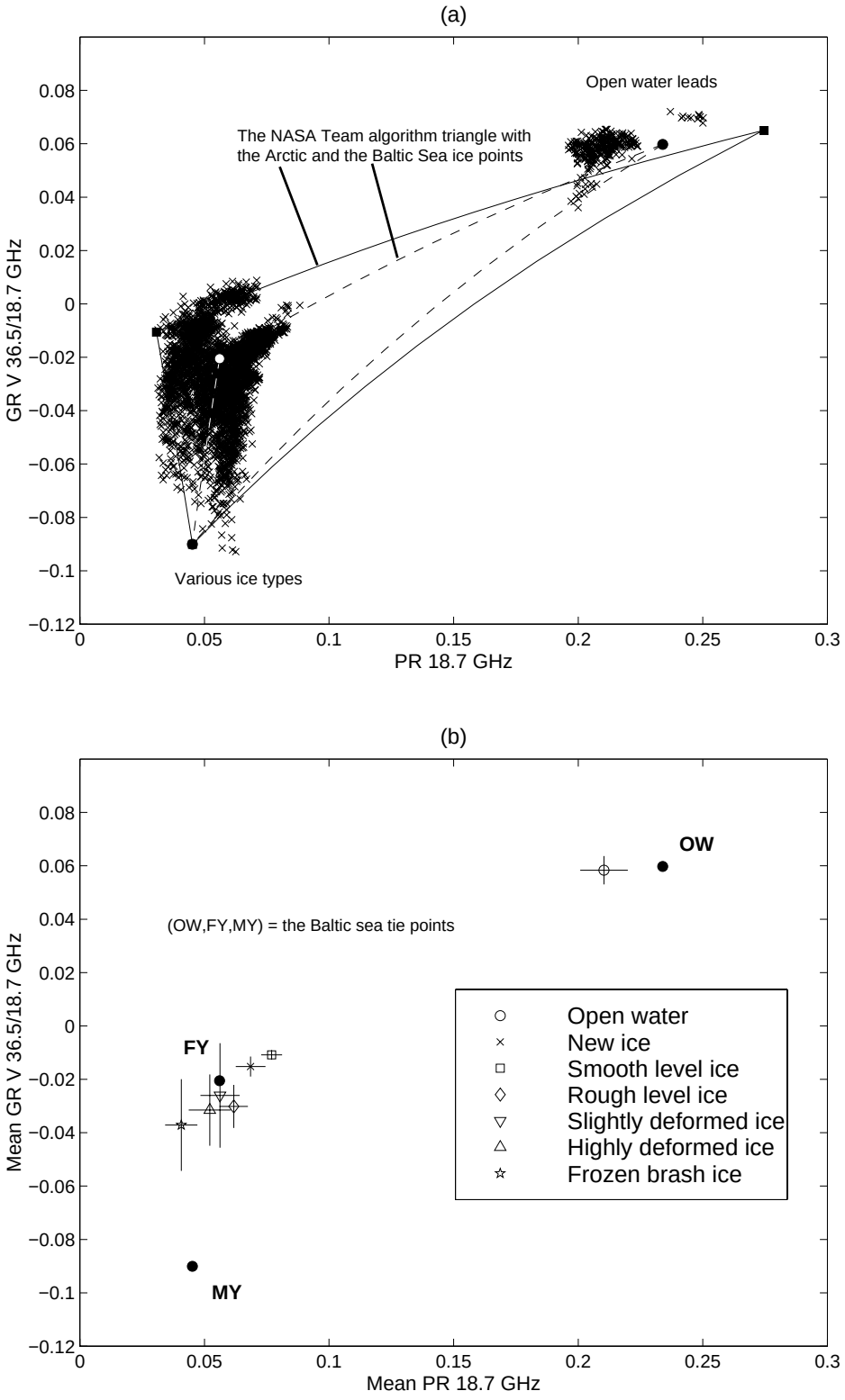

Figure 6.5 Polarization ratio at 18.7 GHz versus V-polarization gradient ratio between 36.5 and 18.7 GHz for various surface types using the IMSI-97 partial dry snow cover data. (a) Scatter plot using the data averaged to a resolution of 100 m. (b) Mean and ±1 standard deviation confidence intervals of the polarization and gradient ratio.

6.5 Summary

The most important results for deriving the Baltic Sea ice concentration with the SSM/I and AMSR-E data are:

(1) The mean PR decreases (max 0.10) at all frequencies with increasing ice deformation, i.e. large scale roughness.

(2) The principal component analysis (PCA) indicated that the airborne radiometer datasets were only one-dimensional, which suggests that only concentration of two Baltic Sea surface types, open water and sea ice in general, can be resolved from spaceborne radiometer data.

(3) Open water leads can be discriminated from all sea ice types using even single-channel data in the frequency range 6.8 to 36.5 GHz, regardless of the wetness of snow cover.

(4) Classification of various ice types is possible under dry snow condition using PR and GR ratios. However, determination of the Baltic Sea ice type concentrations from coarse resolution spaceborne data may not be possible, because the mean $PR-GR$ signatures for various ice types are very close to each other. This is supported by the PCA results.

(5) The results for the partial dry snow cover data suggest that it is possible to use spaceborne radiometer data with the NASA Team and Bootstrap algorithms to map total ice concentration after modification of the reference signatures for open water and 100% ice concentration. Likely, it is not possible to modify the NASA Team algorithm to resolve concentrations of thin ice and all other ice types combined in the Baltic Sea as has been done for the Arctic seasonal ice zones.

7 Conclusions

The intention of the presented work was to conduct basic research on the microwave remote sensing of the Baltic Sea ice in order to support development of operational classification algorithms for spaceborne SAR data (ERS-2, RADARSAT-1, ENVISAT ASAR; forthcoming RADARSAT-2 and TerraSAR-X), and ice concentration algorithms for SSM/I and AMSR-E radiometer data. Additionally, a comprehensive review of the previous work was presented. The main results, and also new scientific knowledge achieved in this work, are summarized as:

- Empirical statistics for C- and X-band σ° signatures of various ice types have been established using a large amount data acquired with the helicopter-borne HUTSCAT scatterometer [P1].
  - It is not possible to reliably discriminate open water and various ice types using only the level of σ°, R_{co}, R_{cr} (i.e. intensity) or std(σ°).
  - Snow wetness has a large effect on the σ° statistics. Notably, when snow cover is wet, the σ° contrasts between various ice types are smaller than in dry snow case. (This has been observed also previously, but the results here with a large data set confirm this firmly).
  - C-band VH-polarized σ° at high incidence angle, e.g. 45º, provides slightly better ice type discrimination accuracy than any other combination of used C- and X-band radar parameters.
  - The σ° contrast between level ice and ice deformations is larger at VH-polarization than at co-polarizations. Thus, VH-polarized SAR images are more suitable for estimating the degree of ice deformation.
- L- and C-polarimetric discriminants for four ice types have been studied using airborne SAR data averaged to simulate coarse resolution spaceborne data (pixel size was 60 by 60 m) [P2].
  - Multiple scattering is stronger at L- than at C-band.
  - C-band results can be generally explained by dominating ice surface scattering.
  - At L-band the scattering process seems to be more complicated and further work in needed to find out the dominating scattering mechanisms.
- Empirical relationships has been established between the radar incidence angle θ_0 and mean C-band HH-polarized σ° (RADARSAT-1 SAR) under dry snow and wet snow condition [P3].
  - The method for deriving the relationship is also applicable for other SAR images.
  - The relationship between σ° and θ_0 is the basis for compensating the σ° incidence angle variation in the SAR images before their classification.
- Standard deviation of σ° for various ice types depends on the length of measurement (l) [P4].
  - It seems that sea ice σ° as a function of l is not completely described either by fractional Brownian motion, a process with a single-scale autocorrelation function or as samples from only one probability distribution (e.g. random fading).
  - The regression coefficients a, b of (4.6) describing the dependency of ln(l) versus ln(std(σ°)) do not discriminate various ice types better than just mean and std of σ°, but their use is preferred due to their scale-invariant comparability with the results of other studies.

  - It is possible that a relation exists between b computed from a profile of large scale ice surface roughness and b computed from a σ° profile.

- There is a large variation of level ice σ° with changing weather conditions. A 1-D high-resolution thermodynamic snow/ice model (HIGHTSI) generally helps to interpret changes in the σ° time series [P5].
  - The modeled snow and ice surface temperature, cases of snow melting, and evolution of snow and ice thickness are related to the changes in σ°.
  - The HIGHTSI model could act as an indicator of various ice and snow conditions and, combined with SAR data, provide an empirical database describing typical relationships between σ° and changing sea ice properties for SAR classification algorithm development.

- Empirical statistics for T_B and PR signatures of various ice types in the frequency range from 6.8 to 36.5 GHz have been established using airborne radiometer data [P6].
  - It is possible to use spaceborne radiometer data with the NASA Team and Bootstrap algorithms to map total ice concentration after modification of the reference signatures for open water and 100% ice concentration. (A previous result confirmed here).
  - Likely, it is not possible to resolve concentrations of thin ice (i.e. new ice) and all other ice types combined in the Baltic Sea, as has been done for the Arctic seasonal ice zones.

7.1 Recommendations for Future Research

In the following are some suggestions for future research concerning microwave remote sensing of the Baltic Sea ice.

Major topics relevant for SAR-based sea ice monitoring

All future field campaigns should include measurements of ice small-scale surface roughness to enable comparison between theoretical σ° models and empirical σ° data for validation of the theoretical models and better interpretation of σ° data.

Large-scale surface ice roughness measurements with a 3-D laser profiler would enable to study relationships between σ° and surface roughness statistics, i.e., extend the study of [P4].

The results of [P5] need to be verified and extended using a larger SAR database with a small average sampling interval, like 2-3 days, and combined with detailed ground truth data (e.g. surface roughness, solar shortwave and thermal longwave radiative fluxes). The HIGHTSI model should be further developed to simulate also bulk or vertical profile of snow wetness and a statistical distribution of snow grain size. Validated theoretical σ° models together with the improved HIGHTSI model should enable to much better understand the changes in the σ° time series.

Capability of L-band SAR data for the Baltic Sea ice monitoring. This can studied using ALOS (Advanced Land Observing Satellite) PALSAR (Phased Array type L-band SAR) data (1.27 GHz; maximum swath width 250 to 350 km with either HH- or VV-polarization). According to (Dierking and Askne 1998), the σ° contrast between level ice and deformed ice types was much larger at L-band than at C-band.

Capability of polarimetric SAR data for the Baltic Sea ice monitoring. Polarimetric discriminants and decomposition theorems (Cloude and Pottier 1996) should provide better ice type discrimination than current single- and dual-channel SAR data. RADARSAT-2 (launch scheduled for 2007) will provide C-band polarimetric data over narrow 25 km wide swaths.

Minor topics relevant for SAR-based sea ice monitoring

Volume scattering models need data on the air bubble size, shape and correlation between the positions of the bubbles in sea ice. Statistics on these variables are very limited and, if possible, they should be acquired in the field campaigns.

Further measurements of the Baltic Sea ice dielectric constant ε_r should be conducted in order to verify the model in (4.1) and (4.2). The study should include measurements of both new thin ice and older thicker ice to determine their ε_r behavior.

Dielectric constant for snow on the Baltic Sea ice has never been investigated. Its measurements for snow covers with different characteristics (density, wetness, grain size) would allow to assess the accuracy of the snow fork instrument (Sihvola and Tiuri 1986) for estimation of snow density and wetness. The instrument calculates density and wetness from the measured ε_r (below 1 GHz) using empirical relations developed for snow on land. Statistics on snow density and grain size are also useful for theoretical σ° modeling.

Capability of X-band SAR data for the Baltic Sea ice monitoring. In near future X-band SAR data are available from TerraSAR-X (launch scheduled for 2007). According to HUTSCAT results in [P1] C-band is slightly better for sea ice monitoring than X-band.

Topics relevant for sea ice monitoring based on radiometer or optical data

SSM/I and AMSR-E radiometer data can provide estimation on the Baltic Sea ice concentration, after modifications of the algorithms for the Artic Sea ice or development of new algorithms (this task is rather easily achieved as the data are free and software tools are available).

MODIS optical and infrared data can provide independent information on the Baltic Sea ice conditions for validation of the SAR and radiometer based sea ice products, after cloud masking and surface type classification algorithms have been developed specially for the Baltic Sea.

General scientific interest

In general, it would be very interesting and useful to study evolution of σ° and T_B signatures for sea ice, from the formation of ice to thick snow covered ice and further through spring melting, using tower-based multi-frequency, multi-incidence angle measurements combined with detailed ground truth measurements.

8 Summary of Appended Papers

[P1]

Backscattering signatures of various Baltic Sea ice types and open water leads were measured with the helicopter-borne C- and X-band HUTSCAT scatterometer during six ice research campaigns in 1992-1997. The measurements were conducted at incidence angles of 23 and 45 degrees. The HUTSCAT data were assigned by video imagery into various surface type categories. The ground data provided further classification of the HUTSCAT data into different snow wetness categories (dry, moist and wet snow). Various basic statistical parameters of backscattering signature data were used to study discrimination of open water leads and various ice types. The effect of various physical parameters (e.g. polarization, frequency, snow condition) to the surface type discrimination was investigated. The results from the data analysis can be used to help the development of sea ice classification algorithms for space-borne SAR data (e.g. Radarsat and Envisat). According to the results from the maximum likelihood classification it is not possible to reliably distinguish various surface types in the SAR images only by their backscatter intensity. In general, the best ice type discrimination accuracy is achieved with C-band VH-polarization σ° at an incidence angle of 45 degrees.

[P2]

The analysis performed in this paper is based on only two fully polarimetric airborne C- and L-band SAR images acquired over the Baltic Sea. The polarimetric discriminants computed from these two scenes are compared briefly with the corresponding results obtained in the Arctic conditions. Then the properties of the polarimetric discriminants as sea ice type classifiers are investigated. The backscatter coefficients with one polarization act as reference discriminants. The comparison between these two classifier sets is carried out with coarse resolution data.

[P3]

Incidence angle dependence of three statistical parameters—the mean of the backscattering coefficient (σ°), standard deviation, and autocorrelation coefficient of texture (s_T and ρ_T) – of the C-band horizontal-horizontal (HH) polarization backscattering signatures of the Baltic Sea ice are investigated using RADARSAT ScanSAR Narrow images and helicopter-borne Helsinki University of Technology Scatterometer (HUTSCAT) data. The analysis of the large amount of data shows that the relationship between the mean σ° in decibel scale and the incidence angle in the range from 19 to 46 degrees is usually well described by a linear model. In general, the RADARSAT and HUTSCAT results agree with each other, and they are also supported by theoretical backscattering model calculations; the more deformed the ice, the smaller the slope between σ° and the incidence angle, and the higher the moisture content of snow or ice, the larger the slope. The derived σ° incidence angle dependencies can be used to roughly compensate the incidence angle variation in the SAR images to help their visual and automated classification. The variability of s_T and ρ_T with the increasing incidence angle is insignificant compared to the variability within each ice type. Their average changes with the incidence angle are so small that, in practice, their trends do not need to be compensated. The results of this study can be utilized when developing classification algorithms for the RADARSAT ScanSAR and ENVISAT HH-polarization Wide Swath images of the Baltic Sea ice.

[P4]

This paper studies whether the standard deviation (std) of the Baltic Sea ice backscattering coefficient (σ°) depends on the length of measurement (l). For many kinds of surfaces, especially for a fractal one, this is the case. The study was conducted using one-dimensional C-band helicopter-borne scatterometer data and ENVISAT synthetic aperture radar (SAR) images. The results with both data sets indicate mostly a strong linear dependence between $\ln(l)$ and $\ln(\mathrm{std}(\sigma^\circ))$ up to a distance of at least a few kilometers. Based on the analysis of empirical and simulated data (fractal and nonfractal profiles), it seems that sea ice σ° as a function of l is not completely described either by fractional Brownian motion or by a process with a single-scale autocorrelation function. Neither can the values of σ° be regarded as samples from only one probability distribution. The regression coefficients describing the dependency of $\ln(l)$ versus $\ln(\mathrm{std}(\sigma^\circ))$ do not discriminate various ice types better than mean and std of σ°. However, the use of regression coefficients instead of mean and std is preferred due to their scale-invariant comparability with the results of other studies. The dependence of $\mathrm{std}(\sigma^\circ)$ on l should also be taken generally into account in the data analysis, e.g., when constructing classifiers for sea ice SAR data.

[P5]

We have compared time series of C-band HH-polarization backscattering coefficients (σ°) of the Baltic Sea land-fast level ice with results from a 1-D high-resolution thermodynamic snow/ice model (HIGHTSI). The σ° time series were obtained from ENVISAT synthetic aperture radar (SAR) images. The study period was from the middle of the winter to the early melt season, February 3 - April 7, 2004. Due to the large incidence angle range of the SAR images, the σ° values were divided into three subseries. In general, the HIGHTSI results greatly helped to interpret the σ° behavior with changing ice and weather conditions. The modeled snow surface temperature, cases of snow melting, and evolution of snow and ice thickness were related to the changes in σ°. Equally useful information could not be obtained solely on the basis of large-scale atmospheric models. Realistic forcing data for HIGHTSI were available in the form of coastal weather observations and model results of the European Centre of Medium-Range Weather Forecasts (ECMWF). The latter make it possible to apply HIGHTSI in the interpretation of SAR data from all ice-covered seas. There were some cases where detailed ground truth, combined with theoretical σ° modeling, would have been needed for interpretation of the σ° trends. A very interesting observation was the large variation of level ice σ° with changing weather conditions, which complicates automatic classification of the SAR images, and thus, the algorithms must be tuned for different ice conditions. The HIGHTSI model could act as an indicator of various ice conditions for algorithm development.

[P6]

Passive microwave signatures of various Baltic Sea ice types and open water leads were measured in the spring of 1995 and in March 1997 with airborne non-imaging microwave radiometers (MWR) operating in the frequency range from 6.8 to 36.5 GHz. The MWR datasets were assigned by video imagery into open water leads and various ice type categories. The ground data provided further classification into dry, moist and wet snow sub-categories. The datasets were used to study the behavior of the brightness temperature and polarization ratio as a function of frequency and the degree of ice deformation; additionally, the dimensionality of multichannel datasets, classification of surface types, and suitability of the SSM/I and AMSR-E data and NASA Team and Bootstrap ice concentration algorithms for the mapping of the Baltic Sea ice were examined. The results indicate that open water leads can be distinguished from sea ice regardless of the snow cover wetness, using even single-channel MWR data. Classification of ice types is possible only under dry snow condition. Determination of the ice type concentrations from the coarse-resolution spaceborne MWR data is not feasible, because the mean signatures for various ice types are very close to each other. The results also suggest that SSM/I and AMSR-E data together with the NASA Team and Bootstrap algorithms can be used to map total ice concentration after modifications of open water and sea ice reference signatures.

References

Barber, D. G., T. N. Papakyriakou, M. E. Shokr, and E. F. LeDrew, "An examination of the relation between the spring period evolution of the scattering coefficient and radiative fluxes over landfast sea ice," Int. J. Remote Sensing, vol. 16, no.17, pp. 3343-3363, 1995.

Barber, D.G., and A. Thomas, "The influence of cloud cover on the radiation budget, physical properties, and microwave scattering coefficient (σ°) of first-year and multiyear sea ice," IEEE Trans. Geosci. Remote Sensing, vol. 36, no. 1, pp. 38-50, 1998.

Barber, D. G., and S. V. Nghiem, "The role of snow on the thermal dependence of microwave backscatter over sea ice," J. Geophysical Research, vol. 104, no. C11, pp. 25789-25803, 1999.

Barber, D. G., J. J. Yackel, and J. M. Hanesiak, "Sea ice, RADARSAT-1 and Arctic climate processes: a review and update," Canadian J. Remote Sensing, vol. 27, no. 1, pp. 51-61, 2001.

Beran, J., Statistics for Long-Memory Processes. London, UK: Chapman & Hall, 1994.

Born, M., and E. Wolf, Principles of Optics. Oxford, UK: Pergamon Press, 1980.

Brown, G. S., "A theory for near-normal incidence microwave scattering from first-year sea ice," Radio Science, vol. 17, no. 1, pp. 233-243, 1982.

Carlström, A., "Discrimination of low salinity sea ice types using VV- and VH-polarization C-band SAR imagery," in Proc. of IGARSS'90, College Park, Maryland, USA, pp. 2233-2236, 1990.

Carlström, A., "A microwave backscattering model for deformed first-year sea ice and comparisons with SAR data," IEEE Trans. Geoscience and Remote Sensing, vol. 35, no. 2, pp. 378-391, 1997.

Carlström, A., and L. M. H Ulander, "Validation of backscatter models for level and deformed ice sea ice in ERS-1 SAR images," Int. J. Remote Sensing, vol. 16, no. 7, pp. 3245-3266, 1995.

Cavalieri, D. J., P. Gloersen, and W. J. Campbell, "Determination of sea ice parameters with the Nimbus 7 SMMR," J. Geophysical Research, vol. 89, no. D4, pp. 5355-5369, 1984.

Cavalieri, D. J., J. P. Crawford, M. R. Drinkwater, D. T. Eppler, L. D. Farmer, R. R. Jentz, and C. C. Wackerman, "Aircraft active and passive microwave validations of sea ice concentrations from DMSP SSM/I," J. Geophysical Research, vol. 96, no. C12, pp. 21989-22008, 1991.

Cavalieri, D. J., "A microwave technique for mapping thin sea ice," J. Geophysical Research, vol. 99, no. C6, pp. 12561-12572, 1994.

Chen, S. S., J. M. Keller, and R. M. Crownover, "On the calculation of fractal features from images," IEEE Trans. Pattern Anal. Mach. Intell, vol. 15, no. 10, pp. 1087-1090, 1993.

Cheng, B., On the modelling of sea ice thermodynamics and air-ice coupling in the Bohai Sea and the Baltic Sea. PhD dissertation, Finnish Institute of Marine Research – Contributions, No. 5, Finland, 2002.

Cheng, B., J. Launiainen, T. Vihma, and J. Uotila, "Modelling sea ice thermodynamics in BALTEX-BASIS", Ann. of Glaciology, vol. 33, no.1, pp. 243-247, 2001.

Cheng, B., J. Launiainen, and T. Vihma, "Modelling of superimposed ice formation and sub-surface melting in the Baltic Sea", Geophysica, vol. 39, no. 1-2, pp. 31-50, 2003.

Christensen, E. L., N. Skou, J. Dall, K. W. Woelders, J. H. Jørgensen, J. Granholm, and S. N. Madsen, "EMISAR: an absolutely calibrated polarimetric L- and C-band SAR," IEEE Trans. Geoscience and Remote Sensing, vol. 36, no. 6, pp. 1852-1865, 1998.

Church, E. L., "Fractal surface finish," Applied Optics, vol. 27, no. 8, pp. 1518-1526, 1988.

Closa, J., B. Rosich, and A. Monti-Guarnieri, "The ASAR Wide Swath mode products," in Proc. IGARSS'03, Toulouse, France, 2003, CD II: 1118-1120, 2003.

Cloude, S. R., and E. Pottier, "A review of target decomposition theorems in radar polarimetry", IEEE Trans. Geoscience and Remote Sensing, vol. 34, no. 2, pp. 498-518, 1996.

Comiso, J. C., SSM/I ice concentrations using the Bootstrap algorithm. NASA technical report RP-1380, NASA Goddard Space Flight Center, Greenbelt, MD, USA, 1995.

Comiso, J. C., D. J. Cavaleiri, C. L. Parkinson, and P. Gloersen, "Passive microwave algorithms for sea ice concentration: A comparison of two techniques," Remote Sensing of Environment, vol. 60, no.3, pp. 357-384, 1997.

Cox, G.F.N., and W. F. Weeks, 1983 "Equations for determining the gas and brine volumes in sea ice samples", J. Glaciology, vol. 29, no. 102, pp. 306-316, 1983.

Dall, J., K. Woelders, S. S. Kristensen, J. Grinder-Pedersen, H. Skriver, S. N. Madsen, and E. Lintz Christensen, "EMISAR deployment in the EMAC campaigns," in EMAC 94/95 Final Results, Workshop Preceedings, ESTEC, The Netherlands, WPP-136, ESA, pp. 19-25, 1997.

Dammert, P., L. Ulander, and B. Larsson, "ERS-1 SAR signatures of sea ice and leads," in Baltic Experiment for ERS-1 (BEERS), L. Ulander, Ed., Research Report No. 51, Winter Navigation Research Board, National Maritime Administration, Norrköping, Sweden, pp. 71-98, 1994.

Dammert, P. B. G., M. Leppäranta, and J. Askne, "SAR interferometry over Baltic Sea ice," Int. J. Remote Sensing, vol. 19, no. 16, pp. 3019-3037, 1998.

Davidson, A. C., and D. V. Hinkley, Bootstrap Methods and their Application. New York: Cambridge University Press, 1997.

Davidson, M. W. J., T. Le Toan, F. Mattia, G. Satalino, T. Manninen, and M. Borgeaud, "On the characterization of agricultural soil roughness for radar remote sensing studies", IEEE Trans. Geoscience and Remote Sensing, vol. 38, no. 2, pp. 630-640, 2000.

Dierking, W., A. Carlström, and L. H. M. Ulander, "The Effect of inhomogeneous roughness on radar backscattering from slightly deformed sea ice," IEEE Trans. Geoscience and Remote Sensing, vol. 35, no. 1, pp. 147-159, 1997.

Dierking, W., and J. Askne, "Polarimetric L- and C-band SAR signatures of Baltic Sea ice observed during EMAC-95," in Proc. 17th EARSel Symposium, Lyngby, Denmark, pp. 329-336, 1998.

Dierking, W., M. I. Pettersson and J. Askne, "Multifrequency scatterometer measurements of Baltic Sea ice during EMAC-95," Int. J. Remote Sensing, vol. 20, no. 2, pp. 349-372, 1999.

Dokken, S. T., B. Håkansson, and J. Askne, "Inter-comparison of Arctic Sea ice concentration using RADARSAT, ERS, SSM/I and in-situ data," Canadian J. Remote Sensing, vol. 26, no. 6, pp. 521-536, 2000.

Drinkwater, M. R., R. Kwok, D. P. Winebrenner, and E. Rignot, “Multifrequency polarimetric synthetic aperture radar observations of sea ice,” J. Geophysical Research, vol. 96, no. C11, pp. 20679-20698, 1991.

Drinkwater, M. R., R. Kwok, E. Rignot, H. Israelsson, R. G. Onstott, and D. P. Winebrenner, “Potential applications of polarimetry to the classification of sea ice”, in Microwave Remote Sensing of Sea Ice, F. Carsey ed., Washington D.C.: AGU, pp. 419-430, 1992.

Drinkwater, M. R., R. Francis, G. Ratier, and D. J. Wingham, “The European Space Agency's Earth Explorer Mission CryoSat: measuring variability in the cryosphere”, Ann. of Glaciology, vol. 39, no. 1, pp. 313-320, 2004.

Eicken, H. and M. A. Lange, “Development and properties of sea ice in the coastal regime of the southern Weddell Sea,” J. Geophysical Research, vol. 94, no. C6, pp. 8193-8206, 1989.

Eppler, D. T., and 14 co-authors, “Passive microwave signatures of sea ice,” in Microwave Remote Sensing of Sea Ice, F. Carsey, Ed., Washington D.C.: AGU, pp. 47-71, 1992.

Ewe, H. T., H. K. Low and H. T. Chuah, “Fractal surface dimension for classification of remotely sensed data”, in Proc. 18th ASIAN Conf. on Remote Sens., Kuala Lumpur, Malaysia, pp. I-5-1 - I-5-6, 1997.

FracLab: A fractal analysis toolbox for signal and image processing. INRIA - The French Nat. Inst. For Res. in Comput. Sci. and Control. Available: http://www.irccyn.ec-nantes.fr/hebergement/FracLab/index.html, 2007.

Fung, A. K., Microwave Scattering and Emission Models and Their Applications. Norwood, MA, USA: Artech House, Inc., 1994.

Fung, A. K., Z. Li, and K. S. Chen, “Backscattering from a randomly rough dielectric surface,” IEEE Trans. Geoscience and Remote Sensing, vol. 30, no. 2, pp. 356-369, 1992.

Gambini, M., M. Mejail, J. Jacobo, and C. Delrieux, “SAR image segmentation through B-spline deformable contours and fractal dimension,” in Proc. ISPRS, Istanbul, Turkey, 5 p., 2004.

Gatelli, F., A. M. Guarnieri, F. Parizzi, P. Pasquali, C. Prati, and F. Rocca, “The wavenumber shift in SAR interferometry,” IEEE Trans. Geoscience and Remote Sensing, vol. 32, no. 4, pp. 855-865, 1994.

Gohin, F., “ Some active and passive microwave signatures of Antarctic sea ice from midwinter to spring 1991,” Int. J. Remote Sensing, vol. 16, no. 11, pp. 2031-2054, 1995.

Graham, L. C., “Synthetic interferometer radar for topographic mapping,” Proc. of the IEEE, vol. 62, no. 6, pp. 763-768, 1974.

Grandell, J., and M. Hallikainen, Modeling and retrieval of snow and sea ice characteristics in the frequency range 6 to 90 GHz. Report 21, Laboratory of Space Technology, Helsinki University of Technology, Finland, 1994.

Grandell, J., J. A. Johannessen, and M. Hallikainen, “Comparison of ERS-1 AMI wind scatterometer and SSM/I sea ice detection in the Baltic Sea,” The Photogrammetric Journal of Finland, vol. 15, no. 1, pp. 6-23, 1996.

Granskog, M. A., M. Leppäranta, T. Kawamura, J. Ehn, and K. Shirasawa, ”Seasonal development of the properties and composition of landfast sea ice in the Gulf of Finland, the Baltic Sea”, J. Geophys. Res., vol. 109, no. C02020, doi: 10.1029/2003JC001874, 2004.

Granskog, M., Investigations into the physical and chemical properties of Baltic Sea ice. PhD dissertation, Division of Geophysics, Department of Physical Sciences, University of Helsinki, 2004.

Granskog, M., T. Vihma, R. Pirazzini, and B. Cheng, "Superimposed ice formation and surface energy fluxes on sea ice during the spring melt-freeze period in the Baltic Sea," J. Glaciology, vol. 52, no. 176, pp. 119-127, 2006.

Grönvall, H., and A. Seinä, "The IMSI results in the Baltic Sea - digital sea ice products to the users at sea," in Proc. of POAC'99, Helsinki, Finland, pp. 210-219, 1999.

Haapala, J., Modelling of the seasonal ice cover of the Baltic Sea. PhD dissertation, Report Series in Geophysics No. 42, Department of Geophysics, University of Helsinki, 2000.

Haas, C., "Airborne electromagnetic sea ice thickness sounding in shallow, brackish water environments of the Caspian and Baltic Seas," In Proc. OMAE2006, Hamburg, Germany, 6 p., 2006.

Hall, D. K., J. R. Key, K. A. Casey, G. A. Riggs, and D. J. Cavalieri, "Sea ice surface temperature product from MODIS," IEEE Trans. Geoscience and Remote Sensing, vol. 42, no. 5, pp. 1076-1087, 2004.

Hallikainen, M., "A new low-salinity sea ice model for UHF radiometry," Int. J. Remote Sensing, vol. 4, no. 3, pp. 655-681, 1983.

Hallikainen, M., "Microwave remote sensing of low-salinity sea ice," in Microwave Remote Sensing of Sea Ice, F. Carsey, Ed., Washington D.C.: AGU, pp. 361-373, 1992.

Hallikainen, M., F.T. Ulaby, and M. Abdelrazik, "Dielectric properties of snow in the 3 to 37 GHz range," IEEE Trans. Antennas Propagat., vol. AP-34, no. 11, pp. 1329-1340, 1986.

Hallikainen, M., and P.-V. Mikkonen, "Sea ice studies in the Baltic Sea using satellite microwave radiometer data," in Proc. of IGARSS'86, Zurich, Switzerland, pp. 1089-1094, 1986.

Hallikainen, M. T., M. Toikka, and J Hyyppä, "Microwave dielectric properties of low-salinity sea ice," in Proc. of IGARSS'88, Edinburgh, UK, pp. 419-420, 1988.

Hallikainen, M., and D. P. Winebrenner, "The physical basis for sea ice remote sensing," in Microwave Remote Sensing of Sea Ice, F. Carsey, Ed., Washington D.C.: AGU, pp. 28-46, 1992.

Hallikainen, M., and M. Toikka, "Classification of sea ice types with radar," in Proc. of 22nd European Microwave Conference, Espoo, Finland, pp. 957-962, 1992.

Hallikainen, M., J. Hyyppä, J. Haapanen, T. Tares, P. Ahola, J. Pulliainen, and M. Toikka, "A helicopter-borne eight-channel ranging scatterometer for remote sensing - Part I: system description," IEEE Trans. Geoscience and Remote Sensing, vol. 31, no. 1, pp. 161-169, 1993.

Hallikainen, M., M. Kemppinen, J. Pihlflyckt, I. Mononen, T. Auer, K. Rautiainen, J. Lahtinen, S. Tauriainen, and H. Valmu, "HUTRAD: airborne multifrequency microwave radiometer," in Proc. 2nd ESA Workshop on Millimetre Wave Technology and Applications, Espoo, Finland, ESA WPP-149, pp.115-120, 1998.

Hanesiak, J. M., J. J. Yackel, and D. G. Barber, "Effect of melt ponds on first-year sea ice ablation – integration of RADARSAT-1 and thermodynamic modelling," Canadian J. Remote Sensing, vol. 27, no. 5, pp. 433-442, 2001.

Herland, E.-A., and R. Berglund, “Demonstration of operational sea-ice monitoring in the Baltic Sea with ERS-1 SAR“, Int. J. Remote Sensing, vol. 16, no. 17, pp. 3427-3439, 1995.

Hyyppä, J., and M. Hallikainen, “Classification of low-salinity sea ice types by ranging scatterometer,” Int. J. Remote Sensing, vol. 13, no. 13, pp. 2399-2413, 1992.

Hyyppä, J., M. Mäkynen, and M. Hallikainen, “Calibration accuracy of the HUTSCAT airborne scatterometer”, IEEE Trans. Geoscience and Remote Sensing, vol. 37, no. 3, pp. 1450-1454, 1999.

Jevrejeva, S., “Severity of winter seasons in the northern Baltic Sea between 1529 and 1990: reconstruction and analysis,” Climate Research, vol. 17, no. 1, pp. 55-62, 2001.

Jevrejeva, S. and J. C. Moore, “Singular spectrum analysis of Baltic Sea ice conditions and large-scale atmospheric patterns since 1708,” Geophysical Research Letters, vol. 28, no. 23, pp. 4503-4506, 2001.

Johansson, R., Laser based surface roughness measurements of snow and sea ice on the centimeter scale. Research Report 162, Chalmers Univ. Tech., Sweden, 1988.

Karvonen, J., “Baltic Sea Ice SAR segmentation and classification using modified pulse-coupled neural networks,” IEEE Trans. Geoscience and Remote Sensing, vol. 42, no. 7, pp. 1566-1574, 2004.

Karvonen, J., Compaction of C-band synthetic aperture radar based sea ice information for navigation in the Baltic Sea. PhD dissertation, Report D17, Laboratory of Computer and Information Science, Helsinki University of Technology, Espoo, Finland, 2006.

Karvonen, J., and M. Similä, “Pulse-coupled neural networks for sea ice SAR image segmentation and classification,” Proc. SPIE, vol. 3728, pp. 333-350, 1999.

Karvonen, J., M. Similä and M. Mäkynen, “An iterative incidence angle normalization algorithm for sea ice SAR images,” in Proc. IGARSS’02, Toronto, Canada, CD III: 1524-1528, 2002.

Karvonen, J., M. Similä, and I. Heiler, “Ice thickness estimation using SAR data and ice thickness history,” in Proc. IGARSS’03, Toulouse, France, CD I: 74-76, 2003.

Karvonen, J., M. Similä, J. Haapala, C. Haas, and M. Mäkynen, “Comparison of SAR data and operational sea ice products to EM ice thickness measurements in the Baltic Sea,” In Proc. IGARSS’04, Anchorage, Alaska, USA, DVD V: 3021-3024, 2004.

Karvonen, J., M. Similä, and M. Mäkynen, “Open water detection from Baltic Sea ice Radarsat-1 SAR imagery,” IEEE Geoscience and Remote Sensing Letters, vol. 2, no. 3, pp. 275-279, 2005.

Kawamura, T., K. Shirasawa, N. Ishikawa, A. Lindfors, K. Rasmus, M. A. Granskog, M. Leppäranta, T. Martma, and R. Vaikmäe, “Time series observations of the structure and properties of brackish ice in the Gulf of Finland, the Baltic Sea,” Ann. of Glaciology, vol. 33, pp. 1-4, 2001.

Kemppainen, H., Applicability of synthetic aperture radar in interpretation of sea ice in the Baltic Sea (in Finnish). M. Sc. Thesis, Department of Civil Engineering and Surveying, Helsinki University of Technology, Espoo, Finland, 1989.

Kolkki, O., “A review on the climate in Finland (in Finnish),” Ilmat. Lait. Tied., vol. 18, 1969.

Kurvonen, L., and M. Hallikainen, “Classification of Baltic Sea ice types by airborne multifrequency microwave radiometer,” IEEE Trans. Geoscience and Remote Sensing, vol. 34, no. 6, pp. 1292-1299, 1996.

Launiainen, J., and B. Cheng, “Modelling of ice thermodynamics in natural water bodies,” Cold Regions Science and Technology, vol. 27, no. 3, pp. 153-178, 1998.

Lensu, M., The evolution of ridged ice fields. PhD dissertation, Report M-280, Ship Laboratory, Helsinki University of Technology, 2003.

Leppäranta, M., and A. Seinä, ”Statistics of fast ice thickness along the Finnish coast,” Finnish Marine Research, vol. 249, pp. 62-71, 1982.

Leppäranta, M., and T. Manninen, ”The brine and gas content of sea ice with attention to low salinities and high temperatures”, Finnish Institute of Marine Research, Internal Report no. 2, 1988.

Leppäranta, M., and T. Thompson, ”BEPERS-88 sea ice remote sensing with synthetic aperture radar in the Baltic Sea,” Eos, vol. 70, no. 28, pp. 698-699, 708-709, 1989.

Leppäranta, M., R. Kuittinen, and J. Askne, ”BEPERS pilot study: an experiment with X-band synthetic aperture radar over the Baltic Sea ice,” J. Glaciology, vol. 38, no. 128, pp. 23-35, 1992.

Leppäranta, M., and R. Hakala, “The structure and strength of first-year ice ridges in the Baltic Sea,” Cold Regions Science and Technology, vol. 20, no. 3, pp. 295-311, 1992.

Leppäranta, M., Y. Sun, and J. Haapala, ”Comparisons of sea ice velocity fields from ERS-1 SAR and a dynamic model,” J. Glaciology, vol. 44, no. 147, pp. 248-262, 1998.

Lopez-Martinez, C., L. Ferro-Famil, and E. Pottier, “Tutorials of POLSARPRO: The polarimetric SAR data processing and educational tool”. Available: http://earth.esa.int/polsarpro/, 2007.

Lundin, M., SAR remote sensing of snow covered sea ice in brackish water – Investigations from the Baltic Sea. Licentiate thesis, Tech. Rep. no 395L, Dep. of Radio and Space Science, Chalmers Univ. of Tech., Sweden, 2001.

Mallat, S., “A theory for multiresolution signal decomposition: the wavelet representation,” IEEE Trans. Pattern Anal. Mach. Intell., vol. 11, no. 7, pp. 674-693, 1989.

Manninen, T., “Effects of ice ridge properties on calculated surface backscattering in BEPERS-88,” Int. J. Remote Sensing, vol. 13, no. 13, pp. 2467-2487, 1992.

Manninen, T., “Statistical calculations of 3D-orientation parameters of flat symmetrical polyhedrons,” Pattern Recognition Letters, vol. 14, no. 3, pp. 207-211, 1993.

Manninen, T., “Orientational approximation of convex polygons with rectangles,” Pattern Recognition Letters, vol. 15, no. 7, pp. 677-682, 1994.

Manninen, T., Microwave surface backscattering and surface roughness of Baltic Sea ice. PhD dissertation, Report 265, Finnish Marine Research Institute, Helsinki, Finland, 1996a.

Manninen, T., “Surface morphology and backscattering of ice-ridge sails in the Baltic Sea,” J. Glaciology, vol. 42, no. 140, pp. 141-156, 1996b.

Manninen, T., “Surface roughness of Baltic Sea ice,” J. Geophysical Research, vol. 102, no. C1, pp. 1119-1139, 1997a.

Manninen, T., “Multiscale surface roughness and bacscattering,” Progress in Electromagnetics Research, vol. PIER 16, pp. 175-203, 1997b.

Manninen, A. T., “Multiscale surface roughness description for scattering modelling of bare soil,” Physica A, vol. 319, pp. 535-551, 2003.

Manninen, A. T., and L. M. H. Ulander, “Forestry parameter retrieval from texture in CARABAS VHF-band SAR images,” IEEE Trans. Geoscience and Remote Sensing, vol. 39, no. 12, pp. 2622-2633, 2001.

Mahrt, L., “Stratified atmospheric boundary layers,” Boundary-Layer Meteorol., vol. 90, no. 3, pp. 375-396, 1999.

Mattia, F., and T. Le Toan, ”Backscattering properties of multi-scale rough surfaces,” J. Electromagnetic Waves and Applications, vol. 13, no. 4, pp. 493-527, 1999.

Maykut, G. A., “Energy exchange over young sea ice in the central Arctic,” J. Geophysical Research, vol. 83, no. C7, pp. 3646-2658, 1978.

Maykut, G. A., “Large-scale heat exchange and ice production in the central Arctic,” J. Geophysical Research, vol. 87, no. C10, pp. 7971-7984, 1982.

Meadows P., and P. Wrigth, “ASAR APP and APM image quality”, in Proc. of Envisat validation workshop 2002, Frascati, Italy, ESA SP-531, 16 p., 2003a.

Meadows P. J., and P. A. Wrigth, “ASAR image mode product quality,” in Proc. IGARSS’03, Toulouse, France, CD II: 1112-1114, 2003b.

Mätzler, C., R. Ramseier, and E. Svendsen, “Polarization effects in sea-ice signatures,” IEEE J. Oceanic Engineering, vol. OE-9, no. 5, pp. 333-338, 1984.

Nghiem, S. V., R. Kwok, S. H. Yueh, and M. R. Drinkwater, “Polarimetric signatures of sea ice, 2. Experimental observations”, J. Geophysical Research, vol. 100, no. C7, pp. 13681-13968, 1995.

Palosuo, E., “Crystal structure of brackish and freshwater ice,” IASH, vol. 54, pp. 9-14, 1961.

Palosuo, E., “The Gulf of Bothnia in winter. II. Freezing and ice forms,” Merentutkimuslaitoksen julkaisu/Havsforskningsinstitutets skrift, vol. 209, pp. 1-64, 1963.

Pirazzini, R., T. Vihma, M. A. Granskog, and B. Cheng, “Surface albedo measurements over sea ice in the Baltic Sea during the spring snowmelt period,” Ann. of Glaciology, vol. 44, pp. 7-14, 2006.

Pulliainen, J., Investigation on the backscattering properties of Finnish boreal forests at C- and X-band: a semi-empirical modeling approach. PhD dissertation, Report 19, Laboratory of Space Technology, Helsinki University of Technology, Espoo, Finland, 1994.

Pulliainen, J., J.-P. Kärnä, and M. Hallikainen, “Development of geophysical retrieval algorithms for the MIMR,” IEEE Trans. Geoscience and Remote Sensing, vol. 31, no. 1, pp. 268-277, 1993.

RADARSAT International (RSI), RADARSAT data products specifications. Report RSI-GS-026, version 3/0, 2000.

Rignot, E. and R. Kwok, “Characterization of spatial statistics of distributed targets in SAR data,“ Int. J. Remote Sensing, vol. 14, no. 2, pp. 345-363, 1993.

Rosich, B., P. J. Meadows, and A. Monti-Guarnieri, “ENVISAT ASAR product calibration and product quality status,” In Proc. CEOS SAR Workshop 2004, Ulm, Germany, 8 p., 2004.

Rothrock, D. A., D. R. Thomas, and A. S. Thorndike, “Principal component analysis of satellite passive microwave data over sea ice,” J. Geophysical Research, vol. 93, no. C3, pp. 2321-2332, 1988.

Roueff, F., and J. Lévy Véhel, “A regularization approach to fractional dimension estimation,” In Proc. Fractal –Fractals and Beyond, M. M. Novak, Ed. Singapore: World Scientific, 14 p., 1998.

Ruck, G. T., Radar Cross Section Handbook. New York, USA: Plenum Press, 1970.

Saloranta, T. M., “Modeling the evolution of snow, snow ice and ice in the Baltic Sea”, Tellus, vol. 52A, no. 1, pp. 93-108, 2000.

Scheuchl B., D. Flett, R. Caves, and I. Cumming, “Potential of RADARSAT-2 data for operational sea ice monitoring,” Canadian J. Remote Sensing, vol. 30, no. 3, pp. 448-461, 2004.

Seinä, A., and J. Peltola, “Duration of ice season and statistics of fast ice thickness along the Finnish coast 1961-1990,” Finnish Marine Research Report no. 258, Finnish Institute of Marine Research, Finland, pp. 1-46, 1991.

Seinä, A., and E. Palosuo, “The classification of the maximum annual extent of ice cover in the Baltic Sea 1720-1995,” Meri Report no. 27, Finnish Institute of Marine Research, Finland, pp. 79-91, 1996.

Seinä, A., E. Palosuo, and H. Grönvall, ”Ice Service of Finnish Institute of Marine Research 1919-1994 (in Finnish),” Report series of Finnish Institute of Marine Research, no 32, 1997.

Seinä, A., H. Grönvall, S. Kalliosaari, J. Vainio, P. Eriksson, and J.-E. Lundqvist, “WMO sea ice nomenclature: terminology for the Baltic Sea in English, Finnish and Swedish,” MERI Report No. 43, Finnish Marine Research Institute, Finland, 2001.

Seinä, A., P. Mälkki, and H. Grönvall, ”GSE programme benefits to Baltic Sea ice navigation,” In Proc. of the 4th EuroGOOS, Brest, France, pp. 667-672, 2006.

Shepherd, N., “Extraction of beta nought and sigma nought from RADARSAT CDPF products“, Tech. Rep. AS97-5001 Rev. 2, Altrix Systems, Ottawa, Canada, 1998.

Sihvola, A., and M. Tiuri, “Snow fork for field determination of the density and wetness profiles of snow pack,” IEEE Trans. Geoscience and Remote Sensing, vol. 56, no. 5, pp. 717-721, 1986.

Similä, M., “SAR image segmentation by a two-scale contextual classifier,” in Proc. Image and Signal Processing for Remote Sensing, SPIE vol. 2315, Rome, Italy, pp. 434-443, 1994.

Similä, M., “SAR image classification according to the ice deformation,” in Proc. of the second International Workshop on ERS Applications, London, UK, pp. 211-214, 1996.

Similä, M., and J. Helminen, “The identification of the deformed sea ice fields from ERS-SAR image by wavelets,” in Proc. IGARSS'95, Firenze, Italy, vol. 2, pp. 868-870, 1995.

Similä, M., E. Arjas, M. Mäkynen, and M. Hallikainen, ”Bayesian classification model for sea ice roughness from scatterometer data, “ IEEE Trans. Geoscience and Remote Sensing, vol. 39, no. 7, pp. 1586-1595, 2001.

Similä, M., J. Karvonen, C. Haas, and M. Hallikainen, ”C-band SAR based estimation of Baltic Sea ice thickness distributions,” in Proc. IGARSS’06, Denver, Colorado, USA, 4 pp., 2006.

Sun, Y., A. Carlström, and J. Askne, “SAR image classification of ice in the Gulf of Bothnia,” Int. J. Remote Sensing, vol. 13, no. 13, pp. 2489-2514, 1992.

Sun, Y., “Automatic ice motion retrieval from ERS-1 SAR images using the optical flow method,” Int. J. Remote Sensing, vol. 17, no. 11, pp. 2059-2087, 1996.

Therrien, C. W., Decision Estimation and Classification, an Introduction to Pattern Recognition and Related Topics. New York: John Wiley & Sons, 1987.

Tiuri, M., M. Hallikainen, and A. Lääperi, ”Microwave radiometer theory and measurements of sea ice characteristics,” Report S89, Radio Laboratory, Helsinki University of Technology, 1976.

Tiuri, M., M. Hallikainen, and A. Lääperi, ”Radiometer studies of low-salinity sea ice,” Boundary-Layer Meteorology, vol. 3, no. 1, pp. 361-371, 1978.

Tiuri, M., A. Sihvola, E. Nyfors, and M. Hallikainen, ”The complex dielectric constant of snow at microwave frequencies”, IEEE J. Oceanic Engineering, vol. OE-9, no. 5, pp. 377-382, 1984.

Touzi R., W. M. Boerner, J. S. Lee, and E. Lueneburg, “A review of polarimetry in the context of synthetic aperture radar: concepts and information extraction”, Canadian J. Remote Sensing, vol. 30, no. 3, pp. 380-407, 2004.

Ulaby, F. T., R. K. Moore, and A. D. Fung, Microwave Remote Sensing: Active and Passive, Volume I. Reading, Massachusetts, USA: Artech House, 1981.

Ulaby, F. T., R. K. Moore, and A. D. Fung, Microwave Remote Sensing: Active and Passive, Volume II. Reading, Massachusetts, USA: Artech House, 1982.

Ulaby, F. T., R. K. Moore, and A. D. Fung, Microwave Remote Sensing: Active and Passive, Volume III. Reading, Massachusetts, USA: Artech House, 1986.

Ulander, L. M. H. “Interpretation of Seasat radar-altimeter data over sea ice using near-simultaneous SAR imagery,” Int. J. Remote Sensing, vol. 8, no. 11, pp. 1679-1686, 1987.

Ulander, L. M. H., Radar remote sensing of sea ice: measurements and theory. PhD dissertation, Technical Report no. 212, Chalmers Univ. of Tech., Göteborg, Sweden, 1991.

Ulander, L. M. H., and A. Carlström, “Radar backscatter signatures of Baltic Sea ice”, In Proc. IGARSS’91, Espoo, Finland, pp. 1215-1218, 1991.

Voipio A., The Baltic Sea. Amsterdam, Holland: Elsevier Oceanography Series No. 30, 1981.

Weeks, W. F., A. J. Gow, P. Kosloff, and S. Digby-Argus, “The internal structure, composition and properties of brackish ice from the Bay of Bothnia,” in CRREL Monograph M 90-01, pp. 5-15, 1990.

Welch, B. L., “The significance of the difference between two means when the population variances are unequal,” Biometrika, vol. 29, pp. 350-362, 1938.

Wensnahan, M., G. A. Maykut, T. C. Grenfell, and D. P. Winebrenner, “Passive microwave remote sensing of thin sea ice using principal component analysis,” J. Geophysical Research, vol. 98, no. C7, pp. 12453-12468, 1993.

Winebrenner, D. P., L. D. Farmer, and I. R. Joughin, “On the response of polarimetric synthetic aperture radar signatures at 24 cm wavelength to sea ice thickness in Arctic leads”, Radio Science, vol. 30, no. 2, pp. 373-402, 1995.

Wisman, V., A. Cavanie, D. Hoekman, K. Boehnke, and C. Schmullius, “Land surface observations using the ERS-1 Windscatterometer,” Final report for ESTEC Contract: 11103/94/NL/CN, 54 p., 1996.

WMO, “Sea Ice Nomenclature: Terminology, codes and illustrated glossary,” Word Meteorological Organization, WMO No. 259-TP-145, Geneva, 1989.

Yordanov, O. I., and A. Guissaird, “Approximate self-affine model for cultivated soil roughness,” Physica A, vol. 238, no. 1-4, pp. 49-65, 1997.

Zebker, H. A., and R. M. Goldstein, “Topographic mapping from interferometric synthetic aperture radar observations,” J. Geophyscial Research, vol. 91, no. B5, pp. 4993-4999, 1986.

Zhang, Z., On modelling ice dynamics of semi-enclosed seasonally ice-covered seas. PhD dissertation, Report series in Geophysics No. 43, Dept. of Geophysics, University of Helsinki, 2000.